Imperial College
London

Development of Laser Wakefield Accelerators

Jan-Niclas GRUSE

November 2020

Supervisor: Prof. Zulfikar NAJMUDIN

Submitted in partial fulfilment of the requirements for the degree of Doctor of Philosophy in Physics of Imperial College London and for the Diploma of Imperial College London

Department of Physics
Imperial College London
Prince Consort Road
SW7 2AZ
United Kingdom

Declaration of Originality

Everything presented in this work is my, the author’s, own, if not stated otherwise and correctly referenced in the text.

Jan-Niclas Gruse November 2020

Copyright Declaration

Abstract

This thesis investigates theoretically and experimentally the wakefield generation, electron acceleration and x-ray emission in laser driven plasma wakefield acceleration.

In preparation for a multi-stage laser accelerator with multiple laser, one of the Astra-Gemini laser pulses at $100\,\mathrm{TW}$ was used to reflect off a plasma mirror, a $125\,\mu\mathrm{m}$ Kapton foil. Its reflectivity of up to 70% and beam quality was measured. The beam was then self-guide it through a gas cell in preparation for a staged plasma wakefield accelerator. These were one of the first measurements at such intensities of $4 \times 10^{17}\,\mathrm{W\,cm^{-2}}$ where the beam was injected into a gas cell. To test the usability of this beam to drive an accelerator stage, the guiding efficiency was measured and compared to particle-in-cell simulation. The simulations modelled the propagation of multi-Gaussian low beam quality laser beams at densities $0.25 - 0.75 \times 10^{18}\,\mathrm{cm^{-3}}$. Self-focusing of imperfect laser beams below the critical power is reported and simulation show potential 100s MeV energy increase and a strong argument for beam quality optimisation is made by showing that the potential energy could be increased even further close to $1\,\mathrm{GeV}$.

The same Astra-Gemini laser at $150\,\mathrm{TW}$ was used to accelerate a bunch of electrons in a single gas cell and to optimise betatron radiation. The unique properties of the betatron radiation including a high peak photon flux of $7.5 \pm 2.6 \times 10^{8}\,\mathrm{ph\ \ mrad^{-2}}$ and a synchrotron spectrum with critical energy of $14.6 \pm 1.3\,\mathrm{keV}$ was used in imaging industrial samples. The obtained data was post-processed to remove source based imaging artefacts such as bremsstrahlung hits obscuring the sample. The samples included a topography XCT sample for performance validation, a pouch cell battery and composite cylinder with a kink band failure. The results took advantage of phase-contrast enhancement show-casing its advantage compared to conventional XCT machines.

Finally, a machine learning algorithm, based on Bayesian optimisation, was implemented on the $5\,\mathrm{TW}$ Astra laser to optimise electron and x-ray properties with $1\,\mathrm{Hz}$ repetition rate. This work prepared the diagnostics and extracted the physical quantities used for the Gaussian process regression. It was used to investigate the optimisation process itself, the correlation of parameters for the enhancement of x-ray brightness with ionisation injection, based on N_2 doped He-gas. A brilliance of $4.1 \pm 1.0 \times 10^{20}\,\mathrm{ph\ \ s^{-1}\,mm^{-2}\,mrad^{-2}\,0.1\%BW^{-1}}$ with a critical energy of $2.7 \pm 0.3\,\mathrm{keV}$ can be reported at such low power as of $5.6 \pm 0.2\,\mathrm{TW}$. Furthermore, the reported energy of the electrons also exceeds similar laser power experiments.

Role of the Author

The results in this thesis are based on three experiments performed at the Central Laser Facility on the Astra-Gemini TA2 and TA3 laser system. The author acknowledge the work of the staff at the Central Laser Facility (CLF) in the planning and execution of the experiments and funding from STFC for the support of the John Adams Institute of Accelerator Science by grants ST/J002062/1 and ST/P000835/1.

4. **TA3 April - May 2018** The data from a campaign on staging laser wakefield accelerators is presented in Chapter 4. The Target Area Operators were R. Shalloo and M. J. V. Streeter. I was responsible for the post plasma-interaction diagnostics, which are all presented in detail in the chapter. The results of the density measurements were provided by colleague M. Backhouse. N. C. Lopes contribution in form of the development of the *tape drive* made the experiment possible. N. Bourgeois helped significantly as link scientist from the CLF

5. **TA3 December 2017 - January 2018** The industrial imaging was a joint venture between the multiple organisations, including the CLF, the Warwick Manufacturing Group (WMG) and the National Composite Centre (NCC). Target area operator was D. R. Symes. I took over large proportion of the responsibility in taking the data. Comparing xCT 3D scans of the topological sample and the battery was contributed by J. M. Warnett and the kink band composite render is credited to L. R. Pickard. The denoising code was provided by N. C. Lopes and the density measurements by C. I. D. Underwood.

6. **TA2 June 2019 - November 2019** The principal investigator M. J. V. Streeter was simultaneously the target area operator, together with R. Shalloo and the author as deputy. The analysis code was mostly composed by the author, M. J. V. Streeter, R. Shalloo and C. I. D. Underwood. Of this, the author was responsible for the electron spectrometer and x-ray code. Similarly, my contribution to the experiment was the set-up of the electron and x-ray diagnostic as well as setting up the pre-interaction laser diagnostic, the far-, near-field and wavefront detector. The operating system was mostly entirely developed by S. J. D. Dann and the optimisation code by him and M. J. V. Streeter.

The simulations were performed with the EPOCH code, which was developed under UK Engineering and Physics Sciences Research Council grants EP/G054940/1, EP/G055165/1 and EP/G056803/1.

Acknowledgements

The experiments I participated in through-out my time at Imperial were tough, frustrating, sleepless and difficult. Of course I am very grateful that I was able to experience them and I learned a tremendous amount. The days and nights at those experiments would have been entirely unbearable without my colleagues and friends from Imperial Matt, Rob, Elias, Sav, Jon, Emma, George, Nelson, Brendan and Michael; from York, Chris, Chris, Chris, Chris and Matt; and from CLF, Nic, Chris, Stephen and Dan.
Luckily, the time was spent mostly at Imperial and all the great people there made my PhD program an amazing experience. The post-grad pub $\hbar$ provided the necessary pints and the conversations I had were stimulating, fun and eye-opening. I cannot stress how much I appreciated all the people in the plasma group. There are way too many people to list them all, but a special shout-out to Luke and Robbie, my fellow PhD candidates and with whom I shared my office and had one too many chats during work time.
I want to point out Matt, Jon, Rob and Stuart for the large amount of professional input and discussions for some reasonably good work. Thanks to George, Luke, and Matt for dealing with my poor grammar. Last but not least, great thanks to my supervisor Zulf, who challenged me a lot and who's corrections, inspirations, corrections, guidance and corrections made this thesis possible. Thanks to him, my work reached a standard I am proud of.

Schlussendlich möchte ich mich bei meiner Familie und ganz besonders meinen Eltern bedanken. Ihr habt mich meine gesamte Studienkarriere so tatkräftig unterstützt, dass ich mich voll und ganz auf die Uni konzentrieren konnte. Dies hat dazu geführt, dass ich jetzt an diesen Punkt angelangt bin. Ein weiterer besonderen Dank geht an Oma Lotti und Barbara, die mich durchweg unterstützten.

Contents

List of Figures

List of Tables

Chapter 1

Introduction

The history of particle accelerators began decades before the first dedicated particle accelerator device. Wilhelm Röntgen discovered an unknown radiation while working with a Crookes-Hittorf tube in 1895. Formerly referred to as cathode rays, that radiation is nowadays known as x-rays[1]. The discovery earned him the very first Nobel prize in physics in 1901. In a Crookes-Hittorf tube, electrons are accelerated from a cathode to an anode. The accelerated electrons hit the end of the glass tube where the electrons emit x-rays through bremsstrahlung. The capability of this penetrating radiation was quickly identified as versatile diagnostic in medical, biological, and industrial imaging. An image of a human hand taken by W. Röntgen in 1896 can be seen in Fig. 1.1. Even though electrons are accelerated, these devices are not being considered particle accelerators nowadays as these are commonly referred to devices, which accelerate particles to greater than MeV energies[2].

The first physics-related application of such energetic particles was the discovery of the nucleus in the famous experiments led by Rutherford in 1911[4]. These experiments helped Niels Bohr with his formulation of the structure of an atom for which he was later awarded a Nobel prize in 1922. $5\,\mathrm{MeV}$ *alpha*-particles were deflected off Au-nuclei to proof the existence of a localised positively charged core. The particle were naturally decaying from Radon-222, but the necessity of particle accelerators for fundamental research was evident. The first accelerator is often credited to Cockroft and Walton, which accelerated protons to $400\,\mathrm{keV}$[5]. The device was used to intentionally split lithium nuclei, for which they received the Nobel prize in 1951. Such Cockroft-Walton accelerators are still in use, e.g. as injector and first stage accelerator of the proton accelerator at the Paul-Scherrer Institute[6]. The accelerator uses a small DC or slowly varying AC input to create a large DC field to accelerate the particles.

---

[1] [1] W. C. Röntgen. *Annalen der Physik* (1898).

[2] [2] US Department of Public Health.

[3] ([3] A Haase and G. L.&. E. Umbach. *Röntgen Centennial* (1997))

[4] [4] E. Rutherford. *The London, Edinburgh, and Dublin Philosophical Magazine and J. of Sc.* (1911).

[5] [5] J. D. Cockcroft and E. T. S. Walton. *Nature* (1932).

[6] [6] *The PSI proton accelerator* URL: `https://www.psi.ch/en/media/the-psi-proton-accelerator` (visited on 08/27/2020).

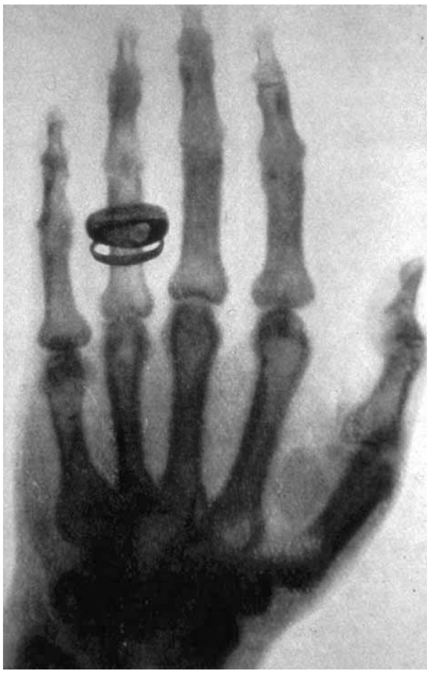

Figure 1.1: X-ray image of a colleague taken by Wilhelm Röntgen[3] in 1896 (image courtesy of wikimedia).

Different approaches using time varying fields became the trend to accelerate particles directly. Noticeable advances in accelerators, such as the cyclotron[7], synchrotron[8] and betatron[9] are still widely used. The time-varying fields applied to accelerate the particles are what is referred to as the *radio frequency* range (RF) and the largest accelerator mankind has ever built, the Large Hardon Collider at CERN[10], uses RF technology. Several modern technological advancements enable $14\,\mathrm{TeV}$ proton collisions at the LHC. Such major steps include the superconducting cavities, and bending magnets, which respectively accelerate and bend the particles onto their paths. The LHC is a $8.6\,\mathrm{km}$-diameter circle, in which the protons circulate with $1768\,\mathrm{Hz}$, taking advantage of the same accelerating cavities numerous times. The superconducting cavities achieve gradients of $5.5\,\mathrm{MV\,m^{-1}}$ and each provide the beam $2\,\mathrm{MV}$. The fundamental understanding such as the standard model (SM) of particle interactions has been investigated with these machines. With its most famous discovery of the Higgs-boson completing the SM and whose prediction was awarded the Nobel prize in 2013.

The standard model fails to predict multiple questions such as matter-antimatter asymmetry and neutrino oscillations and as such going *beyond* the standard model is the next big milestone in particle physics. It requires more energy in the centre of mass. This begs the question of why the charged particles are not kept in their trajectories

---

[7] [7] E. O. Lawrence and D. Cooksey. *Physical Review* (1936).
[8] [8] E. M. McMillan. *Physical Review* (1945).
[9] [9] D. W. Kerst. *Physical Review* (1941).
[10] [10] L. Evans. *NJP* (2007).

to take advantage of the accelerating structure for longer. Unfortunately, the energy of the particles is limited through two major ways.

For one, the Lorentz force keeping the particle on their trajectory and the centripetal force determines the radius of curvature $\rho = p/qB$, with p being the momentum of the particles and B the magnetic field. If the energy is to increase, either the radius or the magnetic field must increase as well. The previously mentioned superconducting magnets already provide the highest feasible magnetic field strength possible to-date. Thus, the radius of the apparatus has to be increased if the energy is to be increased. This is the reason, why the LHC has such large circumference of $27\,\mathrm{km}$ and why the next generation of circular collider, the *Future Circular Collider* (FCC) is proposed to have a circumference of $100\,\mathrm{km}$ to reach collision energies of $100\,\mathrm{TeV}$[11].

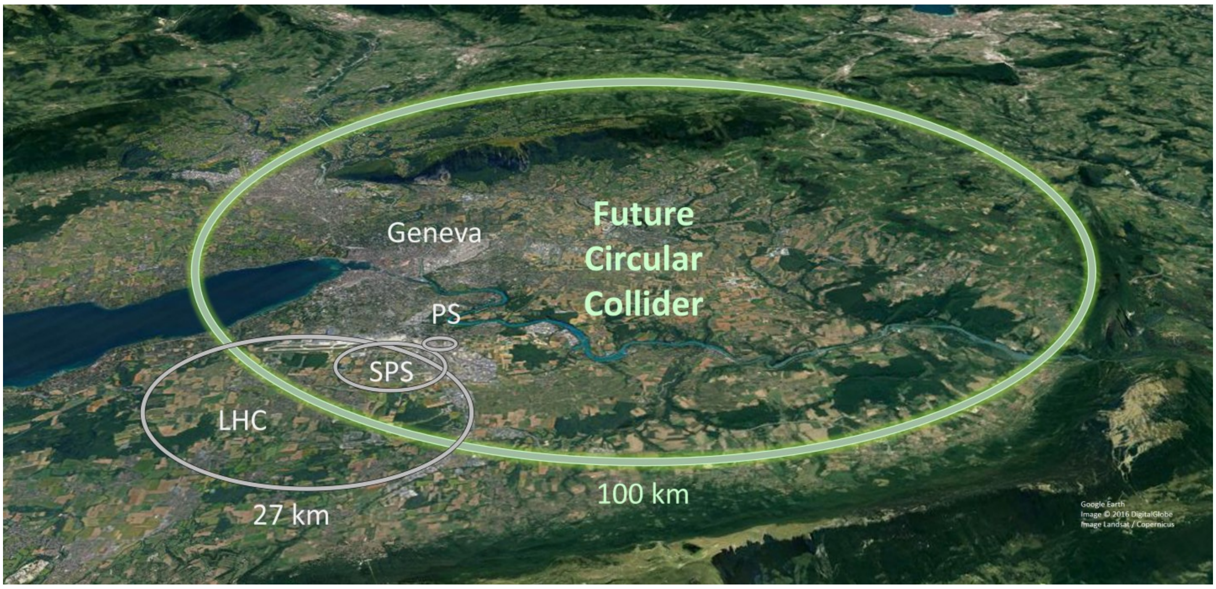

Figure 1.2: The size of the FCC compared to the LHC, the Super Proton Synchrotron (SPS), and the Proton Synchrotron (PS). Image courtesy[12] . The FCC would encircle the French *Prealps Salève*.

The second limitation of the energy is based on the choice of particles. The LHC collides protons. But as protons consists of sub-particles (quarks, gluons), cleaner studies could be done by using more fundamental particles, such as electrons and positrons. However, charged particles also emit radiation when accelerated and a circular motion is an inwards acceleration. The radiation on large scale facilities was discovered at a commercially built synchrotron in 1947[13] and is since known as *synchrotron radiation*. It is characterised by a broad spectrum with a critical energy, thus will be discussed in more details in the theory section of this work. The emitted power obeys $P \propto E^4/(m^4\rho^2)$. So if the mass of the particle is reduced by a certain factor, the

---

[11] https://home.cern/science/accelerators/future-circular-collider accessed 27.08.2020

[12] ([11] *CERN Future Circular Collider* URL: https://cds.cern.ch/images/OPEN-PHO-ACCEL-2019-001-2 [visited on 09/01/2020] (2019))

[13] [12] F. R. Elder *et al. Physical Review* (1947).

emitted power increases by the same factor to the power of 4. If electrons and protons both have the same energy and their trajectory the same radius of curvature, the power of synchrotron radiation emitted by protons is reduced to the one of electrons by a factor of $1/1843^4 \approx 10^{-13}$. The energy loss for electrons (and positrons) is so severe that this limits the maximum energy in storage rings. The centre-of-mass energy of the electron positron collision of Large-Electron-Positron (LEP) collider, the predecessor inside of the now LHC ring, was around $104.5\,\mathrm{GeV}$ compared to the $13\,\mathrm{TeV}$ centre-of-mass energy at the LHC.

Originally a parasitic mechanism, synchrotron radiation as a tool became of such importance that accelerators were built purely dedicated to being light sources. This is known as the difference between the first generation of synchrotron light source and the second generation. The second generation light source used alternating magnetic poles in a straight line to *wiggle* the electrons numerous times and are called *Wigglers*. If the trajectory of the electrons can be modelled with consecutive arcs with a definite radius of curvature the spectrum can be described with synchrotron radiation. However, if the electron trajectory becomes more like a repetitive oscillating motion, it can partially interfere with itself to radiate in harmonic frequencies. If the electrons follow a perfect oscillating motion modelled with sinusoidal function, it ultimately emits in a single wavelength. The transition between the synchrotron spectrum to a harmonic spectrum is described by the undulator parameter[14]

$$K = eB\frac{\lambda_u}{2\pi m_e c} \tag{1.1}$$

The undulator period λ_u is the wavelength of the electron motion and the angle of emission being $\propto K/\gamma$ indicates the difference between the second generation, and third generation of light sources. If the cone of emission is within the particle motion, $K/\gamma < 1$, the light can interfere continuously with itself creating strong harmonic light, which is known as *undulator* radiation. The fourth generation, the *Free-Electron Laser*, takes advantage of self-modulation inside the undulator[15]. The emitted radiation interacts back with the electron bunch itself and modulates its energy. The energy modulation turns into a density modulation through the motion inside the undulator. This *microbunching* divides the electron beam into many beam slices with spatial separations so that coherent radiation is emitted.

Many generations of synchrotron light sources are still in constant use. A notable example here in the UK is the Diamond Light Source[16]. The applications of these

---

[14] [13] Helmut Wiedemann. *Particle accelerator physics* (1994).

[15] A undulator is a Wiggler with $K/\gamma < 1$

[16] `https://www.diamond.ac.uk/` accessed 27.08.2020

sources are numerous from resolving single protein structures[17], validating the authenticity of art[18] to examining new engineering techniques for lightweight inter-metallic alloys[19].

If the circular motion of the particles is an obstacle due to the loss in energy, then a linear structure could be the answer to reach higher energies. The particles would only experience the accelerating structures once, but would not lose energy through emitting light as they are bent into circular motion by a magnet. Many such accelerators exist (e.g. Stanford Linear Accelerator Centre) and one design project with a chance of implementation is the International Linear Collider (ILC)[20]. The ILC is a $\approx 31\,\mathrm{km}$-long electron-positron collider with a centre-of-mass energy of $200 - 500\,\mathrm{GeV}$, later $1\,\mathrm{TeV}$. The reason for the long length of this accelerator is due to another technical limitation of the superconducting cavities. These have a thermal breakdown limit, such that the accelerating field does not exceed $0.1\,\mathrm{GV\,m^{-1}}$[21]. Hence, the energy increase requires lengthening of the accelerator.

The high costs and large physical requirements of conventional accelerators are creating demand for alternatives. One such alternative, most-likely the largest alternative research field, is the study of plasma-based accelerators. This work is concentrating on a sub-category of this field, the laser-based plasma wakefield acceleration.

1.1 Laser-based Plasma Accelerators

A system with enough energy can enter a state at which the ions and electrons are continuously separated. If the system additionally shows a collective electromagnetic-based behaviour and is quasi-neutral, then it can be considered to be a plasma. Plasma is often considered to be the fourth state of matter. Similar to the common states of matter, the state of plasma does not solely depend on its temperature, but also on the density. Even though mostly referring to ions and electrons, a plasma can exists between more exotic particles, such as for example quark and gluons.

Compared to classic states of matter, the binding between individual atoms and their electrons are broken in a plasma. This inspired Vladimir Veksler[22], and then Fainberg[23] to formulate the idea of using plasma to accelerate particles. The start of the field of laser plasma acceleration is considered to be Tajima's and Dawson's paper

---

[17] [14] R. D. Kornberg. *Proceedings of the National Academy of Sciences* (2007).
[18] [15] J. Dik *et al. Analytical Chemistry* (2008).
[19] [16] P. Erdely *et al. Metals* (2016).
[20] [17] T. Behnke *et al.*, Proceedings 2013.
[21] [18] N. A. Solyak. *AIP Conference Proceedings* (2009).
[22] [19] V. I. Veksler, Proceedings (1956).
[23] [20] Y. Fainberg. *Uspekhi Fizicheskih Nauk* (1967).

in 1979[24], which introduced the idea of using a laser to create high longitudinal electric fields in a plasma to accelerate electrons. The strong fields of a short laser pulse, which is here known as a driver, expel electrons from its path, leaving ions behind, which, since they are much heavier, they are left behind. The stationary ions create positively charged regions. The repelled electrons experiences a retracting force due to the ions and return on-axis. As they overshoot, they begin to oscillate with plasma frequency ω_p. This can be pictured as a pendulum wave, moving with the speed of the driver. Electrons, which happen to move with the same speed as the driver inside the ion cavity experiencing a continuous electric field, which accelerates them. Tajima and Dawson predicted field strengths exceeding $100\,\mathrm{GV\,m^{-1}}$, which exceeds the field strength of the conventional accelerating modules by several orders of magnitude.

As the laser pulses in 1979 were neither powerful enough, nor short enough to fit inside single plasma wave wavelengths, the first experimental studies were based on a technique from 1972 suggested by Rosenbluth et al.[25] who proposed the excitation of a plasma wave by interfering two parallel propagating laser beams with different frequencies. A resonance excitation occurs if the frequency difference of the two laser beams, or *beatwave* is equal to the plasma frequency. The plasma wave was measured by Clayton et al. in 1985[26] and externally injected electron were accelerated in 1993[27] by the same group. As the plasma wave depends on the laser field strength, the plasma frequency changes with increasing amplitude, causing the limitation of this technique. Beatwave accelerators were followed by the self-modulated (SM-LPWA) regime using a single laser pulse. In SM-LPWA the laser initiates plasma waves, which modulates itself due to the created density modulation into packets of the length of the plasma wave wavelength[28].

The field of laser plasma wakefield acceleration achieved a major milestone with the first experimental quasi monoenergetic (<3% energy spread) electron beam acceleration in 2004, simultaneously by three separate groups, Mangles et al., Geddes et al. and Faure et al.[29].

An example of a typical simple set-up of a laser plasma wakefield acceleration experiment can be seen in Fig.1.3. Note the difference in scale as compared to the conventional accelerators, as the acceleration can happen here over only a few multiple

---

[24] [21] T. Tajima and J. M. Dawson. *PRL* (1979).

[25] [22] M. N. Rosenbluth and C. S. Liu. *PRL* (1972).

[26] [23] C. E. Clayton *et al. PRL* (1985).

[27] [24] C. E. Clayton *et al. PRL* (1993).

[28] [25] N. E. Andreev *et al. Pis'ma Zh. Eksp. Teor. Fiz.* (1992); [26] J Krall *et al. PRE* (1993); [27] A. Modena *et al. Nature* (1995); [28] E. Esarey *et al. PRL* (1998).

[29] [29] S. P. D. Mangles *et al. Nature* (2004); [30] C. G. R. Geddes *et al. Nature* (2004); [31] J. Faure *et al. Nature* (2004).

$100\,\mu m$[30]. The laser pulse beam path follows the red path, and is focused into the gas from a solenoid gas jet. The laser beam is commonly extracted by a wedge, plasma mirror or reflecting foil. The electron beam can be analysed by a dipole magnet, which sweeps the electrons onto a phosphorescent screen, where the position depends on the energy of the electrons.

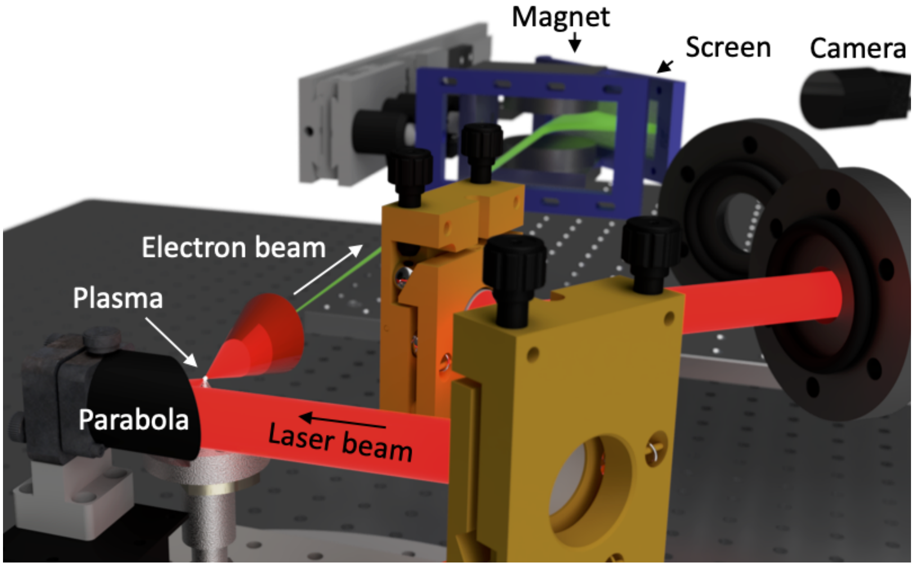

Figure 1.3: Example of a simple LPWA experiment, rendered in 3D. The red beam indicates the laser pulse which is focused into a gas from a gas jet, and accelerated electrons (green). The electrons can be diagnosed with a magnet onto a phosphorescent screen seen by a camera. Note that the vacuum tank and lead shielding are not displayed here for illustrative purposes.

Quasi monoenergetic acceleration was accomplished by new development in laser engineering. The chirped-pulse amplification technique, published in 1985 by Donna Strickland and Gerard Mourou who were awarded the Nobel Prize in 2018 for its discovery, allowed the generation of high intense and ultra short laser pulses utilised for discoveries in various fields of physics and beyond. Such laser pulse with intensities of $1.5 \times 10^{18}\,\mathrm{W\,cm^{-2}}$ in $40\,\mathrm{fs}$ were crucial for the experiment by Mangles' and the others. These laser pulse length was close to the plasma wave wavelength used for acceleration so that no modulation of the laser pulse was required[31]. The peak energy of the electrons has increased rapidly since the first monoenergetic electron beam with a current record at $7.8\,\mathrm{GeV}$[32]. A semi-logarithmic plot of the year of publication vs the electron energy can be seen in Fig. 1.4 (a) and the laser power vs electron energy in logarithmic scale in Fig. 1.4 (b). Details about each publication shown in the plots can be found in App. A.1.

---

[30] [32] F. Salehi *et al.* *Optics Letters* (2017); [33] D. Guénot *et al.* *Nat. Photonics* (2017); [34] D. Gustas *et al.* *PRAB* (2018).

[31] longitudinal pulse compression, which shortened the laser beam into a single wake most-likely happened supporting the process

[32] [35] A. J. Gonsalves *et al.* *PRL* (2019).

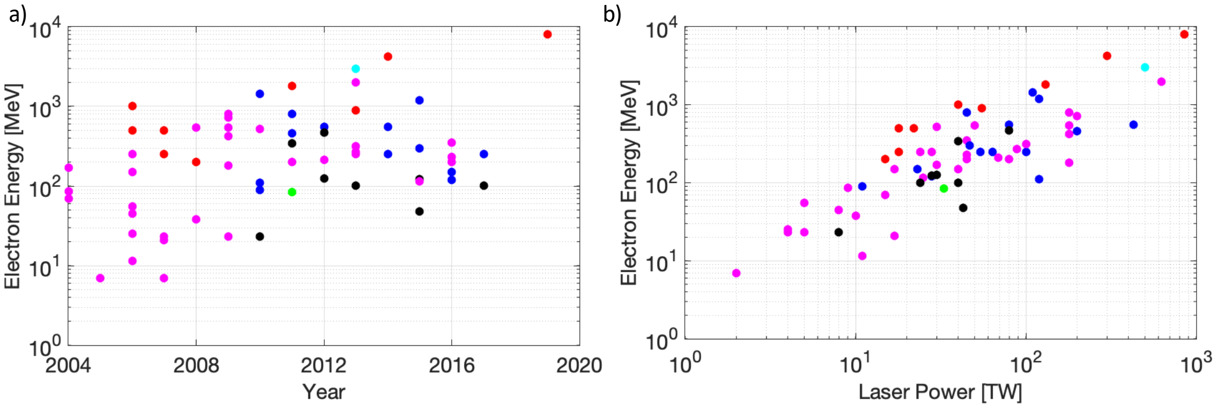

Figure 1.4: a) Year of the publication compared to the electron energy reported. The energy scale is logarithmic. b) Laser energy and yielded electron energy in a double logarithmic plot. Adapted image[33]. The colour corresponds to different experimental set-ups, self-injection (magenta), ionisation injection (blue), acceleration using a capillary discharge (red), down-ramp injection (black), optical injection (green) and non-categorised (cyan).

The first experiments relied on self-injection of the electrons. Controlled injection and guiding can improve stability[34], energy spread[35], emittance[36] and charge[37] and there are many sophisticated techniques, which will be summarised through-out the theory chapter.

1.2 Application of Laser Plasma Wakefield Accelerators

The application of accelerators for particle physics has already been discussed above. Laser-based accelerators might not be suitable to replace conventional accelerators anytime soon. The requirements to create a *Higgs-factory* such as the ILC is meant to be[38] are beyond the current capabilities of laser-based accelerators. But recent experiments in fundamental quantum electro-dynamic (QED) research have used electron bunches accelerated through LPWA[39]. The driver of the wakefield does not only have

---

[33] ([36] S. P. Mangles. *CAS-CERN Accelerator School: Plasma Wake Acceleration 2014, Proceedings* (2014))

[34] [37] S. Banerjee *et al. PRST - AB* (2013); [38] A. Martinez De La Ossa *et al. PRL* (2013); [39] M. Tzoufras *et al. PRL* (2014); [40] S Kuschel *et al. PRL* (2018); [41] C. McGuffey *et al. PRL* (2010); [42] J. Faure *et al. Nature* (2006); [43] S. P. D. Mangles *et al. Physics of Plasmas* (2007); [44] A. R. Maier *et al. PRX* (2020).

[35] [45] G. Golovin *et al. PRST - AB* (2015); [46] G. G. Manahan *et al. Nat. Com.* (2017).

[36] [47] M. Migliorati *et al. PRST - AB* (2013); [48] R. Weingartner *et al. PRST - AB* (2012); [49] Z. Qin *et al. Physics of Plasmas* (2018); [50] S. Kneip *et al. PRST - AB* (2012).

[37] [41] C. McGuffey *et al. PRL* (2010).

[38] [51] C. B. Schroeder *et al. Phys. Rev. Spec. Top. - Accel. Beams* (2010).

[39] [52] J. M. Cole *et al. PRX* (2018); [53] K. Poder *et al. PRX* (2018).

to be a laser pulse, but can be a relativistic particle beam as well having other great advantages, which going into detail would be beyond the content of this thesis. Both fields of study are closely related and generalised in the term *Plasma Wakefield Acceleration* (PWA) to create a joint venture with a committee in the UK[40].

An example of particle-based plasma wakefield acceleration suitable for particle physics is the recent demonstration of electron acceleration with the $400\,\mathrm{GeV}$-proton bunch from CERN's SPS in the self-modulated regime[41]. The high energy density of the proton bunch could potentially accelerate electrons up to TeV[42].

The accelerated electrons are not the only beam that can be extracted from the plasma. The restoring force of the ions on the electrons acts not only longitudinally, but also transversely. Some electrons are injected off-centre. This results in transverse oscillations and hence radiation emitted. The frequency of the radiation is Lorentz-boosted into a forward going beam due to the relativistic energy of the electrons, yielding photon energies of 1-10s keV with a broad synchrotron spectrum characterised by a critical energy[43]. Furthermore, its small temporal and spatial characteristics increases its spectral peak brightness to be comparable to third generation synchrotron sources, such as the European Synchrotron Radiation, which yields a spectral peak brilliance of $6.6\times10^{21}\,\mathrm{ph\ s^{-1}\,mm^{-2}\,mrad^{-2}\,0.1\%BW^{-1}}$[44] at $10\,\mathrm{keV}$ photon energy. The spectral peak brightness is shown in Fig. 1.5 for several LPWA-experiments. The x-ray source is short and intrinsically coupled to a laser driver. This allows the x-ray source to be synchronised to other light sources for pump-probe experiments. Numerous experiments rely on this, as for example, the previously mentioned QED and radiation reaction experiments[45].

The usage of this so-called betatron radiation is versatile[47] and has provided insights into many problems. For example warm dense matter dynamics through x-ray absorption spectroscopy[48], tomographic imaging of biological tissues[49], time-resolved

---

[40] [54] B. Hidding *et al. ArXiv* (2019).
[41] [55] E. Adli *et al. Nature* (2018).
[42] [56] M. Wing. *Philosophical Transactions of the Royal Society A* (2019).
[43] [57] E. Esarey *et al. PRE* (2002).
[44] `https://www.esrf.eu/home/UsersAndScience/Accelerators/ebs---extremely-brilliant-source/ebs-parameters.html` accessed 01.09.2020
[45] [52] J. M. Cole *et al. PRX* (2018); [53] K. Poder *et al. PRX* (2018).
[46] ([58] M. S. Bloom *et al. PRAB* (2020); [59] S. P. D. Mangles *et al. APL* (2009); [60] M. Schnell *et al. PRL* (2012); [61] A. Rousse *et al. PRL* (2004); [62] A. Döpp *et al. Light: Science & Applications* (2017); [63] J. Wenz *et al. Nat. Com.* (2015); [64] S. Kneip *et al. Nature Physics* (2010); [58] M. S. Bloom *et al. PRAB* (2020); [65] J. C. Wood *et al. Scientific Reports* (2018); [66] J. M. Cole. (2015); [67] X. Wang *et al. Nat. Com.* (2013))
[47] [68] F. Albert and A. G. R. Thomas. *Plasma Phys. Control. Fusion* (2016).
[48] [69] M. Z. Mo *et al. Rev. Sci.* (2013); [70] B. Kettle *et al. PRL* (2019).
[49] [63] J. Wenz *et al. Nat. Com.* (2015); [71] J. M. Cole *et al. Plasma Phys. Control. Fusion* (2016); [52] J. M. Cole *et al. PRX* (2018); [72] A. Döpp *et al. Optica* (2018).

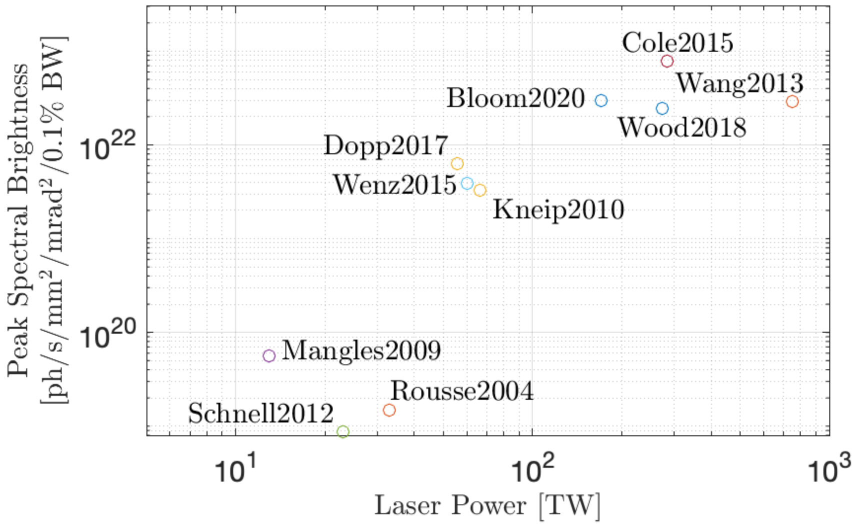

Figure 1.5: Shown are the spectral peak brightness for different LPWA-experiments in respect to laser power. The values are standardised calculations in correspondence to the authors of the first cited paper[46] , and details can be found in App. A.2.

shock-front propagation[50]. Material science has taken advantage of this source for adaptive manufacturing[51] and microstructures[52] and is also presented in this work.

1.3 Thesis Outline

The thesis is divided into a theory section, method section and three chapters containing experimental, theoretical and computational work. The theory chapter summarises the necessary foundation to explain and *partially* understand the results. The theory chapter also contains work of the author investigating electric field-strengths in wakefield for differently shaped laser pulses, solving a set of 1D differential equations. The methods contains general diagnostics used in the experiments and which the author worked with/set them up as well as talking about basic limitations and principles of the used simulation code EPOCH.

The following three chapters contain the main work of this thesis and are based on three individual experiments:

4. **Reflectivity and guiding of a high-intensity laser pulse reflected off a plasma mirror:** A laser pulse is reflected off a plasma mirror and through a

---

[50] [65] J. C. Wood *et al. Scientific Reports* (2018).
[51] [73] M Vargas *et al. Plasma Phys. Control. Fusion* (2019).
[52] [74] A. E. Hussein *et al. Scientific Reports* (2019).

gas cell. The reflection and guiding properties are investigated experimentally and using simulations

5. **Compact Laser-Driven Accelerator X-ray Sources for Industrial Imaging:** The x-ray flux of a betatron source is increased by scanning the electron density inside a gas cell and efforts of explaining the experimental findings are presented. This includes a modified and more general algorithm based on literature and simulations. The source is characterised in the second part of the chapter and was used as an industrial imaging source.
6. **Machine Learning on Enhancement of X-ray Yield of Betatron Radiation at Low Power Systems:** Bayesian optimisation is applied on a low-power laser system to enhance the x-ray signal and the data is analysed and interpreted on automation and correlations of input parameters.

Chapter 2

Theory

Short intense laser pulses are injected into plasma gas cells to accelerate electrons within cm up to GeV energies. The electric field of the laser pulse creates a density modulation in the plasma and by doing so creates ion cavities, in which trapped electrons can exploit longitudinal electric fields. It is essential to understand the theory behind short laser pulses and their physics in a plasma environment. This chapter is divided into sections exploring laser pulses without a medium and then introduces the state of a plasma. Finally, the two topics are combined to explore laser plasma-wakefield acceleration and the limitations and features are investigated, such as x-ray production.

2.1 Short Laser Pulses

The fundamental equations to understand short laser pulses originate in the Maxwell-equations. If not otherwise stated, the equations and detailed derivations can be found in[1]. The Maxwell-equations for the electric and magnetic field in an arbitrary medium are

$$\text{Gauss' Law} \qquad \vec{\nabla} \cdot \vec{E} = \frac{\rho}{\epsilon} \tag{2.1}$$

$$\text{Gauss' Law for Magnetism} \qquad \vec{\nabla} \cdot \vec{B} = 0 \tag{2.2}$$

$$\text{Faraday's Law of Induction} \qquad \vec{\nabla} \times \vec{E} = -\frac{\partial \vec{B}}{\partial t} \tag{2.3}$$

$$\text{Ampère's Circuital Law} \qquad \vec{\nabla} \times \vec{B} = \mu \vec{j} + \frac{\eta^2}{c^2} \frac{\partial \vec{E}}{\partial t} \tag{2.4}$$

with $\vec{E} = \vec{E}(\vec{x}, t)$ being the electric field, and $\vec{B} = \vec{B}(\vec{x}, t)$ the magnetic field. c is the speed of light and η the refractive index in the propagating medium. ρ is the charge density, $\vec{j}$ the current density, μ the permeability, and ϵ the permittivity. It is convenient to define a vector potential $\vec{A}(\vec{x}, t)$ and a scalar potential $\Phi(\vec{x}, t)$, which oblige the Lorenz gauge condition. By defining the magnetic field and using the Maxwell-equation it

---

[1] [75] B Saleh and M Teich. *Fundamentals of Photonics* (2007).

follows that,

$$\vec{B}(\vec{x},t) = \vec{\nabla} \times \vec{A}(\vec{x},t) \tag{2.5}$$

$$\vec{E}(\vec{x},t) = -\frac{\partial}{\partial t}\vec{A}(\vec{x},t) - \vec{\nabla}\Phi(\vec{x},t) \ . \tag{2.6}$$

This will be useful for later purposes (see Sec. 2.5). The charge and current density vanishes in absence of a source and the Maxwell-equations yield the wave equation of the electric field,

$$\vec{\nabla}^2\vec{E} - \frac{\eta^2}{c^2}\frac{\partial^2\vec{E}}{\partial t^2} = 0 \ . \tag{2.7}$$

A solution for the electric field is an oscillating real function, but commonly, the wave is defined by a complex form as,

$$\vec{E} = \vec{E}_A(\vec{x}) \exp^{-i(\omega_0 t - \vec{k}\vec{x} + \varphi(t))} \ , \tag{2.8}$$

where ω_0 is the central frequency, which is correlated with the wavenumber as $\omega_0 = ck_0/\eta$. The real part is the actual physical electric field. The additional term $\varphi(t)$ can be a time-varying phase and can result in complex shapes of the pulse, e. g. a third-order variation can result in small pre-pulses[2]. For this summary, the time dependence of the phase will be neglected. This ansatz results for Eq. (2.7) in the *paraxial ray wave equation* in cylindrical coordinates (for the derivation see App. B.2)

$$\frac{\partial^2\vec{E}_A(\vec{x})}{\partial r^2} + \frac{1}{r}\frac{\partial\vec{E}_A(\vec{x})}{\partial r} - 2ik\frac{\partial\vec{E}_A(\vec{x})}{\partial z} = 0 \ . \tag{2.9}$$

2.1.1 The Hermite-Gaussian Laser Pulse

Equation (2.9) has an infinite set of solutions called Hermite-Gaussian Polynomials[3]. The first order of solution is mostly sufficient to describe the pulse and is called the Gaussian beam

$$\vec{E}_A(\vec{x}) = \vec{E}_0\frac{w_0}{w(z)}\exp\left(-\frac{r^2}{w(z)^2}\right)\exp\left(-ik\frac{r^2}{2R(z)}\right)\exp(i\phi(z)) \tag{2.10}$$

---

[2] [76] M Miyagi and S Nishida. *Applied optics* (1979).

[3] [75] B Saleh and M Teich. *Fundamentals of Photonics* (2007), Ch. 3.3.

where the beam parameters are defined as the following

$$\text{Beam Waist} \qquad w(z)^2 = w_0^2\left[1+\left(\frac{z}{z_R}\right)^2\right] \tag{2.11}$$

$$\text{Radius of Curvature} \qquad R(z) = z\left[1+\left(\frac{z_R}{z}\right)^2\right] \tag{2.12}$$

$$\text{Gouy Phase} \qquad \phi(z) = \tan^{-1} z/z_R \tag{2.13}$$

$$\text{with the Rayleigh-length} \qquad z_R = \pi w_0^2/\lambda \tag{2.14}$$

$$\text{Beam Divergence} \qquad \theta = \lim_{z\to\infty}\frac{w(z)}{z} = \frac{\lambda}{\pi w_0}\ . \tag{2.15}$$

The beam waist w_0 is the radius at $z = 0$, at which the electric field drops transversely by a factor of 1/e. The Rayleigh-length is the longitudinal distance at which the spot size increases by $\sqrt{2}$. The beam divergence is the angle between the beam size and the distance to the focal plane in thee limit far from focus. A visualisation with Matlab of these parameters can be seen in Fig. 2.1.

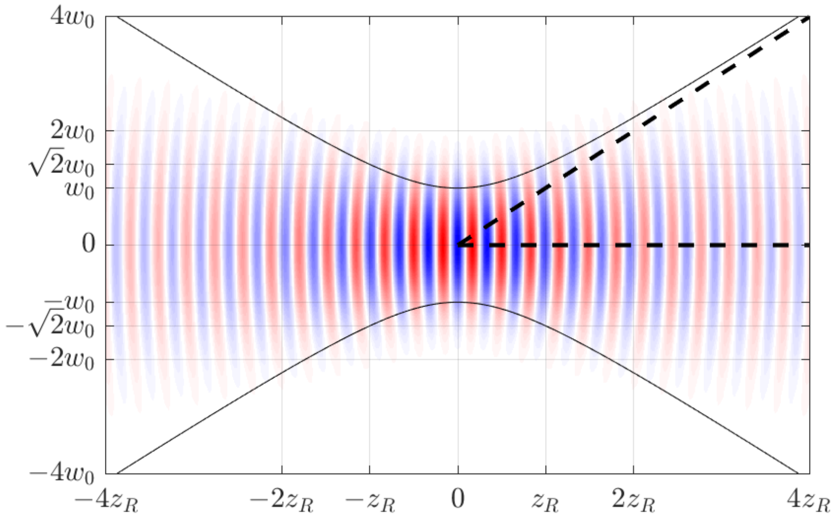

Figure 2.1: Real part of the electric field of a Gaussian beam propagating in z. The beam waist is plotted with a solid black line and the angle of divergence can be seen between the dashed black lines.

The flow of the electromagnetic power is given by the Poynting-vector $\vec{S} = \frac{1}{\mu_0}\vec{E}\times\vec{B}$ and of practical importance is the time-average flow of power per unit area called intensity I. For the electric field above, Eq. (2.8), with a linear polarisation $\vec{E}_0 = E_0\hat{x}$, the intensity yields

$$I = \langle\vec{S}\rangle = \frac{1}{2}\frac{E_0^2}{c\mu_0}\ . \tag{2.16}$$

The intensity has the practical units of W/cm^2. The intensity integrated over the transverse space results in the power of the laser and its peak value is called the *peak power*. Integrated further over its longitudinal component or equivalent, over time, results in the energy of the laser pulse.

Denote that often the Gaussian envelope laser pulse function is divided into a transverse part in space and a longitudinal part in time, in which the time-dependent term is assumed with yet another Gaussian envelope. Ignoring the phase dependence, the intensity has then the form[4],

$$I(r,t) = I_0 \exp(-t^2/\tau^2)\exp(2r^2/w^2)\ . \tag{2.17}$$

As the pulse duration and the spot size is usually measured by taking the *Full-Width-Half-Maximum* (FWHM) of the intensity, the power and the energy respectively is then given in those terms by (see App. B.3 for details)

$$E = \sqrt{\frac{\pi}{\log(2)}}\frac{\pi}{8\log(2)} w^2_{\text{FWHM},I}\tau_{\text{FWHM},I} I_0\ . \tag{2.18}$$

Thus, to achieve ultra-high intensities with a given energy, the pulse ought to be as short and as narrowly focused as possible. The pulse duration is Fourier-limited by the bandwidth if the additional phase term in Eq. (2.8) is eliminated. Through Fourier-transformation one can show that in the limit, the bandwidth and pulse duration correlates with

$$\omega_{\text{FWHM},I} \cdot \tau_{\text{FWHM},I} = 4\log(2) \approx 2.8 \tag{2.19}$$

in which $\omega_{\text{FWHM},I}$ is the FWHM bandwidth of the spectrum[5]. With Eq. (2.19) it follows that for a short pulse, the bandwidth should be as broad as possible.

To minimise the spot size of the laser beam off-set reflecting parabolas are used as these avoid picking up additional phase terms because the light is reflected rather than propagating through material as for a refractive lens[6]. The focus spot size for a collimated beam after the focusing optic w'_0 is[7]

$$2w'_0 = \frac{4}{\pi}\lambda F_\# \text{ or } w'_{\text{FWHM},I} = \frac{2\sqrt{2\log(2)}}{\pi}\lambda F_\# \approx 0.75\lambda F_\# \tag{2.20}$$

which includes the wavelength λ and the F-number $F_\#$. The F-number can be seen

---

[4] [75] B Saleh and M Teich. *Fundamentals of Photonics* (2007), Ch. 22 B..

[5] Note that the definition of the FWHM differs from the source as here it is defined by the FWHM of the intensity and not from the complex envelope function.

[6] The light does travel through some finite thickness of the surface of the mirror strictly speaking, which is important for ultra-short laser pulses but is neglected here.

[7] [75] B Saleh and M Teich. *Fundamentals of Photonics* (2007), Ch. 3.

as the focusing ratio, as it is the division of the focus length f and the diameter before focusing D, hence $F_{\#} = f/D$. Tight focusing can be achieved by using a short-focusing lens and a large diameter pulse.

2.1.2 Index of Refraction and Guiding in a Medium

The previous section describes the propagation of light in vacuum using reflective and transmissive lenses. Once we focus the laser pulse into the plasma and want accelerate electrons over large distances, it is important to consider the transverse response of the laser pulse due to the refractive index in the plasma. This section introduces the topic in a classical form by inserting a laser beam into graded-index (GRIN) optical components. As mentioned in Sec. 2.1, light propagates with a reduced speed of light through a medium, characterised by the index of refraction η. The optical path length (OPL) between point A and B is $OPL = \int_A^B \eta(\vec{r})\mathrm{d}s$, in which $\mathrm{d}s$ is the differential element of the path. Optical rays travel through these two points A and B *along the path with the least amount of time*. This is referred to as *Fermat's principle* and is expressed with $0 = \delta \int_A^B \eta(\vec{r})\mathrm{d}s$. This can be used to derive *Snell's Law* $\eta_1 \sin\theta_1 = \eta_2 \sin\theta_2$. Snell's Law describes the refraction of rays at the border of different media. This can be exploited by using specific transverse depending path length differences to create lenses. A focusing lens has a longer optical path length in the centre, simply by having more material on-axis than off-centre. The focus point is the point at which all rays propagated the same optical path length is independent on their transverse position.

A non-homogeneous medium with a transverse dependant gradient, a GRIN optical component, can be used to guide a laser beam through a medium. When choosing the right gradient of the refractive index, the off-centred rays have a lower index of refraction and are *faster* than the centred ones, leading to a focusing effect in the medium. Naturally, the beam defocuses after focusing and once reaching the outer perimeter of the medium, the beam re-focuses. This is repeated over many oscillations thus the beam is guided.

Even though the mechanisms for focusing and defocusing in plasma are different than in a static glass medium, the difference in optical path lengths is the fundamentals to understand the various effects discussed in Sec. 2.7.1.

2.1.3 Polarisation of Laser Pulses

In this section, the vector characteristics of the electric field will be discussed. The envelope function of Eq. (2.8) contains the direction of the electric field and must obey the Maxwell equations as well. Due to Faraday's Law of Induction and Ampère's Circuital Law the electric field, $\vec{E}$ is orthogonal to the magnetic field $\vec{B}$ and both are orthogonal to the wavevector $\vec{k}$ in a vacuum (see App. B.1 for details). The direction in which the vector of the electric field is pointing is called the polarisation. As the propagation direction is in direction of the wavevector, the polarisation only needs to be described with two components. A common representation is the *Jones Vector*[8] $\vec{A} = A_x\hat{x} + A_y\hat{y}$. This has implications on the reflection and transmission of light on boundaries with different refractive indices. The sum of the electric field coupled into the material must equal the electric field inside the material[9], the same is valid for the magnetic field. Because the magnetic field is orthogonal to the electric field and because it can be expressed by the electric field and the refractive index, it creates a set of equations. The equations are different for the electric field being *parallel* (p-pol.) to the plane of reflection and *senkrecht* (senkrecht = orthogonal in German[10]; s-pol.). The solutions are referred to as *Fresnel*-equations and have great importance when setting up an experiment as mirrors used in these high intensities as presented in this work are designed for only certain polarisation directions.

The manipulation of the polarisation can be achieved using birefringent crystals and polarisers. It is a huge topic so that the reader is referred to[11] for more details on linear and circular polarisation and to[12] for more details on radially and azimuthal polarised light.

2.1.4 Chirped Pulse Amplification

A technique is used known as *chirped-pulse amplification* (CPA)[13] to produce extremely short pulses with ultra-high intensity. The aforementioned phase term $\varphi(t)$, Eq. (2.8) or $\tilde{\varphi}(\omega)$, respectively in the spatial or frequency-domain, is used to stretch the pulse with a set of gratings after its generation from an oscillator. Hence, the peak intensity drops several magnitudes and the power thresholds of the optics in the laser system are not overcome when amplifying the laser pulse. The pulse will be compressed after amplification by removing the previously introduced phase-term with yet another set of gratings, increasing the peak intensity again by several orders of magnitude. Techniques built based on CPA are optical-parametric CPA (OPCPA)[14] or frequency domain optical parametric amplification[15] (FOPA). Both techniques can have an oscillator with a different wavelength than the amplified final pulse as it uses optical parametric

---

[8] [75] B Saleh and M Teich. *Fundamentals of Photonics* (2007), Ch. 6 B.

[9] This is not true at dielectrics, but since the solutions are applied to glass wedges, see Sec. 4.2.1, the discussion of this topic is reduced to a minimum.

[10] Parallel means parallel in German

[11] [75] B Saleh and M Teich. *Fundamentals of Photonics* (2007), Ch. 6.

[12] [77] K. J. Moh *et al. Applied optics* (2007); [78] I. Moreno *et al. Optical Engineering* (2012); [79] S Carbajo *et al. Optics Letters* (2014).

[13] [80] D. Strickland and G. Mourou. *Opt. Commun.* (1985).

[14] [81] A. Dubietis *et al. Opt. Commun.* (1992); [82] I. Ross *et al. Opt. Commun.* (1997).

[15] [83] B. E. Schmidt *et al. Nat. Com.* (2014).

amplification (OPA)[16]. Two laser beams are overlaid in a birefringent crystal in OPA and under the condition of momentum and energy conservation, one of the beams can be amplified by the energy of the other beam, the pump, if phase-matching conditions are obeyed.

2.2 Single Particle Motion

The motion of an electron in a planar lightwave can be described by the Lorentz force

$$\frac{\mathrm{d}p}{\mathrm{d}t} = -e(\vec{E} + \vec{v}_e \times \vec{B}) \tag{2.21}$$

This can be simplified by assuming non-relativistic electrons to understand the physics and behaviour for lower intensity light waves. Non-relativistic electrons are expressed with the condition $|\vec{v}_e \ll c|$ and thus the curl in Eq. (2.21) can be neglected. The velocity of the electron is given by the integration of Eq. (2.21) as

$$\vec{v}(\vec{x}, t) = -\frac{e}{m_e} \int \vec{E}_0 \cos(\omega_0 t - \vec{k}\vec{x})\mathrm{d}t = \vec{v}_{e,\text{quiv}} \cdot \sin(\omega_0 t - \vec{k}\vec{x}) \tag{2.22}$$

in which the real part of the electric field, given in Eq. (2.8), is used and it is assumed that the electron is initially at rest. The *quiver velocity* is hereby defined as $\vec{v}_{e,\text{quiv}} = e\vec{E}_0/m_e\omega_0$. Once the quiver velocity approaches c, the second part of Eq. (2.21) is not negligible any more and this approximation fails. Therefore, it is convenient to define a normalised value to quantify this threshold. This is known to be the normalised vector potential,

$$a_0 = \frac{e|\vec{E}_0|}{m_e\omega_0 c} \approx 0.856 \cdot \sqrt{I[10^{18}\text{W/cm}^2]} \cdot \lambda[\mu m] \tag{2.23}$$

The electric field is replaced by the intensity with Eq. (2.16). $a_0 > 1$ is the relativistic regime, where the velocity of the electrons after it experiences the force of the light wave approaches the speed of light. The average energy over a cycle of the light wave is the *ponderomotive potential*

$$U_p = \left\langle \frac{1}{2} m_e \vec{v}^2_{e,\text{quiv}} \right\rangle = \frac{e^2}{4m_e\omega_0^2}|\vec{E}_0|^2 \approx 9.33 \cdot 10^{-6} I\lambda^2[\text{eV}]\ . \tag{2.24}$$

This definition allows to define a conservative force, which is called the *ponderomotive force* $\vec{F}_p = -\vec{\nabla}U_p$. This force pushes the electrons towards lower intensities.

---

[16] [84] S. A. Akhmanov *et al. Physics Faculty, Moscow State University* (1965).

2.3 The Effect of the Magnetic Field on the Electron Motion

The physics in this section investigates the relativistic regime. Once a_0 approaches 1, the magnetic field begins to give the electron a longitudinal velocity component. The detailed mathematical derivations can be found in App. B.9. In summary, the equations of motion for a stationary electron in a planar monochromatic wave with a linear polarisation in $\hat{e}_x$ and a direction of propagation in $\hat{e}_z$ (:= longitudinal) is

$$z(t) = \frac{c}{2}\int \cos^2(\omega\tau)\mathrm{d}\tau^{17} = \frac{ca_0^2}{8\omega}\left[2(\omega t - kz) + \sin(2(\omega t - kz))\right] \tag{2.25}$$

$$x(t) = ca_0\int \cos(\omega\tau)\mathrm{d}\tau = \frac{ca_0}{\omega}\sin(\omega t - kz) \tag{2.26}$$

which shows a longitudinal drift of the electrons. The average normalised momentum is straightforward, using the normalised momentum $\hat{p_z} = p_z/m_e c$ Eq. (B.90), the drift velocity v_D, and by multiplying it with $c/<\gamma>$

$$<\hat{p_z}> = <\frac{a^2}{2}> = \frac{a_0^2}{2} < cos(\tau) > = \frac{a_0^2}{4} \tag{2.27}$$

$$<v_D> = c\frac{<\hat{p_z}>}{<\gamma>} = c\frac{a_0^2}{4}\cdot\frac{1}{1+\frac{1}{2}<a^2>} = c\frac{a_0^2}{4+a_0^2} \tag{2.28}$$

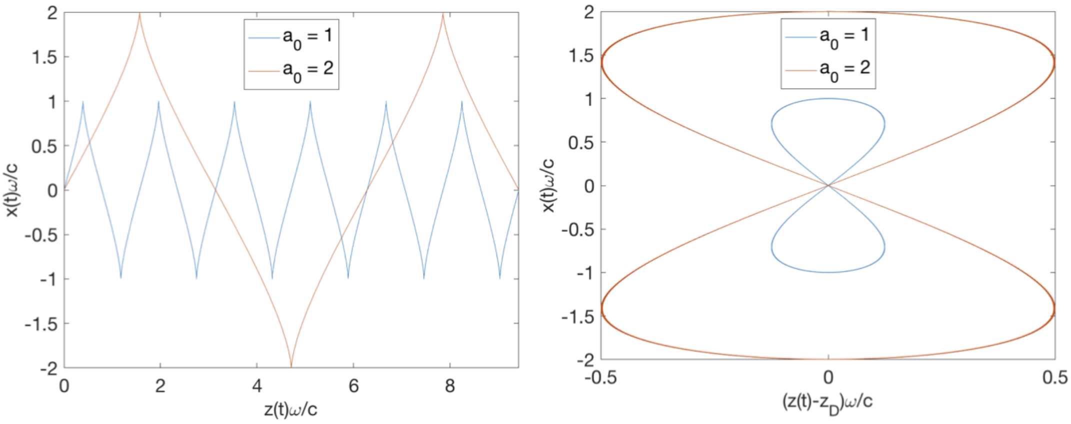

Figure 2.2: Electron motion in vacuum for strong electric fields. On the left the laboratory frame and on the right the moving frame, in which the drift motion is subtracted. The drift velocity is the derivative of the drift motion $v_D = \partial z(t)/\partial t$.

The trajectories of an electron in different regimes can be seen in Fig. 2.2. As the electron moves with the drift velocity and a periodically transverse motion in the

---

[17] The substitution $\tau = t - z(t)/c$ is performed in order to solve the integral. For details see App. B.9.

lab-frame, the moving frame shows a trajectory commonly referred to as the *figure-of-8-motion*. A larger normalised vector potential yields a larger longitudinal motion as $z(t)/x(t) \propto a_0$. The average energies achieved depends solely on a_0^2 [18]and for $a_0 = 1$ ($\approx 3.3 \cdot 10^{18}$ W/cm^2 for $\lambda = 800\,\mathrm{nm}$) the electron reaches an energy of $125\,\mathrm{keV}$. These energies are insufficient to call it a particle accelerator (< 1 MeV[19]). To achieve higher energies with such laser intensities, a plasma can be used, which will be investigated in the following, see Sec. 2.8.

2.4 Ionisation Mechanism

The laser pulse interacts with ionised gas, which under certain conditions can be defined as plasma (see Sec. 2.5). There are several ways to produce a plasma for LWPA. One way is a discharge capillary, where a strong current passes through gas and ionises it. Another method is to use either a second prepulse or the pedestal of the main laser pulse to ionise the gas. Experimental examples are mentioned in Sec. 2.6. There are different regimes to describe the ionisation mechanisms depending on the intensity of the laser pulse. The photoelectric effect requires a photon with energy large enough to overcome the electric binding potential of the nuclei. As most laser systems used for LWPA have much longer wavelengths than this process requires, this is not applicable here. Instead, **multiphoton ionisation**, first measured in[20], can occur for sufficiently large intensities. An electron absorbs several photons simultaneously and the combined energy is large enough to ionise it from the atom. If the intensity of the laser pulse increases further, the electric potential of the nuclei can be disturbed and creates an effective potential with a finite barrier, through which the bound electrons can tunnel out. The process is called **tunnel ionisation**. The effect was first mentioned in 1966 by Perelomov et al.[21] for hydrogen atoms and then later generalised by Ammosov et al.[22]. The probability of ionisation is calculated by using first-order perturbation theory and solving the Hamiltonian of the bound states and the ionised state. The model is known as the ADK model (by the authors' names M. Ammosov, N. Delone and V. Krainer). A parameter to distinguish these regimes is the Keldysh-parameter[23] $\gamma_K = \sqrt{E_I/(2U_p)}$, which includes the ionisation energy E_I and the ponderomotive potential $U_p \propto I_0 \cdot \lambda^2$. The likelihood depends on the intensity (for

---

[19] [2] US Department of Public Health.

[19] The momentum in eV/c units is given straightforward by $< p_z >= a_0^2/4 * (m_e c^2/e$ [eV/c] or explicitly $< p_z > \approx a_0^2/8$ [MeV/c].

[20] [85] G. S. Voronov and N. B. Delone. *Sov. Phys. JETP* (1966).

[21] [86] A. M. Perelomov *et al. Sov. Phys. JETP* (1966).

[22] [87] M. V. Ammosov *et al. Sov. Phys. JETP* (1986).

[23] [88] L. V. Keldysh. *Sov. Phys. JETP* (1965).

details for the ponderomotive potential recall Sec. 2.2). For $\gamma_K \gg 1$, multi-photon ionisation dominates, but for $\gamma_K \geq 1$ tunnel-ionisation starts to become more important. The effective potential can be written as

$$V(r) = -\frac{Z^* \mathrm{e}^2}{4\pi\epsilon_0 r} - \mathrm{e}|E_0|r \tag{2.29}$$

in which e is the elementary charge and Z^* the effective charge of the atom. This assumes that the wavelength of the pulse is much larger than the electron displacement of r in this system. A special case occurs, once the electric field becomes so strong that the potential barrier diminishes and the electron is no longer bound to the atom. This is called **barrier-suppression ionisation** (BSI). By setting the derivative of Eq. (2.29) to zero to find the maximum potential, one can deduce at what intensity the electron is immediately ionised at

$$I_{BSI} = |E_0|^2/(2\mu_0 c) = \frac{E_I^4 \pi^2 c \epsilon_0^3}{2Z^{*2} e^6} \approx 4 \cdot 10^9 \frac{E_I^4[\mathrm{eV}]}{Z^{*2}} \left[\text{in W cm}^{-2}\right] . \tag{2.30}$$

This threshold was first shown in another formalism in[24]. For hydrogen, $E_I = 13.6$ eV and $Z^* = 1$, this yields to intensities around $I_{\mathrm{BSI}} = 1.4 \cdot 10^{13}$ W/cm^2, which is far lower than the intensities achieved in the experiments presented in this work meaning that BSI is the main mechanism.

These are the classical ionisation mechanisms for high intensities and lower densities. In this work, an ultra-intense and short laser pulse are also reflected on a solid target. Special treatment must be applied in this case and the mechanisms responsible for ionisation on solids are still under investigation as seen in[25]. The fs-laser pulse ionises the target faster than the plasma can expand, which results in a high, nearly solid density plasma. In such dense plasmas, further ionisation can occur by different mechanisms. The high-density results in more ionisation by **pressure ionisation**. The partly ionised atoms' electric fields suppress their mutual potential which ionises more electrons[26]. Kim1994 At higher temperatures, the cross section of impact ionisation increases and collisional ionisation can occur[27]. The cross section peaks around $\approx 100\,\mathrm{eV}$ for H[28], but then decreases again if the temperatures is increased further.

---

[24] [89] H. R. Reiss. *Physical Review A* (1970).

[25] [90] J. Osterholz *et al. PRL* (2006).

[26] [91] R. P. Drake. (2006), Ch. 3.2.2.

[27] [92] H. R. Griem. (1997), Ch. 6.2.

[28] [93] Y.-K. Kim and M. E. Rudd. *Phys. Rev. A* (1994).

2.5 Plasma-Parameters

Mostly three conditions ought to be fulfilled to call an ionised gas a plasma[29]. In an environment, in which ions and electrons are separated, a point source can be shielded by proper arrangement of the charged particles. This effect is called Debye-shielding and this **Spatial Quasi-Neutrality** is one requirement for a homogeneous plasma. A point source attracts the surrounding charge, which then shields it to the outside. Due to the finite temperature of the charged particles, this shielding is not infinitesimal, but some particles with enough thermal energy move around and escape the influence of the source so that only a finite electric field leaks out around the source. The size of this field is the Debye-length

$$\lambda_D = \sqrt{\frac{\epsilon_0 k_B T}{n_e e^2}} \tag{2.31}$$

and its derivation can be seen in App. B.4. The whole system of length L must be larger than this length to have Debye-shielding. And therefore, the first condition is $\lambda_D \ll L$, the spatial quasi-neutrality.

The electrons can interact with each other within a sphere of this Debey-length. The premise is that the amount of charged particles, the density, is high enough to create **Collective Behaviour**, for example, the collective shielding of single particles is one of these effects and can only occur if the number of particles is sufficient. Mathematically, the number of particles N_D in this sphere of size λ_D is

$$N_D = n_e \cdot \frac{4}{3}\pi\lambda_D^3 = \frac{3}{4}\pi\left(\frac{\epsilon_0 k_B}{e^2}\right)^{\frac{3}{2}} \cdot \sqrt{\frac{T^3}{n_e}} \approx 1.38 \cdot 10^6 \cdot \sqrt{\frac{T^3}{n_e}} \tag{2.32}$$

and it must obey $N_D \gg 1$.

Finally, a third condition is formulated to separate systems, between those dominated by hydrodynamic forces and those by electromagnetic forces. Let t_{col} be the mean time between collisions of the charged particles with neutral atoms and ω_p the plasma oscillation frequency, or *plasma frequency* ω_p, the last condition is expressed as

$$\omega_p \cdot t_{\text{col}} > 1 \ . \tag{2.33}$$

The plasma frequency is the oscillation frequency of a charged particle displaced in an ionised background and this relation states the time for oscillation must be shorter than the time of the collision with neutral atoms. The oscillation frequency can be obtained by integrating the simplified Gauss' Law, Eq. (B.52), for a charged particle, which is

---

[29] [94] F. F. Chen. *Plasma Physics Controlled Fusion* (1984).

misplaced from its origin by δx. Using the equation of motion, $F = m_e\ddot{x}$ this yields,

$$E(x) = -\int\limits_0^{\delta x} \frac{en_{e,0}}{\epsilon_0} = -\frac{en_{e,0}\delta x}{\epsilon_0} \tag{2.34}$$

$$F(x) = -eE(x) = -\frac{e^2 n_{e,0}}{\epsilon_0}\delta x = m_e\ddot{x} \tag{2.35}$$

where the final differential equation describes the equation of a harmonic oscillator, with the frequency being,

$$\omega_p = \sqrt{\frac{n_e e^2}{\epsilon_0 m_e}} \approx 5.6 \cdot 10^4 \cdot \sqrt{n_e\ [\text{cm}^{-3}]}[\text{in rad/s}] \text{ or} \tag{2.36}$$

$$\lambda_p \approx 3.3 \cdot 10^4 \cdot \sqrt{n_e\ [\text{cm}^{-3}]}^{-1}\ [\text{in m}] \tag{2.37}$$

and it is called the plasma frequency. The expression of Eq. (2.33) ensures that electromagnetic interactions dominate the system rather than conventional hydrodynamic forces. The wavelength of a relativistic plasma wave λ_p is given by $\lambda_p = 2\pi c/\omega_p$.

2.6 Electromagnetic Wave Propagation in a Plasma

After the derivation of the particle motion in the laser field, the effect of the plasma on the electric field propagation needs to be investigated. In particular, the phase velocity v_ϕ and group velocity v_g[30]

$$v_\phi = \omega/k = \frac{c}{\eta} \tag{2.38}$$

$$v_g = \frac{\partial\omega}{\partial k} \tag{2.39}$$

as well as the focusing behaviour of a laser pulse in plasma. Note that η is the refractive index of the medium in which the laser pulse propagates. Perturbation theory for the electron velocity $\vec{v}$, current density $\vec{j}$, electric field $\vec{E}$ and magnetic field $\vec{B}$ in the first order is used to find the dispersion relation in a plasma. In detail: (valid for all four parameter) $\vec{E} = \vec{E}_0 + \vec{E}_1$ with the condition that $\vec{E}_0 \gg \vec{E}_1$, as well as $\partial\vec{E}_0/\partial t = \partial\vec{E}_0/\partial x = 0$. By keeping in mind that any multiplication or cross product between the perturbations can be neglected and assuming plane waves $\exp(-i(\omega t - \vec{k}\vec{x}))$, it follows for a light pulse

---

[30] [75] B Saleh and M Teich. *Fundamentals of Photonics* (2007), Eq. 5.6-1.

propagating through a plasma,

$$\vec{\nabla} \times \dot{\vec{B}}_1 = \frac{1}{\epsilon_0 c^2} \frac{\partial \vec{j}_1}{\partial t} + \frac{1}{c^2} \ddot{\vec{E}}_1 \tag{2.40}$$

$$\vec{\nabla} \times \left(\vec{\nabla} \times \vec{E}_1 \right) = -\vec{\nabla} \times \dot{\vec{B}}_1 \tag{2.41}$$

for the time derivative of Ampère's circuital law and Faradays's Law of induction. Eliminating the magnetic field and using the derivatives and the plane wave approximation yields,

$$-\left(\vec{k} \underbrace{\left(\vec{k} \cdot \vec{E}_1 \right)}_{=0} - i^2 k^2 \vec{E}_1 \right)^{31} = \frac{i\omega}{\epsilon_0 c^2} \vec{j}_1 + \frac{\omega^2}{c^2} \vec{E}_1 \tag{2.42}$$

$$\left(\omega^2 - c^2 k^2 \right) \vec{E}_1 = i\omega (n_0 e \vec{v}_{e,1}) / \epsilon_0 \tag{2.43}$$

in which $\vec{j}_1 = n_0 e \vec{v}_{e,1}$ was used as well as $\vec{k} \cdot \vec{E}_1 = 0$ assumed the propagation direction is perpendicular to the electric field. Finally, integrating the first order of the equation of motion $m_e \partial \vec{v}_{e,1} / \partial t = -e\vec{E} \approx e\vec{E}_1 / i\omega$ and inserting it, the dispersion relation follows

$$\omega^2 = \omega_p^2 + c^2 k^2 \; . \tag{2.44}$$

Note that the definition of the plasma frequency is used $\omega_p^2 = n_0 e^2 / \epsilon_0 m_e$. The dispersion relation Eq. (2.44) results in the phase and group velocity (see App. B.6 for more details):

$$v_\phi = c \sqrt{1 + \frac{\omega_p^2}{c^2 k^2}} \tag{2.45}$$

$$v_g = \frac{c^2}{v_\phi} = \eta c \tag{2.46}$$

The phase velocity can be faster than the speed of light c, but the group velocity, with which the envelope of the laser pulse propagates and which contains information, cannot. The final expression of the group velocity in Eq. (2.46) originates from the definition of the phase velocity in Eq. (2.38). By comparing the phase velocity Eq. (2.45) with its definition in Eq. (2.38), the refractive index can be determined (again see App. B.6 for more details) as,

$$\eta = \sqrt{1 - \frac{\omega_p^2}{\omega^2}} = \sqrt{1 - \frac{n_e}{n_{\text{crit}}}} \tag{2.47}$$

---

[31] Using the vector identity $\vec{\nabla} \times \left(\vec{\nabla} \times \vec{V} \right) = \vec{\nabla} \left(\vec{\nabla} \cdot \vec{V} \right) - \Delta \vec{V}$

by defining a critical density $n_{\text{crit}} = \omega^2 \epsilon_0 m_e / e^2$. The critical density depends on the laser frequency and indicates the density above which the refractive index becomes imaginary. An imaginary index of refraction implies reflection of the laser pulse. A part of the pulse will still penetrate into the medium with an exponential attenuation. If $\omega_p > \omega$, the wavenumber k can be expressed as $k = i/c\sqrt{\omega_p^2 - \omega^2}$ using the dispersion relation, Eq. (2.44). Therefore, the electric field decays exponentially in the over critical plasma as $E \propto \exp(ikx) = \exp(-|k|x) = \exp(-\sqrt{\omega_p^2 - \omega^2} x/c)$. The distance over which the pulse decays with $1/e$ defines the skin depth,

$$\delta = \frac{c}{\sqrt{\omega_p^2 - \omega^2}} \tag{2.48}$$

2.7 Nonlinear Optics in a Plasma

Unfortunately, the previous section is a simplification of the phenomena occurring in a plasma and a few occurrences can only be explained by considering nonlinear effects. A correction is applied when using laser pulses with relativistic intensities $a_0 > 1$ of $\gamma_0 = (1 + a_0^2)^{1/2}$ as described in Sec. 2.3 affecting the plasma frequency $\omega_p'^2 = \omega_p^2/\gamma_0$, see App. B.8. The pulse can propagate even further into over-critical plasma with this correction. This additional penetration is called *self-induced relativistic transparency*. The refractive index (2.47) can be corrected assuming $\omega_p/\omega, a_0, \delta n/n_0, \delta\omega/\omega_0 \ll 1$. A detailed mathematical analysis is in App. B.8. The refractive index yields

$$\eta \approx 1 - \frac{1}{2}\frac{\omega_{p,0}^2}{\omega_0^2} \cdot \left(1 + \frac{\delta n}{n_0} - 2\frac{\delta\omega}{\omega_0} - \frac{a_0^2}{4}\right) \tag{2.49}$$

2.7.1 Transverse Focusing and Self-Guiding

It is also this correction due to the dispersion that causes the pulse to experience a focusing effect. As the refractive index depends on the intensity and a Gaussian beam has a finite transverse profile, the refractive index changes transversely. This correction changes the phase and group velocity transversely. The centre of the beam slows down, similar to a lens, in comparison to the lower intense regions around it.

Fig. 2.3 illustrates the effect of transverse refractive index profiles due to an increase in phase velocity off-axis. The angle can be estimated with $\tan(\theta) \approx \theta = (v_{\phi,w} - v_{\phi,0})\Delta t/w = \Delta v_\phi \Delta t/w$. The difference in beams waist Δw in the right of Fig. 2.3 is calculated with the previous mentioned angle to be $\Delta w \approx \theta(-v_G \Delta t)$. The two relations and the definitions of the phase and group velocity in Eq. (2.39) and (2.46) are

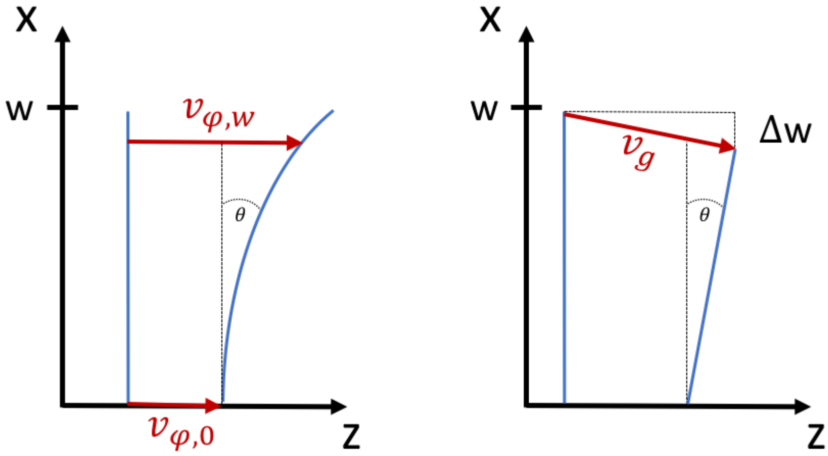

Figure 2.3: Due to the transverse changing refractive index the phase velocity changes off-axis (left) and the beam waist w decreases (right). Note that the angle and path differences are greatly exaggerated to visualise the problem.

combined to yield,

$$\Delta w = \theta(-v_G \Delta t) = (\Delta v_\phi \Delta t/w)(-v_G \Delta t) \underbrace{=}_{v_G = v_\phi/c^2} (\Delta v_\phi \Delta t/w)(-v_\phi/c^2 \Delta t) \tag{2.50}$$

$$\frac{\Delta w}{\Delta t \Delta t} = -\frac{v_\phi \Delta v_\phi}{w c^2} \,. \tag{2.51}$$

Finally, approximating the rate of change of the phase velocity with $\Delta v_\phi \approx \frac{\partial v_\phi}{\partial r} w$ and expressing the phase velocity in terms of the refractive index yield to an acceleration of the beam waist depending on the refractive index

$$\frac{\partial^2 w}{\partial t^2} \approx -\eta c \frac{\partial v_\phi}{\partial r} = \frac{c^2}{\eta} \frac{\partial \eta}{\partial r} \,. \tag{2.52}$$

As the refractive index follows $\eta = \sqrt{1 - n_e/n_{crit}}$, it is clear that for lower electron density on-axis, thus higher η on-axis and decreasing with r, the beam waist $\frac{\partial \eta}{\partial r} < 0$ decelerates. This is of most importance when considering the limitations of LPWA as explored in Sec. 2.10, in which some of the most popular techniques exploiting this mechanism are described.

2.7.2 Relativistic Self-Focusing

If the focusing due to the refractive index stems from the intensity of the laser pulse and hence the normalised vector potential in Eq. (2.49), the effect is called *relativistic self-focusing*[32]. Eq. (2.52) can be used to investigate the laser beams behaviour under such circumstances. The change of the beam size is then due to two parts, which ought

---

[32] [95] P. Sprangle *et al.* *APL* (1988); [96] P. Sprangle *et al.* *PRL* (1992).

to cancel each other. The diffraction originating from the Gaussian beam propagation and the focusing due to the relativistic effect is:

$$\frac{\partial^2 w}{\partial t^2} = \left[\frac{\partial^2 w}{\partial t^2}\right]_{\text{diffraction}} + \left[\frac{c^2}{\eta}\frac{\partial \eta}{\partial r}\right]_{\text{relativistic focusing}} \overset{!}{=} 0 \tag{2.53}$$

Inserting the equation for the beam waist of a Gaussian propagation (Eq. (2.11)) on the left, and the mass increasing effect from Eq. (2.49) leads to the critical power criteria. If the laser beam exceeds this critical power, the pulse self-focuses inside the plasma. Starting with Eq. (2.11), transforming $\partial t \to \partial z/c$ and reducing the effect to be close to the focus spot[33], one can use a 2nd order Taylor-expansion to approximate $w(z) \propto w_0(1 + \frac{1}{2}\frac{z^2}{z_R^2})$, which leads to,

$$\frac{\partial^2 w(z) c^2}{\partial z^2} = \frac{c^2 w_0}{z_R^2} = \frac{c^2 w_0 \cdot \lambda^2}{pi^2 w_0^4} = \frac{4c^2}{k_0^2 w_0^3} \; . \tag{2.54}$$

The right hand side of Eq. (2.52) transforms to

$$\frac{c^2}{\eta}\frac{\partial \eta}{\partial r} = \frac{c^2}{\eta}\frac{\omega_{p,0}^2}{8\omega_0^2}\frac{\partial a_0^2}{\partial r} \; . \tag{2.55}$$

To transform Eqs. (2.54) and (2.54) into power, some assumptions are needed. First, the refractive index is approximated to $1/\eta \approx 1$, which is true if both the vector potential a_0 and density is not too large. Second, for simplification, a triangular approximation for the derivative of a_0 is assumed: $\frac{\partial a_0^2}{\partial r} \approx -a_0^2/w_0$[34] yields

$$\frac{4c^2}{k_0^2 w_0^3} = c^2 \frac{\omega_{p,0}^2}{8\omega_0^2}\frac{a_0^2}{w_0} \tag{2.56}$$

$$\frac{\omega_0^2}{k_0^2}\frac{32}{\omega_{p,0}^2} = a_0^2 w_0^2 \; . \tag{2.57}$$

Eq. (2.57) can be transformed into something more useful by using the definition of a_0, Eq. (2.23), and by further substituting the relation between electric field and intensity,

---

[33] This is plausible as the vector potential is the highest at the beam focus $I \propto \frac{1}{w(z)^2} \to a_0 \propto \frac{1}{w(z)}$ so that the effect is maximised.

[34] For purposes later revealed, note that if we assume a Gaussian laser beam, a more accurate result would be $\frac{\partial a_0^2}{\partial r} = \frac{\partial}{\partial r} a_0^2 \exp -2r^2/w_0^2 = -a_0^2 4r/w_0^2 \exp -2r^2/w_0^2 \overset{r=w_0}{\to} -\frac{a_0^2}{w_0}\frac{4}{e^2} \approx -\frac{1}{2}\frac{a_0^2}{w_0}$

Eq. (2.16). Inserting the power of a Gaussian laser beam, Eq. (B.19), finally yields:

$$\frac{1}{2}\pi w_0^2 a_0^2 = \frac{32\pi}{2} c^2 \frac{1}{\omega_{p,0}^2} \tag{2.58}$$

$$\rightarrow \underbrace{\frac{1}{2}\pi w_0^2 I}_{P} \cdot \frac{2e^2\mu_0}{m_e^2\omega_0^2 c} = 16\pi c^2 \frac{1}{\omega_{p,0}^2} \tag{2.59}$$

$$P = \frac{8\pi m_e^2 c^3}{e^2\mu_0}\frac{\omega_0^2}{\omega_{p,0}^2} \rightarrow P_c[\mathrm{GW}] \equiv 17.46\frac{\omega_0^2}{\omega_{p,0}^2} \tag{2.60}$$

The final expression defines the *critical power*. It states that, if the injected laser pulse equals this power, the beam is self-guided, because it oscillates electrons transversely to relativistic energies, which modifies the refractive index.

This effect is crucial in plasma physics as it increases the length over which the intensity stays high increasing the maximal electron energy. Otherwise, the energy gain is limited solely by the diffraction of the Gaussian beam propagation, which is referred to as the *diffraction limit*. This is discussed in Sec. 2.10 and includes a summary of more schemes, which are able to guide the laser pulse in the plasma.

2.7.3 Longitudinal Effects of the Plasma on the Laser Pulse

Not only do transverse effects alter the pulse shape, but also longitudinal effect occur, as a laser pulse has a longitudinal gradient of the intensity as well. This gradient is responsible for a longitudinal ponderomotive force, which pushes the electrons at the front of the laser pulse forward. The laser pulse experiences a longitudinal density profile, which changes the refractive index, see Eq. (2.49).

A laser pulse of length L, where the front edge of the pulse propagates with the group velocity $v_{G,1}$ and its back with $v_{G,2}$ propagates through the plasma. Using the approximation of $L\frac{v_{G,2}-v_{G,1}}{L} \approx L\frac{\partial v_G}{\partial z}$, the rate of change of the pulse length yields

$$L_2 - L_1 = \Delta L = (v_{G,2} - v_{G,1})\Delta t = L\frac{v_{G,2} - v_{G,1}}{L}\Delta t \tag{2.61}$$

$$\frac{1}{L}\frac{\Delta L}{\Delta t} \approx \frac{1}{L}\frac{\partial L}{\partial t} \approx \frac{\partial v_G}{\partial z}\,. \tag{2.62}$$

Transforming Eq. (2.62) into the co-moving frame $\xi = z - ct$ and $\tau = t$, see App. B.10 for details, and using the group velocity Eq. (2.46), the change of the pulse duration can be determined to be

$$\frac{1}{L}\frac{\partial L}{\partial \tau} = \frac{\partial v_G}{\partial \xi} = c\frac{\partial \eta}{\partial \xi} \tag{2.63}$$

Recalling the non-linear refractive index Eq. (2.49) indicates that the pulse can stretch and compress depending on density perturbations, local differences of the central wavelength and intensity differences. For example, a strong longitudinal ponderomotive force, as discussed in the beginning of this section, leads to a higher electron density in front of the pulse, which has a positive slope $\frac{\partial \delta n}{\partial \xi} > 0$, changes the pulse duration

$$\frac{1}{L}\frac{\partial L}{\partial \tau} \propto -\frac{\partial \delta n}{\partial \xi} < 0 \tag{2.64}$$

and compresses the pulse.

Additionally, pulse compression can produce new wavelengths as well: a perfectly compressed Gaussian pulse with a flat phase, will be compressed according to the mechanism just described, but since the pulse compresses, consequently, new wavelengths have to be produced. For a positive density ramp, the frequency increases ([35], similar derivation as above) and a positive chirp of the pulse develops. The pulse compression in the front depletes also more energy in the front. This decreases the longitudinal intensity asymmetrically. The front etches away[36], and decreases the effective group velocity by,

$$v_{etch} = c\frac{\omega_p^2}{\omega_0^2} \tag{2.65}$$

$$v_{G,\mathit{eff}} \approx c\left(1 - \frac{3}{2}\frac{\omega_p^2}{\omega_0^2}\right) \tag{2.66}$$

Decreasing the group velocity is an issue as it limits the achievable electron energies, as the dephasing length is shortened (see Sec. 2.10). However, this effect can be overcome by for example introducing a pre-cursor[37].

The laser pulse changing the local density can alter the refractive index, which can then shift the central frequency and can reduce or increase the intensity. The propagation of an intense laser pulse in plasma has multiple consequences and their effects can amplify themselves. Pulse compression has been observed to decrease the pulse duration by a factor of > 3[38] and increase the power by > 2[39].

---

[35] [97] W. B. Mori. *IEEE Journal of Quantum Electronics* (1997).

[36] [98] C. D. Decker *et al.* *Physics of Plasmas* (1996).

[37] [39] M. Tzoufras *et al.* *PRL* (2014).

[38] [99] J. Faure *et al.* *PRL* (2005); [100] J. Schreiber *et al.* *PRL* (2010).

[39] [101] M. J. Streeter *et al.* *PRL* (2018).

2.8 Laser Plasma-Wakefield Acceleration

The goal is to accelerate electrons in the plasma as first proposed by Tajima and Dawson in 1979[40]. This section will summarise the mechanism and point out scaling laws through which the energy of the electrons can be estimated. The electrons are repelled off-axis through the ponderomotive force and create longitudinal density modulations. As the ions in the plasma are much heavier than the electrons, the ions remain stationary and the charge separation create strong longitudinal and transverse periodic electric fields, called wakefields. Particles in the right phase of a the wakefield can exploit these electric fields and be accelerated. A short review of a linear wakefield model in 1D will introduce the concept and give non-relativistic limits and trajectories, before numerical solutions of non-linear equation of motions are presented.

2.8.1 Linear 1D Laser-Plasma Wakefield Acceleration

The differential equations for the linear case of laser-plasma wakefield acceleration originating from the continuity equation (B.107), Gauss' Law (2.1) and equation of motion (2.21) yield (a detailed derivation can be seen in App. B.11):

$$\frac{\partial^2 n_1}{\partial \xi^2} + k_p^2 n_1 = \frac{1}{2} n_{e,0} \frac{\partial^2 a^2}{\partial \xi^2} \tag{2.67}$$

$$\frac{\partial^2 E}{\partial \xi^2} + k_p^2 E = -\frac{1}{2} k_p^2 \frac{m_e c^2}{e} \frac{\partial a^2}{\partial \xi} \tag{2.68}$$

$$\frac{\partial^2 \Phi}{\partial \xi^2} + k_p^2 \Phi = \frac{1}{2} k_p^2 \frac{m_e c^2}{e} a^2 \tag{2.69}$$

This set of equations is expressed in the co-moving frame $\xi = z - ct$. The wakefield phase velocity, driven by the laser with the group velocity v_g, travels at that same driving velocity. This will be essential, when the maximum possible energy is calculated. Accelerated electrons, travelling with approximately the speed of light can overtake the wakefield as the speed of the pulse is reduced by the refractive index (see Sec. 2.6 and 2.10).

An important limit of the wakefield accelerator is the *cold wavebreaking limit*. It originates from the Gauss' Law and describes the extreme at which a sinusoidal perturbation of density n_1, which creates the electric field, reaches its maximum value, which is the cold density of the plasma $n_{e,0}$. Assuming a harmonic oscillation, the maximum

---

[40] [21] T. Tajima and J. M. Dawson. *PRL* (1979).

electric field reaches,

$$\frac{\partial E(\xi)}{\partial \xi} = -\frac{e n_{e,0}}{\epsilon_0}\sin(k_p\xi) \tag{2.70}$$

$$\Rightarrow E(\xi) = \frac{e n_{e,0}}{\epsilon_0 k_p}\cos(k_p\xi) \tag{2.71}$$

$$\Rightarrow E_0 = \frac{m_e}{e}\underbrace{\frac{e^2 n_{e,0}}{\epsilon_0 m_e}}_{=\omega_p^2}\frac{c}{\omega_p} = \frac{m_e c\omega_p}{e} \approx 960\sqrt{n_e[10^{18}\mathrm{cm}^{-3}]}[\mathrm{MV\,cm}^{-1}] \tag{2.72}$$

However, the assumptions of the differential equations break, before a field strength of this maximum can be reached as small perturbations in the density and laser field strength are required for the derivation. Nevertheless, it is convenient to normalise the electric field strength to that limit. This limit can be exceeded for very large vector potentials, which will be discussed in the next Sec. 2.8.2.

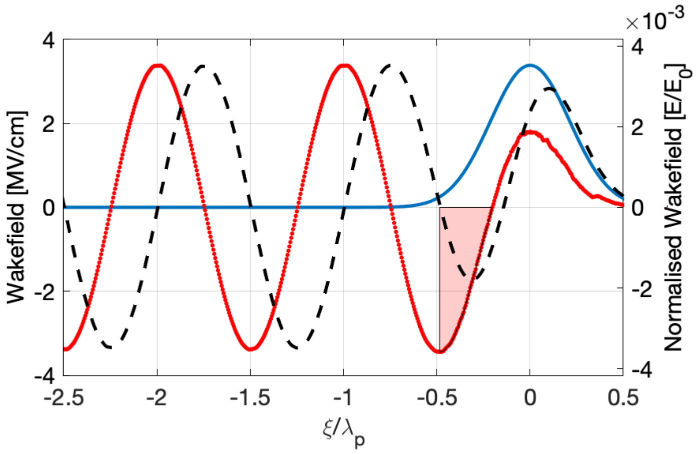

Figure 2.4: Wakefield properties for $a_0 = 0.1$, a density of $n_{e,0} = 10^{18}\mathrm{cm}^{-3}$ and a pulse duration of $FWHM = 0.5\lambda_p$. The blue curve is the squared vector potential a, the electron density $n_1 - n_{e,0}$ follows in dashed black, which result in a longitudinal electric field E_z in red dots. The right axis label depicts the field strength normalised to the cold wavebreaking limit. The squared vector potential and density is normalised to the maximum value of the electric field in this plot.

The linear wakefield for a vector potential of the form of a Gaussian $a(\xi) = a_0\exp(-\xi^2/L^2)\sin(k_0 x)$ with a strength of $a_0 = 0.1$, a pulse length of $L = \lambda_p/\sqrt{(}8\log(2))$[41] and a density of $n_e = 1\times 10^{18}\,\mathrm{m}^{-3}$ can be seen in Fig. 2.4. As one can see, the density and electric field follows a harmonic oscillator function just after a first initial kick from the driver. The electrons are pushed towards the front of the laser pulse due to the ponderomotive force, which then follows an electron depleted area. This triggers the oscillation. The electric field follows the density perturbation with a

---

[41] As described in App. B.13, the variance of a Gaussian function, here a^2 is related to the $FWHM$ of the squared function (squared, since the intensity of a pulse is commonly measured instead of the electric field) as $\sigma^2 = FWHM^2/(2\log(2))$. In this case, $FWHM = 0.5\lambda_p$.

delay of $\pi/2$, which makes sense as the derivative of the electric field is the density perturbation. The maximum[42] electric field peaks at $3.4\,\mathrm{MV\,cm^{-1}} = 0.0035 \cdot E_0$.
The maximum energy gain is estimated, by calculating the maximal energy gain in the co-moving frame $W = \int eE\mathrm{d}\xi$, Lorentz transform the energy into the boosted frame and inverse Lorentz transform into the laboratory frame. A detailed derivation is seen in App. B.14. Here, the maximal energy gain yields $1.04\,\mathrm{MeV}$.

2.8.2 Non-Linear 1D Laser-Plasma Wakefield Acceleration

Once the normalised vector unit is driven by a laser pulse with relativistic intensity, $a_0 \ll 0$ is not valid and the perturbations are not valid anymore. The derivation of the non-linear differential equations, first shown in[43], is summarised in this work by following the equations in[44] in App. B.12. It yields

$$\frac{\partial^2\phi}{\partial\xi^2} = \frac{k_p^2}{2}\left(\frac{1+a^2}{(1+\phi)^2} - 1\right) \tag{2.73}$$

The electric field and electron density can be calculated using Gauss' Law and Poisson's equation as in Sec. 2.8.1 (and calculated in App. B.11). These equations are valid for arbitrary field strengths and arbitrary pulse shapes. Eq. (2.73) can be solved analytically for certain pulse shapes (e.g. a flat-top profile,[45]), but must generally be solved numerically, which was done in the previous section, Fig. 2.4. For a higher vector potential of $a_0 = 2$, the solution can be seen in Fig. 2.5 a) ($n_0 = 1 \times 10^{18}\,\mathrm{m^{-3}}$, $FWHM = 0.5\lambda_p$).

Fig. 2.5 depicts the wakefields for different pulse shapes. The detailed differences in pulse shapes are explained in App. B.13, but they are essentially: a cosine Fig. 2.5 b), a super-Gaussian of 10th order c), and a flat top d) shaped vector potential profile. The pulse duration defines the full width at which the intensity ($I \propto a^2$) drops to its half. The comparison of the achievable electron energies is done, keeping the maximum vector potential constant.

Keeping the vector potential constant changes the energy in the pulse. However, the difference is rather small and the change in energy is calculated in App. B.13. Keeping a_0 fixed, simplifies the comparison between the pulse shapes here. The maximal electric field differs for all pulse shapes and increase from a)-d). This can be explained

---

[42] technically the minimal electric field as electrons are accelerated forwards in a negative electric fields

[43] [102] V Berezhiani *et al.* *Physics Letters A* (1990).

[44] [103] P Gibbon. *Short Pulse Laser Interactions with Matter* (2005), Ch. 4.3.

[45] [104] S. V. Bulanov *et al.* *JETP Letters* (1989).

by the higher gradient of the intensity thus higher ponderomotive force between a)-d)[46]. The increased gradient produces a sharper pre-cursor density bulb, which then produces a higher electric field. It is worth noting further, that the pulse width for the highest maximal energy gain is not the same between the different pulse shapes. The summary of the highest energy gains for each pulse shape, and their optimal pulse duration as well as the dephasing lengths, can be seen in Table 2.1. The sharper gradients of the super-Gaussian and flat-top profile support a longer pulse duration. This is of interest experimentally as for limited bandwidth, shaping the pulse shape would ultimately increase the pulse duration as well.

Pulse Shape	$\xi_{\frac{1}{2}}/\lambda_p$	Energy Gain $[\mathrm{MeV}\ (1/E_0)]$	Deph. Length $[\mathrm{mm}]$
Gaussian	0.4	848 (0.88)	16.9
Cosine	0.39	938 (0.98)	17.4
Super Gaussian	0.65	1226 (1.28)	19.3
Flat Top	0.76	1238 (1.29)	19.4

Table 2.1: Depicted are the maximum energy gains for the different pulse shapes with their respectively optimal pulse length to achieve those energies and the dephasing length for each shape.

A more detailed discussion on the Gaussian pulse shape-based wakefield properties is presented in the following. The depleted region from the electrons is often referred to as bubble and creates a sharp sawtooth electric field that does not resemble a harmonic wave-function anymore. It follows that the longitudinal electric field is skewed and increased in field strength. The maximum electric field for the Gaussian pulse shape rises from $3.4\ \mathrm{MV\,cm^{-1}} = 0.0035 \cdot E_0$ to $824\,\mathrm{MV\,cm^{-1}} = 0.84 \cdot E_0$ for the used density of $n_0 = 1 \times 10^{18}\,\mathrm{cm^{-3}}$. This is a factor of 242, while the vector potential only increased by a factor of 20.

The increase in energy is non-linear, because multiple effects are adding up. Apart from the increase in the maximum electric field already mentioned, the wakefield wave wavelength elongates, which increases the length over which electrons can be accelerated. Fig. 2.6 shows the maximum energy gain for a scan of pulse duration and normalised vector potential. The electric field was normalised to the cold wave-breaking limit, before calculating the energy gain to produce a density-independent result, while also the pulse duration is normalised to the plasma wave wavelength. Note, that the depletion of the pulse energy and diffraction is not taken into account for these simulations, but the group velocity and etching velocity of the laser pulse are included in that these change the dephasing length (details on the limitation mechanism in the next

---

[46] As seen in App. B.13, $\cos^2$ does indeed has a higher gradient than the Gaussian function and it is visually convincing that the super-Gaussian and then the flat top profile have an even higher maximal gradient.

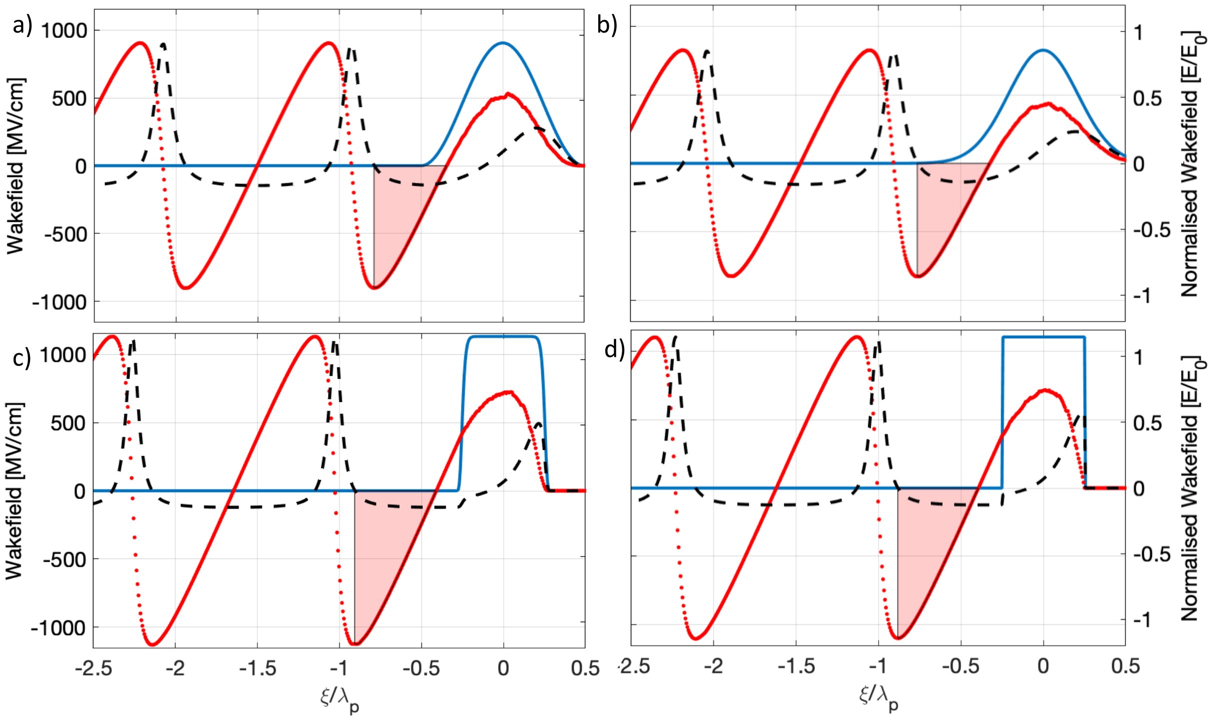

Figure 2.5: Wakefield properties for different pulse shapes and a normalised vector potential of $a_0 = 2$. As Fig. 2.4, the blue curve is the squared vector potential a^2, the electron density n_e in dashed black, and the longitudinal electric field E_z in red dots. a) corresponds to a Gaussian pulse shape, b) to a cosine, c) to a super-Gaussian of the 10th order and d) to a flat-top intensity profile.

Sec. 2.10). The energy gain is not constant for a fixed a_0, but also varies with changing pulse duration as the conversion of the pulse energy has an optimum, which is on average $\xi_{\frac{1}{2}}/\lambda_p = 0.37$ for a Gaussian profile.

An estimate of the maximum field strength of a linear polarised laser pulse with a flat top profile has been found previously to be[47]:

$$(E/E_0)_{\text{Flat Top}} = \frac{a_0^2}{\sqrt{4 + 2a_0^2}} \tag{2.74}$$

An $a_0 = 2$ yields 1.15, which is higher than for a Gaussian profile. This is as expected as a flat top profile has a steeper gradient thus higher ponderomotive force pushing the electrons off-axis. A scan of the electric field depending on the normalised vector potential for a Gaussian intensity profile leads to the empirical formula,

$$(E/E_0)_{\text{Gauss}} = \frac{1}{2}\frac{a_0^2}{\sqrt{1 + a_0^2}} \tag{2.75}$$

---

[47] [105] E. Esarey *et al.* *Reviews of Modern Physics* (2009), fol. Eq. 25.

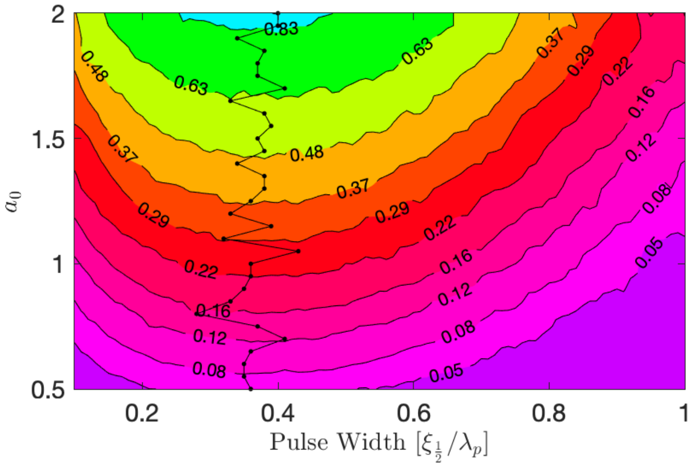

Figure 2.6: Maximum energy gain for a linear and non-linear 1D Gaussian pulse shape scan. The pulse duration $\xi_{\frac{1}{2}}$ and the normalised vector potential was varied ($0.5 \leq \xi_{\frac{1}{2}}/\lambda_p \leq 1$ and $0.5 \leq a_0 \leq 2$ in 37×61 simulations). The contour show the energy gain, where the electric field was normalised to the cold wavebreaking limit, Eq. (2.72). The black dotted line refers to the pulse length at which the energy gain is maximised.

or including time dependence

$$(E/E_0)_{\text{Gauss}} = \frac{1}{2}\frac{a_0^2}{\sqrt{1+a_0^2}}\left(4\left(\frac{\xi_{\frac{1}{2}}}{\lambda_p}\right)^3 - 8.6\left(\frac{\xi_{\frac{1}{2}}}{\lambda_p}\right)^2 + 4.9\left(\frac{\xi_{\frac{1}{2}}}{\lambda_p}\right) + 0.1\right) \tag{2.76}$$

as depicted in Fig. 2.7.

The maximal electric field in units of the cold wavebreaking limit is shown in Fig. 2.8 (a). This was used to model the Eq. (2.76), which models the behaviour closely, to estimate the energy gain in an experimental set up quickly. The mismatch of the Eq. (2.76) and the result of the simulation is shown in Fig. 2.8 (b). The mismatch increases for longer pulse duration and lower normalised vector potential. The basic plasma wave wavelength is $111\,\mathrm{fs} - 29\,\mathrm{fs}$ for densities of around $1 \times 10^{18}\,\mathrm{cm}^{-3} - 1.5 \times 10^{19}\,\mathrm{cm}^{-3}$. The equation is a reasonable approximation for quick estimations of the wakefield amplitude.

2.8.3 Laser Plasma Wakefield Acceleration in multiple Dimensions

Electron acceleration in a laser plasma accelerator is not as simple as was discussed in the previous sections. The matching parameter and scaling of the process become much more complex in the non-linear 3D regime. The finite focus spot size creates

---

[48] ([105] E. Esarey *et al. Reviews of Modern Physics* (2009), fol. Eq. 25)

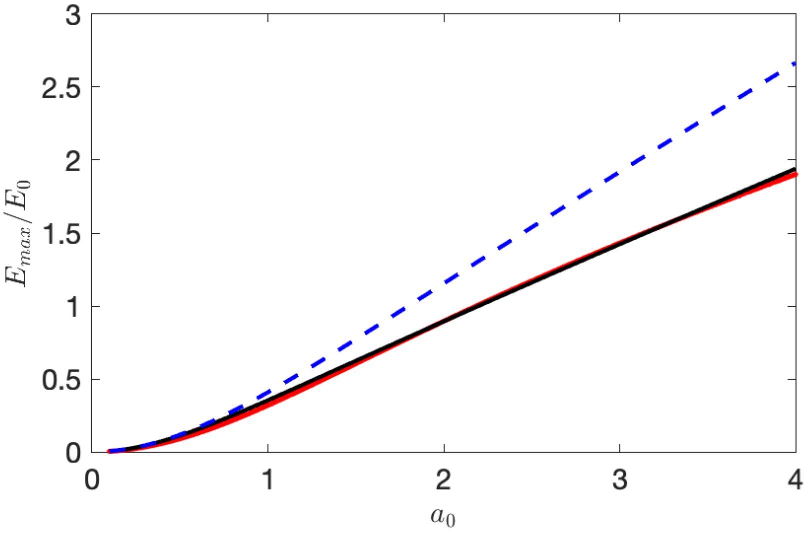

Figure 2.7: Maximum electric field normalised to the cold wave breaking limit for a Gaussian laser profile. The pulse width is fixed to be $0.4\lambda_p$. In red the maximum electric fields obtained through 1D solutions as described in Sec. 2.8.2 and in black Eq. (2.75). The scaling for a flat top profile[48] is depicted in blue.

yet another transverse gradient and ponderomotive force. The ion-cavity inside the plasma has a transverse dimension of the plasma wave wavelength, which means that the focus spot needs to be matched with the plasma density to transport its energy into the wake. A 2D simulation can be seen in Fig. 2.9.

The simulation was performed using the particle-in-cell code (PIC-code) EPOCH[49]. More details about the simulations and PIC-code follow in Sec. 3.4. This simulation was executed with an $a_0 = 0.75$, $\xi_{\frac{1}{2}}/\lambda_p = 0.31$ and a focus spot size of $w_{\frac{1}{2}}/\lambda_p = 1.3$ at a density of $n_0 = 0.75 \times 10^{18}\mathrm{cm}^{-3}$. The density perturbations are shown at the top

---

[49] [106] T. D. Arber *et al. Plasma Phys. Control. Fusion* (2015).

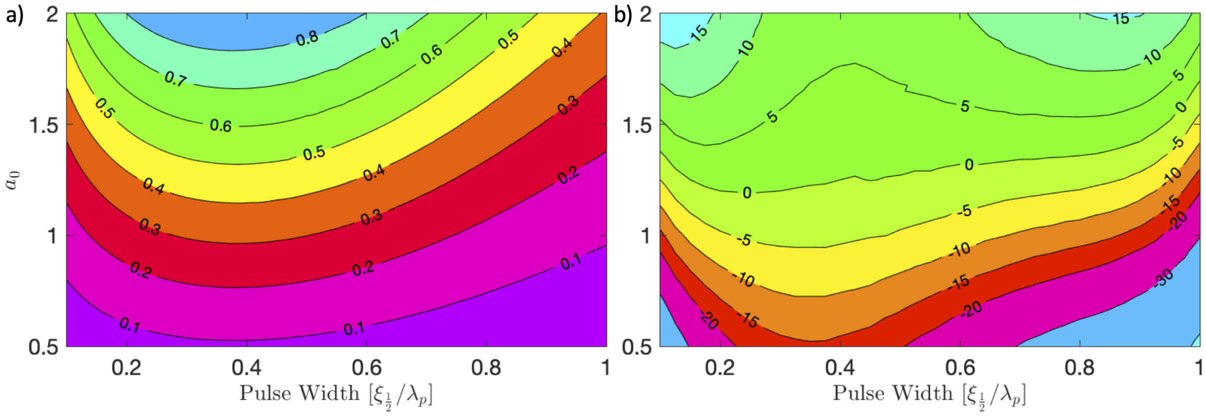

Figure 2.8: a) Amplitude of the accelerating field of a gaussian laser pulse in units of the cold wavebreaking limit. b) Difference between the model function to estimate the electric field amplitude and the result of the simulation in %.

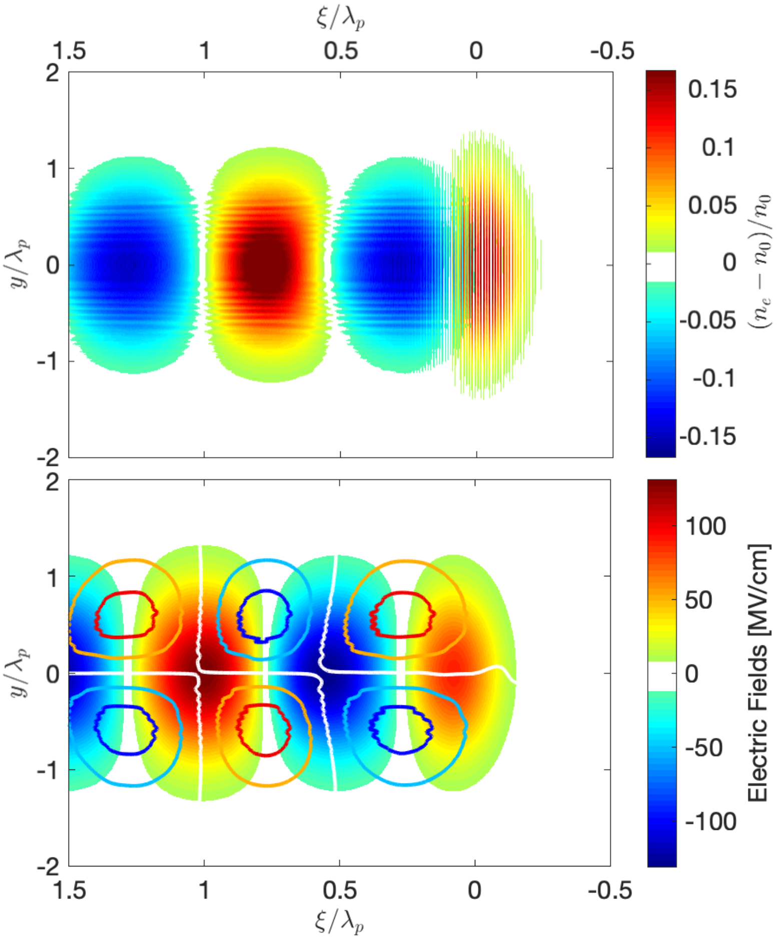

Figure 2.9: 2D Simulation with PIC-code EPOCH of a Gaussian laser pulse. The normalised density perturbation is depicted at the top. The imprint of the laser pulse causing the wakefield can be seen as it causes small perturbations in the density at $\xi/\lambda_p \approx 0$. The longitudinal electric field is seen at the bottom. The transverse electric field is overlaid on top as a contour. Note that the ratio between longitudinal field and transverse fields is 5.3:1 for illustrative purposes.

of Fig. 2.9 and it can be seen that the laser pulse creates electron-free bubbles on-axis, similar to the 1D case. Transversely, the bubble extends to a length of around the plasma wave wavelength. The bottom of Fig. 2.9 shows the longitudinal and transverse electric field scale by a ratio of 5.3:1 to facilitate visualisation. The first blue region is the accelerating field. However, the transverse field changes sign half-way through the region (longitudinally). This change is the difference between focusing and defocusing forces. The first section diverges the beam. This field originates from the electron density spikes. The accelerating field is drawn from the peak of the electron density to the minimum, but transverse focusing only occurs in the electron deprived region.

A brief note on the PIC-code: As the physics are not generally solvable analytically

for 3D non-linear wakefields, particle-in-cell codes are often used to simulate the interaction with a high normal vector potential laser pulse and a plasma (i.e.[50]). In 2007 W. Lu et al.[51] performed in-depth 3D simulations and combined phenomenological observations with simple physical models to propose *scaling laws* for $a_0 \leq 2$. These scaling laws estimate the energy, energy spread, charge and efficiency by matching the laser beam properties with the plasma properties.
The first experimental demonstration of electrons accelerate in a laser wakefield was in 1995[52] with an external injected electron beam. The first self-injected electron beam, which is self-injected by driving a strong wake beyond its breaking point was shown in[53], and the first quasi-monoenergetic electron beams were observed in 2004[54]. Note that monoenergetic was defined here by ±3 % at FWHM.

2.9 Trapping and Injection of Electrons into the Wakefield

Producing highly accelerating electric fields was investigated in the last section, but these fields do not accelerate electrons if these electrons are not trapped in the wakefield. Quite naturally, a trapped electron must be contained in the potential of the wakefield and not escape. In this context, escaping occurs, if the longitudinal kinetic energy of the electron exceeds the potential energy:

$$e\phi' > (\gamma_e' - 1)m_e c^2 \tag{2.77}$$

$$e\phi > \left(\gamma_e(1-\beta_e\beta_p) - \frac{1}{\gamma_p}\right) m_e c^2 \text{ [55]} \tag{2.78}$$

where the second line has been Lorentz transformed. A commonly used threshold for self-injection is derived by assuming underdense plasma ($\beta_p \approx 1$ and $\rightarrow \gamma_p \gg 1$) and cold electrons ($\beta_e \approx 0$ and $\rightarrow \gamma_e \approx 1$), which results in $e\phi/m_e c^2 > 1$ or in form of the electric field[56] $E_{trap} > m_e c\omega_p/e = E_0$. Thus, self-injection occurs if the cold-wavebreaking limit is exceeded. Generally, self-injection is more complicated in

---

[50] [107] R. Fonseca *et al.* (2002); [106] T. D. Arber *et al. Plasma Phys. Control. Fusion* (2015); [108] R. Lehe *et al. Comput. Phys. Commun.* (2016).

[51] [109] W. Lu *et al. PRST - AB* (2007).

[52] [110] F. Amiranoff *et al. PRL* (1995).

[53] [111] W. B. Mori *et al. PRL* (1994); [112] D. W. Forslund *et al. Physics of Fluids* (1975).

[54] [29] S. P. D. Mangles *et al. Nature* (2004); [30] C. G. R. Geddes *et al. Nature* (2004); [31] J. Faure *et al. Nature* (2004).

[55] The potential transforms as $\phi' = \gamma_p \phi$, see App. B.14 and the Lorentz factor as $\gamma_e' = 1/\sqrt{1-(\beta_p-\beta_e)^2/(1-\beta_p\beta_e)^2}$

[56] $\phi \rightarrow cE/\omega_p$

multiple dimensions. It was experimentally observed 1995[57], as well as studied in 3D-PIC simulations[58]. Several attempts have been made by the community to derive analytical expressions for the trapping condition, of which it is notable to mention[59]. Self-injection is not the only way electrons can be trapped. While the condition for trapping remains in the different schemes, that is that the electrons must have the right kinetic energy and position within the ion-cavity, the initiation of injection can vary greatly and is an on-going major field of interest in the community.

The first controlled injection schemes date back to self-modulated wakefield experiment. An additional laser beam was used orthogonally to the main laser beam to add enough momentum to the electrons to inject them into the wakefield[60]. Counter propagating laser beams can also be used[61], where the beatwave pattern of the colliding laser pulse exceeds the wave-breaking limit and injects electron locally.

The phase velocity of the plasma wave can also be altered, instead of changing the intensity of the laser to trap electrons. As seen in the previous Sec. 2.8.1 the back of the bubble consists of a sharp density spike, which propagates along with the wake. The bubble expands backwards if the plasma density is decreased abruptly, and the electrons formerly in the spike region are then inside the bubble and potentially trapped. This is referred to as density down ramp injection, proposed, and investigated analytically and in simulations in 1998[62] and experimentally demonstrated 2008[63] by focusing into the downstream side of a gas jet.

Another major technique, which was used as an injection method in this work, Sec. 6 is known as ionisation injection. This technique utilises different ionisation energies of multi-species gases. The theory was first presented by M. Chen et al. in 2006[64] and it was first shown experimentally by Rowland-Rees et al. in 2008[65] and then verified in a controlled way in 2010[66]. A nitrogen-doped noble gas (He) can significantly increase the injected charge. While the outer shell electrons are pre-ionised before the main laser pulse arrives, the inner shell electrons of the dopant gas are only ionised at the peak of the focusing laser pulse as they have a higher ionisation threshold. Hence, electrons are introduced inside the wakefield and immediately trapped. This method can be longitudinal localised as well as proposed in[67], by creating a gas cell with two

---

[57] [27] A. Modena *et al. Nature* (1995).
[58] [113] A. Pukhov and J. Meyer-ter Vehn. *APB* (2002).
[59] [114] I. Kostyukov *et al. PRL* (2009); [115] A. G. Thomas. *Physics of Plasmas* (2010).
[60] [116] D. Umstadter *et al. PRL* (1996).
[61] [117] E. Esarey *et al. PRL* (1997); [42] J. Faure *et al. Nature* (2006).
[62] [118] S. Bulanov *et al. PRE* (1998).
[63] [119] C. G. R. Geddes *et al. PRL* (2008).
[64] [120] M. Chen *et al. J. Appl. Phys.* (2006).
[65] [121] T. P. Rowlands-Rees *et al. PRL* (2008).
[66] [41] C. McGuffey *et al. PRL* (2010); [122] A. Pak *et al. PRL* (2010).
[67] [38] A. Martinez De La Ossa *et al. PRL* (2013).

separate volumes and gas mixtures, or by using secondary pulses, e.g. the two-colour injection method[68].

2.10 Limitations of Laser Wakefield Acceleration

There are three main mechanics limiting the maximum achievable energy of the trapped electrons

- Laser diffraction
- Electron dephasing
- Pump depletion

Diffraction of a laser pulse will decrease the peak intensity and with that the normalised vector potential. The total distance at which the intensity drops by $\sqrt{2}$ on either side of the beam waist is referred to as the **diffraction limit**. The Gaussian beam propagation description, Sec 2.1.1 defines the distance over which the intensity drops from the beam waist by $\sqrt{2}$ as the Rayleigh length z_R. This thus sets the diffraction limit to $2z_R$ for a Gaussian laser pulse with the ideal beam quality. There are multiple ways to overcome this limit as indicated in Sec. 2.7.2. If the power of the laser pulse exceeds the critical power the laser pulse is guided. One of the first techniques of controlling propagation was using a two-pulse technique[69]. By sending a pre-pulse into a gas cell, it can produce a density channel through which the main laser pulse is guided for more than 20 Rayleigh lengths. A similar density channel can be produced by a gas-filled capillary discharge[70]. A discharge circuit is passed through a capillary filled with a gas creating a parabolic transverse density profile. The concept of a discharged capillary waveguide was explored in different ways, e.g. the guiding radius varied longitudinally[71] or multiple gases were injected into the system to increase the guiding efficiency[72]. A recently investigated method includes the hydrodynamic expansion of plasma columns produced by optical field ionisation[73], where a laser focus is stretched over the length of the gas cell via an axicon lens, creating a transverse density profile.

Dephasing of the electron bunch and laser pulse is due to the lower group velocity of the laser pulse in the plasma than c. Since the relativistic electron's velocity is in

---

[68] [123] L. L. Yu *et al. Phys. Rev. Lett.* (2013).
[69] [124] C. Durfee and H. M. Milchberg. *PRL* (1993).
[70] [125] D. J. Spence *et al. J. Opt. Soc. Am. B* (2003).
[71] [126] D. Kaganovich *et al. APL* (1999).
[72] [127] M. S. Kim *et al. APL* (2013).
[73] [128] R. J. Shalloo *et al. Phys. Rev. E* (2018).

good approximation c, the electrons overtake the accelerating and focusing region of the plasma bubble, which has a length of $\lambda_p/4$ in the linear regime and are decelerated beyond that. Using the group velocity in the linear regime, see Eq. (2.46), the velocity difference between electrons and laser pulse can be estimated as $\Delta v = c - v_G \approx c\frac{1}{2}\frac{\omega_p^2}{\omega_0^2}$. The *dephasing length* L_d yields

$$L_d = c\frac{\lambda_p/4}{\Delta v} = \frac{1}{2}\frac{\lambda_p^3}{\lambda_0^2} \,. \tag{2.79}$$

However, determining the dephasing length is not as trivial as indicated here and many different figures of merits have been given in the literature. The difference originates in the length over which the electrons are considered to be accelerated and the effective group velocity of the laser as the accelerating and focusing regime tends to $\sqrt{a_0}\lambda_p/2$ in the non-linear regime.

Additionally, the wakefield wave wavelength is not constant with a_0 and its effect varies if 1D or 3D is considered. Scaling laws for moderate intensities ($a_0 > 2$) have been derived in[74] and a summary has been presented. An abbreviated version is seen in Table 2.2 with the most important acceleration parameters.

	a_0	w_0	L_d	L_{pd}	$< E_{acc} >$	$\Delta W/mc^2$
1D	< 1	λ_p	$\frac{1}{2\pi}\frac{\lambda_p^3}{\lambda_0^2}$	$\frac{\lambda_p^2}{\lambda_0^2}\frac{c\tau}{a_0^2}$	$a_0^2 E_0$	$a_0^2\frac{\lambda_p^2}{\lambda_0^2}$
1D	> 1	λ_p	$\frac{2}{\pi}a_0^2\frac{\lambda_p^3}{\lambda_0^2}$	$\frac{\lambda_p^2}{\lambda_0^2}\frac{c\tau}{3}$	$a_0 E_0$	$4a_0^2\frac{\lambda_p^2}{\lambda_0^2}$
3D	> 2	$\frac{\sqrt{a_0}}{\pi}\lambda_p$	$\frac{2\sqrt{a_0}}{3\pi}\frac{\lambda_p^3}{\lambda_0^2}$	$\frac{\lambda_p^2}{\lambda_0^2}c\tau$	$\frac{\sqrt{a_0}}{2}E_0$	$\frac{2}{3}a_0\frac{\lambda_p^2}{\lambda_0^2}$

Table 2.2: Summary of the scaling laws presented by Lu et al.[75] for matched conditions that is focusing the beam to the size of the bubble radius in 1D and 3D. These include the the matched spot size w_0, the dephasing length L_d, the pump depletion L_{pd}, the average accelerating electric field $< E_{acc} >$ and the energy gain $\Delta W/mc^2$. The plasma wave wavelength $\lambda_p = 2\pi/k_p$ is the wavelength of the relativistic wave in the linear regime, τ the pulse duration, and E_0 the cold wave-breaking limit.

There are possibilities to also overcome this limitation. Similar to the previous problem, the wakefield velocity must be controlled to match the velocity of the electrons. This can be done by tapering the density profile in a capillary discharge via changing

---

[74] [109] W. Lu *et al.* *PRST - AB* (2007).

[75] ([109] W. Lu *et al.* *PRST - AB* (2007), Tab. 1)

the capillary diameter or segmenting the capillary[76]. Furthermore, different gas feed-lines in the capillary can inject different gas or different pressures at various locations to not only counter diffraction but simultaneously lengthen the dephasing length (also in[77]). A different approach for gas jets was conducted by a using shock front with a knife-edge method[78]. Normally, a gas jet produces a slowly rising and falling density ramp with a reasonably constant density profile intersection. Using a razor blade, the profile can be changed to create a sharp density increase. As the density increases, the plasma wavelength increases rapidly (see Eq. (2.37)) and the relative centre of the wakefield moves towards the laser pulse and the phase of the electrons decreases[79]. Because the laser energy depletes and because as the density decreases, the wakfield strength and self-focusing deceases, the technique has its limit as well.

Changing the velocity of the axial focus using spatio-temporal couplings in combination with an axiparabola have been recent proposals to achieve *quasi dephasing free* acceleration[80]. However, these are theoretical approaches as to-date of submitting this work, but indicate more possible solutions to this problem.

Energy depletion is a much more fundamental issue. The laser energy is depleted by generating the wakefield and its corresponding electric field. The laser pulse is not able to continue driving the plasma wave. The pump depletion length L_{pd} is defined with

$$\frac{\partial \varepsilon}{\partial (ct)} = -\frac{\varepsilon}{L_{pd}} \tag{2.80}$$

being the length at which the energy ε drops by $\exp(-1)$.

An estimate can be made by considering the energy density and its volume for both the laser and the plasma wave. However, a more rigorous derivation can be found by Shadwick et al.[81], where the depletion length is calculated to scale as

$$L_{pd} \approx 1.4 \frac{\lambda_p^3}{\lambda^2} \begin{cases} 2/a_0^2, & \text{for } a_0^2 \ll 1 \\ 1 & \text{for } a_0^2 \gg 1 \end{cases} \tag{2.81}$$

for a Gaussian laser pulse with optimised pulse length, using Eq. [10] by Shadwick et al. and note that Eq. [10] is divided by k_p $(\rightarrow 8.7/2\pi \approx 1.4)$. One consideration has

---

[76] [126] D. Kaganovich *et al. APL* (1999); [129] P. Sprangle *et al. Phys. Rev. E* (2001).
[77] [127] M. S. Kim *et al. APL* (2013).
[78] [130] E. Guillaume *et al. PRL* (2015).
[79] [131] B. B. Pollock *et al. PRL* (2011).
[80] [132] A. Debus *et al. Phys. Rev. X* (2019); [133] J. P. Palastro *et al. Phys. Rev. Lett.* (2020); [134] C. Caizergues *et al. Nat. Photonics* (2020).
[81] [135] B. A. Shadwick *et al. Physics of Plasmas* (2009).

been mentioned in Sec. 2.7.3, the etching of the front of the laser pulse, and is not taken into account in this formula.

The limitation due to pump depletion is fundamental and can't be overcome easily. One approach is two use staged LPWA with two independent laser pulses. This will be discussed in Sec. 2.12.

2.11 Radiation Emitted in Laser Plasma-Wakefield Acceleration

A large portion of this work will analyse the radiation emitted from the accelerated electrons inside the plasma bubble. A short overview will be given about the spectrum of this radiation and its origin.

2.11.1 Introduction to Synchrotron Radiation and its Opening Angle

Starting by introducing the opening angle of radiation emitted by a charged particle, moving longitudinal in z and emitting due to a transverse oscillation. From the rest frame of the charged electron, the wavefronts are separated by a distance of λ'. In the laboratory frame, the distance between the wavefronts is different, because a Lorentz transformation has to be performed. A first wavefront is emitted at t_0 and a second wavefront at t_1, which results in a time difference of $\Delta t = t_1 - t_0$. The first wavefront travelled with the speed of light a distance of $c\Delta t$, while the charged particle travelled a shorter distance of $v_e\Delta t$, with v_e being the velocity of the particle. Hence, the wavefronts have a wavelength of $\lambda = c\Delta t - v_e\Delta t$. The time in the lab frame has to be converted into the rest frame of the electrons, which can be done by the conventional Lorentz transformation,

$$t = \gamma(t' + \frac{v_e x'}{c^2}) \tag{2.82}$$

$$\Delta t = \gamma t'_1 - \gamma t'_0 + \frac{\gamma v_e}{c^2} \cdot \underbrace{(x'_1 - x'_0)}_{\text{Rest frame}\to 0} \tag{2.83}$$

$$\Delta t = \gamma \Delta t' \tag{2.84}$$

The wavelength in the rest frame λ' can be expressed as $\lambda' = c\Delta t'$ and the observed wavelength can therefore be calculated to be,

$$\lambda = (c - v_e)\Delta t = (1 - \beta)\gamma\lambda' \tag{2.85}$$

and finally using the approximation for $\gamma \gg 1$ of

$$(1-\beta) = \frac{(1-\beta^2)}{1+\beta} = \frac{1}{1+\beta}\frac{1}{\gamma^2} \overset{\beta\to 1}{\approx} \frac{1}{2\gamma^2} \tag{2.86}$$

results in the transformation of the wavelength to,

$$\lambda \approx \frac{\lambda'}{2\gamma} \,. \tag{2.87}$$

This result states that a wavelength emitted in the rest frame of a charged particle will be reduced by the Lorentz factor, which can be three orders of magnitudes for LPWA particles. It can also be expressed in the *betatron wavelength* λ_β. This wavelength is the wavelength of the oscillation, which the electrons undergo inside the wakefield. The electrons travelling the distance in time $\lambda_\beta/c = \Delta t$. As discussed, this time can be transformed into the rest frame as $\Delta t = \gamma\Delta t'$. Hence, the radiation wavelength depends on the betatron frequency λ_β as,

$$\lambda \approx \frac{\lambda_\beta}{2\gamma^2} \,. \tag{2.88}$$

The opening angle of radiation emitted as dipole radiation can be approximated with this identity as well. Dipole radiation is emitted in a $\sim \sin^2(\theta)$ distribution in the rest frame of an oscillating particle[82]. If the particle moves with a longitudinal velocity, the wavevector is transformed and the radiation is preferably emitted towards the observer on-axis. This can be proven by decomposing the wavevector of the radiation into a longitudinal component $\hat{z}$, and transverse component $\hat{x}$ and using Eq. (2.87).

$$\begin{gathered}
\begin{array}{cc} \text{Rest frame} & \text{Lab frame} \\ \vec{k}' = \vec{k}'_x + \vec{k}'_z & \vec{k} = \vec{k}_x + \vec{k}_z \end{array} \\
\vec{k}'_x = \vec{k}_x \\
\vec{k}_z = \frac{2\pi}{\lambda} = 2\gamma\frac{2\pi}{\lambda'} = 2\gamma\vec{k}'_z \\
\theta \approx \frac{k_x}{k_z} \approx \frac{k'_x}{2\gamma k'_z} = \frac{1}{2\gamma}\tan(\theta') \sim \frac{1}{\gamma}
\end{gathered} \tag{2.89}$$

The last step is an approximation, but it is enough to show, that the opening angle is on the order of the reciprocal Lorentz factor.

---

[82] [136] J. D. Jackson. (1999).

2.11.2 Transverse Propagation of the Electrons inside the Plasma Cavity

This section discusses the radiation originating from the movement of the electrons inside the cavity. The electric fields inside the plasma cavity also have transverse components as seen in Sec. 2.8.1. Hence, the electrons accelerated longitudinally also oscillate in the transverse motion, which from an observer on-axis is dipole radiation. To investigate the radiation, it is required to look at the motion of the electrons. Assuming a simplified model, in which the electrons have a constant energy γ[83] the equation of transverse motion yields

$$F_\perp = -\frac{m_e\omega_p^2}{2} r_\perp \Rightarrow \ddot{r}_\perp + \frac{\omega_p^2}{2\gamma} r_\perp = 0 \tag{2.90}$$

The solution is a sinusoidal function with a frequency of $\omega_\beta = \omega_p/\sqrt{2\gamma}$. This frequency is referred to as the betatron frequency. The electrons oscillation frequency is Lorentz boosted forward as discussed before. Also, the angle of emission is skewed into the direction of propagation. The average opening angle of the radiation depends on the energy and can be determined to be $< \theta^2 >^{\frac{1}{2}} = 1/\gamma$, see Eq. 2.89. The ratio between maximum angle of the electron motion $\mathrm{d}r_\perp/\mathrm{d}z$ and the opening angle of the radiation $1/\gamma$ can enter two regimes, which are called the *wiggler*- and *undulator-regime*. The *wiggler-strength parameter* $K = \gamma \mathrm{d}r_\perp/\mathrm{d}z$ can be calculated as

$$\left|\frac{\mathrm{d}r_\perp}{\mathrm{d}z}\right|_{z=0} = \left|\frac{\mathrm{d}r_\perp}{c\mathrm{d}t}\right|_{z=0} = \frac{r_\beta\omega_\beta}{c} \tag{2.91}$$

$$\Rightarrow K = \frac{\mathrm{d}r_\perp/\mathrm{d}z}{< \theta^2 >^{\frac{1}{2}}} = \frac{r_\beta\gamma\omega_\beta}{c} = r_\beta\gamma k_\beta \tag{2.92}$$

The undulator regime at $K \ll 1$ describes an electron motion within the cone of radiation emission. An observer experiences a continuous light pulse (continuous emission of the electron). The radiation interferes constructively and destructively and the spectrum consists of a fundamental wavelength and its harmonics.

If the motion of the electrons is greater than the fundamental emission cone, $K > 1$, the observer experiences pulses of light. Based on Fourier theory, the pulse of light must consist of a spectrum with a broader bandwidth. LPWA have source sizes of $\approx 1\,\mu\mathrm{m}$[84] with GeV-energies at densities of $\approx 1\,\mathrm{cm}^{-3}$[85], which results in $K \approx 6$ and even higher values have been reported[86]. Betatron radiation is therefore rather to

---

[83] It must be mentioned, that the average power of the emitted radiation scales with $\propto \sqrt{\gamma^3}$ ([115] A. G. Thomas. *Physics of Plasmas* (2010), Eq. 62). So even if the energy of the electrons changes, the emitted radiation is mainly characterised at its peak energy.

[84] [60] M. Schnell *et al. PRL* (2012); [50] S. Kneip *et al. PRST - AB* (2012).

[85] [137] Kristjan Poder, PhD Thesis, Imperial College London (2016).

[86] [138] K. T. Phuoc *et al. PRL* (2006).

be identified in the wiggler regime than in the undulator regime and this will thus be investigated further in the next section.

2.11.3 Typical Frequency of Synchrotron Radiation

The typical frequency of synchrotron radiation is approximated by estimating the pulse length of a synchrotron pulse, which is finite because the charged particle emits light with an opening angle as just discussed. Given the situation in Fig. 2.10, an observer would be able to see the light at t_0 from the lower part of the emission. The last light emitted in time and observed will occur at t_1. The light travel with the speed of light straight to the observer (green line) of distance $c\Delta t$, while the electron travels along the arc and with a reduced velocity of v_e compared to the light. The time difference and hence the pulse width is therefore

$$\Delta t = \left(2\frac{1}{\gamma}\cdot\rho\right)\cdot\frac{1}{\beta c} - 2\cdot\rho\sin(1/\gamma)\cdot\frac{1}{c} \tag{2.93}$$

$$\Delta t \overset{\gamma\gg 1}{\approx} \frac{2\rho}{\beta\gamma c}\left(1-\gamma\beta\left(\frac{1}{\gamma}-\frac{1}{6}\frac{1}{\gamma^3}\right)\right) = \frac{2\rho}{\beta\gamma c}\left(1-\beta+\frac{\beta}{6\gamma^2}\right) \tag{2.94}$$

$$\approx \frac{2\rho}{\beta\gamma c}\beta\left(\frac{1}{2\gamma^2}+\frac{1}{6\gamma^2}\right) \tag{2.95}$$

$$\Delta t = \frac{4}{3}\frac{\rho}{c\gamma^3} \tag{2.96}$$

where the radius of curvature is ρ and the same approximation of Eq. (2.86) was used. The typical frequency is therefore around,

$$\omega \approx \frac{3c\gamma^3}{2\rho}\ . \tag{2.97}$$

2.11.4 The Spectrum of Synchrotron Radiation

It can be shown that the intensity distribution per solid angle and frequency follows[87]

$$\frac{\mathrm{d}^2 I}{\mathrm{d}\omega\mathrm{d}\Omega} = \frac{e^2\omega^2}{16\pi^3\epsilon_0 c}\left|\int_{-\infty}^{\infty} \vec{n}\times(\vec{n}\times\vec{\beta})e^{i\omega(t-\vec{n}\cdot\vec{r}(t)/c)}\mathrm{d}t\right| \tag{2.98}$$

which would allow the reconstruction of the spectrum at an observing point, if the velocity $\vec{\beta}$ and position $\vec{r}(t)$ of the particles are known.

---

[87] [136] J. D. Jackson. (1999), Eq. 14.67.

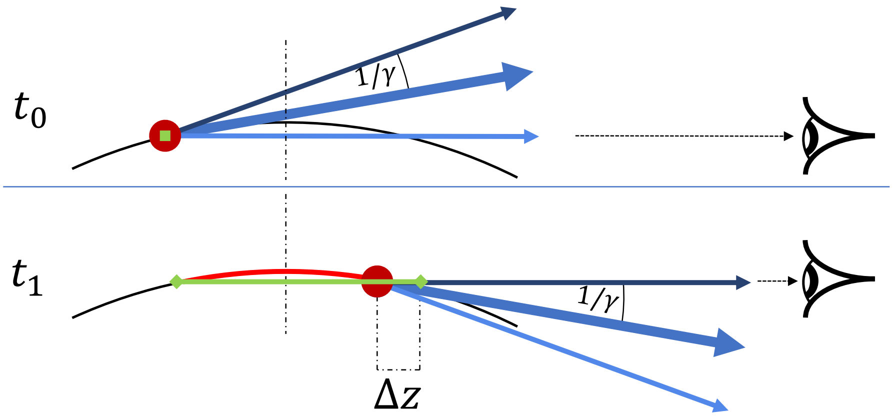

Figure 2.10: Pulse width of synchrotron Radiation. An observer on-axis will start to see light emitted at t_0, because the opening angle, $1/\gamma$ of the emitted light. The last point at which light can be observed is at t_1. The green line is the path length, the light has travelled from the first point and the red line is the path travelled by the electron, which creates a time difference between the first light emitted and the last.

Since the orbit of the electrons in the plasma cavity is reasonably approximated with an oscillation (prev. Sec. 2.11.2), more can be deducted. The maximum acceleration of the electrons occurs at their maximal displacement from the centre. The motion can be compared to an instantaneous circular motion whose spectrum is described by a synchrotron spectrum[88],

$$\frac{\mathrm{d}^2 I}{\mathrm{d}\omega \mathrm{d}\Omega} = \frac{e^2}{12\pi^3\epsilon_0 c}\left(\frac{\omega\rho}{c}\right)^2\left(\frac{1}{\gamma^2}+\theta^2\right)^2\left[K^2_{\frac{2}{3}}(\xi)+\frac{\theta^2}{(1/\gamma^2)+\theta^2}K^2_{\frac{1}{3}}(\xi)\right] \tag{2.99}$$

$$\frac{\mathrm{d}^2 I}{\mathrm{d}E \mathrm{d}\Omega} = \frac{3e^2}{4\pi^3\hbar\epsilon_0 c}\frac{\gamma^2}{(1+\gamma^2\theta^2)}\xi^2\left[K^2_{\frac{2}{3}}(\xi)+\frac{\gamma^2\theta^2}{1+\gamma^2\theta^2}K^2_{\frac{1}{3}}(\xi)\right] \tag{2.100}$$

where Eq. 2.100 is the same equation as Eq. 2.99, but rewritten with $E = \hbar\omega$. $K_{\frac{2}{3}}(\xi)$ and $K_{\frac{1}{3}}(\xi)$ are the modified Bessel-functions 2nd kind and $\xi = \frac{\omega\rho}{3c\gamma^3}(1+\gamma^2\theta^2)^{3/2} = \frac{E}{2E_c}(1+\gamma^2\theta^2)^{3/2}$. θ is the observation angle and ρ the instantaneous radius of curvature. That leaves $E_c = \hbar\omega_c$, which is referred to as the critical energy and determines the shape of the spectrum. It is defined at $\xi = 1/2$ on-axis ($\theta = 0$). That is, because the Bessel functions and hence the intensity becomes very small for $\xi \gg 1$ and very small for $\xi \ll 1$. $\xi(\theta = 0) = 1/2$ results in a critical energy expression of

$$E_c = \hbar\omega_c = \hbar\frac{3}{2}\gamma^3\frac{c}{\rho} \tag{2.101}$$

This equation is familiar as it is the typical frequency derived as Eq. 2.97. Examples of synchrotron spectra are shown in multiple sections of this work, see Fig. 3.3 and Fig. 6.8.

---

[88] [136] J. D. Jackson. (1999), Eq. 14.79.

2.12 Staged Laser Plasma-Wakefield Acceleration

The limitations mentioned in Sec. 2.10 can mostly ameliorated by choosing correct guiding in the plasma as mentioned. The limitation of the depletion length cannot be overcome this way. Instead, one approach is to stage two independent laser plasma-wakefield acceleration stages. Staged laser wakefield accelerators have been already experimentally investigated[89]. The difference is that the staging consists of one injection stage and one acceleration stage with a single laser pulse in these former examples. One laser pulse does not overcome the issue of the depletion length. In contrast to the single laser pulse approach, two acceleration stages each with their independent laser pulses was demonstrated by Steinke et al. in 2016[90]. As the technique requires two laser pulses, the energy of the electron can therefore be potentially doubled. The first laser pulse is injected into a gas cell, in which electrons are injected and accelerated to their maximal energy before they exit the plasma. The laser pulse and electron bunch are separated with a thin foil, which is being used as a plasma mirror (PM). The energetic electrons pass through the PM, while the laser pulse is reflected. The electron bunch passes through yet another PM, which is used to inject a second laser pulse. The electron beam and laser pulse are spatially overlapped and temporally synchronised so that when both are injected into the second gas cell, the created wakefield by the laser pulse accelerates the electron beam even further. In the experiment presented by Steinke, an electron beam with central energy of $120\,\mathrm{MeV}$ was accelerated further to achieve an energy gain of about $100\,\mathrm{MeV}$. However, the charge coupling efficiency was as low as 3.5%. As mentioned, the second laser pulse was injected with a PM, but it is worth mentioning that a second method was proposed recently. A curved plasma channel could be used to bend the laser beam into accelerator[91], but this is only a theoretical proposal at the time of this work.

The technique might be limited by the injection efficiency as if it is below 1, each stage will decrease the accelerated charge. Furthermore, the emittance of the electron bunch is also increased by passing through the plasma mirror and one has to try and limit this by first fully understanding the effect.

Plasma Mirrors are the optimal choice for staged LPWA as thin foils of $25\,\mathrm{\mu m}$ can be used for them. The importance of its thickness is that they do not absorb the electron bunch and have only potentially little effects on the electron beam. The effect on the emittance of the electron beam is an on-going research field and depends on the

---

[89] [127] M. S. Kim *et al. APL* (2013).

[90] [139] S. Steinke *et al. Nature* (2016).

[91] [140] J. Luo *et al. PRL* (2018).

details of the set-up[92]. The laser pulse is of such high intensity that it would destroy conventional optics since these must be placed close to the focal plane of the laser (here 5-20 mm) in this concept. The intensity reaches $\gg 10^{14}$ W/cm^2, which ionises the material through optical field ionisation[93]. This effect is used to reach an electron density above the critical density and the surface starts to reflect the laser pulse (see Sec. 2.6). PM have been used as optical switches early on[94]. A transmittable optics can be turned reflected once a pulse with high enough energy produces overdense plasma. This can be utilised for an experiment when a laser pulse with high temporal contrast is crucial, such as for proton acceleration with laser pulses on thin foils[95]. Amplified spontaneous emission (ASE) of CPA systems (see Sec. 2.1) can produce a high background intensity. By using an optical switch, the low background is transmitted through the transmittable optic, before the main pulse arrives and gets reflected[96]. A theory about the mechanisms involved can be found in[97]. Note that the polarisation of the light is important for the efficiency of the reflectivity. In p-polarisation, which is in the plane of reflection, the light accelerates electrons into the vacuum for the first half of the oscillation and in the second half, the electrons are accelerated back into the plasma surface. Due to the skin effect, the electrons accelerated into the plasma cannot transfer their kinetic energy back to the laser field. This effect, known as vacuum heating or *Brunel absorption*. The energy loss is impracticable for staging LWPA as the reflectivity is much lower, as shown by Shaw in 2016[98]. It has relevance when producing high harmonics[99]. In this work, the reflectivity of PMs is investigated to prepare a staged LPWA experiment.

---

[92] [141] Y. Sentoku *et al. Phys. Rev. Lett.* (2003); [142] A. Debayle *et al. Phys. Rev. E* (2010); [143] G. Raj *et al. Phys. Rev. Res.* (2020).

[93] Optical field ionisation is used for the combined ionisation through BSI and tunnelling ionisation ([144] T. Ichino *et al.* (2007), Ch. Optical-field Ionization (OFI) by Femtosecond Laser Pulses of Time-Dependent Polarisation)

[94] [145] C. Rolland and P. B. Corkum. *J. Opt. Soc. Am. B* (1986); [146] U Teubner *et al. J. Phys B - At. Mol. Opt.* (2001).

[95] [147] T. Ceccotti *et al. PRL* (2007).

[96] [148] H. C. Kapteyn *et al. Optics Letters* (1991); [149] B. Dromey *et al. Rev. Sci.* (2004).

[97] [150] C. Thaury *et al. Nature Physics* (2007); [151] H Vincenti *et al. Nat. Com.* (2014).

[98] [152] B. H. Shaw *et al. Physics of Plasmas* (2016).

[99] [153] A. Debayle *et al. Phys. Rev. E* (2015); [154] Z.-Y. Chen and A. Pukhov. *Nat. Com.* (2016).

Chapter 3

Methods

This chapter covers all the technical details applied to extract the physics described in the later chapters. The *Central Laser Facility*'s (CLF) laser system *Gemini* was used to pursue the experiments in the target areas 2 and 3. The energy of the electrons and the charge were measured with an electron spectrometer, where the electron trajectory had to be modelled to calibrate the spectrometer. X-ray signal was obtained by using direct and indirect charged-coupled devices (CCDs) and the transmission of the x-rays through a set of different materials was used to deduct the x-ray spectrum. The particle-in-cell code EPOCH was used to simulate electron behaviour in plasma and to understand observations.

3.1 High Power Laser Systems: The Gemini Laser Facility

High power laser systems were generally discussed in Sec. 2.1.4. The laser system used in this work was at the CLF at the *Rutherford Appleton Laboratory*. The technical aspects of the system are thoroughly described in[1] and are just summarised in this section. The facility provides two *Astra Target Areas* (ATA), originating from the same front-end. The higher peak power laser beam arm is further referred to as ATA3 and the lower power, but higher repetition arm as ATA2[2]. The figure of merits are taken from[3] for ATA2 and ATA3 respectively, but their exact values during the experiments will be provided in the respective chapters.

The system starts with a titanium-sapphire oscillator with a central wavelength of $800\,\mathrm{nm}$ at $75\,\mathrm{MHz}$. The pulses are stretched and amplified, then reduced to $10\,\mathrm{Hz}$ with Pockels cells. After another set of amplifiers, half of the pulses are sent to TA2, where two gratings and a retro-reflector compresses the beam to $40\,\mathrm{fs}$ with around $500\,\mathrm{mJ}$ and horizontal polarisation. The beam has a diameter of $50\,\mathrm{mm}$.

---

[1] [155] C. Hooker *et al.*, Proceedings (2006); [156] C. J. Hooker *et al.*, Proceedings (2008).

[2] The number refers to it's the order of construction.

[3] [157] R. Pattathil; [156] C. J. Hooker *et al. 2008 Conference on Quantum Electronics and Laser Science Conference on Lasers and Electro-Optics, CLEO/QELS* (2008).

The second half of the pulses are sent to be amplified further. However, the beam is split into two beams, which are individually amplified and compressed to up to $\sim 7\,\mathrm{J}$ in $\sim 42\,\mathrm{fs}$ during our experiments. Splitting the beam gives the system dual-beam capability, where both beams can be delayed relative to each other. The beam has a diameter of $150\,\mathrm{mm}$.

3.2 Electron Diagnostic

Electrons were deflected by a dipole magnet onto a scintillating Lanex screen (Gd_2O_2S:Tb,[4]) generated in the interactions and imaged by a camera to characterise them. Depending on the energy, the electron will be deflected to a certain position on the screen. The electron spectrum was obtained by imaging the screen with a camera. The image seen by the camera needs to be fully spatially calibrated to know the position of the electrons on the screen.

3.2.1 Electron Trajectory Tracking

The transportation matrix for the electrons through the dipole field and the free space propagation has to be determined. The electrons are deflected by the Lorentz force and a tracking code was conducted, to relate the electron position on the screen to the electron's energy. The code is generalised for any calibration of electron spectrometer and requires the distances and positions of the electrons, magnet(s) and Lanex screens as an input. The code was used in Ch. 6 to calibrate the spectrometer. The working principal of the code are presented here and a test case. The test case is to determine the minimal step size (see below) and if the code follows physics.

The code is based on a *Runge-Kutta algorithm of 4th order*[5]. Based on the Lorentz force the set of equations follow,

$$\begin{array}{c|c}
\text{General notation} & \text{Applied Problem} \\
f = y' & \vec{f} = \vec{v}\,' = \vec{a} = -\dfrac{e}{\gamma m_e}\vec{v} \times \vec{B} \\
f(x_n, y_n) = Y_n' & \vec{f}(\vec{x}_n, \vec{v}_n) = -\dfrac{e}{\gamma m_e}\vec{v}_n \times \vec{B}(\vec{x}_n) \\
y_{n+1} = y_n + \dfrac{1}{6}h(\vec{k}_1 + 2\vec{k}_2 + 2\vec{k}_3 + \vec{k}_4) & v_{n+1} = v_n + \dfrac{1}{6}h(\vec{k}_1 + 2\vec{k}_2 + 2\vec{k}_3 + \vec{k}_4)
\end{array} \tag{3.1}$$

where the general notation follows[6] and where h is a step size, which must be sufficiently small. In the context of this problem, it has been chosen to be the hypotenuse

---

[4] [158] A. G. Glendinning *et al. Phys. Med. Biol.* (2001).

[5] [159] E. Süli and D. F. Mayers. 2012.

[6] [159] E. Süli and D. F. Mayers. 2012, Eq. 12.33.

of the spatial grid transformed into time by the speed of light $h = \sqrt{(\Delta X)^2 + (\Delta Y)^2}/c$, which was found to be reasonable by testing the code for a well-known case (see below). The factors $\vec{k}_n$ are seen in Table 3.1. The magnetic field $\vec{B}(\vec{x}_n)$ is taken at the position x_n and only taken at this single position[7] as the magnetic field is slowly changing compared to the resolution grid and this increases the algorithm speed.

$\vec{k}_1 = \vec{f}(\vec{x}_n, \vec{v}_n)$	$\vec{k}_2 = \vec{f}(\vec{x}_n, \vec{v}_n + \frac{1}{2}h\vec{k}_1)$
$\vec{k}_3 = \vec{f}(\vec{x}_n, \vec{v}_n + \frac{1}{2}h\vec{k}_2)$	$\vec{k}_4 = \vec{f}(\vec{x}_n, \vec{v}_n + h\vec{k}_3)$

Table 3.1: The elements to evaluate the Runge-Kutta algorithm to track electrons in a magnetic field. Note that $\vec{x}_n$ does not change contrary to[8], which is because the magnetic field of the dipole magnet is slowly changing compared to the grid size and therefore can be evaluated once per simulation step.

The position of the electrons is just as important as the velocity. Fortunately, by calculating the velocity, the differential equation of the position is easy to calculate. The same algorithm can be used, but for $\vec{f} = \vec{x}\,' = \vec{v}$ in the first row of Eq. (3.1).

The algorithm has been verified, simulating a $2.31\,\mathrm{MeV}$ electron, placed within a homogeneous $200\,\mathrm{mT}$ dipole magnetic field with a diameter of $150\,\mathrm{mm}$ with only a longitudinal velocity. These values are arbitrary and have simply the purpose of validating the physics. The electron followed its orbit 20 times in the simulation and the trajectory with the magnet and additional information about the resolution of this specific test can be seen in App. C.1 (set up Fig. C.1). The radius of the electron's trajectory was determined with a circular fit to be $3.75\,\mathrm{mm}$ with a residual of 2.14×10^{-16}. Using the analytical formula to calculate the radius yields $\rho = p/(e \cdot B) = 3.75\,\mathrm{mm}$, which means that the code produced the same radius as the physical model. The energy of the electron was tracked during the simulations to see if they might vary, but it turned out that the energy also barely varied with a standard deviation of $1.3 \times 10^{-13}\,\mathrm{MeV}$.

3.2.2 Charge Calibration

Here, the charge calibration is generally described. The detailed calibration of the spectrometer is presented in Sec. 6.2.1. The light emitted by the scintillating Lanex screen is proportional to the charge impacting for electrons with an energy $> 2\,\mathrm{MeV}$[9]. However, the screen is imaged with lenses and the camera image is not calibrated in absolute charge. This has been done by adding a set of image plates at the location of the Lanex screen for a calibrating set of shots. Image plates refer to a sensor based on fluorescence. Energetic particles excite the material and a scanner can read-out the

---

[7] More correctly, the first arguments in Table 3.1 would also vary, see ([159] E. Süli and D. F. Mayers. 2012, Eq. 12.33).

[9] [160] S. R. Nagel, PhD Thesis, Imperial College London (2009).

absolute charge which impacted on the plates. The reader is referred to[10] for technical details on the image plates and its background.

3.3 X-ray Diagnostic

3.3.1 Selection of the X-ray Detection Camera

The x-ray signal in the experiments are obtained with two cameras, which differ in the way they register x-rays.

Both cameras are silicon-based charged coupled devices (CCD), however one of them, the *Andor iKon-M 934 BR-DD* is a *direct detection* camera. The silicon is exposed directly to the x-ray and the thickness of the chip allows a high absorption of the x-ray energy in the silicon. The process creates electron-hole pairs, which are registered by electronics, which means that the charge registered is directly proportional to the energy of the incident photons[11][12]. The advantage of direct detection cameras is their sensitivity, which is ~ 100-times higher than indirect detection camera used. However, that is only true for lower energy x-rays, simply because the absorption of silicon drops significantly above the k-edge of $1.89\,\mathrm{keV}$[13], see Fig. 3.1.

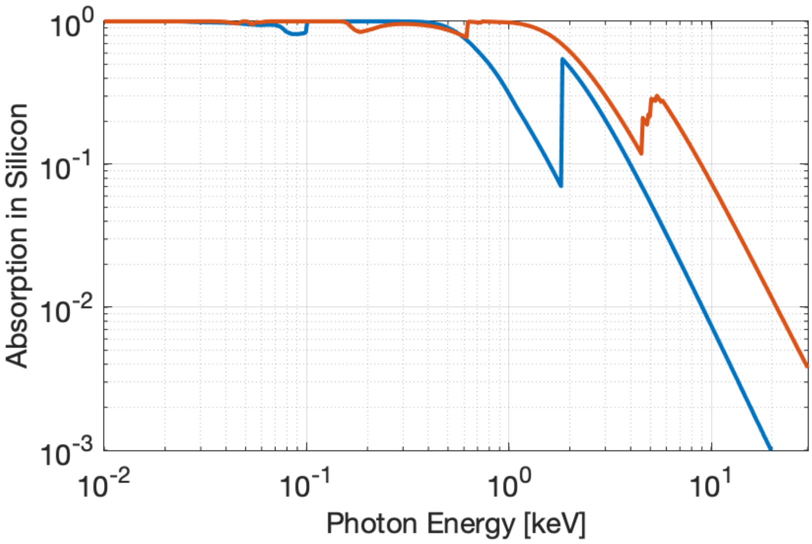

Figure 3.1: Absorption of x-rays in a silicon layer (blue) and in a CsI layer (orange) of $1\,\mu\mathrm{m}$ thickness[14] between $10\,\mathrm{eV}$ and $30\,\mathrm{keV}$. The absorption drops rapidly above $1.89\,\mathrm{keV}$ for Si and above $5.57\,\mathrm{keV}$ for CsI.

---

[10] [160] S. R. Nagel. (2009); [161] S. Kneip. (2010).

[11] [162] J. R. Janesick *et al.* *OpticalEngineering* (1987).

[12] [163] *Direct Detection Processing* DOI: `10.1007/978-3-540-49206-1_4` 1995.

[13] [164] B. L. Henke *et al.* (1993).

[14] ([164] B. L. Henke *et al.* (1993))

The second camera, *Andor iKon-L 936*, is an *indirect detection* camera. A scintillating CsI crystal, doped with thallium for higher performance[15], is mounted in front of the CCD. The x-rays entering the crystal deposit energy, which then emit photons in a broad spectrum around $550\,\mathrm{nm}$, where the quantum efficiency (QE) of the silicon detector is much higher. The increase in QE does not compensate for the loss of the transformation from x-ray to optical photon, and the performance of the camera is generally lower than for the direct detection camera in the 1-10 keV regime. However, as the absorption line shown in Fig. 3.1, the absorption spectrum is shifted to higher x-ray energies, where the QE of the direct detection camera is significantly lower[16].

3.3.2 X-ray Image Preparation

A summary of the necessary steps to prepare the raw image data before averaging each filter and producing a signal data point can be found extensively discussed in[17]. First, a dark image has to be subtracted from the image due to thermal noise. A flat field image is then subtracted to remove any artefacts of the specific camera chip. The flat field image is a set of illuminated images of the camera, which captures irregularities due to the CCD structure. Artefacts can be produced, for example, by the fibre coupling into the indirect detection camera. Each camera has a slightly different coupling efficiency depending on the individual pixel. The differences create irregularities because the fibres used are of finite size, here $6\,\mu\mathrm{m}$[18]. These can be seen in Fig. 3.2 where the small black spots are the same size as individual pixels. The pixel size is $13.6\,\mu\mathrm{m}$. Also, a hexagonal pattern can be detected in a larger scale. This pattern has a diameter of $\approx 82\,\mathrm{px} \rightarrow 1.2\,\mathrm{mm}$. The pattern originates from the production of fibre optical plates, where a set of microscopic glass fibres up to $2\,\mathrm{mm}$ are bundled and then drawn-out, under which process the diameter of each fibre is reduced. The significantly thinner bundle is then joined with another bundle of equal diameter fibres and heated again and drawn out. This process is repeated until the fibres have a diameter of $6\,\mu\mathrm{m}$ and the bundle the size of the camera chip. Thus multiple patterns can be seen.

3.3.3 Spectrum Reconstruction

The spectral reconstruction used in this work is based on the work presented in[19]. It assumes the electron emission spectrum can be modelled as an on-axis synchrotron

---

[15] [165] I. Fujieda *et al. IEEE Transactions on Nuclear Science* (1991).

[16] Note that the absorption line neglects the effect of the doped Thallium as its concentration is as low as 0.02%-0.03% ([166] J. G. Rocha *et al. Proceedings of IEEE Sensors* (2004))

[17] [167] J. C. Wood, PhD Thesis, Imperial College London (2016).

[18] [168] *X-Ray Scintillator* URL: `https://www.hamamatsu.com/resources/pdf/etd/FOS_ACS_GPXS_ALS_TXPR1024E.pdf` (2020).

[19] [64] S. Kneip *et al. Nature Physics* (2010).

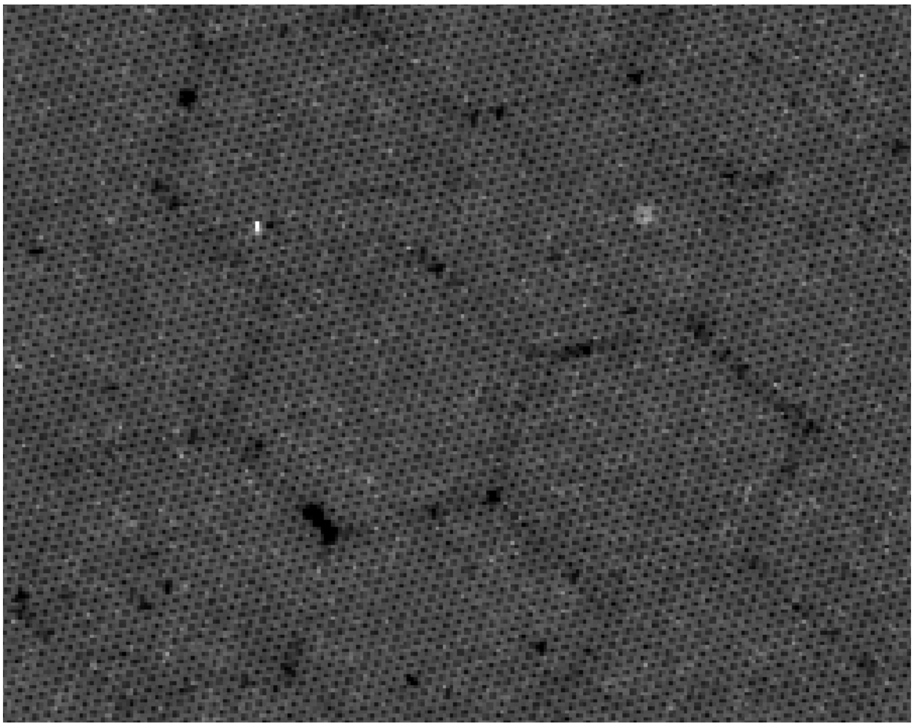

Figure 3.2: Flatfield image of the indirect detection camera used in this work, *Andor iKon-L 936*. The colour scale is 0.85-1.4 to show the differences between individual pixels (see text 3.3.2 for more details).

spectrum, whose differential intensity is given by Eq. 2.100,

$$\left.\frac{\mathrm{d}^2 I}{\mathrm{d}E\mathrm{d}\Omega}\right|_{\theta=0} \propto \gamma^2 \xi^2 K^2_{\frac{2}{3}}(\xi) \tag{3.2}$$

Here, $\xi = \frac{E}{2E_c}$ assuming that the radiation is on-axis and the energy of the photons E. Based on a variation of the Beer-Lambert law for the transmission,

$$t_m(E) = \exp(-\mu_m(E)\rho_m d) \ , \tag{3.3}$$

the attenuation of the spectrum through different materials, as a function of photon energy E, can be estimated[20]. The quantity μ_m is the mass absorption coefficient commonly in $\mathrm{cm\,g^{-1}}$ for a specific material, which can be found in[21], here indicated with the subscript m and ρ_m its density (in this case in $\mathrm{cm^{-3}}$) and d its thickness. A detector signal C_m is composed of the attenuated x-ray signal through the material and reduced by the quantum efficiency $QE(E)$. Due to the electronics of the CCD, the x-ray photons detected by the camera have a linear[22] conversion factor α into electron-hole pairs[23].

---

[20] Eq. 3.3 is a variation because the integral of the general formula has been evaluated as being the thickness of the material the x-ray signal is propagating through

[21] [164] B. L. Henke *et al.* (1993).

[22] This is only true within a limited energy range, see citation for specific range

[23] [163] *Direct Detection Processing* DOI: `10.1007/978-3-540-49206-1_4` 1995.

If the pre-factor of Eq. 3.2 can be summarised as,

$$N_{ph} = \int\limits_{E_{min}}^{E_{max}} \frac{\mathrm{d}^2 I}{\mathrm{d}E\mathrm{d}\Omega}\bigg|_{\theta=0} \mathrm{d}E \tag{3.4}$$

which is the number of photons between the energies E_{min} and E_{max}, the signal in counts detected from the camera is,

$$C_m = \alpha N_{ph} \int\limits_{E_{min}}^{E_{max}} E S(E, E_{crit}) QE(E) t_m(E) \mathrm{d}E\ . \tag{3.5}$$

Here $S(E, E_{crit}) \equiv \frac{\tilde{I}(E, E_{crit})}{\mathrm{d}E\mathrm{d}\Omega}\bigg|_{\theta=0} = (E/2E_{crit})^2 K^2_{\frac{2}{3}}(E/2E_{crit})$ is Eq. 3.2 normalised to the number of photons N_{ph}.

The spectrum depends only on the number of photons and the critical energy. If the signal is now obtained for different material, C_1 and C_2, the ratio between both signals depends only on the critical energy:

$$\frac{C_1}{C_2} = \frac{\int\limits_{E_{min}}^{E_{max}} E S(E, E_{crit}) QE(E) t_1(E) \mathrm{d}E}{\int\limits_{E_{min}}^{E_{max}} E S(E, E_{crit}) QE(E) t_2(E) \mathrm{d}E} \tag{3.6}$$

As an example, see Fig. 3.3. Two materials, Mg and Al, each $12.8\,\mu\mathrm{m}$ thick are used to filter the energy spectrum differently. $12.8\,\mu\mathrm{m}$ Al is often used to filter the laser light and shield the x-ray camera, but the Mg is only instructive to explain this technique in general. The filters used in the different experiments are presented in their respective chapters 5 and 6. The signal on the detector is integrated and the ratio between both does only depend on the critical energy as seen in Fig. 3.4[24]. The first-order derivative depicted in red in Fig. 3.4 indicates at which energy the change of signal is the highest. That is where this method is most accurate because small differences lead to greater changes. In this case, the method is most accurate between the k-edges of both materials. The sensitivity is essential when designing a set of filters for a source since the ratio of the materials must vary the most around the expected energy of the source. Since the critical energy is not known before the experiment and can be variable, the number of filtering materials, must be more than two to cover a wide bandwidth of possible energies.

---

[24] That is true if the number of photons remains the same for both detector areas.

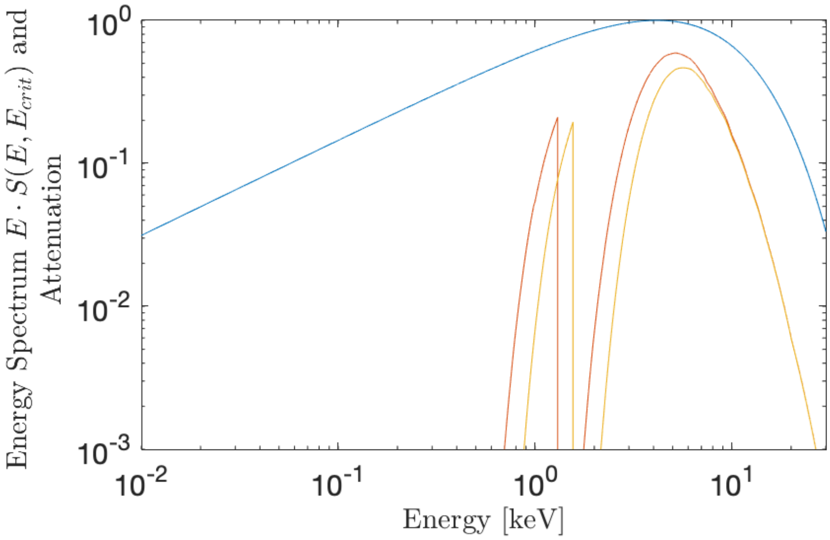

Figure 3.3: Energy Spectrum with $5\,\mathrm{keV}$ critical energy $E \cdot S(E, E_{crit})$ in blue and the attenuated spectrum by the propagation through $12.8\,\mu\mathrm{m}$ Mg in red and Al in yellow and modified by the quantum efficiency of the direct detection camera (see Sec. 3.3.1).

3.3.4 Noise when Reconstructing the Spectrum

An artificial signal on the detector can falsify the estimated critical energy. Unfortunately, a lot of noise is generated in the process of LPWA. A large number of relativistic electrons are generated. These electrons can create particle showers and bremsstrahlung when they hit high-Z material between the source and the detector. This includes the exit of the gas cell, the magnet of the electron spectrometer and the vacuum chamber itself.

The mismatch of the estimated critical energy by a uniform increase of signal in the detector, $Signal_{det} = Signal_{True} + \Delta$, can be seen in Fig. 3.5. The overestimation of the detected signal is linear to the introduced level of noise. This is especially important if the signal from the x-rays is low. This work differentiates two cases and handles them separately. For one, bremsstrahlung creates localised high pixel values, where charge can spread over to neighbouring camera pixels and in the second case, uniform noise from the particle showers near the camera.

Bremsstrahlung has to be handled locally and the technique used is comparable with a median filter[25], where individual pixels are compared to the median of the surrounding pixel in a rectangle of size r. But since the photons generated by

---

[25] [169] T. S. Huang *et al.* *IEEE Transactions on Acoustics, Speech, and Signal Processing* (1979).

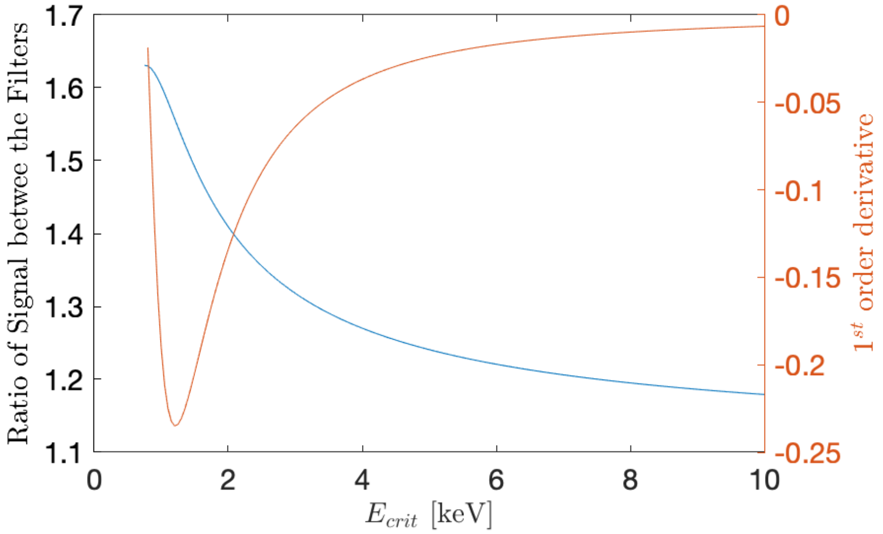

Figure 3.4: The ratio of the integrated signal between the two materials C_{Mg}/C_{Al} depending on the critical energy of the synchrotron spectrum in blue. Depicted in red the 1st order derivative, see text for more details.

bremsstrahlung can exceed 100s of MeV[26], the cloud of electron-hole (e-h) pairs generated can be the size of several pixels[27]. The cloud of e-h pairs spills signal over multiple pixels, thus the classical median filter has to be adapted to account for that, this was developed by[28]. The filter defines a radius r_1 for the neighbourhood and introduces a second radius r_0, which has to enclose the signal of a high energetic photon. A pixel value is compared to the median of the signal between r_0 and r_1. If the values inside exceed the average surrounding it by a certain ratio, it is considered to be noise. A new value is constructed from the average from the neighbourhood (between r_0 and r_1). The radii and the ratio, which determines the threshold where the value is considered to be too high (or too low) has to be carefully chosen through trial and error.

A high-Z filter can be used to measure the uniform noise on a shot. A thick high-Z filter (depending on the critical energy and x-ray flux, and can be for example $50\,\mathrm{\mu m}$ tungsten, see Sec. 6) should theoretically absorb the x-rays generated through the betatron-oscillation process. The importance of this method is shown in App. C.2.

3.4 Particle-In-Cell Code: EPOCH

Dissecting the inside of a wakefield bubble and the exact moment of injection has massive benefits to understanding how these mechanisms work and how to improve

---

[26] [170] C. D. Baird *et al. CLF Annual Report 2017-18* (2020).
[27] [163] *Direct Detection Processing* DOI: `10.1007/978-3-540-49206-1_4` 1995, Fig 1 extrapolated.
[28] [171] N. Lopes. (2018).

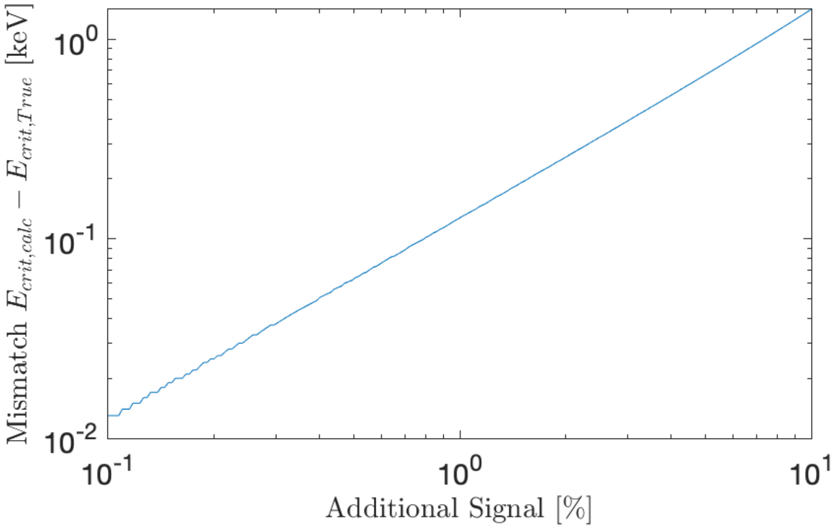

Figure 3.5: Mismatch of the critical energy due to additional signal on the detector. The true signal of a $5\,\mathrm{keV}$ synchrotron spectrum through the two filter described in Sec. 3.3.3 ($12.8\,\mu\mathrm{m}$ Mg and Al). The additional signal in % of the Mg signal is added to both signals as $Ratio = (Signal_{Mg} + \Delta_{\%} \cdot Signal_{Mg})/(Signal_{Al} + \Delta_{\%} \cdot Signal_{Mg})$.

their efficiency. It is experimentally very challenging, but one can also try to investigate these phenomena with computer simulations. The analytical difficulties regarding LPWA were discussed in Sec. 2.8. Thus codes have been written to replicate the physics. The first simulations on this topic were presented in the same publication as the topic was first proposed, by Tajima and Dawson in 1979[29], as a 1D spatial code with 3 velocity and field dimensions. Various codes with different assumptions and for different purposes have been developed over the years.

One of these codes is EPOCH[30], which directly solves Maxwell's equations for the electromagnetic fields due to the plasma, any added particles and any laser pulse(s). To accurately model the physics, one would have to solve the equations for every single particle. However, it can be sufficient to combine particles in close vicinity to each other, which leads to the concept of particle-in-cell (PIC) codes. Macroparticles represent a discrete number of (real) particles. The simulation grid constructs vertices, containing the full information of electromagnetic fields and the number of microparticles and their momenta. The core of any PIC code, including the EPOCH code, consists of the particle pusher and the field solver. Despite particle interaction, this describes the behaviour of a kinetic plasma. In summary, the three main steps and methods are:

---

[29] [21] T. Tajima and J. M. Dawson. *PRL* (1979).

[30] [106] T. D. Arber *et al. Plasma Phys. Control. Fusion* (2015).

1. *Particle pusher* - Particles undergo the Lorentz force, the particle's position is changed using a 2^{nd} order particle push[31][32]

2. *Weight and shape of the particles* - The charge and currents within the grid vertices are updated, by summing over the macroparticles. Depending on how many particles these represent, they vary in their *particle weight*. Generally speaking, they can also have different weight distribution. However, the standard in EPOCH is a triangular shape, which was not changed for the simulations in this work.

3. *Field solver* - Maxwell's equations are updated with the *finite-difference time-domain method* (FDTD), which is a standard in PIC codes (see[33]).

The triangular shape defines a centre location of a distribution (e.g. particle distribution) with three extensions on how far the field reaches yielding a total volume of $2\Delta X \times 2\Delta Y \times 2\Delta Z$ in 3D. The FDTD updates and evaluates the Maxwell-equations at each full time-step and half time-step.

The 2D EPOCH code will be used both in Ch. 4 and Ch. 5. The limitations of the code as well as the correct initial input parameters need to be ensured. This section outlines the consequence of a finite step size on the achievable energy in 1D. The gained knowledge feeds into the 2D simulations in terms of choosing a resolution and creating the concept of virtual electron injection. The guiding of laser pulses in 2D is then discussed as it will be crucial in the discussion of Ch. 4.

3.4.1 Resolution of Simulations in EPOCH

Running simulations in EPOCH require a set of inputs. While the physical inputs, such as laser energy, duration, focus spot size and electron density are rather self-explanatory, the correct number of macro-particles, the resolution grid size and the time-step are not trivial. Luckily, the time step of the simulation is determined through computational requirements, see[34] and[35] [36], and the time step follows the Courant-Friedrichs-Lewy (CFL) condition[37] to be

$$c\Delta t = \alpha \frac{1}{\sqrt{(\Delta x)^{-2} + (\Delta y)^{-2}}} \tag{3.7}$$

---

[31] referred to as *Boris push*, named after its author

[32] [172] J. P. Boris, Proceedings (1971).

[33] [106] T. D. Arber *et al. Plasma Phys. Control. Fusion* (2015), Sec. 2.1.

[34] [173] A. Taflove and S. C. Hagness. *Computational Electrodynamics: The Finite-Difference Time-Domain Method* (1995).

[35] [66] J. M. Cole, PhD Thesis, Imperial College London (2015).

[36] avoiding exponential growth of the electromagnetic fields through the 2D FDTD algorithm, when inserted into the planar wave equation

[37] [174] R. Courant *et al. Mathematische Annalen* (1928).

where $\alpha < 1$. If nothing else is specified, EPOCH sets $\alpha = 0.95$, but the time-step resolution can be reduced to be lower than 0.95 however, this has not been investigated in this work. It reduces the decision on the time step to the size of the spatial grid resolution. The spatial resolution changes numerical dispersion, which cannot be avoided. The laser pulse propagates even in a vacuum with $< c$ in the simulations. The numerical group velocity in vacuum for 1D simulations is[38]

$$\beta_{G,num} = \frac{\cos\left(\frac{\pi}{R_x}\right)}{\sqrt{1 - 0.95^2 \sin\left(\frac{\pi}{R_x}\right)^2}} \tag{3.8}$$

where R_X is the resolution of the simulation normalised to the laser wavelength in the longitudinal axis. To estimate how severe the reduction of the group velocity in the plasma is, 1D scans have been performed in preparation of choosing the correct longitudinal resolution for 2D scans as the reduction in computational expense is significant. The group velocity for different resolutions can be seen in Fig. 3.6. The figure of merit used is the dephasing factor as defined in[39].

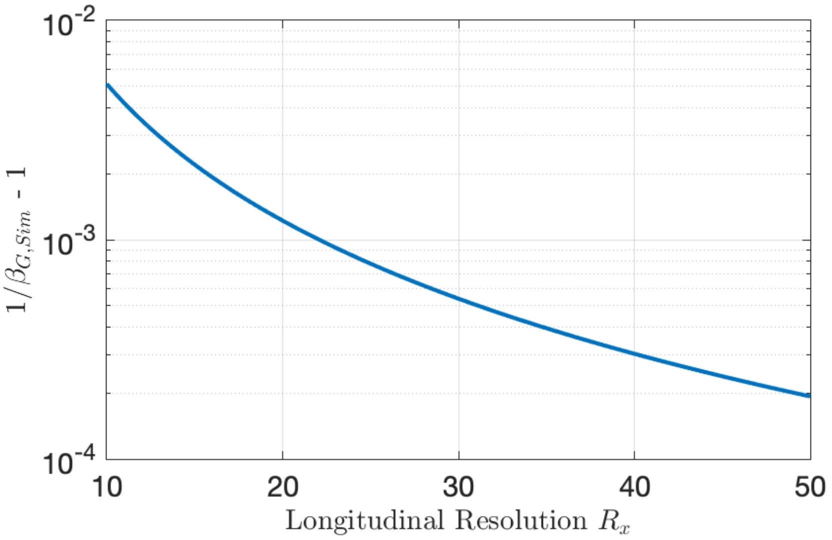

Figure 3.6: The group velocity dispersion for different resolutions R_x in 1D.

2D scans are performed to investigate the correct guiding of a laser pulse and the strength of the plasma wakefield as it is of vital importance to estimate the possible energy growth of the electrons in a staged LPWA experiment, see Sec. 2.12.

---

[38] [66] J. M. Cole, PhD Thesis, Imperial College London (2015), Eq. 3.66.

[39] [175] B. M. Cowan *et al.* *Journal of Computational Physics* (2011).

1D Scans in Resolution, Particle-per-Cell and Density

The scan performed in this section varied the resolution between $\Delta x = \lambda_0/15$, $\lambda_0/20$, $\lambda_0/25$, $\lambda_0/30$ and $\lambda_0/35$, for the density range of $n_e = 0.25 — 1 \times 10^{18}\,\mathrm{cm}^{-3}$ in $0.125 \times 10^{18}\,\mathrm{cm}^{-3}$ steps. Additionally, the particles per cell were varied between 1, 5, 10. However, this turned out to not change the investigated values[40], which is why the results of those simulations are not depicted in Fig. 3.7. As the simulations are in preparation for the experiments discussed in Sec. 2.12, the input parameters are matched to the ones in the experiment: The injected laser pulse has a vector potential of $a_0 = 0.675$ and a pulse duration of $40\,\mathrm{fs}$. To estimate the energy gain of electrons, probe electrons were continuously injected on axis with energy of $1\,\mathrm{GeV}$ with a relatively low density, $n_e = 1 \times 10^{15}\,\mathrm{cm}^{-3}$ to ensure an undisturbed creation of the plasma wave. The injection was halted once the simulation window started moving, which happened after the laser pulse propagated $3\lambda_p$. The simulation box enclosed $3.5\lambda_p$ and the length of the simulation was set to be longer than the estimated dephasing length.

The velocity of the laser pulse compared to that of the electrons determines the dephasing length as calculated in Eq. (2.79). Fig. 3.7 a) shows the group velocity and the speed of the electrons normalised on the linear group velocity of light in a plasma. While the electron's velocity does not change, v_G changes depending on the resolution. The observed group velocity for the different resolutions are normalised to the **numerical** group velocity Eq. (3.8), which is seen in black crosses. The black crosses are on the line of the numerical group velocity. The observed group velocity seems to be solely influenced by the resolution of the simulation. The resolution does not further effect the dispersion caused by the plasma. To reiterate, this investigation found that the resolution does not change the effect of the plasma on the laser pulse propagation and thus the numerical and plasma-based dispersion are uncorrelated with respect to one-another.

The effect on the group velocity seems low as it is in the ${}^0\!/_{00}$-level, but has a major implication on the dephasing length, seen in c), because of Eq. (2.79): $L_d \propto \dfrac{1}{1-\beta_G}$. The dephasing length was estimated by the effective group velocity in the simulation (dashed) and by recording the trajectory of the injected electrons (dotted). Both are in agreement and mismatch the theoretical dephasing length based on the theoretical group velocity, seen in the inset (black).

The maximal electric field is indicated in Fig. 3.7 c) and shows little variation between the different resolutions. The maximal electric field from the numerical solutions discussed in Sec. 2.8.2 is added as well (black) and fitted to the findings of the PIC

---

[40] Another single simulation with 200 particles-per-cell at a density of $n_e = 1 \times 10^{18}\,\mathrm{cm}^{-3}$ was performed to verify this observation.

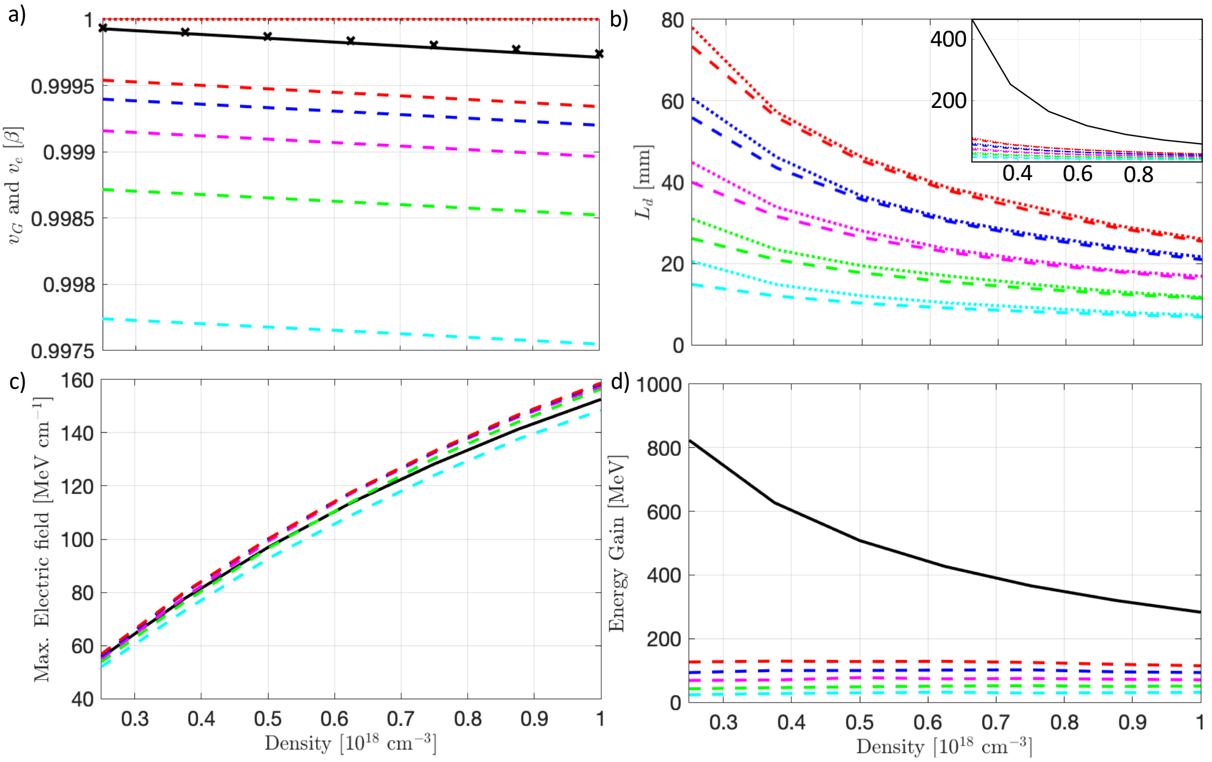

Figure 3.7: 1D EPOCH scans varying the resolution of the simulation grid $\Delta x = \lambda_0/15$ (cyan), $\lambda_0/20$ (green), $\lambda_0/25$ (magenta), $\lambda_0/30$ (blue) and $\lambda_0/35$ (red). a) the group velocity v_G/c of the laser pulse (dashed) and the velocity of the electrons v_e/c (dotted, these overlay on each other) in the simulations. The theoretical v_G/c (black) and the simulation $v_G/c/\beta_{G,num}$ from Eq.(3.8) (black crosses). b) The dephasing length calculated with the effective group velocity with Eq. (2.79) (dashed) and the dephasing length observed by inserted electrons overtaking the plasma wave in the simulation (dotted). The theoretical dephasing length depicted in the inset (black). c) The maximal electric field from the simulation is compared to the electric field resulting from the numerical solution of the wakefield Sec. 2.8.2 (black). d) The maximum energy gain of the electrons in the simulation and the energy gain of the numerical solutions with $\Delta W = 2E_{max}L_d/\pi$ (black).

code. Finally, d) shows the energy gain in the simulations compared to the theoretical energy gain, based on $\Delta W = 2E_{max}L_d/\pi$ using the theoretical dephasing length (black). In short: The numerical dispersion a) reduces the dephasing length b), which reduces the energy gain d).

These differ significantly, which is due to the reduced dephasing length due to the reduced numerical group velocity. The energy gain shown is based on the injected electrons and their gain after travelling $\lambda_p/4$ in the wave frame[41]. The energy gain is calculated taking only the second quarter of the plasma wave phase into account as the first quarter would defocus the beam. The reduction depends strongly on the resolution and decreases heavily with an increase in density. It ranges from

---

[41] The energy gain was calculated with $\Delta W = 2E_{max}L_d/\pi$ as well, which confirmed the depicted figures.

$\approx 23.5\,\mathrm{MeV}$ instead of $\approx 823.5\,\mathrm{MeV}$ for $0.25 \times 10^{18}\,\mathrm{cm}^{-3}$ at a resolution of $\Delta x = \lambda_0/15$ to $\approx 114.8\,\mathrm{MeV}$ instead of $\approx 283\,\mathrm{MeV}$ for $1 \times 10^{18}\,\mathrm{cm}^{-3}$ at a resolution of $\Delta x = \lambda_0/35$. The findings of this section imply that the group velocity and the sequential figures must be handled with caution.

The numerical dispersion can be used to adapt dephasing length and thus the energy gain when performing simulations to get real physical quantities. The way this is implemented in Ch. 4 is by introducing virtual electrons post-simulation. The data of the simulations provide the electric fields at each time-step. The energy in- or decrease is calculated for electrons in every possible phase. These electrons are then moved by the reduced speed of light depending on the resolution of the simulation found in this section. This provides a more accurate energy gain/loss than injecting electrons during the simulations as these would travel with the speed of light. However, any beam loading effect is neglected here and the wakefield is undisturbed from the total charge of the electron beam.

3.4.2 Electric Field Strength in 2D

2D EPOCH simulations have been performed to investigate the acceleration properties and guiding. The effect on the observed group velocity in the simulation of the previous chapter was also seen in 2D. The effective group velocity of the electric field follows the relation in Fig. 3.6 as the laser pulse is travelling only in $\vec{x}$-direction. The simulations covered the same physical parameter space as before, but with an $a_0 = 0.75$ and with fixed simulation resolution of $\Delta x = \lambda_0/20$, as the scans are much more computationally expensive. The transverse resolution was varied between $\Delta y = \lambda_0/3$, $\lambda_0/6$, $\lambda_0/9$ with minimal changes in behaviour. This might only happen for scenarios without self-injection as the transverse resolution could play an important role when scattering the electrons into the wakefield. However, in the context of this work, which focused on the guiding properties and achievable accelerating forces, the transverse resolution turns out not to change the results.

The maximum electric field on-axis can be seen in Fig. 3.8. The field in 2D is lower than the maximum field observed in the 1D simulations. One explanation is that the laser pulse is transversely finite and plasma electrons are partially expelled to the side and not returning back on-axis and hence lowering the electron density at the back of the bubble with respect to the 1D case where the electrons cannot deflect off-axis.

2D Scans Investigating Focusing and Guiding of Laser Pulses

For some simulations performed in this work, no injection of electrons is observed as the densities are too low and the laser pulse normalised vector potential is only mildly

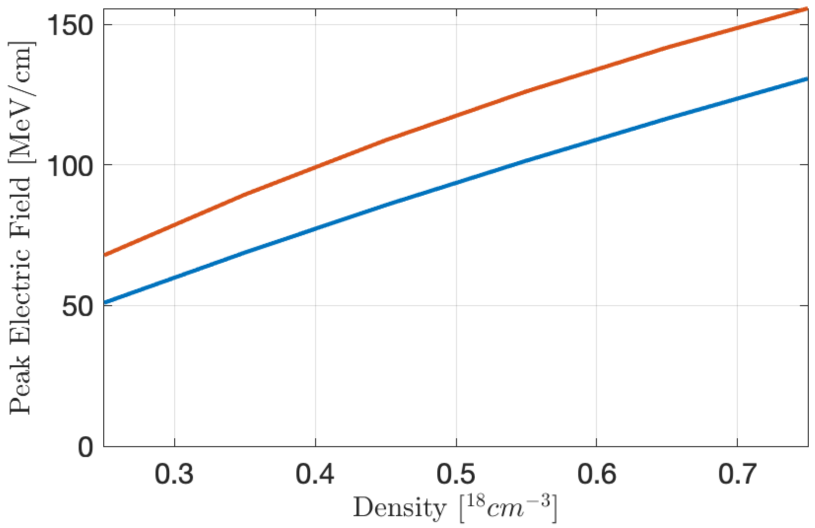

Figure 3.8: The accelerating electric field depending on the density shortly after the wakefield is initiated for a 2D EPOCH simulation (blue) and 1D simulation (red).

relativistic, $a_0 < 1$. Externally injected electrons are required to take advantage of the accelerating field. The acceleration length is then determined by the dephasing length or the diffraction of the laser in the plasma. Here, it is focused on the laser guiding in the plasma without exploiting external guiding mechanism.

The numerical solution of the differential equation for guiding in plasma could be used to approximate the behaviour in a plasma without expensive PIC-codes and is also investigated in this section. By using differential equations based on Eq. (2.53) one can create a set of more general differential equations to solve numerically:

$$\frac{\partial^2 w}{\partial z^2} = \left[\frac{\partial^2 w}{\partial z^2}\right]_{\text{diffraction}} + \left[\frac{1}{\eta}\frac{\partial \eta}{\partial r}\right]_{\text{relativistic focusing}} \tag{3.9}$$

$$\left[\frac{\partial^2 w}{\partial z^2}\right]_{\text{diffraction}} = \frac{w_0}{z_R^2}\left(\frac{w_0}{w(z)} - \frac{w_0^3}{w(z)^3}\frac{z^2}{z_R^2}\right) \tag{3.10}$$

$$\left[\frac{1}{\eta}\frac{\partial \eta}{\partial r}\right]_{\text{relativistic focusing}} \approx \frac{\partial \eta}{\partial r} \approx \frac{\omega_{p,0}^2}{8\omega_0^2}\frac{\partial a^2}{\partial r} \tag{3.11}$$

$$\tag{3.12}$$

in which the diffraction term was derived using Eq. (2.11) and the relativistic focusing by using Eq. (2.52). Assuming Gaussian focussing, the normalised vector potential can be modelled with Eq. (2.10), since $a \propto |\vec{E}_A|$. This leads to

$$a = a_0 \frac{w_0}{w(z)} e^{-\frac{r^2}{w(z)^2}} \tag{3.13}$$

$$\frac{\partial a^2}{\partial r} = -a_0^2 \frac{w_0^2}{w(z)^2} \frac{2 \cdot 2r}{w(z)^2} e^{-2\frac{r^2}{w(z)^2}} \tag{3.14}$$

$$\left.\frac{\partial a^2}{\partial r}\right|_{r \to w(z)} = -\frac{4a_0^2}{e^2} \frac{w_0^2}{w(z)^3} \tag{3.15}$$

if the derivative is evaluated at $w(z)$. Then the equations can be re-written using the Rayleigh length as,

$$z_R = \frac{\pi w_0^2}{\lambda} = \frac{k_0 w_0^2}{2} \tag{3.16}$$

$$\frac{w_0}{z_R^2} = \frac{4}{k_0^2 w_0^3} . \tag{3.17}$$

The differential equations follow as,

$$\frac{\partial \eta}{\partial r} \approx -\frac{k_p^2}{8k_0^2} \frac{4a_0^2 w_0^2}{w(z)^3 \exp(2)} \tag{3.18}$$

$$= -\frac{k_p^2 a_0^2 w_0^2}{8\exp(2) w(z)^3} \cdot \underbrace{\frac{4}{k_0^2 w_0^3}}_{=\frac{w_0}{z_R^2}} w_0^3 \tag{3.19}$$

$$= -\frac{k_p^2 a_0^2 w_0^5}{8\exp(2) w(z)^3} \frac{w_0}{z_R^2} \tag{3.20}$$

$$\Rightarrow \frac{\partial^2 w}{\partial z^2} = \frac{w_0}{z_R^2} \left(\frac{w_0}{w(z)} - \frac{w_0^3}{w(z)^3} \frac{z^2}{z_R^2} - \frac{k_p^2 a_0^2 w_0^5}{8\exp(2) w(z)^3} \right) \tag{3.21}$$

The total energy inside the wakefield with respect to the energy of the laser pulse is not negligible when propagating over long distances. The energy creating the wakefield is extracting energy from the laser pulse and therefore, a_0 depends on x as well. It can be estimated by calculating the energy in a single wakefield cycle

$$\begin{aligned}
U_E &= \frac{1}{2}\epsilon_0 \int E_{field}^2 \mathrm{d}V && (3.22)\\
&= \frac{1}{2}\epsilon_0 E_{max}^2 \int\limits_0^{\lambda_p} \sin(k_p\xi)\mathrm{d}\xi \cdot 2\pi \int\limits_0^{\infty} r \exp\left(-2\frac{r^2}{\lambda_p^2}\right)\mathrm{d}r && (3.23)\\
&= \frac{1}{2}\epsilon_0 E_0^2 \frac{1}{4}\frac{a_0^4}{1+a_0^2}\left(1-\left(\frac{8}{5}\left(\frac{c\tau_{FWHM}}{\lambda_p}-\frac{2}{5}\right)\right)^2\right)\frac{\lambda_p}{2}\frac{\pi\lambda_p^2}{2} && (3.24)\\
\frac{U_E}{\lambda_p} &= \underbrace{\frac{\pi^3}{8}\frac{\epsilon_0 c^4 m_e^2}{e^2}\left(1-\left(\frac{8}{5}\left(\frac{c\tau_{FWHM}}{\lambda_p}-\frac{2}{5}\right)\right)^2\right)}_{\equiv U_{E,0}}\frac{a_0^4}{1+a_0^2} && (3.25)\\
\text{or in density: } U_E &= \frac{\pi^4}{4}\frac{\epsilon_0^{\frac{3}{2}} c^5 m_e^{\frac{5}{2}}}{e^3}\frac{a_0^4}{1+a_0^2}\frac{1}{\sqrt{n}} && (3.26)
\end{aligned}$$

in which the maximum electric field of E_{field} is estimated with Eq.(2.76) for a Gaussian beam. The remaining field is assumed to be transversely Gaussian and oscillating longitudinally. It can be shown that the normalised vector potential depends on x as follows,

$$I = \frac{w_{FWHM}^2 \tau_{FWHM}\left(E-\Delta E\right)}{1.2\times 10^5} \tag{3.27}$$

$$I = I_{init}\left(1-\frac{\Delta E}{E}\right) \tag{3.28}$$

$$\sqrt{I} \propto a_0 = a_{init}\sqrt{1-\frac{\Delta E}{E}} \tag{3.29}$$

based on Eq. (2.23), which determines the consequences of energy loss. Note, that the total energy in the laser pulse here is E. If the loss in energy per plasma wave wakefield λ_p is estimated to be the number of wakefield wavelengths the pulse has propagated through the plasma, z/λ_p, a_0, the normalised vector potential scales with

$$a_0 = a_{init}\sqrt{1-\frac{\Delta U_E}{E}\frac{z}{\lambda_p}} \tag{3.30}$$

$$a_0 = a_{init}\sqrt{1-\frac{U_{E,0}}{E}\frac{a_0^4}{1+a_0^2}z} \tag{3.31}$$

$$\Rightarrow a_0 = \sqrt{\frac{a_{init}^2-1}{2\left(1+\frac{U_{E,0}}{E}za_{init}^2\right)} + \sqrt{\frac{\left(a_{init}^2-1\right)^2}{4\left(1+\frac{U_{E,0}}{E}za_{init}^2\right)^2} + \frac{a_{init}^2}{\left(1+\frac{U_{E,0}}{E}za_{init}^2\right)}}}\,. \tag{3.32}$$

a_0 from Eq. (3.32) can be substituted into Eq. (3.21) and the differential equation can be solved. The only missing information is the initial condition to solve these equations. While the 0th order initial condition is just the beam size, which is well known, the 1st order is the focusing or defocusing due to the unknown relativistic focusing (if the beam is starting at the beam waist). 2D EPOCH simulations have been performed and have been compared to the solution of the differential equation. For these simulations, the equation is adapted to the 2D geometry. In full 3D, the electric field has a factor $w_0/w(z)$ so that the intensity's amplitude changes with $w_0^2/w(z)^2$. The physical interpretation is that the energy spreads over the size of the beam transversely. 2D, consisting of one longitudinal and one transverse dimension, simulations have the issue that these are infinite in the non-simulated transverse dimension. It is as the beam would only focus in one transverse dimension. Thus the intensity in 2D is lower when the beam focuses and higher when defocusing compared to the 3D case. So to incorporate this, the results here are performed adapting the last term of Eq.(3.21) from $w_0^5/w(z)^3 \rightarrow w_0^4/w(z)^2$.

The solution of the differential equation require some initial conditions, which is the the initial beams size and the first-order derivative at the start as mentioned. The derivative is not known and was a variable. Hence, the initial derivative was optimised to yield the best agreement with the EPOCH simulations, which result can be seen in Fig. 3.9. The results of the numerical solutions are in good agreement with the simulations. Only far beyond the Rayleigh length, which is here $z_R = 7.1\,\mathrm{mm}$, the solution of the differential equation show un-physical focusing as seen in Fig. 3.9 on the far right. The power normalised to the critical power P/P_{crit}, which is shown in Fig. 3.10, indicates when the relativistic focusing is larger than the diffraction (discussed in detail in Sec. 2.7.2). The power is below the critical power for all of these simulations. This is an important result of these simulations as the laser still has significant reduction in diffraction. As an example, the spot only increased from $50\,\mathrm{\mu m}$ to $56.5\,\mathrm{\mu m}$ at a power of $P/P_{crit} = 0.8$, opposed to $70.7\,\mathrm{\mu m}$, which is expected in vacuum. The beams seems to slightly focus near the beam waist, which could increase the effect of focusing in 3D even more.

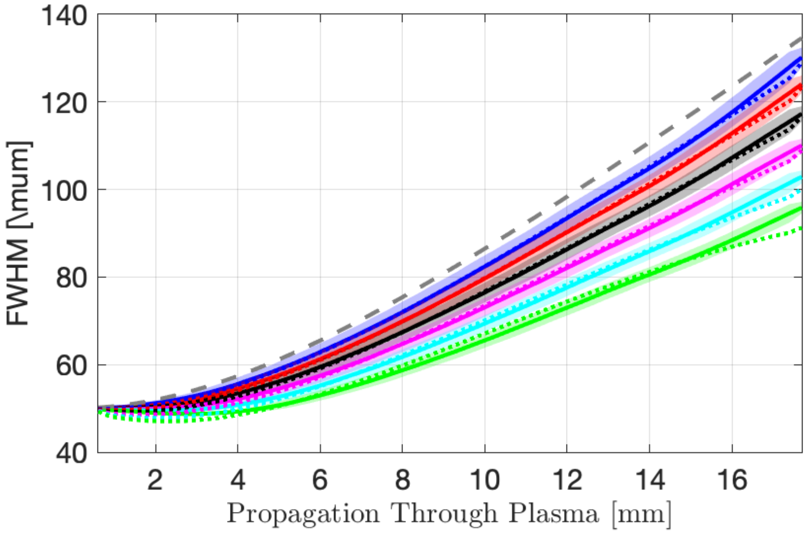

Figure 3.9: Laser beam size inside the plasma for different densities. The Gaussian behaviour in vacuum is shown as a reference (dashed grey). The densities are 0.25 (blue), 0.35 (red), 0.45 (black), 0.55 (magenta), 0.65 (cyan) and $0.75 \times 10^{18}\,\mathrm{cm}^{-3}$ (green). The solid lines refer to the results from EPOCH and the dotted lines from solving the differential equations.

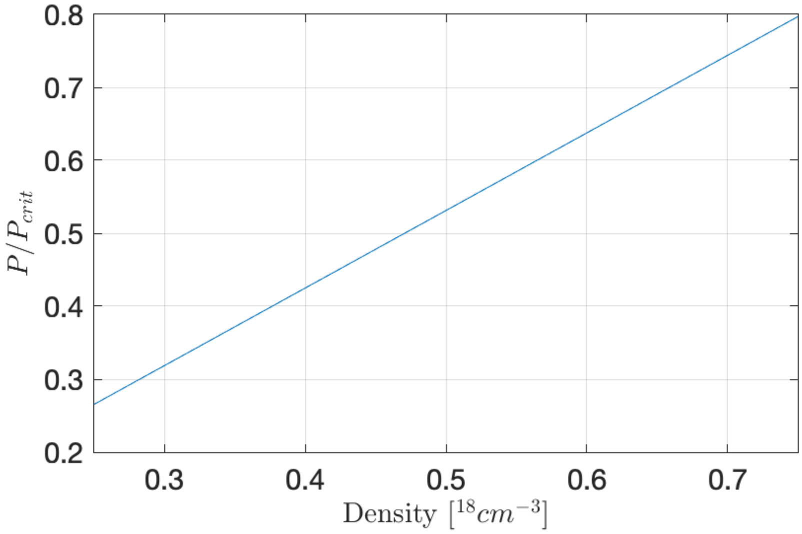

Figure 3.10: The power normalised to the critical power for the densities used in this simulation scan.

Chapter 4

Reflectivity and guiding properties of a high-intensity laser pulse reflected off a plasma mirror

The limitations on LPWA have been discussed previously, see Sec. 2.10 and also possible solutions, see Sec. 2.12. The arguments presented were the motivation for a campaign in 2019, studying the possibility of accelerating an LPWA accelerated GeV-electron beam in a second laser plasma wakefield accelerator. The experimental challenges are vast and include:

(a) GeV acceleration of an electron beam in stage 1

(b) reflecting the second laser pulse off a plasma mirror and injecting it into the second cell creating 100s-$\mathrm{MeV\,cm^{-1}}$ electric field

(c) transverse overlap of the electron beam and the second laser pulse

(d) temporal locking between both laser beams, to ensure the electron beam and second wakefield are in the accelerating and transverse focusing phase

The general set-up is depicted in Fig. 4.1. The campaign was carried out at the Gemini laser facility in TA3, described in Sec. 3.1, which has a dual beam capability, optimal for this experiment. GeV acceleration has been demonstrated numerous times at this facility[1], item (a). The two beams can be delayed relative to each other on the fs-scale with a linear delay-stage, item (d). Not shown in Fig. 4.1 is that the focusing laser pulses are reflected of two turning mirrors before the point of interaction. The dielectric mirror have a polished back surface so that the leakages can be extracted. These pulse copies are used to measure the relative time delay using spectral interferometry by inserting them into an imaging spectrometer. Item (c) requires near- and far-field measurements of both laser beams.

---

[1] [137] Kristjan Poder, PhD Thesis, Imperial College London (2016).

This section focuses its attention on item (b). The intensity on the second plasma mirror was $(3.3\pm0.1)\times10^{17}\,\mathrm{W\,cm^{-2}}$ and to-date, the only other experiment in this regime has been[2]. The reason for that is that plasma mirrors are often used to optimise the time contrast before the interaction at much lower intensities as it has been discussed in Sec. 2.12 or they are used just before focusing them onto the target for ion acceleration, where they show focusing properties at much higher intensities[3].

The creation of a strong accelerating wakefield with a laser pulse reflected from a plasma mirror has not specifically been investigated in previous attempts of this experiment, see[4]. This section includes a summary of the experimental calibrations and methods, reflectivity measurements of the plasma mirror, guiding of the laser pulse through a gas cell with underdense plasma and 2D EPOCH simulations. The simulations presented are used to estimate the wakefield properties with the experimentally measured, imperfect laser beam profile.

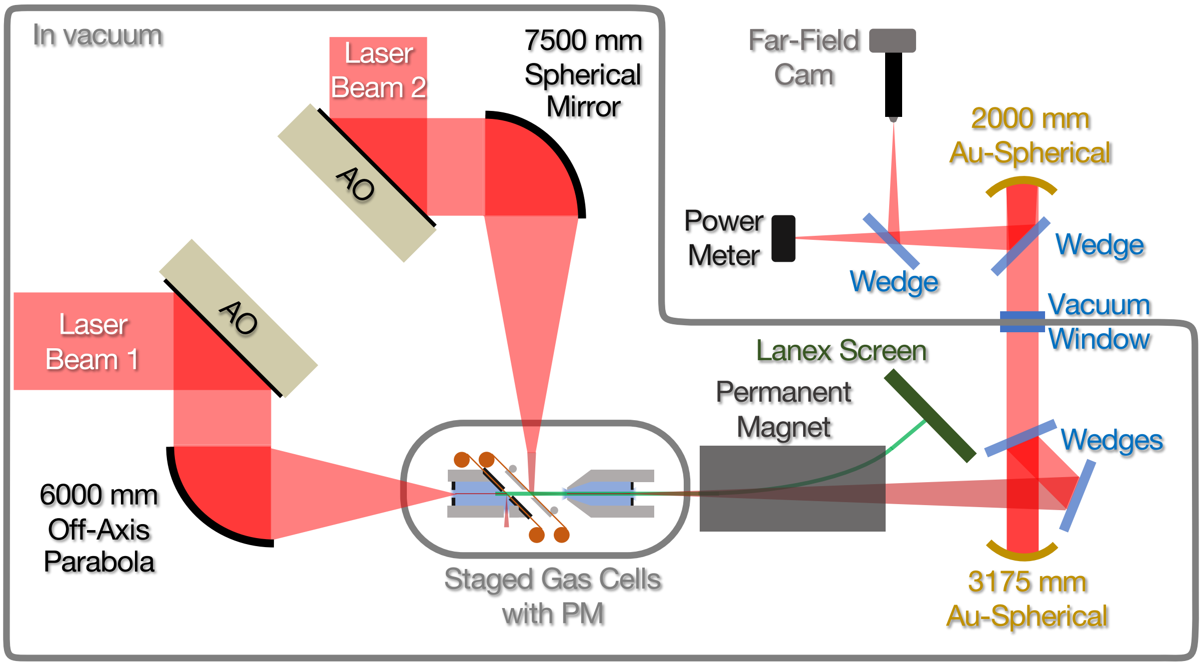

Figure 4.1: The experimental set-up of the campaign for staging two laser wakefield accelerators. It includes the post-interaction diagnostics, which were the main methods of characterising the interaction in this work. The schematic is not to scale and flattened. Note that the electron spectrometer was vertical to decrease noise due bremsstrahlung on the diagnostics. The adaptive optic (AO) was essential to flatten the spatial phase of the laser pulse.

---

[2] [152] B. H. Shaw *et al. Physics of Plasmas* (2016).

[3] [176] H.-E. Tsai *et al. Phys. Plasmas* (2017).

[4] [139] S. Steinke *et al. Nature* (2016); [177] B. H. Shaw. (2015).

4.1 Experimental Set-Up

Both laser beams come into the target area from their respective compressors, each having an individual transmission factor measured to be both around 70%. Both beams have an *adaptive optic* (AO) in their beam path immediately before the focusing optic to reduce aberrations. The f-number were based on previous experiments yielding high and reliable GeV-energies[5]. The first beam is focused with an $f = 6000\,\mathrm{mm}$ off-axis parabola, resulting in an f-number of 40. The AO is even more important for the second beam because the optic was an $f = 7500\,\mathrm{mm}$ focusing spherical mirror and the AO compensated for spherical aberrations introduced by the non-parabolic focusing optic. The f-number was 50 with a $150\,\mathrm{mm}$ beam diameter. The optics before the *interaction point* (IP) were all dielectric coated. The dielectric coating provides the highest damage threshold. Not depicted in the schematic drawing are the folding mirrors, which are between the focusing optic and the IP. One folding mirror per beam was used to obtain a transmitted representation of each laser pulse. The leakage signal served as pointing reference and part of the timing overlap diagnostic in the imaging spectrometer. The gas cell, the second gas cell and Kapton™ tape, which functioned as a plasma mirror can all be seen in detail in Fig. 4.2. The first laser beam was focused into a gas cell for electron injection and acceleration. A tape plasma mirror (PM) at the exit of this gas cell was used to eject the laser beam, while the electron beam passed through the PM. Note that there is an ongoing discussion on the consequences of the electron beam passing through a tape which was hit by a strong laser[6]. And as such there has been measurements with an without a tape at the exit of the first gas cell. These are not presented in this chapter as this chapter discusses the reflection and guiding properties of the second laser beam only.

A second PM injected the second laser beam into the second gas cell. Note that the relative polarisation of both beams was orthogonal, the first laser beam was horizontal and second laser beam was vertical polarised, which resulted in s-polarisation for the second beam in respect to the reflection of the PM. S-polarisation was required, since p-polarisation enhances *Brunel-absorption*[7], thus decreasing the reflectivity of the plasma mirror[8], see Sec. 2.12 for more details. The second laser beam was focused $14.9\,\mathrm{mm}$ downstream from the PM at the entrance of the second gas cell. Following the two gas cells was a permanent magnet in combination with a scintillating Lanex screen, see Sec. 3.2 for details, which acted as an electron spectrometer. The post-interaction laser beam was attenuated by reflecting off two glass wedges at $22°$ to reduce the B-integral in the exit window to an acceptable level of ≈ 0.53. The B-integral

---

[5] [53] K. Poder *et al.*, PhD Thesis, (2018).

[6] [143] G. Raj *et al. Phys. Rev. Res.* (2020).

[7] [150] C. Thaury *et al. Nature Physics* (2007).

[8] [152] B. H. Shaw *et al. Physics of Plasmas* (2016).

is not because the temporal phase is going to be measured, but because the non-linear response of the glass window could distort the spatial phase of the laser pulse as well (e.g. through hot spots) altering the far-field measurement. It was then collimated using a $3175\,\mathrm{mm}$ focal-length Au-coated spherical mirror. The collimated beam was imaged with a second $2000\,\mathrm{mm}$ focal length Au-coated spherical mirror onto the diagnostics. The beam was split with a glass wedge before imaging the far-field, to simultaneously measure the energy with a *Gentec QE8SP-B-BL-D0* energy meter. The diagnostics consisted of an *Andor Neo* 2160×2560 *sCMOS* camera with a microscope objective, which functioned as a far-field camera.

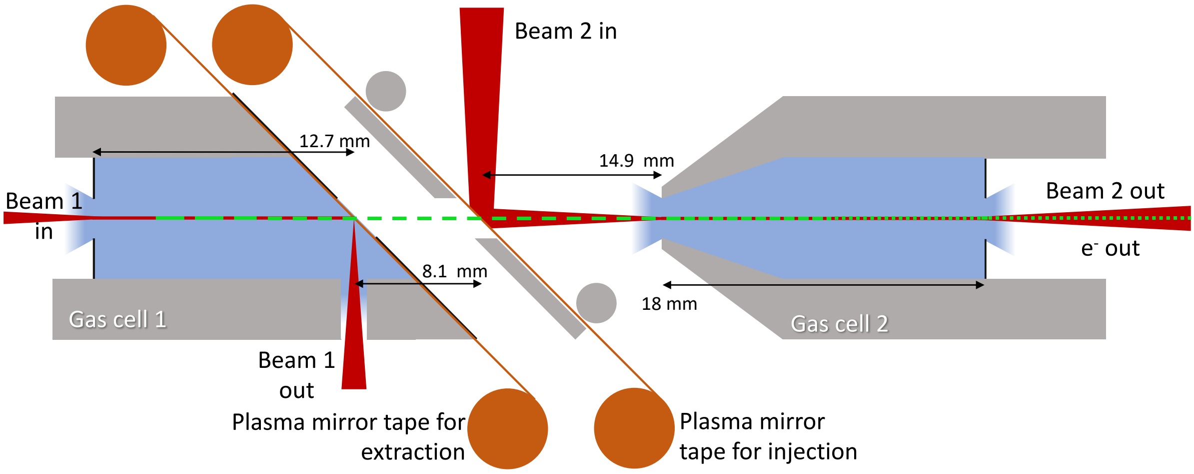

Figure 4.2: Schematic of the two-part accelerator set-up (units in mm). After the first laser beam (beam 1 from the left) injects and accelerates electron, it is reflected by a plasma mirror. The electrons travel through two tapes, where the second tape injects the second laser beam (beam 2 from above) into a second gas cell in which the electron beam is accelerated further.

4.2 Calibration

The chapter discussed the guiding properties of the second laser beam. As such, the focal spot size of beam 2 at the end of the second gas cell needed to be measured. Hence, the far-field camera had to be spatially calibrated. Also energy of the reflection of beam 2 off the PM was required as well as the through-put of the gas cell from the second laser beam. For that the transmission factor between the energy at the IP and the energy recorded on the energy meter next to the far-field camera had to be calibrated.

4.2.1 Energy Calibration

The energy meter for measuring the transmitted laser energy used was a pyroelectric sensor, a special ferroelectric crystal. These develop a measurable electric moment on heating[9]. Measuring the laser energy of beam 2 after the IP would be destructive to the measurement of the electron energy and x-rays, and it would also destroy the laser profile. Hence, the laser energy of beam 2 on-shot was measured farther downstream on a separate set-up, as seen in Fig. 4.2. The optical path from the interaction point to the diagnostic had several optics and glass transmissions, which required a calibration of the transmission. The reflection of the second laser beam on the tape was so close to its focal plane that it would produce a plasma on any solid target, even in the lowest power mode. This would destroy the tape within a few shots and change the reflection coefficient. Therefore, an energy measurement after the reflection of the tape would have been unreliable for calibrating the downstream diagnostic. Thus, the energy diagnostic was calibrated using the **first** laser beam with the gas cells and plasma mirror out of the way. However, the polarisation states of the Gemini laser beams were orthogonal to each other and the polarisation is of high importance when reflecting off the glass wedges, recall the Fresnel equations in Sec. 2.1.3. Not compensating for the polarisation, the ratio of the reflection coefficient of the p- and the reflection coefficient of s-polarisation would have been $\sim 2.6 \times 10^{-4}$ at the energy meter. A half-waveplate was used to change the polarisation state, ensuring the polarisation of the first beam was s-polarisation on all subsequent mirrors for the calibration.

The energy calibration was done in two steps, first, a second *Gentec QE25SP-S-MB* was placed in the vacuum between the IP and the first wedge and the laser energy of the first beam was measured for 1500 shots. Then, the energy meter was removed and another 1500 shots were measured on the energy meter on the diagnostic table. The total transmission factor between the IP and the diagnostic table yielded a transmission factor of $6.6(\pm 0.6) \times 10^{-5}$. One can estimate the transmission factor for perfectly aligned wedges, protected silver and gold mirrors via the Fresnel equations. The wedges were modelled with fused silica[10] and included two reflections off 22° and one transmission. Two reflections off unprotected Au-mirrors and 4 reflections off protective Ag-mirror using data provided of[11] yields a transmission factor of 8.5×10^{-5}. Considering that the angle of the wedges was not precisely measured and that the vacuum window might not transmit 100%, this figure seems to be in a reasonable agreement with the measurements.

---

[9] [178] C. Kittel. (1980), Chap. 8.

[10] [179] I. H. Malitson. *J. Opt. Soc. Am.* (1965).

[11] [180] *Reflectance of Optics with Unprotected Gold Coating* URL: `https://www.thorlabs.com/images/TabImages/Thorlabs_Unprotected_Gold_CoatingM03.xlsx` (visited on 09/06/2020) (2020); [181] *Reflectance of Optics with Protected Silver Coating* URL: `https://www.thorlabs.com/images/TabImages/Thorlabs_Protected_Silver_Coating.xlsx` (visited on 09/06/2020) (2020).

For some shots early in the experiment, there was no energy meter installed. The far-field camera was used as a calorimeter for those shots. A cross-calibration between the far-field camera and the calibrated energy meter was used to obtain the energy measurement for those shots. A background image was used to subtract noise from the camera image and the integrated counts were compared to the measured energy on the energy meter.

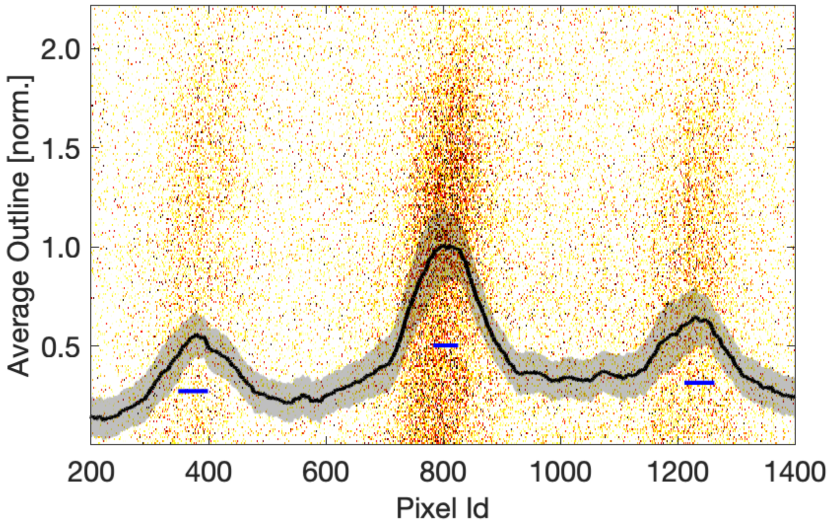

Figure 4.3: Spatial calibration of the far-field camera after the interaction. The grating pattern of the image is shown in the background and the normalised vertically averaged outline and its standard deviation is shown in black. The blue line indicated the location of the peaks and their uncertainty.

4.2.2 Spatial Calibration and Beam Size Measurements

The spatial calibration of the far-field camera was performed using a grating with a spacing of $d = 7\,\mathrm{mm}$. It was placed after the IP between the collimating Au-spherical and the second focusing Au-spherical. The resulting diffraction pattern show maxima at $\sin\theta = m\lambda/d$, with m being the order of maxima, and where θ is the angle between the optical axis and distance to the maxima from the centre. The deflection of the m-th order on the camera is then given by $x_m = mf\tan\theta$, where the focusing length of the optic used to image the beam was f. The resulting camera image is shown in Fig. 4.3. The line-outs (black) of each row were used to determine the location of the peaks, which resulted in an average distance between peaks. The uncertainty of the peaks is shown in blue. The resulting conversion factor was $529 \pm 28\,\mathrm{nm\,px^{-1}}$.

The focal spot size is defined as the $FWHM$ of the intensity profile. Even though most measurements have a single central spot, it was apparent for several shots that a second spot appeared, which can be explained by the poor input spot quality and a consequent poor reflectance off the plasma mirror. Such a case is seen in Fig. 4.4 showing two areas, where the intensity in the second spot is above ½ of the peak intensity of the spot (white and magenta). The quoted spot size is based on the central spot, because one can assume that the central, most dominating part is of most interest for accelerating electrons and responsible for the highest electric field. This is discussed further later in this chapter. The central spot was determined by fitting an ellipse to the outline (red), determining the semi-major and -minor axis.

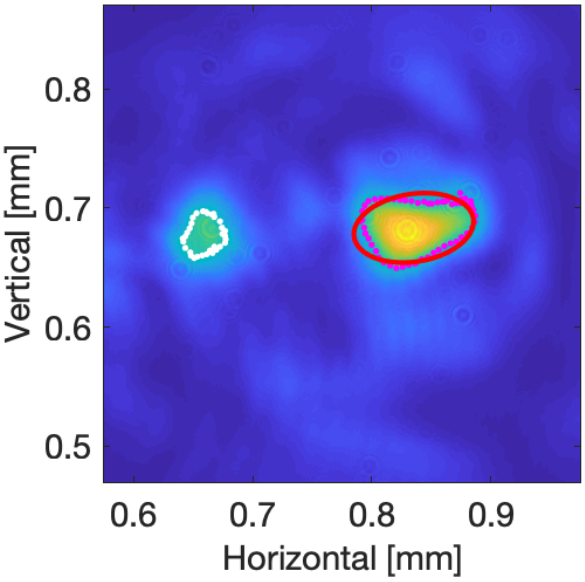

Figure 4.4: Some shots had poor focus spot quality, where two intensity peaks were observed. These peaks are defined as the area in the intensity profile above 0.5 of its peak value appear (white and magenta circles). In these cases, the more dominant peak was chosen to estimate the focus spot size as found by fitting with an ellipse (red).

4.3 Reflectivity and beam quality measurements

The energy observed on the downstream diagnostic relative to the input energy can be seen in Fig. 4.5 in red. The measured reflectivities peak at $73.7\% \pm 8.9\%$ at $4\,\mathrm{J}$ energy per pulse, which is in line with previous measurements[12]. The reflectivity decreases beyond that energy, as does the Strehl-ratio of the laser beam, which indicates the beam quality. This occurred, because the dielectric mirror just before the reflection on the plasma mirror was below specification in this experiment. As a result, the mirror surface burned and was damaged at energies as low as $3\,\mathrm{J}$. For reference, a photograph of the mirror is added in App. D.1, Fig. D.1. This resulted in degradation of reflectivity

---

[12] [152] B. H. Shaw *et al. Physics of Plasmas* (2016).

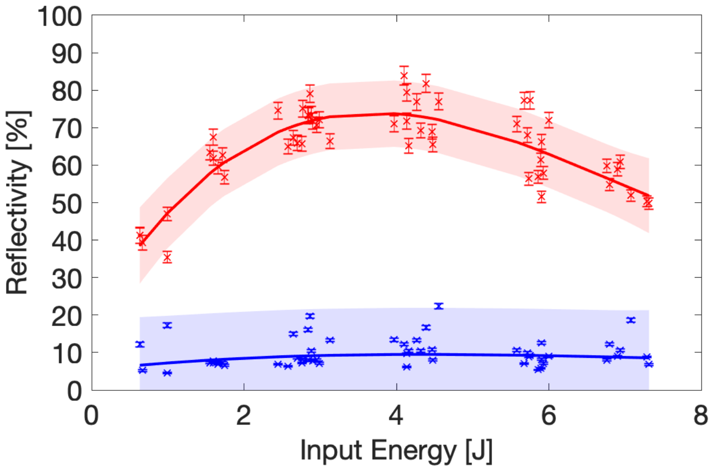

Figure 4.5: The ratio between incident and reflected energy from the plasma mirror (red) including a smoothing function 3$^{\text{rd}}$ order with its uncertainty to follow the trend. Blue points show the ratio of energy within the FWHM to the input energy.

at high energies. This indicates that it may be possible to obtain higher reflectivity if the beam quality **before** reflection off the pm is optimised.

An example microscope image of the low-power laser beam before reflection is shown in the top right corner of Fig. 4.6. The energy within the full-width half-maximum (FWHM) yields $19.2 \pm 1.8\%$ for the microscope image, while a Gaussian beam would enclose 50% of its energy in the FWHM. In case of a top-hat, the Airy-pattern would enclose 48.9% of the energy. Evidently, the quality from the initial laser beam coming to the IP was not optimal.

Fig. 4.6 shows an example beam profile of the reflected beam from the plasma mirror. The beam has a total reflectivity of 72% at $5.5\,\mathrm{J}$ input energy, hence $> 4\,\mathrm{J}$ on target. Normally, Gemini can deliver $> 10\,\mathrm{J}$ on target. The low input energy of the laser was due to the overall performance of the laser system. The FWHM of the encircling ellipsoid is depicted in red and it is obvious that a significant part of the energy lies outside it. There is 12.2% energy encircled compared to the measured 19.2% within the FWHM of the focal spot of the low-power unreflected beam. The energy contained within the reflected focal spot for all shots can be seen in Fig. 4.5 as the blue line. The relative energies enclosed by the FWHM are much more uniform over the whole range investigated, than the total reflectivity. The ratio between the initial Strehl-ratio and the measured Strehl-ratio after the reflection is shown in Fig. 4.7 and is on average $69 \pm 17\%$. This reflectivity is in line with the peak reflectance measured, so reflection has not perceptibly changed the beam quality.

The average spot size reflected off the plasma mirror was $63.7 \pm 16.6\,\mu\mathrm{m}$, defined as the radius creating an area of the same size as the average measured beam size[13].

---

[13] $\pi r^2 = \pi a \cdot b \rightarrow r = \sqrt{a \cdot b}$, where a and b are the semi-major and -minor axes

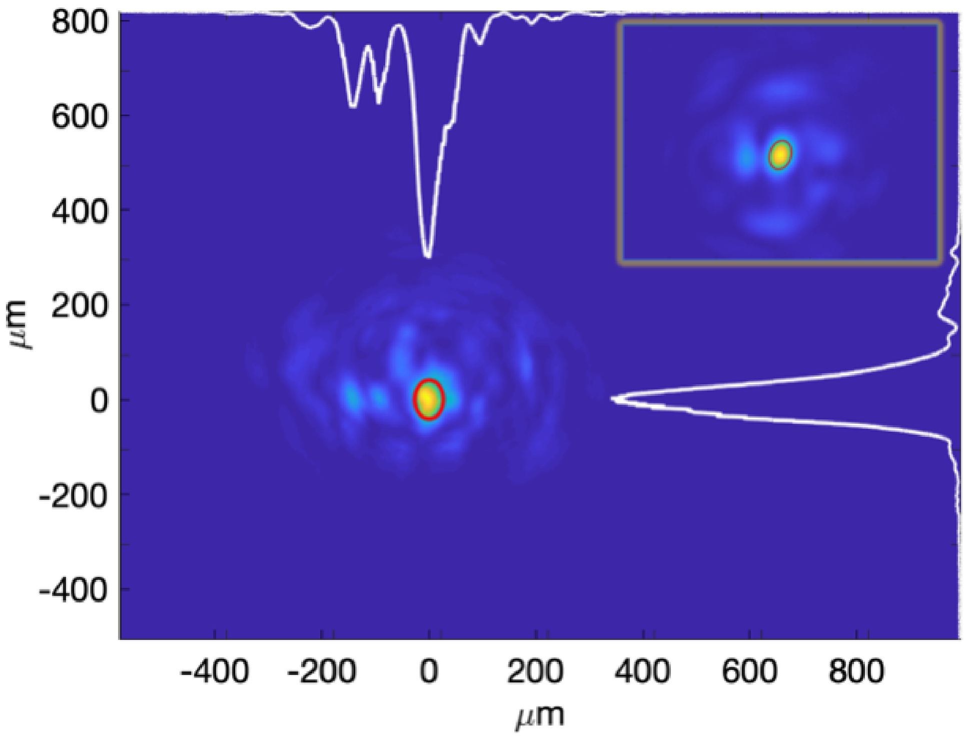

Figure 4.6: The beam profile is shown after reflection from the tape, including the red ellipse covering the FWHM. The line-out along the semi-major and -minor axis of the ellipse is given in white. The low-power beam profile coming onto the plasma mirror was measured with a microscope objective and is depicted in the inset.

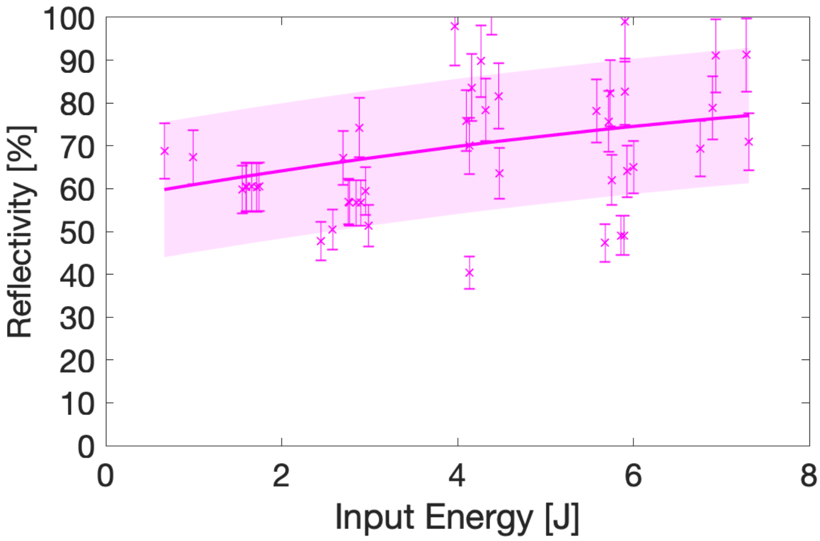

Figure 4.7: The ratio between the energy reflected from the PM within the FWHM of the focal spot to the initial energy within the FWHM focal spot size. The solid line and confidence interval is a quadratic-based Gaussian process regression.

The energy within the FWHM leads to on-target normalised vector potentials, which peak around $a_0 = 0.7$, as seen in Fig. 4.8.

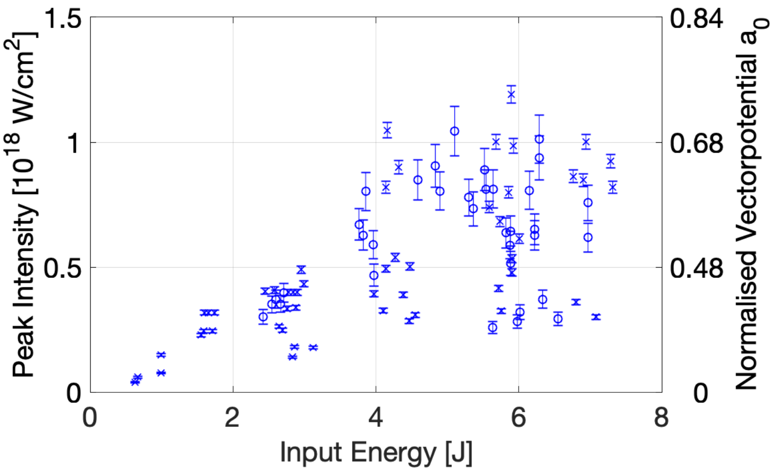

Figure 4.8: The intensity and normalised vector potential of the reflected laser beam from the plasma mirror depending on the input energy. The crosses and circles corresponds to different dates of measurement.

4.4 Guiding of a Plasma-Mirror Reflected Laser Pulse

The suitability of this laser pulse for driving a laser wakefield was tested by determining its ability to self-guide. The guiding of the reflected beam was investigated by passing the beam reflected off the foil into a gas cell of length $18\,\mathrm{mm}$. The gas cell density was varied and the measured focal spot after the gas cell can be seen in Fig. 4.9 with respect to the relativistic plasma wave wavelength corresponding to the applied density. Though there is a large spread of spot sizes for a given plasma wavelength, a clear trend can be observed. Note, that the uncertainty of the plasma wavelength, calculated with Eq. (2.37), is due to the uncertainty in the density, which originates from the technical limitation of the gas pressure system, as it was originally not intended to reach such low pressures. Another systematic error not depicted in the presented error, is due to the change of the gas cell entrance diameter. The entrance and exit diameter of the gas cell increased by the number of shots as the laser widened the holes. The backing pressure of the gas cell was correlated to the density inside the gas cell using interferometry. However, the calibration was performed later in experiment and the density might have been lower at that point in time as the gas cell entrance and exit may have increased in size. This corresponds to a slight shift to the left of the data points in Fig. 4.9 as a decrease in plasma wave wavelength is reciprocal to an increase in plasma density.

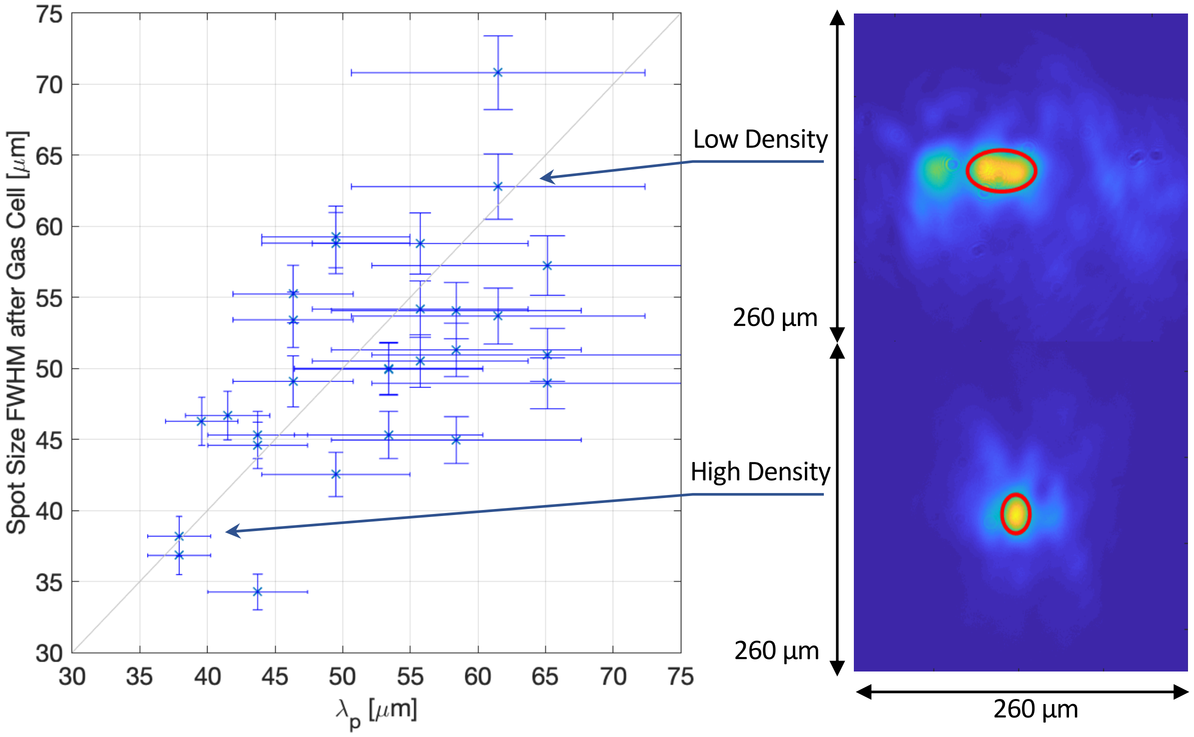

Figure 4.9: The measured focal spot size after the gas cell depending on the plasma wave wavelength. Example laser spots on the right for the highest and lowest density.

For reference, the example spot in Fig. 4.6 has a spot size with an ellipse of $(71.9 \pm 3.7\,\mu\mathrm{m}) \times (43.5 \pm 2.3\,\mu\mathrm{m})$, which corresponds to an average spot size of $55.9 \pm 2.1\,\mu\mathrm{m}$ (in Gaussian error propagation). Using these figures and calculating the matched plasma density, by $w_{\text{FWHM}} \approx \lambda_p \equiv 2\pi c/\omega_p$ yields densities of,

$$n_e = \frac{4\pi^2 c^2 \epsilon_0 m_e}{e^2 w_{\text{FWHM}}^2} = \begin{cases} n_{\text{major}} = 0.23 \times 10^{18}\,\mathrm{cm}^{-3} \\ n_{\text{avg}} = 0.35 \times 10^{18}\,\mathrm{cm}^{-3} \\ n_{\text{minor}} = 0.59 \times 10^{18}\,\mathrm{cm}^{-3} \end{cases} \tag{4.1}$$

for the semi-major axis, average spot size and minor-axis. The energy guided through the gas cell depends on the density as shown in Fig. 4.10. A greater guided energy is observed through the gas cell for lower density.

As seen from Fig. 4.10, the measured transmitted energy increases with decreasing electron density for a constant input energy of $6.6 \pm 0.2\,\mathrm{J}$. The energy increase with decreasing density can be explained by considering the increased guiding of the laser pulse. An increasing proportion of the central laser pulse energy is within the plasma bubble for a decreasing density and therefore guides.

An example beam spot at lower density can be seen on the top of Fig. 4.9 with an average spot size of $62.8 \pm 2.3\,\mu\mathrm{m}$ at a density of $0.29 \pm 0.10 \times 10^{18}\,\mathrm{cm}^{-3}$. The bottom beam spot in Fig. 4.9 is an example image at higher density and the spot size

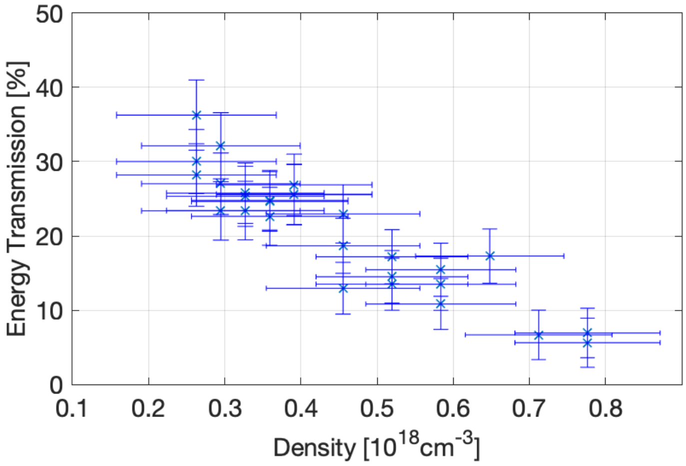

Figure 4.10: The energy exiting the gas cell normalised to the entering energy.

decreased here to $38.2 \pm 1.4\,\mu\mathrm{m}$ for a density of $0.78 \pm 0.10 \times 10^{18}\,\mathrm{cm}^{-3}$.

4.5 Simulations of Wakefield Generation with a Plasma-Mirror Reflected Laser Pulse

To ascertain the applicability of the generated reflected beam to generate an accelerating wakefield, the wakefield generation expected with the laser beam parameters measured in this experiment was simulated. To see the effect on wakefield structure of the measured laser beam, the laser beam was modelled in 2D with the laser profile as Fig. 4.6. The beam profile employed in the simulation can be seen in Fig. 4.11 (a) and (b) in grey for the semi-major and -minor axis. It was found that a 7$^{\mathrm{th}}$-order Gaussian function resembled the beam profile accurately. This modelled laser beam profile was used in 2D particle-in-cell simulations with the code EPOCH. The density was set to match the highest and lowest measured densities in the experiment, at $0.29 \times 10^{18}\,\mathrm{cm}^{-3}$ and $0.78 \times 10^{18}\,\mathrm{cm}^{-3}$ with a laser intensity of $1.26 \times 10^{18}\,\mathrm{W\,cm}^{-2}$ ($a_0 = 0.77$). The density corresponds to a plasma wakefield wavelength of $\lambda_p = 62\,\mu\mathrm{m}$ and $37.8\,\mu\mathrm{m}$. The laser beam profiles at the exit of the gas cell are also depicted in Fig. 4.11 (a) and (b). The laser intensity was tracked as well and shown in Fig. 4.11 (c). The change in intensity is not as smooth as it was for the 1$^{\mathrm{st}}$-order Gaussian as investigated in Sec. 3.4.2. Also, the wings, which are higher-order Gaussian contributions to the focal spot also contribute to the guiding of the laser pulse. For simulation with a profile taken to be that along the semi-major axis profile the intensity wings are focused into the centre of the laser beam, which increases the intensity further, amplifying the focusing effect, which can be observed in Fig. 4.11 (d) in red. The guiding of a simple Gaussian laser pulse in a plasma based on solving the differential equations as estimated in Sec. 3.4.2, is shown as dotted lines. The simulations of the major-axis does follow those solutions reasonably well. That is, because the shape is very similar to a Gaussian. The pulse

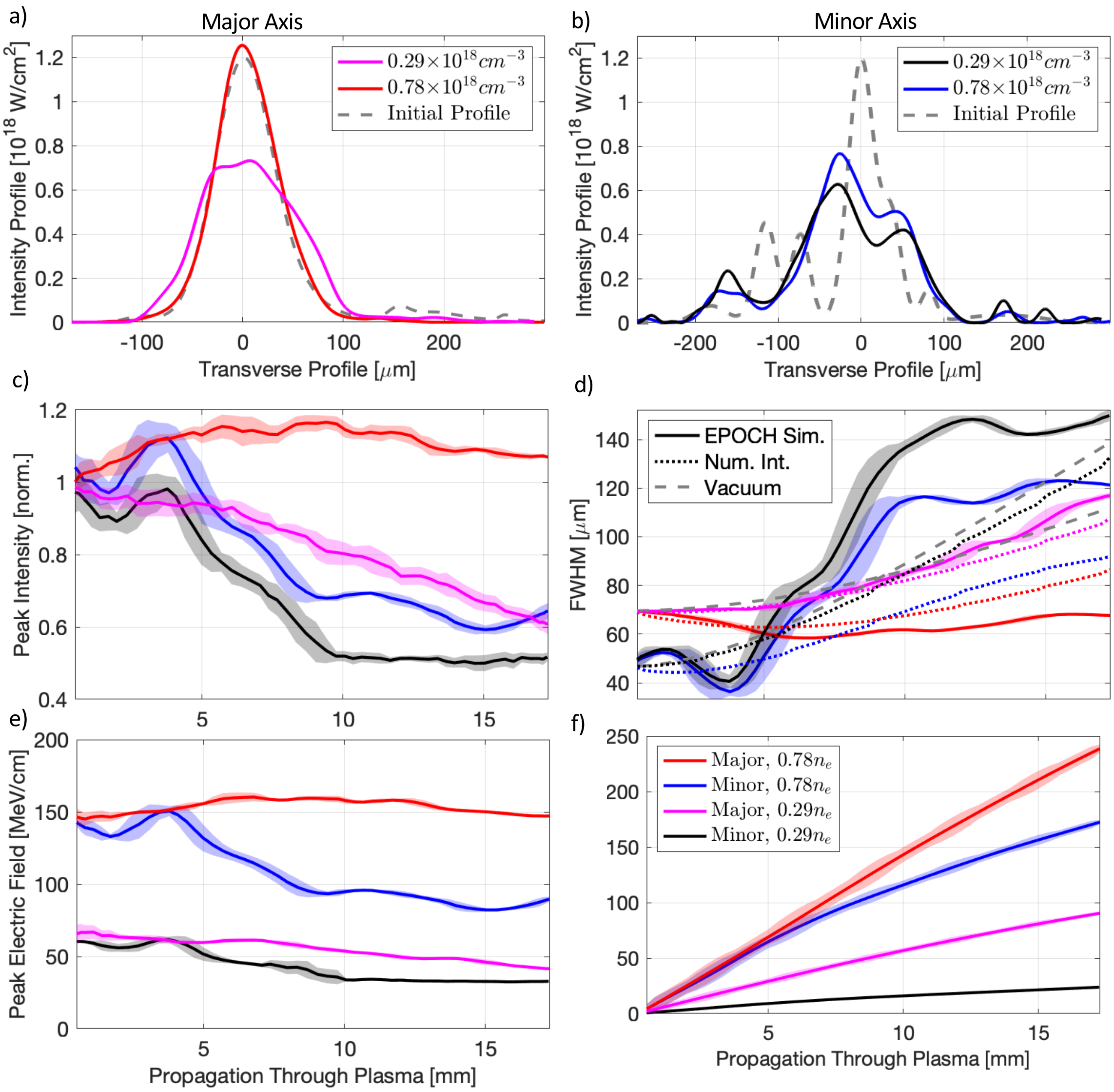

Figure 4.11: Results of 2D EPOCH simulations. The employed intensity profiles for the semi-major and -minor axis are shown in (a) and (b) in grey from the profile measured before the gas cell, Fig. 4.6. (a) and (b) also show the intensity profiles after propagating through the length of the gas cell for two densities, $0.29 \times 10^{18}\,\mathrm{cm}^{-3}$ and $0.78 \times 10^{18}\,\mathrm{cm}^{-3}$, which were measured in the experiment, see Fig. 4.10. (c) shows the change of the intensity normalised to the initial intensity. (d) depicts the FWHM of the profile observed in the EPOCH simulations (solid lines), the beam size from numerically integrating the underlying differential equation, which was discussed in Sec. 3.4.2 (dotted lines) and the beam profile in vacuum propagation for Gaussian beams (dashed lines) for the different densities and beam profiles. The maximal electric field measured in (e) and the energy gain in (f). The colours explained in (f) are applicable for all plots, where $n_e = 1 \times 10^{18}\,\mathrm{cm}^{-3}$.

shape, which has a large amount of energy in the wings does not follow the predictions at all. The sudden deviation and increase in spot size is because the individual Gaussian-modes increase in width and decrease simultaneously, spreading out the the width. The energy in the wings does not contribute to more guiding for simulations using the semi-minor axis profile. It even seems that the energy outside the central peak destructively shapes the plasma channel and the laser profile experiences significant defocusing, thus the opposite effect occurs. While the first impression is a positive observation, that the energy outside the central peak can contribute to the creation of the wakefield by focusing into the central channel, the second set of simulations clearly shows that a large increase of energy in the wings counteracts guiding and therefore also the acceleration process.

The latter is supported by looking at the peak electric field on-axis Fig. 4.11 (e). Even though the normalised vector potential is the same in all simulations at the start, the resulting electric field changes. The lower density yields in a significant lower peak electric field, which is expected from the scaling laws. The higher density shows an increasing difference between the different laser profiles. The resulting electric field from the simulation with the profile found to resemble more a Gaussian-shaped, which is along the major-axis, stays constant around $150\,\mathrm{MeV\,cm^{-1}}$, while the laser profile from the minor-axis decreases below $100\,\mathrm{MeV\,cm^{-1}}$.

The electric field on-axis was used to estimate the potential energy gain that would have been achieved if the electron beam from the first gas cell and the second laser beam had been successfully synchronised. Electrons were initiated in different phases behind the laser pulse and propagated with the effective speed of light described in Sec. 3.4.2. Fig. 4.12 shows an example for the semi-major axis and a density of $0.78 \times 10^{18}\,\mathrm{cm^{-3}}$. Only regions with transverse focusing are shown and the regions at which the electrons would be de-focused are blank. The maximum energy was determined by finding the maximum energy gains from initial phases, which focus the electron beam through-out the entire simulation. This ensures that the externally injected electron bunch can be captured in the wakefield for the required length of acceleration. The predicted energy gain for all simulations is shown in Fig. 4.11 (f) and reaches as high as $238.5\,\mathrm{MeV}$.

4.5.1 Energy Spread

The predicted energy gains depicted in Fig. 4.11 refer to single electrons and does not reflect any longitudinal spread of an injected electron bunch. One can estimate the energy spread of a finite large electron bunch by using a longitudinal flat top electron profile and calculating the average energy and standard deviation depending on the bunch length. Starting from the most preferable initial phase towards lower predicted

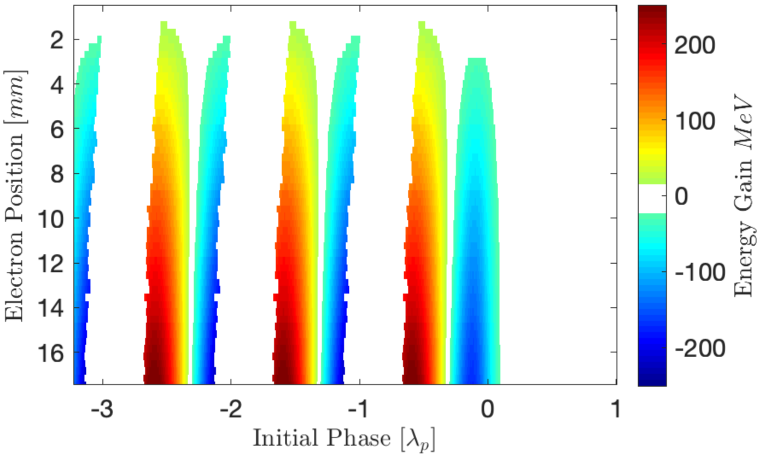

Figure 4.12: Energy gain along the propagation direction through the gas cell (y-axis) for electron initiated in different phases behind the laser pulse (x-axis). This example is for a simulation with the profile found along the semi-major axis at a density of $0.78 \times 10^{18}\,\mathrm{cm}^{-3}$. It excludes data, where electrons would experience defocusing force (white).

energy gain, a virtual electron bunch would consist of electrons with higher energy gain and lower. Those figures can be used to estimate an average and spread of the predicted energy gain. Again, one only considers electrons in the focusing phase of the wakefield. The predicted energy gain and spread for the different simulations can be seen in Fig. 4.13. The plot does not contain the results from the simulation based from the outline of the semi-minor axis at a density of $0.29 \times 10^{18}\,\mathrm{cm}^{-3}$ as the focusing field of the wakefield turned out to be unstable, see App. D.2 for more details on the transverse electric field.

For reference, the plasma wave wavelength is $37.8\,\mathrm{\mu m}$ for $0.78 \times 10^{18}\,\mathrm{cm}^{-3}$ (blue and red in Fig. 4.13) and $62\,\mathrm{\mu m}$ for $0.29 \times 10^{18}\,\mathrm{cm}^{-3}$ (magenta in Fig. 4.13). Hence, the injected electron beam must be a fraction of the plasma wave. In the context of this experiment, one would expect that the first gas cell, using self-injection or possibly ionisation injection, could operate at significantly higher densities, which would limit the electron bunch length to a fraction of the plasma wavelength used here.

As mentioned earlier, these virtual electrons neglect beam loading effects and as such, the wakefields amplitude might have been lower. 100s of pC can significantly alter the field as it is used in some schemes to systematically reduce the emittance[14]. Thus, injecting too much charge might be a disadvantage and concentrating on a low-energy spread and low-emittance injection beam would be beneficial both for the newly-introduced energy spread and in the coupling efficiency of this staging scheme.

The last note might be that the energy spread indicated is directly dependent on the

---

[14] [46] G. G. Manahan *et al. Nat. Com.* (2017).

longitudinal position of the electrons. An electron bunch with the same energy and an energy spread which correlation to the longitudinal position is the opposite would be accelerated on average, and the energy spread would be removed. This is the focus of several research groups, e.g.[15].

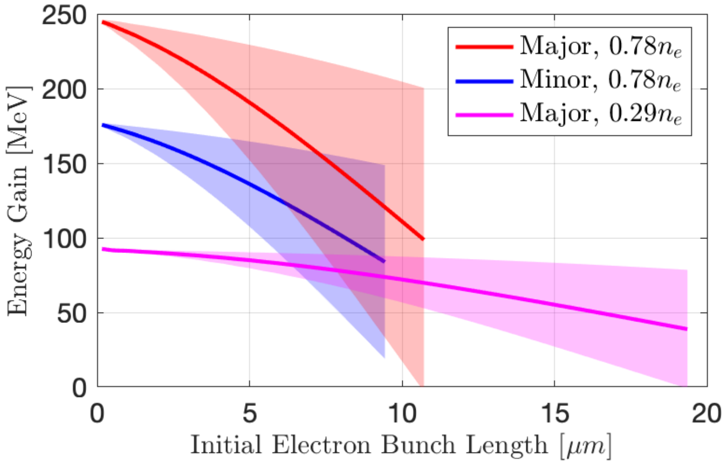

Figure 4.13: The estimated energy and energy spread for injected electron into the wakefield depending on the initial electron bunch length. The colour is the same as in Fig. 4.11, semi-major axis profile and $0.78 \times 10^{18}\,\mathrm{cm}^{-3}$ red, semi-major axis profile and $0.29 \times 10^{18}\,\mathrm{cm}^{-3}$ magenta, semi-minor axis profile and $0.78 \times 10^{18}\,\mathrm{cm}^{-3}$ blue. The result of the semi-minor axis profile and $0.29 \times 10^{18}\,\mathrm{cm}^{-3}$ is only a single data point as the focusing field of the wakefield is unstable, see App. D.2, and is not included.

4.6 Conclusion and Future Optimisation of the Beam Quality

The beam quality during the experiment was not as good as expected. However, the simulations based on the major-axis laser beam profile did support a wakefield, which could have increased the energy of the electrons of more than $238.5\,\mathrm{MeV}$. But, the other simulations based on the laser beam profile deviating more from an optimal Gaussian shape showed laser guiding and the focusing of the electrons inside the wakefield strongly depended on the density. While these simulations indicate that successful acceleration might have had been possible with the explored parameters, the indication of possible electron beam acceleration might have been lost in the fluctuation of the laser beam quality and uncertainty of the density. Optimising the beam quality and symmetry would have a huge impact on another attempt of this experiment. The beam quality reflecting off the plasma mirror set-up used here does not degrade significantly

---

[15] [182] R. D'Arcy *et al. PRL* (2019).

at these high intensities of $(3.3 \pm 0.1) \times 10^{17}\,\mathrm{W\,cm^{-2}}$ as seen in Sec. 4.3. Assuming an ideal case of having 50% of the full energy inside the FWHM, $7\,\mathrm{J}$ would have resulted in an a_0 of 1.6 and an intensity of $5.7 \times 10^{18}\,\mathrm{W\,cm^{-2}}$. A final set of simulations indicates a potential energy gain of $929\,\mathrm{MeV}$ as seen in Fig. 4.14, emphasising the importance of the laser beam quality.

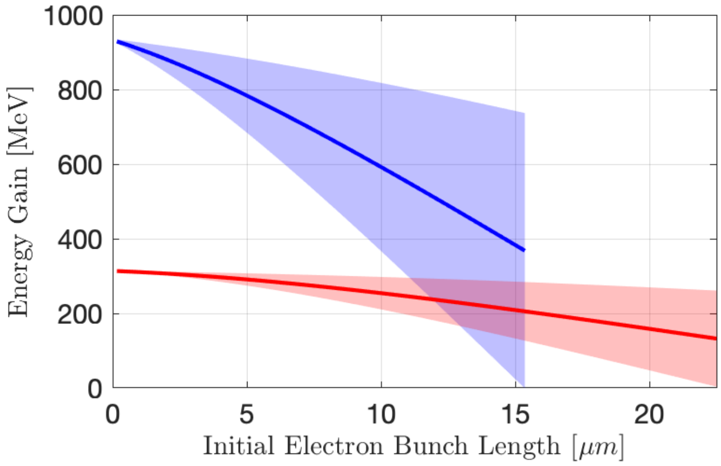

Figure 4.14: The estimated energy and energy spread for the injected electrons into the wakefield depending on the electron bunch length for a Gaussian beam profile with no energy loss in the wings for $w_{FWHM} = 50\,\mathrm{\mu m}$ at $0.29 \times 10^{18}\,\mathrm{cm^{-3}}$ (red) and $0.78 \times 10^{18}\,\mathrm{cm^{-3}}$ (blue).

Furthermore, an increase in density in the experiment and a smaller focus spot size to match the pulse length would increase the theoretical energy gain even more, because the relativistic focusing would increase. This is a very promising result for a future proposal of the experiment.

Chapter 5

Compact Laser-Driven Accelerator X-ray Sources for Industrial Imaging

5.1 Introduction

This chapter focuses on the utilisation of radiation from LPWA as an imaging source for industrial samples and applications. It is an entirely different experiment and was done at a different campaign with a different set-up than the previously described experiment. The experiment was performed at ATA3 at the Gemini laser facility described in Sec. 3.1. The campaign was performed in cooperation with the *National Composites Centre* (NCC)[1] and the Warwick Manufacturing Group (WMG) [2], who provided several samples from different fields in the industry sector and which are described in detail below. The campaign imaged metallic samples via bremsstrahlung radiation and low-density polymer/ carbon-fibre composite materials via betatron radiation. The first section of this chapter investigates the enhancement of betatron radiation in preparation for the second part of the experiment which investigates industrial imaging.

The content of this paper was published as[3] with the author of this thesis being the first author of the paper[4]

Advances in industrial methods, such as additive manufacturing (AM), are enabling the fabrication of better and more complicated products than are achievable with traditional manufacturing. Environmental sustainability is a major incentive to develop less wasteful processes, new materials, and energy storage solutions. For example, many aircraft and automotive components are now produced using lightweight fibre reinforced composites to improve fuel efficiency. In parallel, the more widespread adoption

---

[1] National Composites Centre, Bristol and Bath Science Park, Feynman Way Central, Emersons Green, Bristol BS16 7FS, UK

[2] WMG, University of Warwick, Coventry CV4 7AL, UK

[3] [183] J.-N. Gruse *et al.* *NIMA* (2020).

[4] The copyright policy of *ELSEVIER* can be found at `https://www.elsevier.com/about/policies/copyright`, which states that “the author can use their article in full or in part in inclusion in a thesis or dissertation”.

of electric vehicles is driving investment and innovation in battery technologies. Rapid growth in these sectors means that in some cases demand is outstripping supply and there is a need for industry to increase productivity. Progress in manufacturing needs to be accompanied by improvements in the product inspection tools employed for metrology and quality control. X-ray computed tomography (XCT) is a powerful technique because it allows non-destructive evaluation (NDE) of the internal structure of dense objects. XCT is generally conducted using commercial x-ray tubes and linear accelerators but for some applications, these sources are not able to simultaneously meet the demanding requirements on penetration, scan speed and spatial resolution [5]. Superior imaging capability can be achieved using synchrotron light sources, but these are national-scale facilities which are in high demand meaning access for industrial inspection is limited.

Alternatively, an x-ray source based on betatron radiation could be utilised as it delivers high peak brightness and ultra short x-ray pulses. The number of photons can reach $10^{10}\,\mathrm{ph}$ per pulse in a beam with $10\,\mathrm{mrad}$ divergence and critical energies in the range 10 – 50 keV[6], 10% stability[7] and pulse lengths of <$100\,\mathrm{fs}$[8].

The small size of the laser-driven accelerator is a key advantage compared to conventional synchrotron light sources and the technology has the potential to be used for a broad range of applications[9]. Tomographic imaging of biological samples[10] and time resolved radiography of high energy density plasma[11] has been the topic of research investigations. Imaging of AM objects[12] and complex microstructures[13] has also been reported. The short pulse duration enables radiographic snapshots of fast-moving parts with no motion blur. Also, the source is suitable for x-ray absorption spectroscopy with exceptional time resolution[14]. Because the x-ray source size is of the order of $2r_\beta \approx 1\mu$m, high-resolution imaging can be conducted with high flux x-ray, avoiding the trade-off between source size and power encountered with conventional x-ray machines. Furthermore, the beam has a transverse coherence length of 10's μm within $1\,\mathrm{m}$ of propagation meaning that phase enhancement can be obtained with a compact imaging arrangement[15]. Phase-contrast provides superior image quality for low-density objects that only weakly attenuate x-rays and better distinction between

---

[5] epsrc.ukri.org/files/research/epsrc-x-ray-tomography-roadmap-2018

[6] [71] J. M. Cole *et al.* *Plasma Phys. Control. Fusion* (2016); [52] J. M. Cole *et al.* *PRX* (2018).

[7] [62] A. Döpp *et al.* *Light: Science & Applications* (2017).

[8] [184] K Ta Phuoc *et al.* *Physics of Plasmas* (2007); [185] B. Mahieu *et al.* *Nat. Com.* (2018).

[9] [68] F. Albert and A. G. R. Thomas. *Plasma Phys. Control. Fusion* (2016).

[10] [71] J. M. Cole *et al.* *Plasma Phys. Control. Fusion* (2016); [52] J. M. Cole *et al.* *PRX* (2018); [63] J. Wenz *et al.* *Nat. Com.* (2015); [72] A. Döpp *et al.* *Optica* (2018).

[11] [65] J. C. Wood *et al.* *Scientific Reports* (2018).

[12] [73] M Vargas *et al.* *Plasma Phys. Control. Fusion* (2019).

[13] [74] A. E. Hussein *et al.* *Scientific Reports* (2019).

[14] [185] B. Mahieu *et al.* *Nat. Com.* (2018).

[15] [186] S. Kneip *et al.* *APL* (2011).

items made of similar materials[16]. This technique has been demonstrated on biological samples using plasma-based accelerators[17].

5.2 Imaging Set-up

The experiment was performed with the Gemini laser that provided a laser pulse of duration $49 \pm 3\,\mathrm{fs}$ and $7.2 \pm 0.4\,\mathrm{J}$ on target. The wavefront was optimised with an AO and was focused with an off-axis *f*/40 parabola into a He filled gas cell. The average beam size was an ellipse of $66.0 \pm 13.5\,\mu\mathrm{m} \times 34.1 \pm 6.7\,\mu\mathrm{m}$ and an energy of $32.1 \pm 1.7\%$ inside its FWHM. Orthogonal to the main beam, a second laser pulse was used to measure the plasma electron density interferometrically (not shown in the diagram). The laser beam, electron beam and x-ray beam were directed towards a $25\,\mu\mathrm{m}$ polyimide tape after the gas cell. The polyimide tape functioned as a plasma mirror deflecting most of the undepleted laser energy. A $13\,\mu\mathrm{m}$ aluminium foil protected the sample from any remaining laser light and also filtered out 7% of the energy of a $15\,\mathrm{keV}$-synchrotron spectrum below the K-edge ($1.6\,\mathrm{keV}$).

Focusing x-rays is based on either refractive index deflection or Bragg-reflection. Refractive index deflection means that x-rays propagate through material. This unavoidably results in energy loss. Bragg-reflection only works for a small bandwidth[18] of the radiation. The experimental goal was to achieve a large number of photons for the purpose of high contrast imaging. Therefore the x-ray beam was not focused with any of those x-ray optics, but instead the samples were imaged in a purely free propagation set-up. A free propagation set-up takes advantage of or requires low deflection of the x-ray from the sample since then the imaging plane (the camera) can be placed at a large distance from the sample without blurring the image. This also magnifies the image size on the image plane. Our set-up included three different locations for the samples and required two experimental configurations.

Fig. 5.1 (a) shows the set-up for the highest magnification. The electron beam is deflected with a *kicker*-magnet (a physically small magnet with a large magnetic field) to protect the sample and imaging camera from the electron beam. The energy of the electrons is not measured in this configuration. The sample can be placed as close as $370\,\mathrm{mm}$ from the source. After passing through the target, the x-ray beam propagates through a $250\,\mu\mathrm{m}$ thick polyimide tape, which was the vacuum window. The thickness was thin to reduce the loss of x-rays. The beam then propagated through $2050\,\mathrm{mm}$ of air onto an indirect detection x-ray camera, an *Andor iKon-L 936*. The camera placed at a total distance of $3800\,\mathrm{mm}$ from the source, has a 150 μm thick caesium-iodide

---

[16] [187] M. Stampanoni *et al.* (2006).

[17] [186] S. Kneip *et al. APL* (2011); [188] S. Fourmaux *et al. NJP* (2011).

[18] [189] F. Träger. *Springer Handbook of Lasers and Optics* (2012).

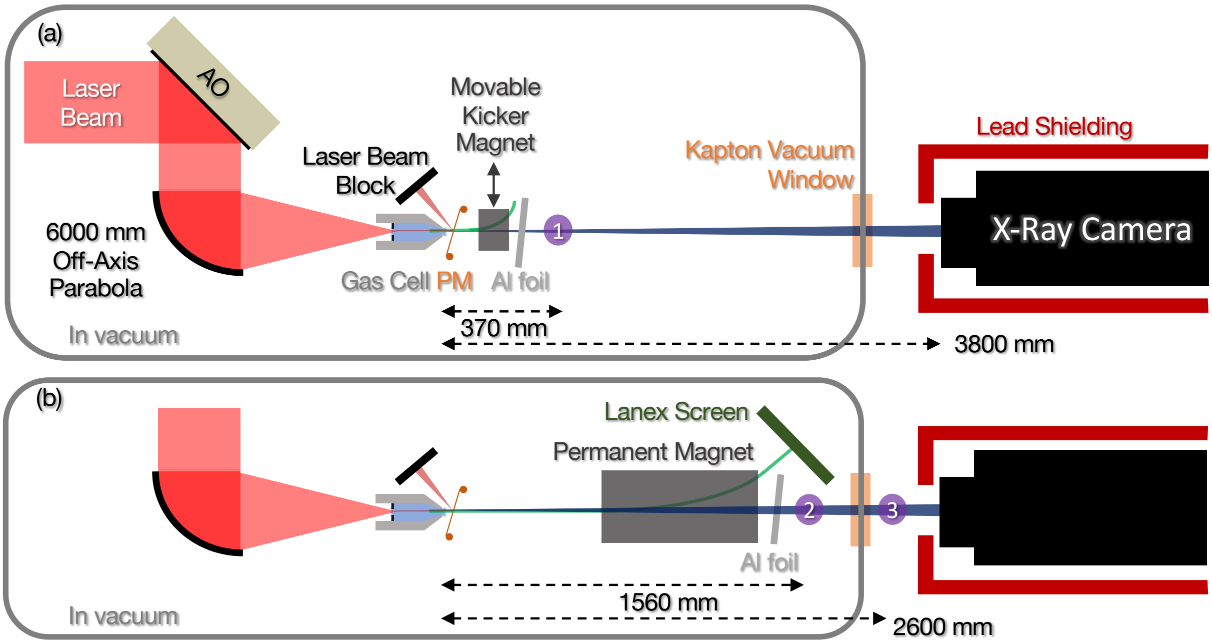

Figure 5.1: The experimental set-up for imaging samples. The laser pulse (red) was focused by an off-axis parabola into a gas cell to accelerate electrons (green), which produced x-rays (blue). Samples were placed as close as possible to the source for a high resolution, (purple **1**), in which case a kicker magnet deflected the electrons off-centre. This kicker magnet was movable and was removed when imaging other samples. A larger permanent magnet with a Lanex screen measured the electron energy (b) while being able to simultaneously take sample measurements with lower magnification. The samples could be placed either in the vacuum or just outside (purple **2** and **3**) depending on their size and magnification requirements. See text for more details.

scintillator fibre-coupled to a 2048×2048 pixel CCD with $13.6\,\mu\mathrm{m} \times 13.6\,\mu\mathrm{m}$. The camera was enclosed in a lead chamber with a small opening on-axis for the x-rays. The lead enclosure was to reduce the noise due to the electrons creating bremsstrahlung and particles showers in the target area.

The second configuration removed the kicker-magnet so that the electron beam enters a larger, well-characterised magnetic field from a set of permanent magnets. The magnet had a maximum magnetic field of $1\,\mathrm{T}$. The electrons were swept vertically onto a Lanex screen, which was imaged with an *Andor Neo* camera. The three components work as an electron spectrometer. A second sample stage inside the vacuum was placed just after the permanent magnet $1560\,\mathrm{mm}$ from the source and the third stage for larger samples was placed just outside the vacuum chamber $2600\,\mathrm{mm}$ from the source. While the sample stage inside the vacuum provided a higher magnification than the stage outside, this last stage had the advantage of quick access and no vacuum compatibility was required.

5.3 X-ray Filter Pack

The concept of retrieving the spectrum from a betatron source was discussed in Sec. 3.3.3. This section summarises the filter pack used in this experiment. The common materials in the beam path during the spectral measurement are summarised in Table 5.1 and the individual filters and their thicknesses in Table 5.2. Fig. 5.2 (a) depicts a radiograph from the filter pack overlapped with the elements in the filter pack. It also shows an image before (a) and after removing noise due to bremsstrahlung as discussed in Sec. 3.3.4.

Beam Path	Thickness $[\mathrm{\mu m}]$
Aluminium foil: Additional light shielding	13
Kapton (C_{22} H_{10} N_2 O_5): Plasma Mirror	25
Mylar (C_{10} H_8 O_4): Mounting substrate for filter	12.8
Kapton (C_{22} H_{10} N_2 O_5): Vacuum window	250
Air: X-rays outside vacuum	2,050,000

Table 5.1: Material and chemical components in the beam path of the x-ray camera. All observed x-rays had to propagate through these materials.

Element	Mo	Sn	Gd	Yb	Ag	Bi	Ag	Au	W	Zn	V
Thickness $[\mathrm{\mu m}]$	50	50	50	50	40	40	20	10	25	5	3

Table 5.2: All the different filters placed as squares in front of the x-ray camera used to reconstruct the spectrum.

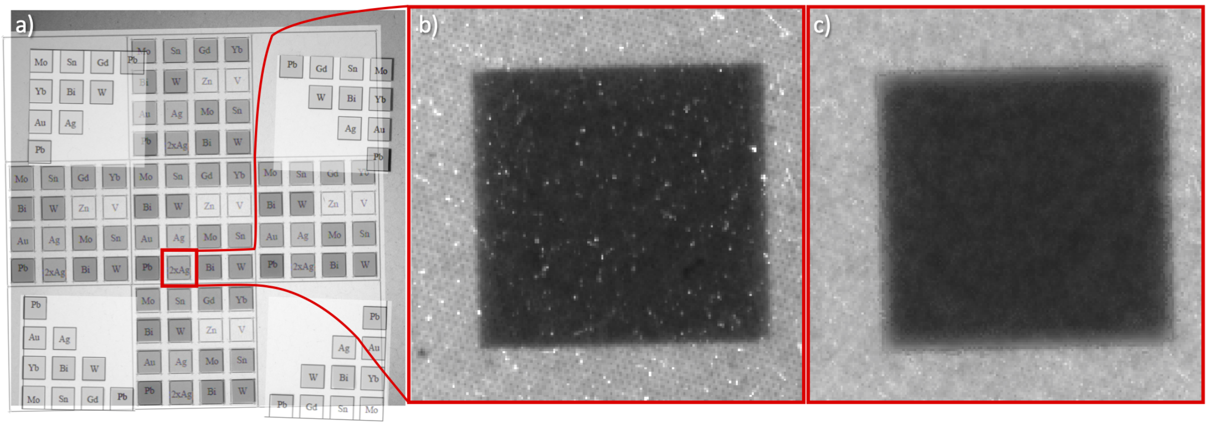

Figure 5.2: (a) A radiograph of the x-ray filter overlapped with the description of the elements used in the filter pack. (b) is a magnification of the central area (marked red in (a)) of an image and (c) the same area after applying post-image processing.

5.4 Optimisation of the X-ray Source

The source was optimised by first changing the focal plane of the laser pulse with the 1st-order Zernicke-polynomial of the AO. Once the laser was focused optimally into the gas cell, the gas pressure inside the cell was varied to optimise the number of counts on the x-ray camera, while the gas cell length was kept at $18\,\mathrm{mm}$. The number of counts indicated the total energy emitted by the electrons under the assumption that the bremsstrahlung does not change its contribution when the electron density is varied.

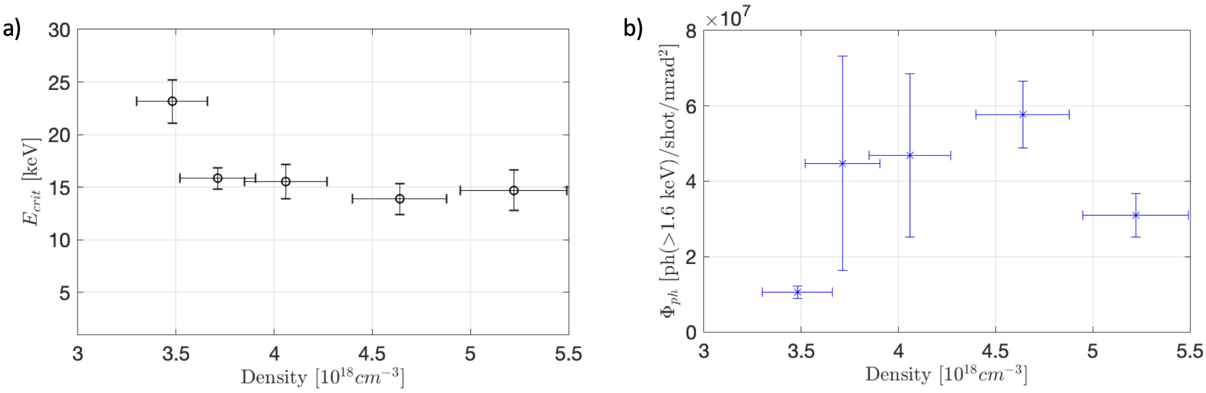

Figure 5.3: The critical energy (a) for different pressures in the gas cell and (b) the resulting photon flux. The unit of the photon flux is explained in Sec. 5.4.

The resulting critical energy for the different densities as well as the photon flux can be seen in Fig. 5.3. Recall that the shape of the synchrotron spectrum only depends on the critical energy, which was described in Sec. 2.11.4. The photon flux is given in number of photons above $1.6\,\mathrm{keV}$ per shot per mrad^2. The threshold of $1.6\,\mathrm{keV}$ was chosen, because Al foil was used to block the laser light and the K-edge of aluminium is at $1.6\,\mathrm{keV}$[19]. Hence, very few photons below its K-edge contributed to the signal on the camera, especially when considering the critical energy, shown in Fig. 5.3 (a), was well above $10\,\mathrm{keV}$.

As seen, there were virtually no x-rays detected below gas densities $3.48 \pm 0.18\,\mathrm{cm}^{-3}$. This lack of x-rays is not surprising considering that no significant accelerated charge was registered below $3.48 \pm 0.18\,\mathrm{cm}^{-3}$. The peak energy and integrated counts on the electron spectrometer camera is depicted in Fig. 5.4. The increase of accelerated charge above this density indicated an increase in injection at around this threshold. Larger critical energies were measured at this threshold density compared to higher densities. However, There is a trade-off with low photon flux. The critical energy does not change within its uncertainty for higher densities, between $3.71 \pm 0.19\,\mathrm{cm}^{-3}$ — $5.22 \pm 0.27\,\mathrm{cm}^{-3}$. Peaking at $3.48 \pm 0.18\,\mathrm{cm}^{-3}$ however, the photon flux does change as seen in Fig. 5.3 (b).

---

[19] [164] B. L. Henke *et al.* (1993).

Fig. 5.5 shows the electron spectra, its estimated peak energy, and corresponding calculated photon flux for each shot. The depicted confidence bounds include the uncertainty of each shot as $\sigma^2_\Phi(n_e) = \sum_i^N (\overline{\Phi(n_e)} - \Phi_i(n_e))^2 + \sigma^2_{\Phi,i}$. This ensures that the uncertainty due to the critical energy is included in the following discussion. It is preferable to keep the critical energy constant for industrial imaging, because a change in that would change the contrast between different materials.

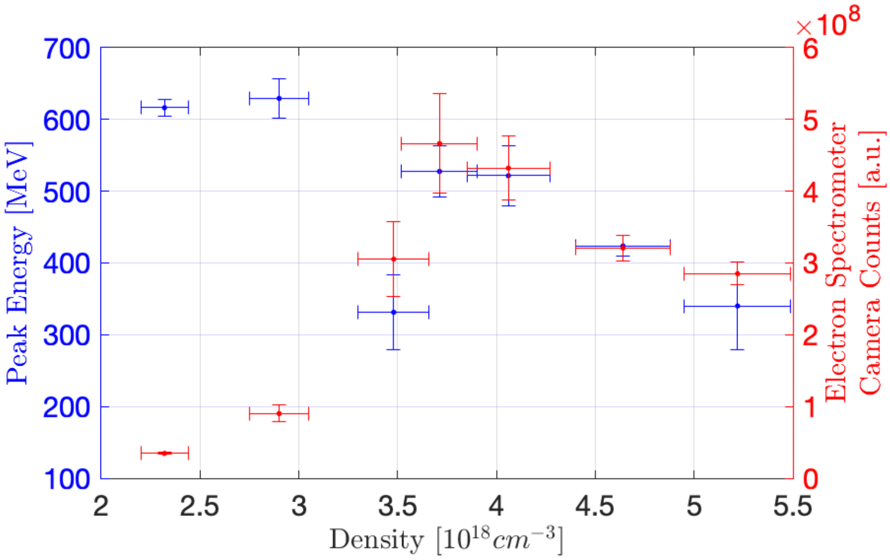

Figure 5.4: Peak electron energy (blue, left) is shown for the density scan and the total integrated charge (red, right) given as the total counts observed from the electron spectrometer camera. The camera was not calibrated during the experiment, but the number of counts should be proportional to the charge impacting the Lanex screen. Note that no x-rays were detected below $3.48 \pm 0.18 \times 10^{18}\,\mathrm{cm}^{-3}$.

The measurements show that while the electron's energy is still low and little charge is injected at $3.48 \pm 0.18 \times 10^{18}\,\mathrm{cm}^{-3}$, a consistent large quantity of charge can be observed at higher densities. Counter intuitively, the charge and also the peak energy for the highest average x-ray flux, at $4.64 \pm 0.24 \times 10^{18}\,\mathrm{cm}^{-3}$, are both lower than they are at lower densities between $3.71 \pm 0.19 \times 10^{18}\,\mathrm{cm}^{-3}$ — $4.06 \pm 0.27 \times 10^{18}\,\mathrm{cm}^{-3}$. Fig. 5.4 shows a summary of the electron spectra, the peak energy (blue) and total charge (red).

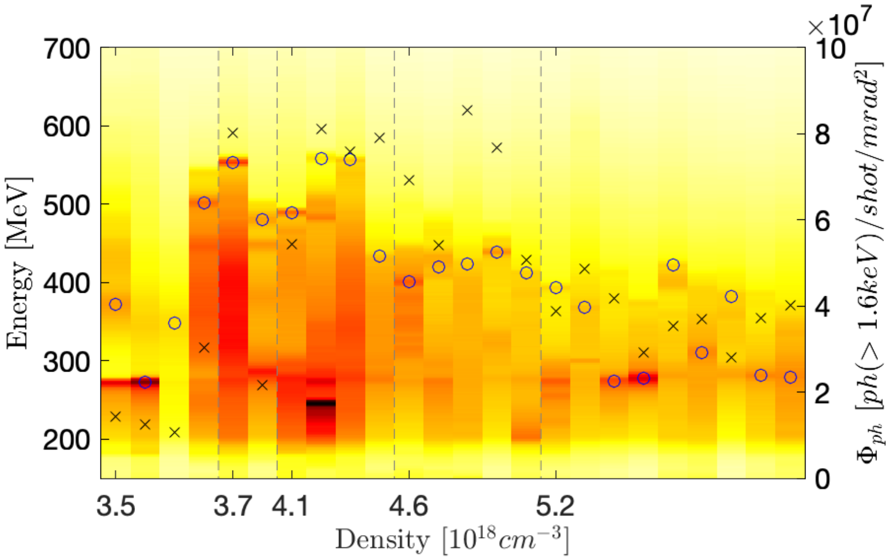

Figure 5.5: Shown in the background are transversely integrated electron spectra for each shot in the density scan. The grey dashed lines indicate shots at the same densities. The blue circles depict the estimated peak energy of the electron spectra at those shots. The black crosses indicate the photon flux from Fig. 5.3.

To relate the x-ray flux with the electron spectrum, the total emitted x-ray energy for a single electron, $E_{e,rad}$ should be considered[20]:

$$E_{e,rad} = \frac{2\pi}{3} r_e m_e c^2 \cdot \gamma^2 \frac{2\pi}{\lambda_\beta} \alpha_\beta^2 N_\beta \tag{5.1}$$

$$\text{with: } \alpha_\beta = \frac{2\pi}{\lambda_\beta} \gamma r_\beta \tag{5.2}$$

$$\text{and: } \lambda_\beta = \sqrt{2\gamma} \lambda_p \tag{5.3}$$

$$\rightarrow E_{tot,rad} = \left(\frac{\sqrt{32}\pi^4}{3} r_e m_e c^2 \right) \cdot \frac{\gamma^{\frac{5}{2}} r_\beta^2 N_\beta}{\lambda_p^2} \propto r_\beta^2 \gamma^{\frac{5}{2}} N_\beta n_e \tag{5.4}$$

In which the radius of curvature of the electron is r_β. The radius depends on the way the electrons are injected and still has not been entirely determined by experiment[21]. The number of oscillations N_β signals the interaction time of the electron with the transverse focusing field. Given the data in Fig. 5.4 only, one would expect more x-ray emission at lower densities as more charge and high energies are present. The reasons why this was not observed are now considered.

Firstly, the electron bunch pointing could be off the x-ray camera, such that the centre of the x-ray beam missed the camera. A quick analysis of the x-ray images

---

[20] [57] E. Esarey *et al. PRE* (2002).

[21] The bunch length has been measured before by using the induced Faraday rotation through the created magnetic field of the electron bunch ([190] A. Buck *et al. Nature Physics* (2011)), but its transverse dimension has not been directly detected.

shows that the predicted centre of the x-ray beam is not fluctuating significantly and so this can be ruled out. It may be worthwhile investigating the electron spectrometer signals individually, which are added in the appendix in Fig. E.2. But the transverse position of the electrons on the screen does not correlate to the x-ray signal either. The observation is not a systematic error of the measurement set-up and must be caused while the electrons undergo oscillations inside the plasma.

Then the question arises what does the number of photons depend on if the critical energy is constant. The number of photons should be proportional to the total energy emitted by a single electron and the charge. According to Eq. (5.1), the total energy depends on the density, n_e, the peak energy of the electrons and oscillation radius of the electrons. If the radius is roughly constant or only slowly varying, the energy and density are the relevant parameters. However, the peak energy of the electron also depends on the density. Thus, one cannot simply increase the density to produce higher photon yield, as the achievable energy is lower due to dephasing. But, the electron energy contributes more to the x-ray flux than the increase through the density. This explains, why the x-ray flux for the highest density is lower but contradicts the fact that fewer photons are emitted for lower densities between $3.71 \pm 0.19 \times 10^{18}\,\mathrm{cm}^{-3}$ — $4.06 \pm 0.27 \times 10^{18}\,\mathrm{cm}^{-3}$ where higher electron energies are recorded. Instead, it might be explained by taking the finite electron bunch length into account.

The irradiated energy in Eq. (5.1) is calculated for a single electron, while the total energy of the radiation has contributions from multiple electrons which are in different phases in the wakefield. If the lower densities optimise the energy of the electron bunch, the centre of the bunch is at its maximum energy gain. Half of the bunch will have dephased and half of the bunch is still accelerating. The bunch is going to be entirely dephased when the density is increased since the dephasing length is decreased. In the case of an entirely dephased electron bunch, each electron has experienced its peak energy inside the wakefield and emitted most of its contribution to the x-rays. Measuring lower peak energy might indicate that more electrons have dephased and emitted more radiation in the process.

Unfortunately, there is one problem with this hypothesis: If the dephasing length is calculated and compared to the constant gas cell length, the dephasing length is lower than the gas cell length for all equations stated in the literature[22], which can be seen in Fig. 5.6. The electron should have overtaken the laser beam long before exiting the gas cell in the current model.

---

[22] Even though the laser pulse should follow the 3D non-linear regime, the 2D non-linear regime and the 1D linear regime are shown to confirm that the gas cell is longer in all cases.

[23] ([36] S. P. Mangles. *CAS-CERN Accelerator School: Plasma Wake Acceleration 2014, Proceedings* (2014))

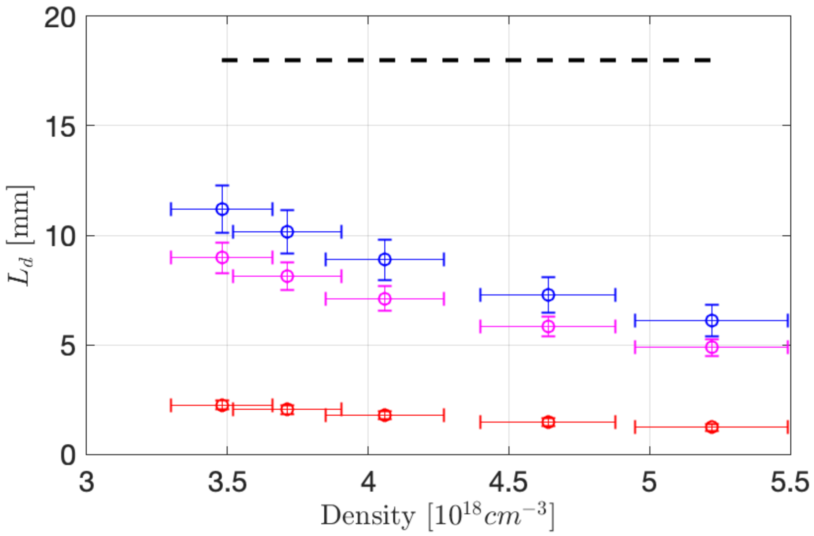

Figure 5.6: Dephasing length for the densities in the x-ray optimisation calculated with different formulas. In blue a simple estimation for a linear wakefield[23] , in magenta for the 1D nonlinear regime by Lu et al. and in red the 3D nonlinear regime from the same work. The gas cell length is indicated with a dashed black line. The initial vector potential of $a_0 > 1$ indicates that the 3D nonlinear regime should apply.

5.4.1 Pre-injection Pulse Evolution with Self-Focusing

One major assumption of the previous discussion is that electrons are immediately injected into the wakefield and accelerated. However, the laser pulse requires some evolution time of self-focusing and -compression before injection starts. This is referred to as *pre-injection pulse evolution* (PIPE) and has recently been the centre of investigations by Bloom et al.[24]. The plasma shapes and compresses the laser pulse thus increasing the normalised vector potential. Although there are some discrepancies in the density and critical energy, the experimental results shown by Bloom et al. are of the same order as the measurements presented here. The deviations are expected as the experiments have some major differences. For one, the gas cell here had a length of $18\,\mathrm{mm}$, while a gas jet was used by Bloom et al., with an estimated constant plasma profile of $8.5\,\mathrm{mm}$ — $13\,\mathrm{mm}$. Furthermore, an $f/20$ off-axis parabola was used compared to the $f/40$ parabola here, which resulted in a much larger focus spot in this experiment.

The PIPE length, L_{PIPE}, depends on the density as higher density accelerates the process inside the plasma and causes the laser pulse to reach equilibrium faster. According to Bloom et al. three cases are to be distinguished. In the first case, the laser pulse is still evolving before the end of the plasma and does not inject any electrons. In the second case, the density is increased and the evolution time/length is decreased,

---

[24] [58] M. S. Bloom *et al*. *PRAB* (2020).

so the laser starts injecting and accelerating electrons. In this case, the pump depletion length and PIPE length is less than the total length of the accelerator and the electron energy is limited by the fraction of how far they proceeded in the accelerating phase of the wakefield. For even higher densities, the last case, the laser depletion length is shorter than the gas cell length, while the PIPE length is short and electrons are injected, meaning the laser depletes before the end of the gas cell and the electrons travel through the cell without a driver.

This model was used to estimate the energies of the electrons and see if the increase in x-ray flux could be explained. However, another mechanism of self-focusing was included by introducing another evolution length, L_{Foc}. The first iteration simplifies the self-focusing and assumes a linear change in spot size scaled to L_{Foc} towards the matched beam size, defined as $\lambda_{p,\mathit{eff}}(z) = \sqrt{a_0}\lambda_p/\pi$[25]. Thus as a_0 changes along the length of propagation, the matched beam size changes and the spot size needs continuous reiteration.

Additionally, some equations used here are more generalised compared to Bloom et al. as non-matched conditions apply, e.g. the normalised vector potential is taken from Eq. (2.23). The essential equations used are seen in Table 5.3. The parameters at the start of the simulation match the experimental laser parameters, explicitly: 32.2%[26] of $7.2\,\mathrm{J}$ in $49\,\mathrm{fs}$ within a beam size of $47\,\mu\mathrm{m}$, injected into a $18\,\mathrm{mm}$ long gas cell.

Mechanism	Equation
Laser Energy Depletion[27]	$\frac{\partial E_l}{\partial z} = -E_{l,0}\frac{n_e}{n_{crit}}\left(E_{max}(a_0,\tau)/E_0\right)^2_{\text{Gauss}}k_p$
Pulse Compression[28]	$\tau(z) \approx \tau_0 - \frac{n_e z}{2cn_{crit}}$
Self-focusing	$\frac{\partial w(z)}{\partial z} = \left(\frac{\sqrt{a_0}\lambda_p}{\pi} - w_0\right)/L_{PIPE}$
Max. Electric Field	$\left(E_{max}(a_0,\tau)/E_0\right)_{\text{Gauss}}$ from Eq. (2.76)
Plasma Wave Wavelength[29]	$\lambda_{p,\mathit{eff}} = \lambda_p\sqrt{a_0(z)}$

Table 5.3: The set of equations used to estimate the energy of the electrons in a wakefield when a PIPE length L_{PIPE} and a focus evolution length L_{PIPE} is included.

The algorithm was iterative and solved the numerical equations with a step size of $\mathrm{d}z = 1/5000$ of the smallest of either the initial dephasing length, pump depletion length or PIPE length. The laser pulse and wakefield parameter, $E_l(z)$, $\tau(z)$ and $w(z)$, were updated at each step. Solely the laser beam propagates through the plasma until its

---

[25] [109] W. Lu *et al. PRST - AB* (2007).

[26] 32.2% in the FWHM instead of 50% as a clean Gaussian beam would enclose. The pulse energy is reduced to effectively $32.2/50 * 7.2\,\mathrm{J} = 4.6\,\mathrm{J}$

position, z, reaches the pre-injection pulse evolution, $z > L_{PIPE}$ at which point a virtual electron is injected at a distance $\lambda_{p,\mathit{eff}}$ behind the laser pulse. The local electric field is calculated by assuming a symmetrical sawtooth field distribution such that the field over the total length of the wakefield can be estimated by,

$$E_{local}(D) = (E_{max}(a_0, \tau))_{\text{Gauss}} \cdot 2\left(\frac{D}{\lambda_{p,\mathit{eff}}(z)} - \frac{1}{2}\right) . \tag{5.5}$$

At injection, $D = \lambda_{p,\mathit{eff}}(z)$, the electrons experience the maximum electric field. The phase is changed at each step by assuming that electrons are moving at the speed of light and the laser moves with $v_{G,\mathit{eff}}$, see Eq. (2.66). If the electrons are in the centre of the bubble, $D = \lambda_{p,\mathit{eff}}(z)/2$, no electric field is present and if the electrons propagate further inside the bubble a decelerating electric field is present. The reason for the introduction of this virtual phase instead of estimating a fixed dephasing length as was done by Bloom et al. is that the plasma wave wavelength, as well as the maximum field strength, can vary with propagation. If the maximum field strength is allowed to vary, then the effective local field on the electron and hence the energy of the electron should be more accurate.

The change of the electron's energy is calculated at each time step by taking the local electric field half a time step before and half a time step after at each time step and multiplying it by the length of a time step. This is effectively a trapezoidal approximation of the change in energy. This process is continued until either the end of the gas cell is reached, the energy of the laser is depleted which is hereby defined as $1/1000$ of the initial laser energy, or until the laser pulse length is nearly singular through compression.

The singularity of the pulse is related to the pump depletion and depends on the etching velocity of the laser, as it is the reason for longitudinal pulse compression. The pump depletion was estimated by the etching velocity in[30]. However, a more accurate and generalised formula from[31] is used here, and is another point over which Bloom et al. and this work differ as well. The minimal pulse length was set to be $5\,\mathrm{fs}$. The algorithm was tested with a lower minimal laser pulse length limit resulting in little difference to the electron energy, because of the time dependence in Eq. (2.76) and the depletion of the laser energy.

---

[30] [109] W. Lu *et al.* *PRST - AB* (2007).

[31] [135] B. A. Shadwick *et al.* *Physics of Plasmas* (2009).

Both, the PIPE length and the self-focusing length are normalised with n_{crit}/n_e in order to reduce the scale length to a density-independent parameter:

$$S_{PIPE} = \frac{n_e}{n_{crit}} \cdot L_{PIPE} \tag{5.6}$$

$$S_{Foc} = \frac{n_e}{n_{crit}} \cdot L_{PIPE} \tag{5.7}$$

The two input variables were varied to minimise the residual sum of squares (RSS) between the peak energy from the experiment and the energy resulting from the algorithm. The result can be seen in Fig. 5.7. The evolution of several parameters of the algorithm computed along the direction of propagation for the two densities $2.32\,\mathrm{cm}^{-3}$ (blue) and $5.22\,\mathrm{cm}^{-3}$ (red) can be seen in Fig. 5.8 .

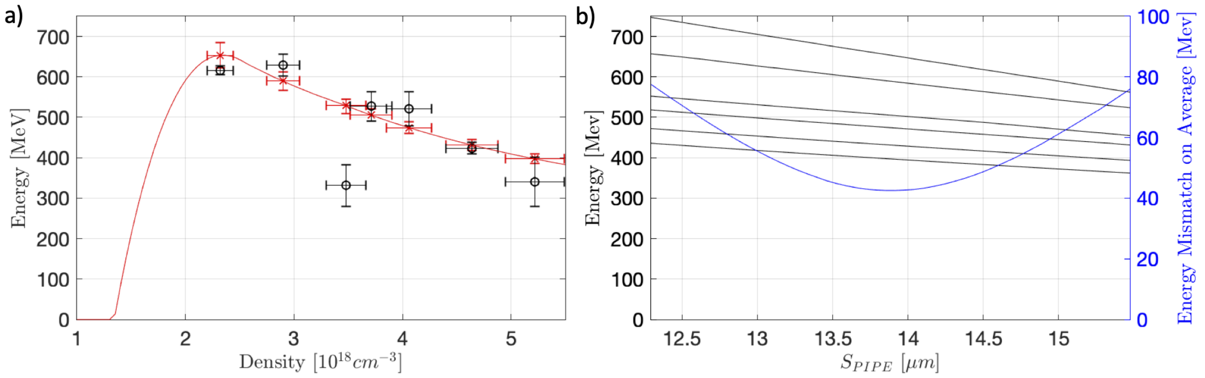

Figure 5.7: (a) The electron energy estimated with the L_{PIPE}/L_{PIPE}-algorithm in red and including the uncertainty at the measured densities. The measured peak energies are shown in black. (b) The energy (black) when changing equally S_{PIPE} and S_{Foc}. The average mismatch from the experimental measurements ($= \sqrt{RSS/N}$) is shown in blue.

The lowest RSS can be seen in Fig. 5.7 b) and was observed for:

$$S_{PIPE} = 13.9 \pm 0.5\,\mathrm{\mu m} \tag{5.8}$$

$$S_{Foc} = 14.3 \pm 0.5\,\mathrm{\mu m} \tag{5.9}$$

The absolute electron energy decreases for an increase in evolution length, because the electrons are injected later and because the laser energy decreases, see Fig. 5.8 (c).

The energy of the electron does fit quite well with the measurements, except at $3.71 \times 10^{18}\,\mathrm{cm}^{-3}$, which is an outlier. It seems surprising that the energy of the laser pulse drops to modestly low values, much lower than the depletion length on its own would allow (as defined by $\partial E_l/\partial z = E_{l,0}/L_{pump}$), while the normalised vector potential still increases and with it, the accelerating electric field. This is due to the decreasing beam size and pulse duration as $a_0 \propto 1/(w(z)\sqrt{\tau})$. The low laser energy is still

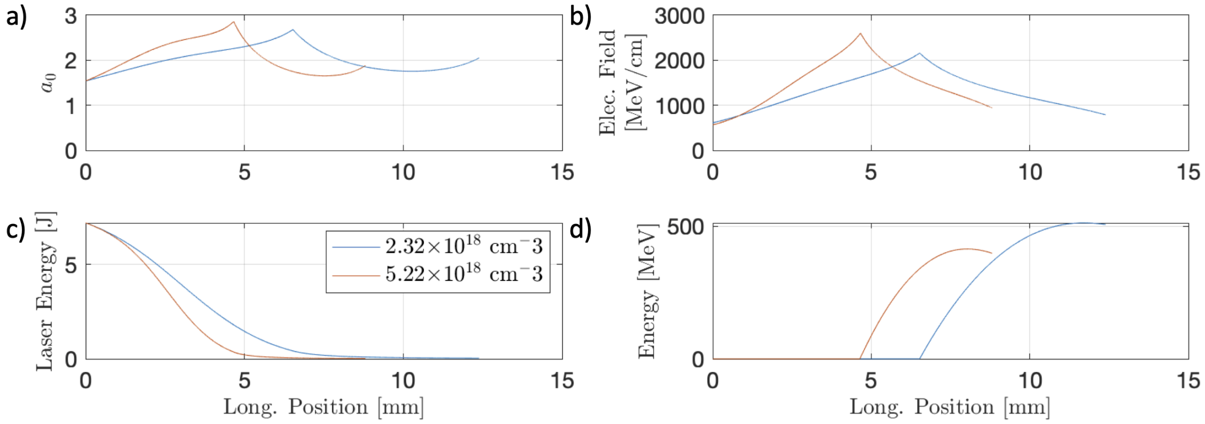

Figure 5.8: The normalised vector potential a_0 (a), laser energy (b), the maximum electric field of the wakefield (c) and the energy of the electrons (d) during the acceleration process including a PIPE and focusing evolution length.The lowest measured density $2.32 \times 10^{18}\,\mathrm{cm}^{-3}$ is shown in blue and highest density $5.22 \times 10^{18}\,\mathrm{cm}^{-3}$ is shown in red.

unexpected but has been reported for small and short laser beams in[32]. Note that in this range of densities, the end of acceleration occurs due to the pulse duration limitation, as was described earlier. Only in the lowest density case, at $2.32 \times 10^{18}\,\mathrm{cm}^{-3}$, is the end of the gas cell reached. The high maximum electric field at the end of the acceleration process is also slightly misleading as the energy curve indicates that the virtual electrons are close to the centre of the bubble, where only a small field is located.

Even though some physics is explained by the algorithm, it leaves two open questions. The rapid increase in charge occurs when this algorithm fails to reproduce the energy of the peak electrons. Although the energy is reproducible at higher densities, the increase of x-ray flux cannot be explained. The energy of electrons for the higher density is overall lower through-out their propagation inside the plasma than for the lower densities. The higher electron energy within the plasma and subsequent dephasing was hypothesised to cause the increased x-ray flux. Nevertheless, the high fluctuation of the flux and the irreproducibility of the energy might indicate another injection process, which might explain the differences in x-ray flux. Due to this, another method in exploring the regime was attempted, by using the simulation code EPOCH to investigates the movement of the electrons inside the plasma.

5.4.2 X-ray Spectrum from Simulations

The electron and wakefield properties in two EPOCH simulations have been investigated. The densities in the simulations were set to $3.7 \times 10^{18}\,\mathrm{cm}^{-3}$ and $4.65 \times 10^{18}\,\mathrm{cm}^{-3}$

---

[32] [191] Z. H. He *et al. NJP* (2013); [33] D. Guénot *et al. Nat. Photonics* (2017); [34] D. Gustas *et al. PRAB* (2018).

to understand the increased x-ray yield at the higher density value. Following from the previous simulations in this work, the resolution of the simulations was fixed at $25/\lambda$ longitudinally and $6/\lambda$ transversely. The number of particles-per-cells (PPC) was increased to 5 PPC compared to previous simulations to provide a smoother density function. The physical parameters follow the previous section, Sec. 5.4.1.

Before presenting the results, note the limitations of simulations due to the chosen limited resolution as discussed in Sec. 3.4. The laser pulse travels with a reduced group velocity through the plasma due to the numerical dispersion, Eq. (3.7). Hence, the energy of the electrons is reduced because the dephasing length is shorter. The time the electrons oscillate inside the wakefield is also smaller than in reality. As the betatron oscillation frequency depends on the electron energy as well, see Eq. (2.87), it varies from the simulation result yet again. Furthermore, the normalised vector potential depends on the intensity, but because the simulations are 2-dimensional, focusing the beam does not increase the intensity linearly as it does in 3D, see Sec. 3.4.2 for details.

These issues question the usage of the simulation. However, the simulations are still of great value: Firstly, the simulations help to identify differences in injection and interaction time between the wakefield and electrons for the two densities. The pulse compression and the focusing length of the laser beam should not depend on the resolution. The time of injection might be different due to the change in normalised vector potential, but the simulation can indicate if electrons are injected at a specific point or if they are injected continuously. The previous model supposed that the electrons were injected after L_{PIPE}. The quantitative impact of the limited resolution is not analysed as it is less important than before with the simulations being performed at much higher densities than the simulations presented previously.

The Injection

The dependence of the electron's energy spectra on their position inside the gas cell for both densities can be seen in Fig. 5.9. The assumption of a single point of injection is invalidated and the energy of the electrons increases and decreases multiple times along the length of the gas cell and new electrons are injected at various points during the simulation. The lower density showed an increase in energy compared to the higher density, which is qualitatively in-line with the experimental observations. However, the electrons do not show a consistent increase and decrease of the energy as one would expect, but the decrease in energy is slower and stops, e.g. see Fig. 5.9 a) at $10\,\mathrm{mm}$. The field strength of the wakefield decreases due to energy depletion and reduction in normalised vector potential. This reduction has also been observed in the PIPE/Self-Focusing algorithm in Fig. 5.8.

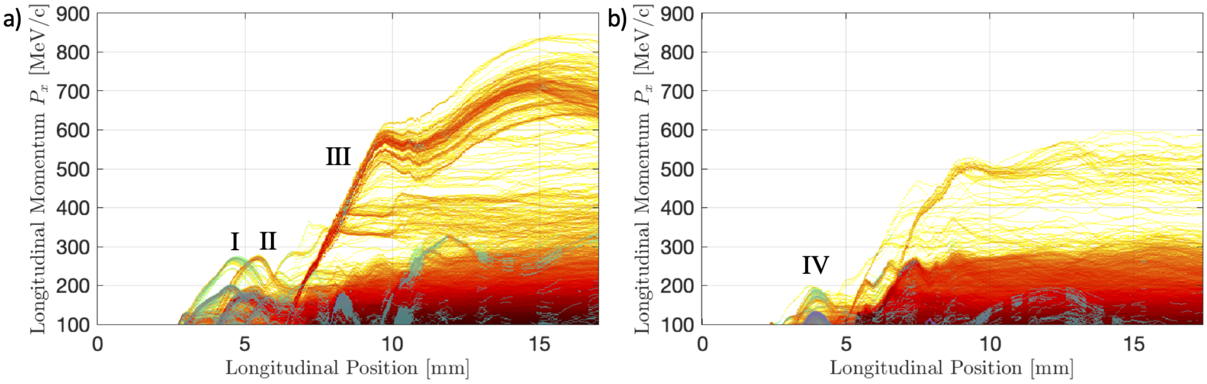

Figure 5.9: The position of the electrons inside the gas cell and their energy spectrum on a logarithmic scale for $3.7 \times 10^{18}\,\mathrm{cm}^{-3}$ (a) and $4.65 \times 10^{18}\,\mathrm{cm}^{-3}$ (b). The electron data depicted with a *cool* colour map (blue/magenta) refers to the electrons considered to contribute to the x-ray radiation, see text for more details. The Latin numerals mark sections of the acceleration process that are explained in the text explicitly.

The electrons undergo multiple acceleration periods and the very first point of injection does not seem to be responsible for producing electrons responsible for the highest measured energy. Nevertheless, when analysing the first batch of injected electrons, the PIPE-length is estimated as

$$L_{PIPE}\left(3.7 \times 10^{18}\,\mathrm{cm}^{-3})\right) = 2.39 \pm 0.54\,\mathrm{mm} \tag{5.10}$$

$$\rightarrow S_{PIPE}\left(3.7 \times 10^{18}\,\mathrm{cm}^{-3})\right) = 5.1 \pm 1.1\,\mathrm{\mu m} \tag{5.11}$$

$$L_{PIPE}\left(4.65 \times 10^{18}\,\mathrm{cm}^{-3})\right) = 2.47 \pm 0.45\,\mathrm{mm} \tag{5.12}$$

$$\rightarrow S_{PIPE}\left(4.65 \times 10^{18}\,\mathrm{cm}^{-3})\right) = 6.6 \pm 1.2\,\mathrm{\mu m} \tag{5.13}$$

The electrons, which peak with respect to their energy before $5\,\mathrm{mm}$ are marked with the *cool* colour map in Fig. 5.9. These electrons are used to estimate the L_{PIPE}. These values are far below the estimated values from the previous section. One could argue in favour of using electrons injected later, which are more greatly accelerated, e.g. marked in Fig. 5.9 a) III, but those electrons are accelerated off-axis. Their trajectories are discussed below in detail.

Laser Properties inside the Wakefield

Laser properties inside the wakefield for both densities (i=1 for $3.7 \times 10^{18}\,\mathrm{cm}^{-3}$ and i=2 $4.65 \times 10^{18}\,\mathrm{cm}^{-3}$) depending on the position inside the gas cell are depicted in Fig. 5.10. The normalised vector potential increases rapidly, beyond the expected value of 3 based on the considerations in the previous section and instead exceeds 4. A reason for this is shown in Fig. 5.10 c.i) in blue, by the transverse beam size. The matched

---

[33] ([100] J. Schreiber *et al. PRL* (2010))

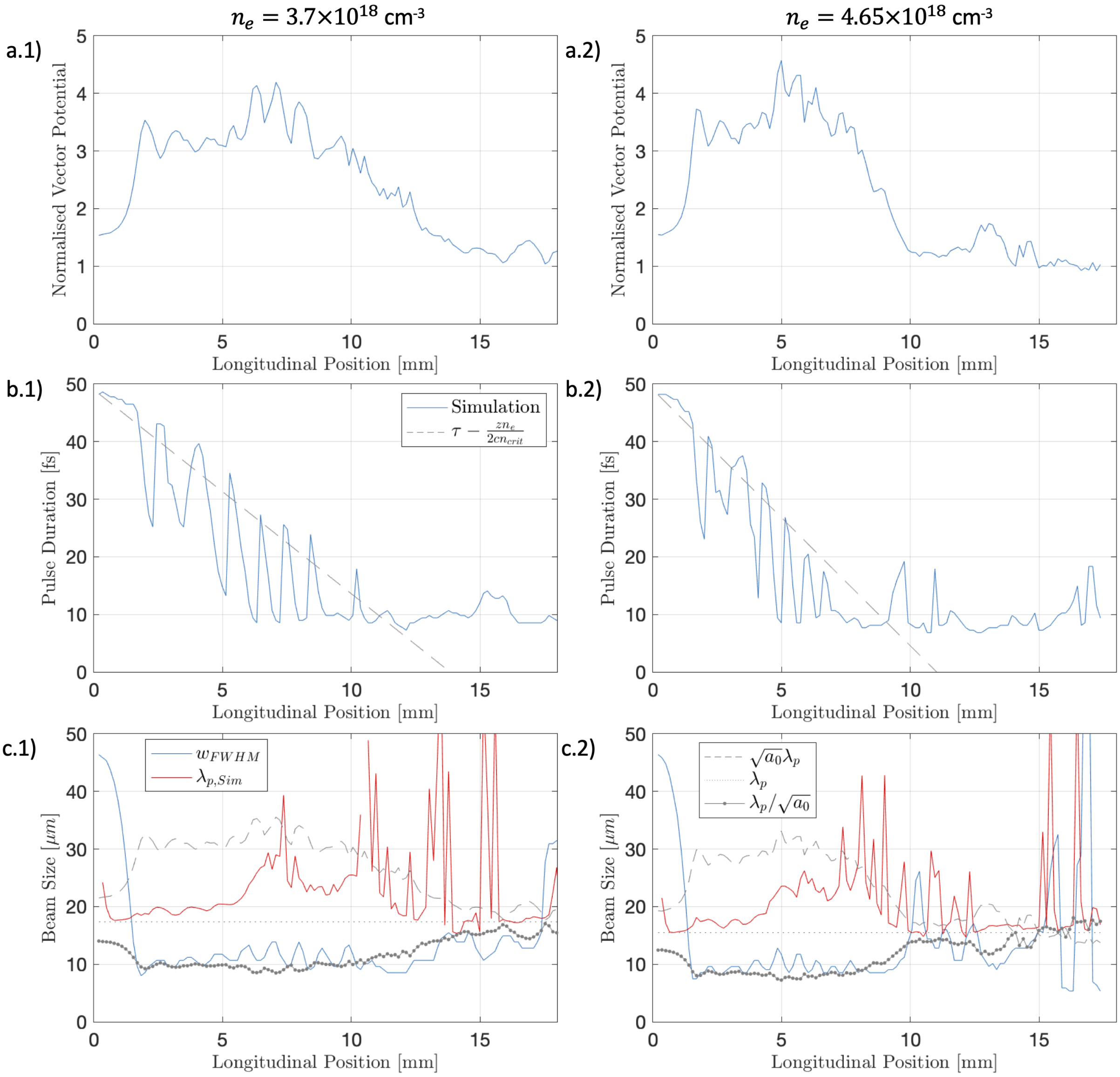

Figure 5.10: The normalised vector potential (a.i), the laser pulse duration (b.i) and the laser pulse beam size (c.i) for $3.7\times10^{18}\,\mathrm{cm}^{-3}$ (i=1) and $4.65\times10^{18}\,\mathrm{cm}^{-3}$ (i=2). The theoretical pulse duration[33] is depicted in (b.i) as a dashed line. The plasma wave wavelength is shown with dots in (c.i), with the effective wavelength found by Lu et al. as a dashed line. The measured wavelength is shown in red and the dashed dotted line follows $\lambda_p/\sqrt{a_0}$ in (c.i).

beam is expected to follow $\lambda_{p,eff} = \sqrt{a_0}\lambda_p$[34], which is shown in the plot as a dashed grey line. However, the beam size is 3 times smaller (blue line) in the simulations. The theoretical plasma wave wavelength λ_p is added as a dotted line along with the measured wavelength in red. The simulated plasma wave wavelength follows the linear plasma wave wavelength at the start of the simulations, but differ later due to the strong focusing of the laser pulse, after which the wakefield structure becomes very irregular.

$\lambda_p/\sqrt{a_0}$ is shown additionally as a dotted line, because it's behaviour seems to

---

[34] [109] W. Lu *et al.* *PRST - AB* (2007).

predict the beam size much better than $\sqrt{a_0}\lambda_p$. Though this might only be true for this density range and not a universal observation.

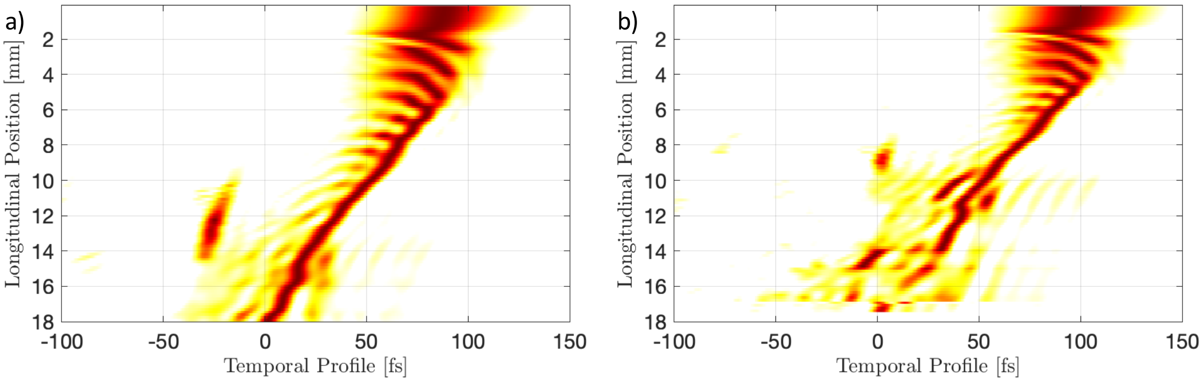

Figure 5.11: The temporal profile on-axis of the laser pulse in simulations for (a) $3.7 \times 10^{18}\,\mathrm{cm}^{-3}$ and (b) $4.65 \times 10^{18}\,\mathrm{cm}^{-3}$. The intensity is normalised at each time step to its respective maximum. As a note, the data in b) after $17\,\mathrm{mm}$ seems perturbed, because the laser pulse is split into many different portions inside the simulation region.

The FWHM of the pulse duration on-axis, shown in Fig. 5.10 b.i), follows roughly the compression estimated by Schreiber et al.[35], but it stops when the pulse reaches $10\,\mathrm{fs}$. This could be used to update the previously developed model in Sec. 5.4.1. Further inspection of the data reveals the bare FWHM of the laser pulse does not capture enough information to tell the whole story. Similar to the mentioned transverse filamentation of the laser pulse, the longitudinal profile splits into multiple pulses as well. Fig. 5.11 shows the on-axis temporal profile for both densities. The oscillating time-dependency, $\cos(kz-\omega t)$, of the laser pulse was removed by using a smoothing filter in the Fourier-domain at frequencies around the laser wavelength. The resulting pulse is the envelope function. As seen, the pulse compresses and the maximum of the pulse slowly moves forward in respect to the theoretical group velocity. But a second local maximum of the laser intensity behind the pulse develops. This phenomenon is based on the temporal-spatial correlation of the laser pulse. The laser pulse splits transversely into several portions as well and some energy circles back from the side into the centre of the wakefield. Effectively, the global maximum of the laser pulse travels forwards and a lower intensity local maximum behind the pulse develops. The second maximum increases in strength while the first decreases until the second maximum becomes the global peak. This procedure repeats several times, which explains the jumps in Fig. 5.10 b.i). A note: One could think that the pulse is modulated with the plasma wave similar to the self-modulating regime, but the distance between the maxima do **not** scale with the plasma wave wavelength, as the pulse is much shorter. However, both simulations show the same phenomena once the pulse length reaches its minimum

---

[35] [100] J. Schreiber *et al. PRL* (2010).

of $10\,\mathrm{fs}$. Another portion of the laser pulse ends up being concentrated on-axis behind the laser pulse later ($> 10\,\mathrm{mm}$ in (a) and $> 8\,\mathrm{mm}$ in (b)) in the simulation. This portion is a plasma wave wavelength behind the laser pulse and its position coincides where the acceleration for the highest accelerated electrons on-axis stops in Fig. 5.9 a) III and Fig. 5.9 b) at the peak of the respective electron spectrum.

Finally, a note on the measured group velocity as it indicates how much the simulation can be trusted in respect to the maximum energy of the electrons at the start of the simulation when the wakefield is somewhat structured. The lower density case yields a group velocity of 0.99974 when normalised to the theoretical group velocity[36]. This would mean that the energy from the simulations would be 90.3% of their expected energy[37]. The difference for the higher density is at a lower level of $0.99988 \rightarrow 96.12\%$. The difference is anticipated because the reduction in group velocity due to the numerical dispersion is the same for both densities, but the physical group velocity is lower for the higher density. So one would expect that the simulations for the higher density predicts reality more precisely.

X-ray Production

All the electrons that are accelerated above $100\,\mathrm{MeV}$ have been tracked during the simulations. And their trajectories have been modelled with sinusoidal functions so that one could estimate their radiation properties. However, the observed wakefield in the simulations were very irregular. Fig. 5.12 shows some example snapshot for both simulations. The laser pulse splits into fragments making the entire acceleration process rather unpredictable after $5\,\mathrm{mm}$. This, however, indicates the strong non-linearity and the complexity of optimising the betatron radiation. One issue is that a lot of electrons are in different parts of the *messy* wakefield and are not captured inside a single bubble to emit continuous radiation. The electrons accelerated beyond $500\,\mathrm{MeV}$ in Fig. 5.9 a) and b) are accelerated sideways off-centre and are not oscillating around an axis. Furthermore, no electrons seemed to have been captured in the first bubble. The simulations did not directly help to decipher the reason why the increased density case showed the highest x-ray yield. It also showed a discrepancy concerning experimental data due to the finite resolution, numerical dispersion, potentially the limitation on the particle-per-cells and simulating in 2D instead of 3D. This was not unexpected and was discussed at the beginning of the section.

---

[36] The group velocity corrected by the non-linear refractive index based on the relative mass increase of the electrons and the etching velocity.

[37] Calculated by estimating the energy reduction due to the decreased dephasing length of $L_d \propto 1/(1 - v_G)$.

Investigating the temporal and spatial focusing of the laser pulse can however be instructive. This is even though the normalised vector potential measured in the simulation will be significantly underestimated as the simulation contain a 2D transverse focusing laser pulse and not 3D. The laser pulse reaches a spot size of $10\,\mu\mathrm{m}$ in these simulations and should enhance the wakefield strength even further in 3D.

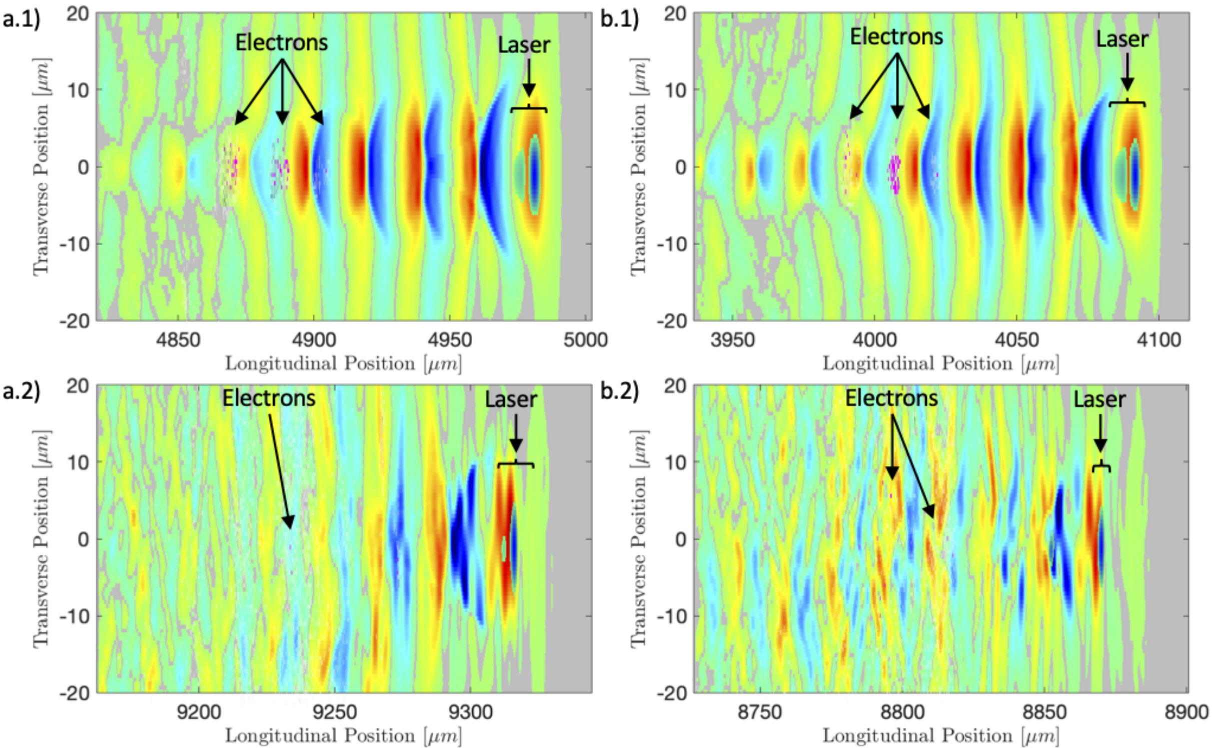

Figure 5.12: Two snapshots of the simulations for $3.7 \times 10^{18}\,\mathrm{cm}^{-3}$ (a.1-2) and $4.65 \times 10^{18}\,\mathrm{cm}^{-3}$ (b.1-2). The snapshots a.1) and b.1) capture the simulation at the first energy peak of the electrons, see Fig. 5.9, and the snapshots a.2) and b.2) around the second higher peak energy, see Fig. 5.9 III. The *jet* colour map refers to the accelerating electric field (background). The *cool* colour map depicts the laser pulse cut off at the FWHM and is annotated. The tracked electrons are shown in a *grey* scale and magenta, if they follow the criteria discussed in Sec. 5.4.2. They are also indicated with arrows and one can see that they do not follow the structure of an electron bunch in a.2) and b.2).

5.4.3 Discussion on Optimising X-ray Yield Based on Betatron Radiation

This chapter has offered many approaches to tackle the question of how x-ray yield depends on the plasma density. Even though previous work has studied this question as well, the dependency on the many variables as laser power, density range and beam size means that further study is necessary. The experimentally evaluated and interpreted data presented here is of help when choosing the right density range for industrial imaging in the following chapter. The explanation of the findings has turned out to be much more challenging and is far from being conclusive. Adding a focusing term in the estimation of the *Pre-injection pulse evolution and self-focusing* algorithm can explain measured electron energy spectra for most densities. However, it fails to give a sufficient answer to the sudden increase of injection and the increase of x-ray yield. More investigation and effort extending the model to estimate the x-ray yield would be helpful. The model assumes a single point of injection and acceleration. This assumption does not seem to be adequate according to the simulations performed in the last section.

The simulation does not reflect the measured data but gives an outlook on what is happening to the laser pulse inside the plasma and how electrons are accelerated. The wakefield structure is irregular. The electrons are not just accelerated once. The electrons are not taking advantage of the high fields in these simulations as well, because they are injected in buckets several cavities behind the laser pulse. The electric fields are much lower and cannot accelerate the electrons to the expected energies. This might be the issue in these simulations as it is not guaranteed that the injection process is fully reflected by the simulation. It also highlights another issue of the simplified acceleration model, because electrons can undergo multiple accelerations and deceleration cycles. This suggests that assuming a monoenergetic electron on a curve being responsible for the betatron radiation is not true and especially the range of energies in the lower energetic spectrum would need correction from the current most-widely assumed model. Luckily, this might not be as pressing as first expected concerning estimating the critical energy in this set-up as the beamline had an Al filter to protect the samples. The lower energy component of the spectrum was filtered out. Secondly, the electron trajectories indicate that around the peak of the electron's energy, the electrons only do a single curvature, because the oscillation period in the simulation is comparable to the acceleration length. This argument is even more relevant when the energy of the electrons is increased further, because of $\lambda_\beta \propto \sqrt{\gamma}$. Therefore, even though the lower energy end of the contribution might feature contributions from a large range of different electron energies and needs an adjustment, the peak electron energy contribution to the radiation is more monoenergetic. The models investigated here do not definitely explain the findings of the experiments, but rather emphasise the complexity of the physics and show that more investigation is necessary.

5.5 Betatron Radiation as an Industrial Imaging Source

The divergence of the x-ray beam ($\sim 10\,\mathrm{mrad}$) allows geometrical magnification. The beamline included three sample stages located at different distances for varying the x-ray field-of-view, as indicated in Fig. 5.1. Samples outside vacuum (position 3) could be positioned anywhere from the rear wall of the chamber to directly in front of the camera. Inside the vacuum chamber, a stage close to the exit window was placed (position 2) yielding a magnification of *M*=2.4, well suited for cm-scale objects. The highest magnification yielded *M*=10.3 with the sample placed 370 mm from the source (position 1). The magnification at position 1 was measured using a JIMA *RT RC-02*[38] resolution target and with a gold grating including a pattern of horizontal and vertical apertures in configuration 2. The image resolution was limited by the point spread function of the scintillator to ($78\,\mathrm{\mu m}$ / *M*)[39].

5.5.1 Optimised X-ray Source

The x-ray source was characterised at the optimum density estimated from the previous density scan of $4.4 \pm 0.4 \times 10^{18}\,\mathrm{cm}^{-3}$ by taking 20 shots. The average peak energy of the electrons was determined to be $435 \pm 7\,\mathrm{MeV}$. The corresponding plasma wave wavelength λ_p implies a maximal x-ray pulse duration $\sqrt{a_0}\lambda_p/c \approx 92 \pm 4\,\mathrm{fs}$, when assuming that the electrons radiated within one plasma wave wavelength with a normalised vector potential of 3 (taken as a maximum from Fig. 5.8). The average critical energy was determined to be $14.4 \pm 1.4\,\mathrm{keV}$ and the number of photons peak at $751 \pm 241\,\mathrm{ph\ \ px}^{-1}$ and average at $618 \pm 340\,\mathrm{ph}$ for the entire beam, with a divergence of $7.6 \pm 0.3\,\mathrm{mrad} \times 5.2 \pm 2.1\,\mathrm{mrad}$. This yields the emitted x-ray flux from the source that peaks at $5.1 \pm 1.7 \times 10^7\,\mathrm{ph\ \ mrad}^{-2}$ per pulse.

By using the Wiggler-strength parameter α_β, the critical energy and the peak energy $\gamma = E/(m_e c^2)$, the radius of the electrons r_β and hence the source size $s_\beta = 2r_\beta$ can be estimated to be (see Sec. 2.11.2 and[40]),

$$r_\beta = \frac{\alpha_\beta}{\gamma k_\beta} = \frac{E_{crit}\lambda_\beta^2}{12\pi^2\gamma^3 c\hbar} = \frac{E_{crit}\lambda_p^2}{6\pi^2\gamma^2 c\hbar}\,, \tag{5.14}$$

$$s_\beta = 2r_\beta = 2.3 \pm 0.3\,\mathrm{\mu m}\,. \tag{5.15}$$

These measurements can be used to estimate the brilliance of the source to be $1.3 \pm 0.6 \times 10^{22}\,\mathrm{ph\ \ s^{-1}\,mm^{-2}\,mrad^{-2}\,0.1\%BW^{-1}}$ in the peak and $1.1 \pm 0.7 \times 10^{22}\,\mathrm{ph\ \ s^{-1}\,mm^{-2}\,mrad^{-2}\,0.1\%BW^{-1}}$ on average[41]. A comparison between other experiments can be seen in Fig. 5.13. Note that the brilliance in that plot is calculated using the laser pulse length and is therefore higher. This was done to unify the way the brilliance was calculated in all of the literature values as has been discussed

---

[38] [192] Japan Inspection Instruments Manufacturers' Association (JIMA). (2012).

[39] [52] J. M. Cole *et al. PRX* (2018).

[40] [57] E. Esarey *et al. PRE* (2002), Eq. 66.

[41] The difference is using the peak of the x-ray beam and using the entire beam with the average photons inside the area.

Sec. 1. The value fits very well in the set of experimental values calculated previously at this facility when correlating the brilliance with the laser power.

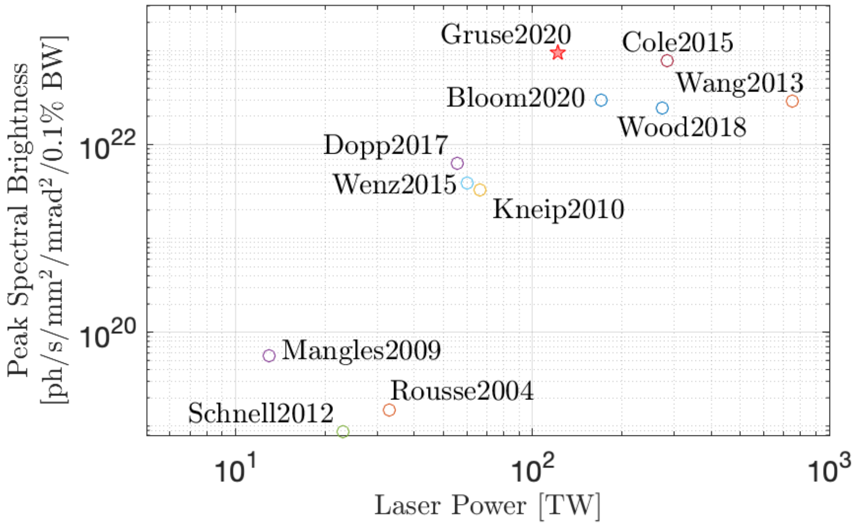

Figure 5.13: The brightness for different experiments from the literature with respect to laser power, as in Fig. 1.5. This experiment (*Gruse2020*) is marked with a red star. The brilliance calculated here exceeds previous measurements performed at this facility[42] . The main difference is the f-number used in this experiment, which decreased the divergence of the x-ray beam significantly.

5.5.2 X-ray Resolution, Contrast and Magnification

Resolution targets were used to determine the possible magnification of the different sample positions. The modulation transfer function (MTF) was calculated depending on the size of the features in the target, which is important to determine what industrial samples can be imaged and what field of view can be achieved. As geometrical magnification is used, the camera chip size and beam size limit the field of view when placing the camera farther from the sample. The sample has to be moved, or the source, which is somewhat more difficult, when imaging at high resolution with high contrast. The contrast is hereby defined as the Michelson-contrast as

$$C = \frac{I_{max} - I_{min}}{I_{max} + I_{min}} \, . \tag{5.16}$$

Details about the MTF, point/edge/line spread function has been discussed thoroughly in previous works, e.g. J. C. Wood 2016[43] and will be summarised only briefly, starting with the concept of resolution. The resolution of a camera is the pixel size as anything

---

[42] ([58] M. S. Bloom *et al. PRAB* (2020); [65] J. C. Wood *et al. Scientific Reports* (2018); [66] J. M. Cole. (2015))

[43] [167] J. C. Wood, PhD Thesis, Imperial College London (2016), Ch. 3.5.6.

smaller is integrated over one pixel. The resolution of the camera would only be that of the imaging system if the object's features could be directly detected without any additional redirection of the light. This is rarely the case.

In the case of the indirect detection camera, light from the individual fibres leak into neighbouring ones, as seen in the flat field Fig. 3.2. The true resolution is the magnification of the imaging system times the resolution of the camera. While this is the fundamental limitation based on the structure of the sensor, the quality of resolution and the capability of resolving small features is furthermore limited by the MTF. The MTF describes how well features of certain sizes, commonly in the unit of line-pair per mm, $\mathrm{lp\,mm^{-1}}$, are transferred onto the detector. Intuitively, larger features with clear edges can be distinguished on an image, whilst smaller features suffer from blurring. The MTF represents the contrast depending on the size of the features. When using a target providing a set of different line pair sizes, one can directly measure the MTF. Another possibility is to measure the edge spread function (ESF), which describes the transition from an infinitely long edge. Its differentiation is known as the line spread function (LSF) and the Fourier-transform is the MTF. This is of vital importance when imaging (industrial) samples as it enables users to choose a minimal magnification of their sample at which the relevant features are resolved while delivering the largest field of view. Note that the MTF and other figures of merits shown here are based on the post-processed image. As the goal is to provide data to potential users after the discussed improvements on the images have been implemented (e.g. noise removal). Hence, the values are significantly better than by J. C. Wood 2016.

Magnification Position 2

The sample stage 2 was placed $1560\,\mathrm{mm}$ from the source with a distance of $2240\,\mathrm{mm}$ to the camera, see Fig. 5.1, yielding a geometrical magnification of ≈ 2.4. However, the exact magnification was measured directly with a resolution target for more reliability. A gold target with different feature sizes ranging from $10.95\,\mathrm{\mu m}$, $23.27\,\mathrm{\mu m}$, $41.1\,\mathrm{\mu m}$, $75.3\,\mathrm{\mu m}$ and $150.1\,\mathrm{\mu m}$ was imaged to find the resolution of the imaging system as well as the contrast, see Fig. 5.14. The resolution yielded $6.6 \pm 0.6\,\mathrm{\mu m\,px^{-1}}$, which corresponds to a magnification of 2.1. The slight differences are acceptable with respect to the uncertainty of the measurements of the distances as the sample position was difficult to access.

To determine a continuous modular transfer function, the edge spread function was taken from the Au target as described in Sec. 5.5.2, which can be seen in Fig. 5.15. A Gaussian function was fitted onto the MTF to determine the continuous values. The MTF leads to a 50% contrast at $12.2\,\mathrm{lp\,mm^{-1}}$ $(81.9\,\mathrm{\mu m})$ horizontally and

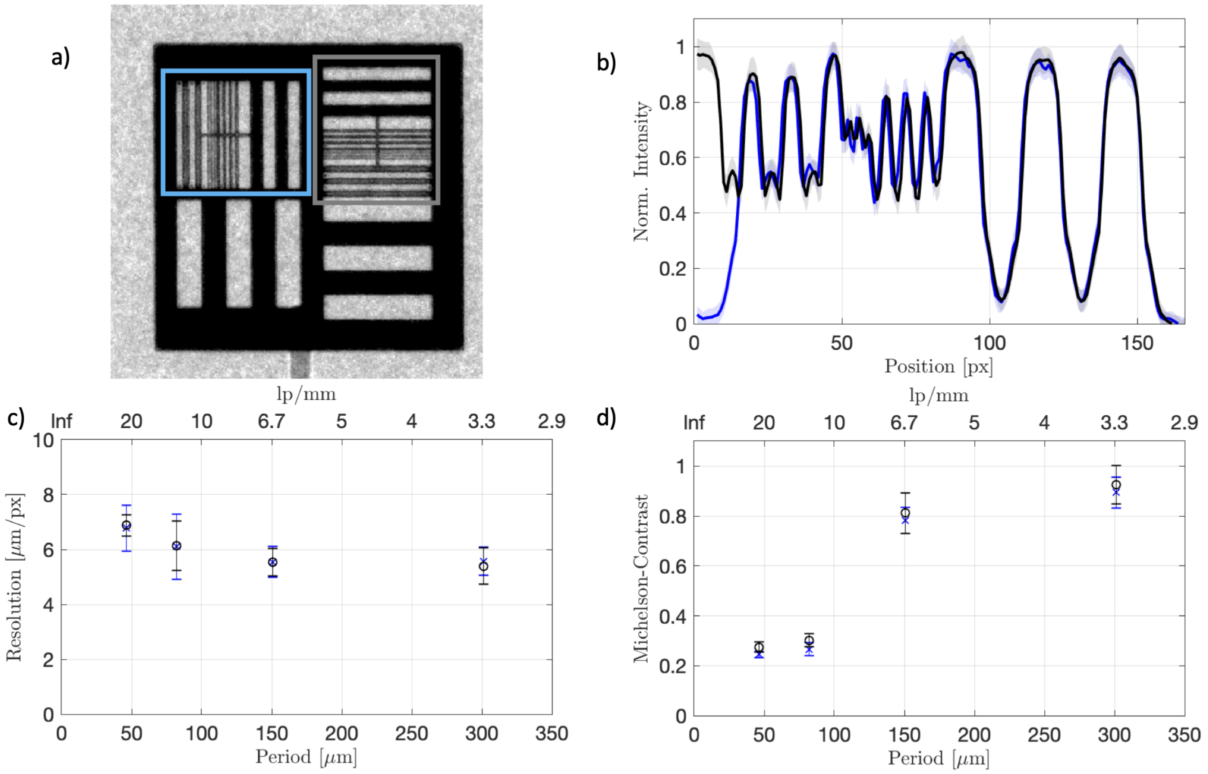

Figure 5.14: (a) Au target with line pairs of different sizes, see sec. 5.5.2 for details. The blue/black rectangle shows the line pairs used for the horizontal/vertical measurements. (b) The normalised average intensity outline. The $150.1\,\mu\mathrm{m}$ features are missing as they are so large that they would dominate the plot. (c) The calculated resolution for the different line pairs. (d) The contrast is calculated from Eq. (5.16).

$13.2\,\mathrm{lp\,mm^{-1}}$ $(75.8\,\mu\mathrm{m})$ vertically and a 10% contrast at $40.4\,\mathrm{lp\,mm^{-1}}$ $(24.7\,\mu\mathrm{m})$ horizontally and $44.4\,\mathrm{lp\,mm^{-1}}$ $(22.6\,\mu\mathrm{m})$ vertically. Having 10% contrast is probably the limitation of what one can resolve confidently, and indeed the smaller line pairs of the Au target in Fig. 5.14 (a) have a period of $10.95\,\mu\mathrm{m}$ and are barely visible. The measurement seems to be slightly better than the resolution limit of the scintillator, which was as mentioned before ($78\,\mu\mathrm{m}$ / *M*)[44], yielding here $\approx 37\,\mu\mathrm{m}$. Better resolution at this stage could be achieved using thinner scintillators, which would mean changing the fibre optical plate (FOP).

To measure individual carbon fibres, which differ in diameter depending on the method of production, one has to resolve $10 - 15\,\mu\mathrm{m}$ mesophase carbon fibres or $5 - 7\,\mu\mathrm{m}$ Poly(-acrylonitrile) (PAN) carbon fibres[45], which here, would have a contrast of less than 3% ($> 0.5\%$ for $> 10\,\mu\mathrm{m}$) and so would be marginally useful. To reach such a resolution, sample position 1 would have to be used.

---

[44] [52] J. M. Cole *et al. PRX* (2018).

[45] [193] K. Acatay. 2017.

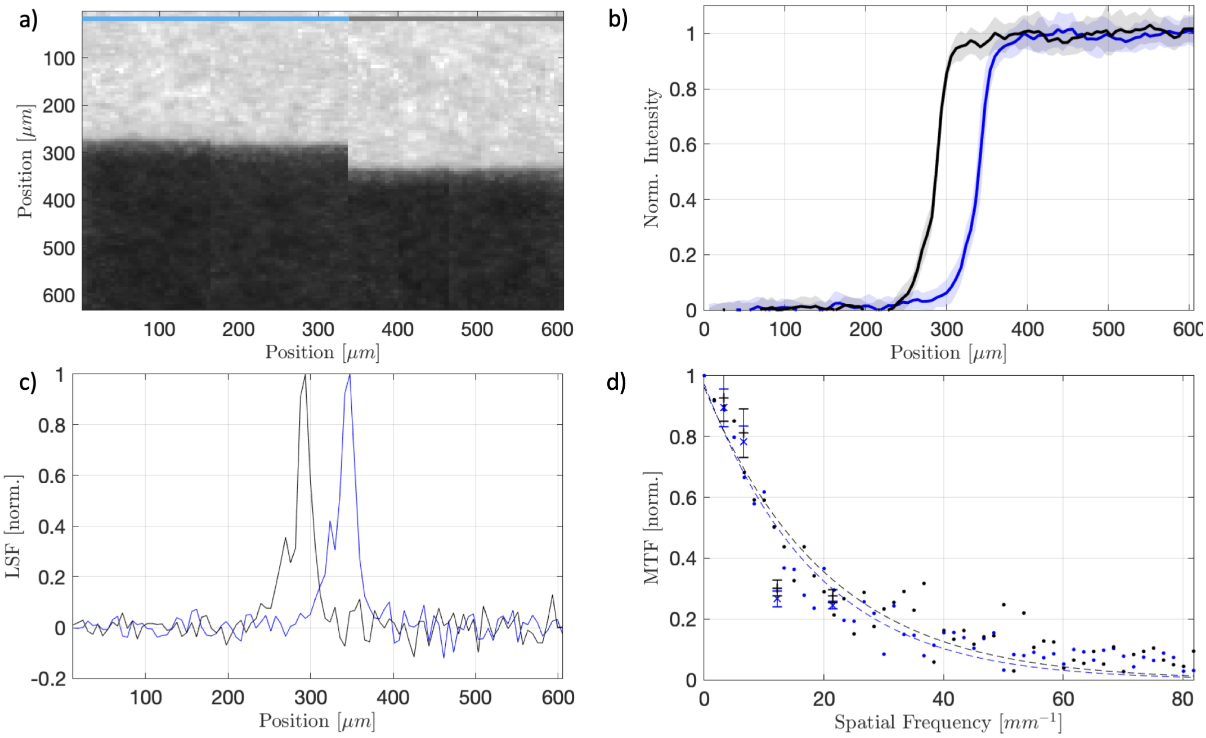

Figure 5.15: (a) The edges from the Au target used for the ESF (b). Blue for the horizontal and black for the vertical measurement. The differentiation of (b) results in the LSF (c), of which the Fourier transform contains the MTF (d). The direct measurements from Fig. 5.14 (d) are added as well as a Gaussian fit to the data (dashed lines).

Magnification Position 1

The highest magnification position was achieved by placing the sample $370\,\mathrm{m\,m}$ from the source, yielding a geometrical magnification of 10.3. Fig. 5.16 (a) shows a JIMA *RT RC-02*[46] high resolution grid and $5\,\mu\mathrm{m}$ slits are easily distinguishable. The $4\,\mu\mathrm{m}$, $5\,\mu\mathrm{m}$ and $15\,\mu\mathrm{m}$ slits were used to estimate a resolution of $1.23 \pm 0.13\,\mu\mathrm{m\,px}^{-1}$. The MTF was not calculated as the sample had no fully absorbing features. The slits were composed of $1\,\mu\mathrm{m}$ of tungsten alternating with $1.1\,\mu\mathrm{m}$ silicon dioxide (SiO_2) on a $60\,\mu\mathrm{m}$ silicon layer. When calculating the energy deposition difference per pixel, it yields $0.5\,\mathrm{keV\,px}^{-1}\,\mathrm{ph}^{\ -1}$ or $0.114\,\mathrm{counts\,px}^{-1}\,\mathrm{ph}^{\ -1}$, which means here $87.4 \pm 28.2\,\mathrm{counts\,px}^{-1}$. This difference is quite small.

Three phenomena are occurring here and need to be kept in mind when imaging larger samples.

Firstly, the $5\,\mu\mathrm{m}$ slits are of sharp quality whereas the $10\,\mu\mathrm{m}$ slits seem to have more blurring. This is because of the longitudinal extent of the source. The source remains

---

[46] [192] Japan Inspection Instruments Manufacturers' Association (JIMA). (2012).

a point source on-axis, but going off-axis, the sample sees effectively an increase in size source, hence the blurring.

Secondly, Fig. 5.16 (b) demonstrates that the image of a stationary sample and detector depends on the pointing stability of the source. Only the angle of the source was changed in (b.2) compared to (b.1) and the image position on the detector changes. Hence, the correlation coefficient of multiple images needs to be maximised while changing their overlaying pixel relative to each other. Practically, one image is fixed and a small cutout with prominent features are taken. Another cutout is taken from a secondary image and the correlation coefficient is calculated. The secondary cutout is then shifted by a single pixel and the procedure is repeated. This has to be repeated until the global maximum of the correlation coefficient is found at which point the images can be averaged. 5 images were taken to produce the data shown in Fig. 5.16 (a).

Lastly, one qualitative observation can be made by investigating the vertical vs horizontal sharpness of the $4\,\mu\mathrm{m}$ slits. Note, that the grid was rotated by 90° and thus the lines in the image going from the top to bottom were horizontal in the experiment. The laser pulse had a horizontal polarisation as well and as the horizontal $5\,\mu\mathrm{m}$ slits in Fig. 5.16 appear sharper, one can infer a smaller source size vertically than horizontally.

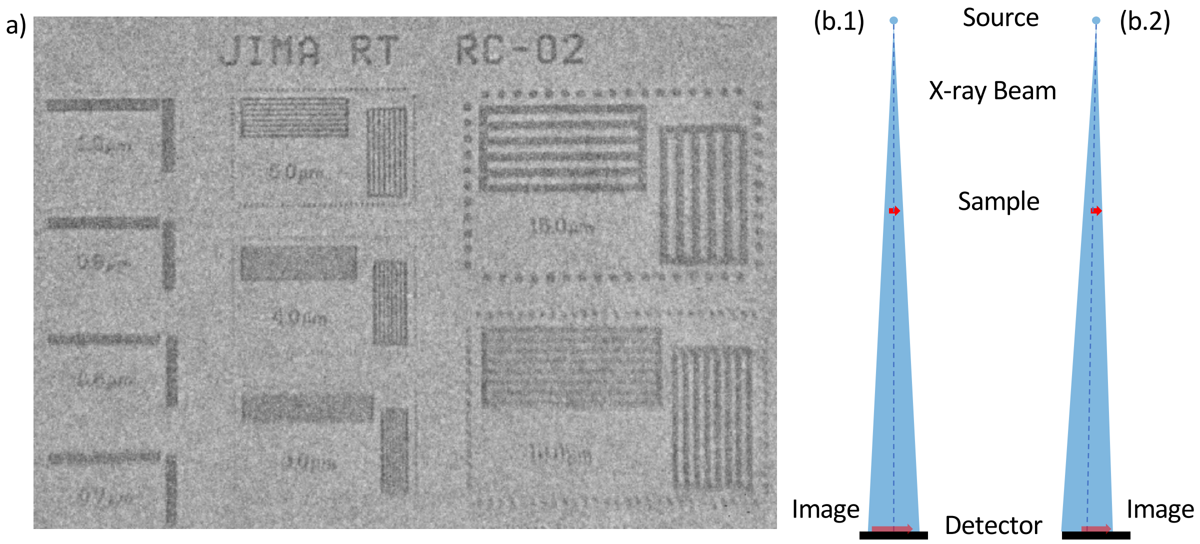

Figure 5.16: (a) The JIMA resolution grid imaged at the highest magnification position. $5\,\mu\mathrm{m}$ slits are clearly visible. The blurring is explained in Sec. 5.5.2. (b) When the sample is close to the source, the pointing stability changes the position of the image on the camera, meaning that when averaging over many shots, the individual images have to be correlate to one another.

5.5.3 Industrial Applications

The images presented in Figs. 5.17 and 5.18 were obtained with the samples placed outside the vacuum chamber with a magnification of M=1.5 at the sample position 3. The sample shown in Fig. 5.19 was imaged at position 2, Sec. 5.5.2. Note, that the 3D rendering data was provided by the co-authors from[47] and adapted to fill this context. Furthermore, the following sections are summaries of the industrial applications rather than the full content for which the reader is referred to the same publication.

Dimensional XCT

To ensure that industrial components meet the required standard for their usages, they need to be accurately measured. This is especially important for additive manufacturing (AM) as these can contain more sophisticated structures than traditional parts. The industrial research community is in search of a definition of an industry-standard [48].

Measuring samples with typical XCT machines have several possible errors based on the operator selected parameters, the alignment of the sample compared to the x-ray beam and even the environment in which the sample is tested[49]. Post-acquisition, the typical *Feldkamp-Davis-Kress* algorithm (FDK)[50] reconstruction introduces further error, including approximations of a small cone-beam. Several attempts have been made to decompose the severity of various parameters[51]. Additionally, round-robin tests have been made by changing the machine and locations for the same measurements[52].

To analyse the performance of a source to image different geometries such as cubes and spheres each with varying dimensions, a topological sample has been created by WMG and a 3D render with a conventional XCT machine is shown in Fig. 5.17 (a). A radiograph with the LPWA source is depicted in Fig. 5.17 (b). This experiment did not have enough time to produce a full tomographic scan due to the limitation of the repetition rate of the laser, $0.05\,\mathrm{Hz}$. However, the radiograph shows sharpness. The laser-betatron x-ray beam is much more colinear compared to the conventional machines, which reduce the errors introduced through the FDK algorithm.

---

[47] [183] J.-N. Gruse *et al. NIMA* (2020).

[48] `amnationalstrategy.uk`

[49] [194] J. P. Kruth *et al. CIRP Ann.-Manuf. Techn.* (2011).

[50] [195] L. A. Feldkamp *et al. J. Opt. Soc. Am. A* (1984).

[51] [196] R. Schmitt and C. Niggemann. *Meas. Sci. Technol.* (2010); [197] J. Kumar *et al. Meas. Sci. Technol.* (2011); [198] P. Müller *et al. IJMQE* (2012); [199] J. Hiller *et al. Meas. Sci. Technol.* (2012).

[52] [200] S. Carmignato. *CIRP Ann.-Manuf. Techn.* (2012); [201] J. A. B. Angel *et al. APA* 2013; [202] A. Townsend *et al. Addit. Manuf.* (2018).

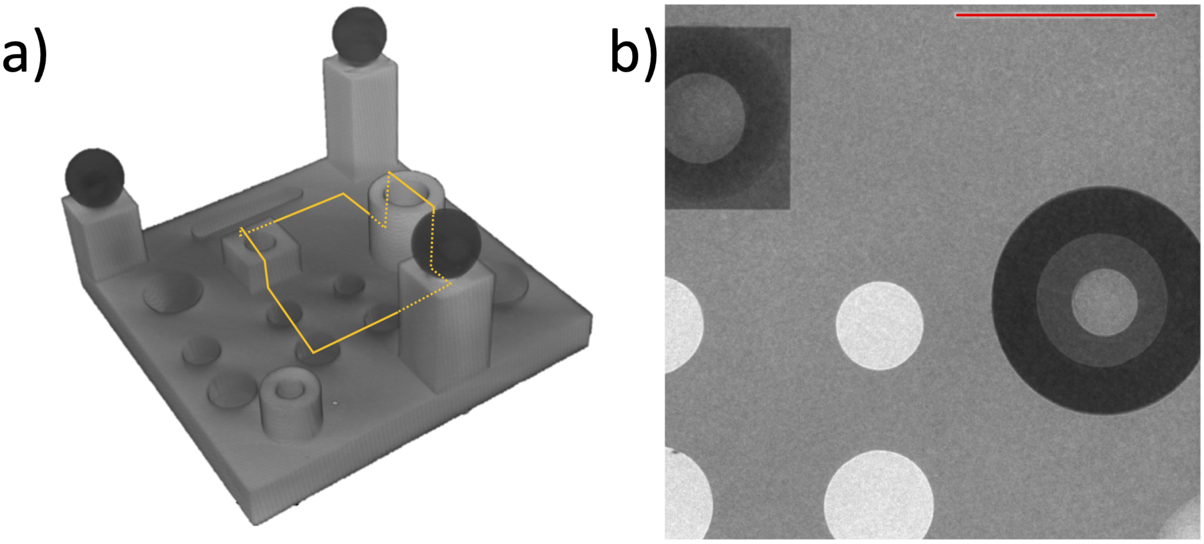

Figure 5.17: Plastic test object with varying sphere diameters, external/internal diameters of cylinders, and plane to plane distances produced for XCT performance verification. (a) tomographic reconstruction using conventional lab x-ray CT (b) radiograph of the test object obtained with the laser-betatron source. The red line indicates 1 cm and the orange rectangle the field of the radiograph.

Battery technologies

To reduce the carbon foot print, the world needs to transition to carbon-neutral technologies[53]. This includes an increase in the efficiency of electric batteries, which require innovation of designs. Prototyping new designs of Li-batteries require a reliable way of identifying a defect in the manufacturing to ensure their quality and safety[54]. A different issue arises here because one produces 6-10 cells per minute and a high-speed scanning solution is desired.

The laser-betatron source is well suited to provide rapid NDE of battery components, as shown by the example image of a pouch cell in Fig. 5.18 (b). Pouch cells consist of a gel layer, alternating between the cathode and anode layers. The electrodes must be sufficiently separated with no contact between them to avoid shorting and can also suffer from other manufacturing defects such as delamination. These individual layers can be observed in a full tomographic reconstruction such as the one shown in Fig. 5.18 (a) and indications of these layers can be also seen in the radiograph, Fig. 5.18 (b). Another potential site for quality issues is the tab area visible at the top of the battery. This region is checked as part of a typical inspection process because poor welding of the tabs to the anode and cathode can result in a defective cell. The radiograph, centred on the tab area, highlights the quality achievable with the laser-betatron source.

---

[53] gov.uk/government/publications/clean-growth-strategy

[54] [203] M. Loveridge *et al. Batteries* (2018).

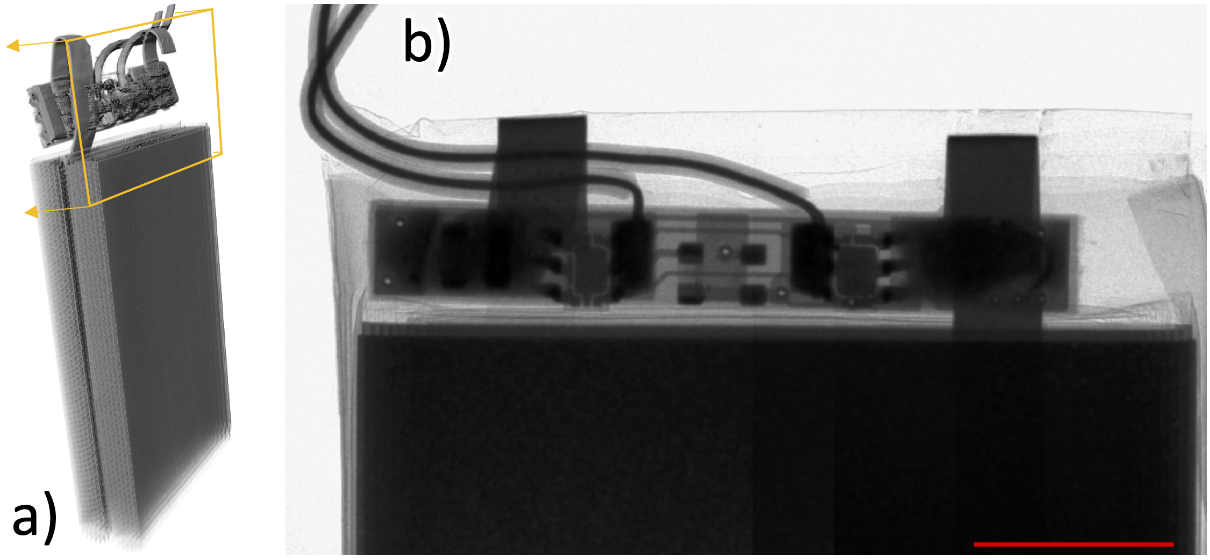

Figure 5.18: (a) Tomographic reconstruction of a pouch cell obtained using conventional lab x-ray CT. Manufacturing defects can occur such as delamination of layers, improper electrode attachment, and poor welding in the tab area highlighted (b) Front view radiograph of the tab area obtained with the laser-betatron source. The red line indicates 1 cm.

Improvements in laser repetition rate will also enable *operando* XCT and time-resolved x-ray absorption spectroscopy (XAS) to examine the activity of battery cells during charge cycles. These methods allow visualisation of the changes in microstructure[55] and mapping of lithium concentration[56], important for understanding battery degradation. Laser-betatron XAS measurements with $<100\,\mathrm{fs}$ temporal resolution have already been reported[57], demonstrating the suitability of the source for this application.

Composite manufacturing

To meet the huge rise in demand for composite products over a broad range of industries, it is essential to increase rates and efficiency in composite manufacturing[58]. NDE is commonly used to assess design features, test manufacturing methods, and inspect the effects of mechanical testing and damage that has occurred over the service life of a part[59].

A major concern is the evolution of defects during manufacture. To be able to understand their formation, it is important to conduct *in-process* XCT to track individual features over time. Gaps in between carbon fibres resulting in defects of the samples affect the mechanical properties. The evolution of how precisely these defects develop

---

[55] [204] M. Ebner *et al. Science* (2013); [205] P. Pietsch *et al. Nat. Com.* (2016).
[56] [206] L. Nowack *et al. Scientific Reports* (2016); [207] J. Wang *et al. Nat. Com.* (2016).
[57] [185] B. Mahieu *et al. Nat. Com.* (2018); [70] B. Kettle *et al. PRL* (2019).
[58] `compositesuk.co.uk/about/industry/uk-composites-strategy`
[59] [208] S. C. Garcea *et al. Composites Science and Technology* (2018).

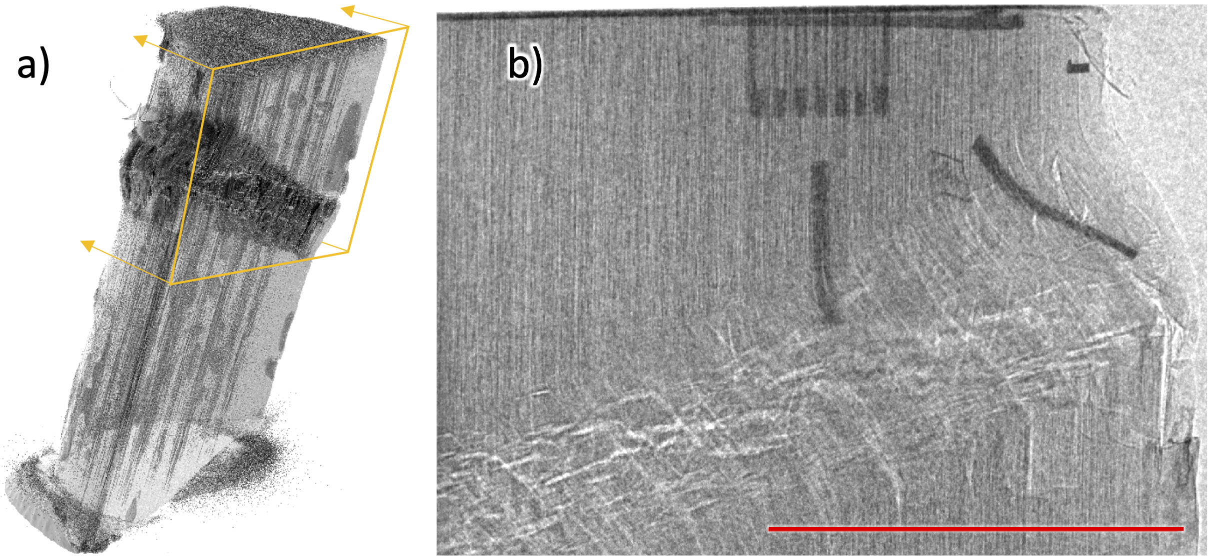

Figure 5.19: Kink band failure in a composite cylinder initiated by impact and propagated by compressive end loading. (a) tomographic reconstruction obtained using conventional lab x-ray CT (b) radiograph obtained with the laser-betatron source with carbon fibre tows visible. The red line indicates 1 cm.

can only be understood by in-situ studies, while partially cured samples seem to not to develop the same properties as shown by[60] and[61]. An issue arises when trying to scan with high resolution as the scan times can be beyond several hours. Synchrotron imaging can be used for fast scanning with mechanical tests as compression[62] of the uncured composite but is impractical for regular use by industrial composite manufacturers because of availability and costs.

These problems could be overcome by employing laser-driven x-ray sources. As an example, we show in Fig. 5.19 (b) a radiograph, obtained with the laser-betatron source, of a composite test sample. This was a cured cylinder made up from an array of small diameter unidirectional IM7 carbon fibre reinforced epoxy resin matrix rods, embedded in a second epoxy resin. XCT is used to assess the effect of a kink-band failure, which was initiated by compressive end loading. This is visible in the tomographic reconstruction shown in Fig. 5.19 (a). The radiograph exhibits good contrast between the carbon fibre and the resin, highlighting the benefit of the x-ray phase enhancement produced with the laser-betatron source. The layers visible in the image are carbon fibre tows that typically have a diameter of order $200\,\mu\mathrm{m}$. Development of this technology to deliver fast scanning at high resolution would address larger-scale challenges, such as inspecting full-scale parts while applying heat, vacuum and/or pressure to the part. In this way, quality assurance and control could be performed before the heat and pressure is applied to cure the resin, reducing scrap, and saving energy, cost and time.

---

[60] [209] L. R. Pickard *et al.*, Proceedings (2017).

[61] [210] L. R. Pickard, PhD Thesis, (2019).

[62] [211] D. F. Sentis *et al. Composites Part A: Applied Science and Manufacturing* (2017).

5.6 Discussion

The improvement of betatron radiation through a density scan has been discussed. The increase in x-ray flux was found to show major differences to electron beam energy and charge measurements. An adapted method for simulating the maximum electron energy through a pre-injection pulse evolution has been applied, which included the evolution of the transverse beam size. While the energies of the electrons have been found to fit well with the developed model, a secondary stage of injection seems to occur. This has not been fully investigated but will be considered in the future. The model also failed to explain the increase in betatron radiation but does indicate that understanding the mentioned second stage might be essential. The PIC-simulations indicated a different limit of the transverse pulse compression. The oscillating pulse length was also a feature not considered before and it could update the proposed model as well. The energy of the electrons did no fit with the measured energies, which was expected, because of the numerical dispersion. An opportunity would be to choose another simulations code to overcome the limitations on the numerical dispersion. FBPIC is a particle-in-cells code solving Maxwell's equation in a cylindrical grid in the spectral phase using decomposing the laser pulse into a set of finite azimuthal modes. As the solutions of the equations in the spectral space are analytically, the code is practically dispersion-free[63]. A simulation including particle tracking with a similar analysis as presented in this chapter could produce valuable insights and clear some pressing questions.

The achieved spectral brilliance in these experiments fits well with previously reported values and its usage for industrial imaging has been proven to be promising for a variety of samples. The possible high magnification has not been taken advantage off yet, but resolution targets of down to $4\,\mu\mathrm{m}$ have been imaged.

Laser-based radiation sources produced with a plasma accelerator have ideal properties for addressing challenges for NDE of industrial samples. Recent improvements in reliability and repetition rate of high power lasers make it feasible to produce these compact x-ray devices for commercial deployment in industrial environments. At the laser energy used here of 7 J (125 TW laser power), commercial products are available operating at 5 Hz (e.g. Thales *Quark200*; Amplitude *Pulsar*) and would increase the average x-ray flux to above $10^{11}\,\mathrm{ph\,s^{-1}}$. Using diode-pumped solid-state technology the repetition rate could be scaled up further[64] and[65]. Improvements in x-ray beam consistency have been demonstrated by reducing pulse-to-pulse fluctuations in the laser and gas target performance[66] and through studies of the stability of electron injection

---

[63] [108] R. Lehe *et al. Comput. Phys. Commun.* (2016).

[64] [212] P. Mason *et al. Optica* (2017); [213] L. Gizzi *et al. NIMA* (2018).

[65] [214] C. L. Haefner *et al.*, Proceedings (2017); [215] W. P. Leemans, Proceedings (2017).

[66] [216] N. Delbos *et al. NIMA* (2018).

mechanisms into the accelerator[67]. One of the benefits of adopting laser-driven technology is the ability to drive different, synchronised secondary sources with the same laser.

An important consideration is the radiation shielding necessary for the electron beam. In an industrial environment, this could be constructed in a similar way to free-electron laser and synchrotron facilities where the electron beam is deflected into a heavily shielded beam dump in the ground while the x-ray beam propagates into an end-station with relatively light shielding.

Although a product based on this technology would be more costly and complex than conventional x-ray machines, it would offer advanced NDE tools that are currently not available in industrial or lab-based settings. In particular, micron-scale resolution tomography with fast scan speed, and ultrafast x-ray absorption spectroscopy could be applied to in-situ inspection and product development. One can imagine that a composite sample, which is curing in an oven can be imaged through a thin temperature resistant windows with such a low divergent x-ray beam as is available here. The curing process and development of artefacts can be observed directly.

---

[67] [62] A. Döpp *et al. Light: Science & Applications* (2017).

Chapter 6

Machine Learning on Enhancement of X-ray Yield of Betatron Radiation at Low Power Systems

The importance of betatron radiation has been widely discussed in this work. The generation requires a high power system, which even though is now widely commercially available, is still expensive to acquire. The energy of a laser system scales similar to an accelerator system. Even though chirped pulse amplification (CPA) exists, an increase in laser energy requires an increase in the diameter of the laser pulse and hence the amplifier crystals, scaling up the costs significantly. A lower power laser system is attractive for small facilities and universities. Recalling the brightness to laser power, Fig. 5.13, the plot emphasises the necessity of enhancing the x-ray yield of low power systems. The challenge of enhancement is the non-linearity of the physical system as partially discussed in Sec. 5. Carefully choosing the machine parameters with respect with each other is required as the parameters are correlated and influence the acceleration properties strongly. A subsequent scan of, e.g. the adaptive optic (AO), dazzler and pressure, is typically how an experimental operator optimises the *machine*. As the pressure changes the plasma wave wavelength, the optimal focus spot size (AO) changes as well and thus an optimisation requires another AO scan to fully explore the response of the system. Thorough scans for the global maximum of the system of N machine parameter scale up with $\prod_i^N t_i$ with t_i being the duration of the scan parameter i. More sophisticated algorithms are necessary to truly optimise a system. The optimisation problem has been under investigation in computer science for decades and more powerful computers have made them recently applicable to the larger public. Hence, they have been applied to physics experiments and even in laser-induced plasma acceleration with the first one in 2015[1] for low-energy electron acceleration $< 1\,\mathrm{MeV}$ by optimising the wavefront (AO) with a *genetic algorithm* (GA).

---

[1] [217] Z.-H. He *et al. Nat. Commun.* (2015).

In a previous campaign at the same laser system, two algorithms have been investigated controlling the spatial and temporal phase of the laser pulse. The experiment succeeded in two publications[2]. A goal function was defined, here the charge of the electron beam and the number of counts on the x-ray camera respectively, which was optimised. The genetic algorithm and Nelder-Mead method both demonstrated a huge increase in both electron charge and x-ray flux.

Based on those successes, this experiment added important machine parameters, such as the pressure in the gas cell and the length of the gas cell. A preprint has been published at the moment of finishing this work[3].

A more sophisticated machine learning approach was investigated here, the Bayesian-based optimisation. Bayesian optimisation is a popular and efficient machine learning technique for correlated, expensive to evaluate systems[4]. There are many algorithms in the Bayesian optimisation family and the algorithm chosen here was based on the Gaussian process estimated improvement (GP-EI)[5]. The reader is referred to the above-mentioned publication on this experiment for a detailed description of the algorithm.

6.1 Experimental Set-up and Control Parameter

The experiment was performed at the lower-power target area of the Gemini laser facility described in Sec. 3.1, ATA2. The laser energy was limited to around $245\,\mathrm{mJ}$, because of performance issues of the amplifier and reduced throughput of the compressor. The $803 \pm 23\,\mathrm{nm}$ laser pulse had a optimal pulse compression of $45\,\mathrm{fs}$. The repetition rate was reduced to $1\,\mathrm{Hz}$ operation, because of the heat-induced deformation of the gratings[6].

The general set-up can be seen in Fig. 6.1. The local laser system included a *Fastlite Dazzler*™[7], which is an *acousto-optic programmable dispersive filter* (AOPDF), capable of changing the temporal phase of the laser pulse. The phase was measured by taking a small portion of the compressed beam through a hole in a mirror at the end of the compressor and applying spectral phase interferometry for direct electric-field reconstruction (SPIDER) with a commercially available device. The system also included an AO and both were capable of being included as machine parameters for the optimisation. The laser beam was injected into the main vacuum chamber and

---

[2] [218] M. J. V. Streeter *et al. Appl. Phys. Lett.* (2018); [219] S. J. D. Dann *et al. Phys. Rev. Accel. Beams* (2019).

[3] [220] R. J. Shalloo *et al.* (2020).

[4] [221] J. Mockus. 1982; [222] B. Shahriari *et al. Proc. IEEE* (2016).

[5] [223] N. Srinivas *et al.*, Proceedings (2010).

[6] [224] V. Leroux *et al. Opt. Express* (2020).

[7] [225] *Dazzler* URL: `https://fastlite.com/produits/dazzler-ultrafast-pulse-shaper/` (visited on 09/04/2020) (2020).

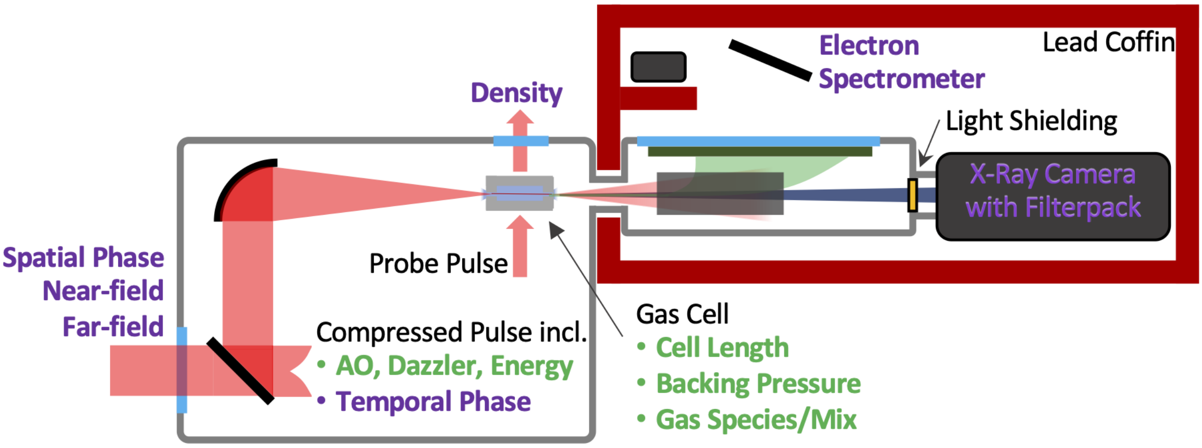

Figure 6.1: Set-up of the Experiment. The laser beam (red) is focused into a gas cell accelerating electrons (green) and producing x-rays (dark blue). The density in the gas cell was diagnosed with a $1\,\mathrm{mJ}$ probe beam (red). The grey outline symbolises the vacuum tank and the dark red the lead shielding. The green text indicates the machine parameter and the purple text the diagnostics. More details in Sec. 6.1.

leakage through a dielectric mirror before the off-set parabola was extracted outside the chamber. The far- and near-field were measured for pointing references as well as the spatial wavefront. The wavefront was measured with a Shack-Hartmann wavefront sensor, the *Imagine Optics HASO4*[8]. The through-put before the compressor to the interaction point (IP) was measured with a *Gentec* energy meter (analogue principle to Sec. 4.2.1) and a laser profile camera before the compressor, which was calibrated in absolute units, measured the energy of the laser pulse on target online.

The laser beam was focused by an $f/18$ off-set parabola with a focusing length of $1\,\mathrm{m}$ into the entrance of a gas cell to $\approx 19\,\mu\mathrm{m}$ FWHM, which resulted in a modest normalised vector potential of $a_0 = 0.55$.

The gas cell was of variable length between $0 - 10\,\mathrm{mm}$ having a movable piston at the exit, which was able to be controlled by the operating system. The gas cell length could also be controlled in the optimisation algorithm. The ceramic entrance and exit hole was originally $200\,\mu\mathrm{m}$.

The gas system was newly installed for this experiment and had to comply with the high repetition rate, $1\,\mathrm{Hz}$ opposed to $0.05\,\mathrm{Hz}$ at ATA3, with little variance to the desired backing pressure and quick change in pressure by the operating system to aid the machine learning algorithm. The schematic of the system can be seen in Fig. 6.2. The centrepiece was a reservoir tank, of which a pressure gauge measured the pressure. The idea was to keep the pressure constant at the desired pressure inside the reservoir

---

[8] [226] *Haso4* URL: `https://www.imagine-optic.com/product/haso4-broadband-2/` (visited on 09/04/2020) (2020).

tank. By opening a solenoid valve to the gas cell the desired pressure was reached inside the gas cell because the volume of the inlet and gas cell was negligible compared to the reservoir. The pressure gauge sent its digital output to the control system. The operating system was based on *EPICS*[9] so that it can be transferred to similar facilities in the future. The control system performed a closed proportional–integral–derivative (PID) loop[10]. It calculated the difference between measurement at the pressure gauge and set value over a short period and adjusted the opening times of the solenoid valves between the reservoir and high-pressure line (fill) and vent. It sent pulse information to a digital delay generator (DDG), which produced a $5\,\mathrm{V}$ pulse signal and which then was translated by an in-house built $5-24\,\mathrm{V}$ converter for opening the solenoids valves. The valve to the gas cell was independently controlled and opened by the trigger of the laser system. The gas mixes used during the experiment were pure helium and a 1% N_2 doped He mixture.

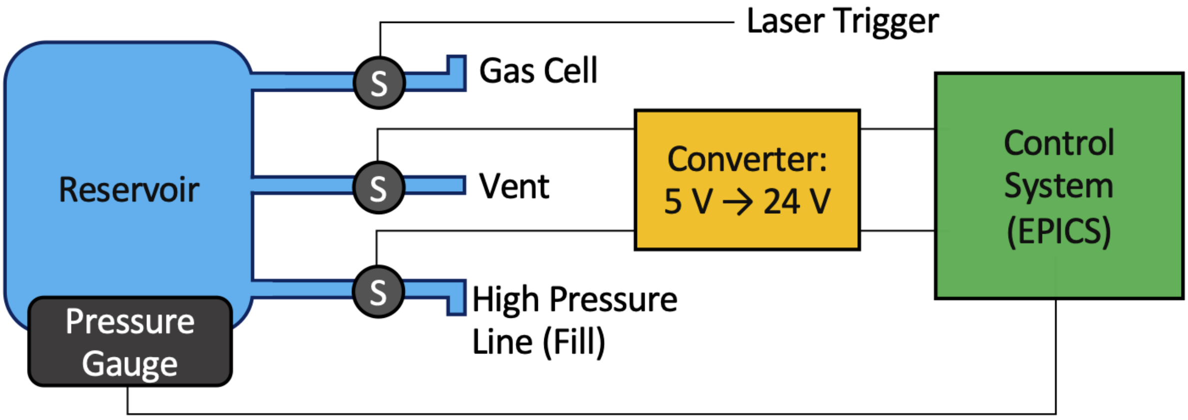

Figure 6.2: The newly implemented gas system for this experiment. The centrepiece was a reservoir, which had a pressure gauge reading sending it to the control system. The control system adjusted the pressure by opening solenoids (S) to either the high-pressure gas line, increasing the reservoir pressure or to the vent reducing the pressure. The reservoir was directly connected to the gas cell where another solenoid was triggered by the laser system's trigger.

The laser pulse accelerated electron beam and generated x-ray beam exited the main chamber through a pipe into a small diagnostic chamber. The diagnostic chamber was surrounded by lead and polypropylene to minimise the radiation produced by the electron to the target area.

The diagnostic chamber contained a permanent dipole magnet with a maximum field strength of $558\,\mathrm{mT}$, which deflected the electron beam onto a Lanex scintillating screen. The general concept of the electron spectrometer was discussed in Sec. 3.2. As seen in Fig. 6.1, the Lanex screen was imaged from outside the vacuum chamber

---

[9] [227] L. R. Dalesio *et al. NIMA* (1994).

[10] The derivative was not taken into account, which meant that it was technically a PI-loop.

through a perspex window with an objective and an *Allied Vision Manta G-235B* camera. The Lanex screen was covered with Al-foil towards the inside, blocking all residual laser light, which consequently made extra filtering for the camera of the Lanex wavelength redundant and increased the signal strength. The camera was shielded with a wall of lead and lead glass as the noise inside the lead shielding chamber was significant.

The x-ray beam continued straight and passed through a light filter, which was two sheets of $200\,\mathrm{nm}$ Al front-coated $12.8\,\mathrm{\mu m}$ Mylar. It was imaged with a direct detection *Andor iKon-M 934 BR-DD* camera, see Sec. 3.3.1, coupled to the vacuum with a filter pack mounted directly in front.

The plasma density inside the gas cell was measured with a $1\,\mathrm{mJ}$, $800\,\mathrm{nm}$ synchronised probe beam using a Michelson interferometer. Due to the limitation of the gas cell, direct measurements were limited to cell length longer than $> 1.7\,\mathrm{mm}$.

6.2 Calibration of the Electron Spectrometer and X-ray Spectrometer

The relevant distances of the electron spectrometer and x-ray camera can be seen in Fig. 6.3.

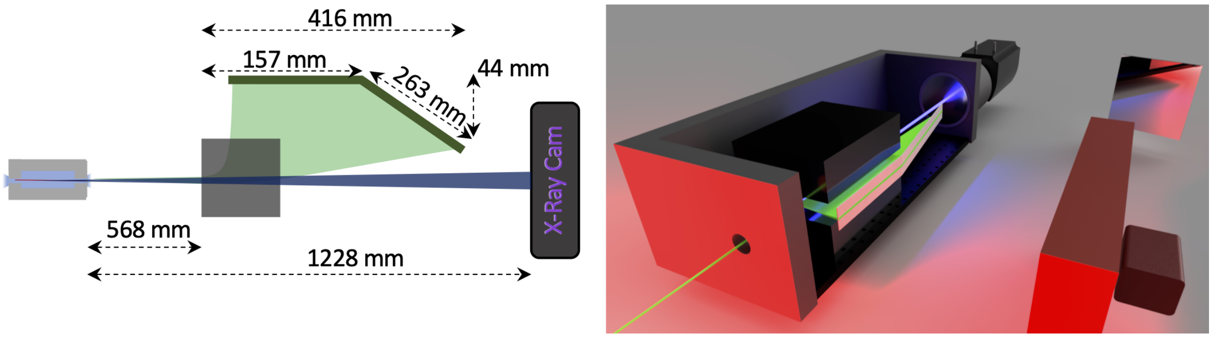

Figure 6.3: Left: The relevant distances of the electron spectrometer and the x-ray camera. The Lanex screen was inclined into the vacuum chamber to increase the maximum energy of the electron spectrometer. The schematic is not to scale, hence a 3D render was produced on the right. The top and side flange of the vacuum chamber was removed to see the electron beam (green) and x-ray beam (blue). The entire set-up seen was enclosed in a layer of lead for shielding of the radiation.

6.2.1 Electron Spectrometer

The calibration of the electron spectrometer required tracking of the electrons onto the Lanex screen. Further, the Lanex screen had to be spatially calibration and finally, the Lanex' light emission had to be calibrated with the electron charge. The spatial calibration of the imaging set-up was performed by using $5\,\mathrm{mm}$ graph paper, positioning it temporarily flat on the Lanex towards the imaging camera. The camera imaged the inclined screen with a $53\,\mathrm{mm}$ objective, which resulted in a skewed image of the actual screen. A four-point transform was used to flatted the image, see[11] for a detailed description of this method.

The calibration of charge was generally discussed in Sec. 3.2.2 and was straight forward by inserting the imaging plate at the position of the Lanex screen and removing it, taking 100 shots in each configuration, then comparing the absolute charge and the camera signal.

The tracking code was discussed in 3.2.1. An electron travelling through the electron spectrometer perfectly on-axis would yield in a high energy resolution of the spectrometer, which solely depends on the resolution of the camera. But the divergence of the beam was measured to be large and as such electrons off-axis had to be considered. An electron beam with a large divergence introduces a large uncertainty on the electron spectrometer. This is visualised in Fig. 6.4. The uncertainty increases with respect to the divergence of the electron bunch. Therefore, the tracking code investigated the position of electrons on the Lanex screen for different positions of the electrons at the entrance of the magnet. The electrons positions was varied between $\pm 5\,\mathrm{mm}$ in $0.5\,\mathrm{mm}$ steps (41 steps in total), corresponding to a maximum divergence of $17.4\,\mathrm{mrad}$.

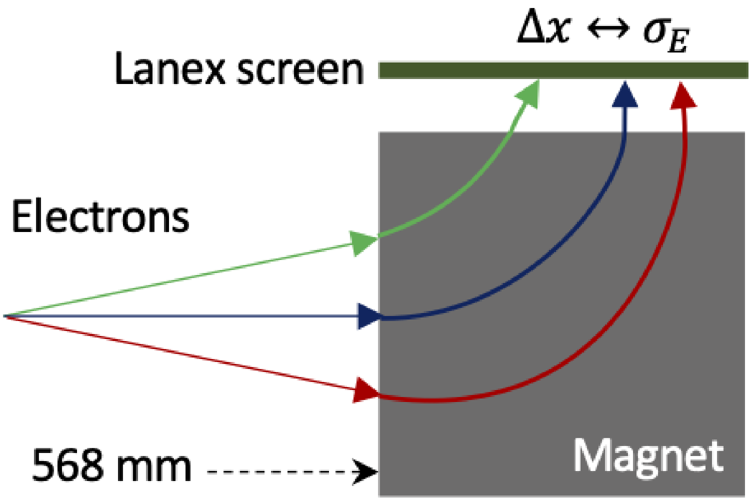

Figure 6.4: Schematic drawing for the explanation of the uncertainty on the energy resolution of the electron spectrometer due to a large divergence. The electrons indicated with different colours have the same energy, but end on different areas on the Lanex, because their position at the entrance of the spectrometer is different.

---

[11] [66] J. M. Cole, PhD Thesis, Imperial College London (2015), Chap. 3.4.2.

The result is a 2D matrix where one dimension is the location of the electron at the entrance of the magnet and the other its energy. The uncertainty of the electron spectrometer is determined by the divergence of the electron bunch. Assuming a symmetrical electron beam, the transverse spread of the electron beam on the Lanex screen can be used to estimate the divergence. However, the travel distance of the electrons from the entrance of the magnet to the location of the Lanex is required to determine the divergence. Fig. 6.5 a) shows the position on the screen of each tracked electron as black dots and their total length of propagation. The propagation distance of the electrons changes depending on the position at the entrance, which introduces another uncertainty, shown in Fig. 6.5 a) in light blue, but the average distance travelled (dark blue) is reasonably accurate and the error is not large.

Once the divergence is known, it is used to choose the transfer matrices of tracked electrons determining what position on the screen corresponds of which electron energy and its uncertainty. Fig. 6.5 b) in red shows the calibration for an electron beam with a divergence of $1.7\,\mathrm{mrad}$[12]. The maximum divergence tracked is also shown in blue corresponding to a divergence of $17.4\,\mathrm{mrad}$

One note on the assumption that the electron beam is symmetrical and that its momentum at the entrance can easily be divided into a longitudinal and transverse component. This assumes that the beam is a laminar. This is reasonable though, because of the source size of the electron beam, which starts around $\approx\mathrm{\mu m}$ and the long distance to the entrance to the electron spectrometer. A potentially non-laminar beam would become laminar due to the long distance travelled in free space.

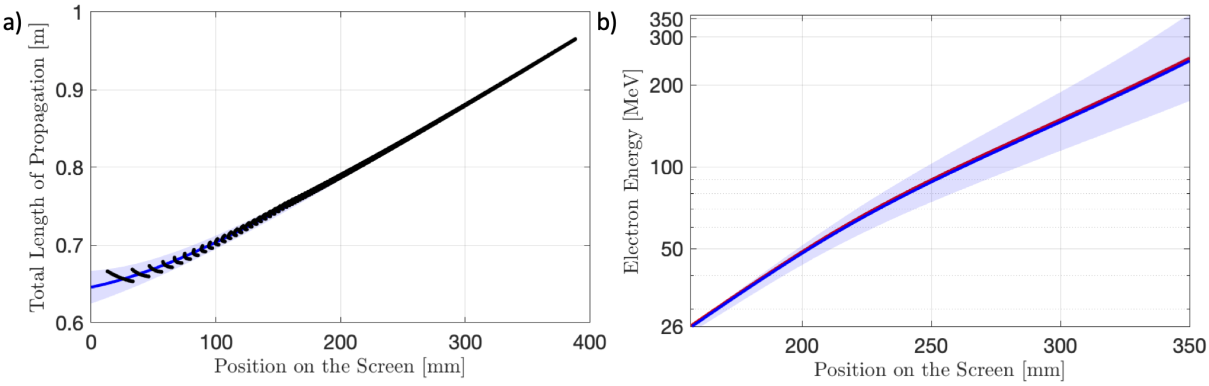

Figure 6.5: a) The average propagation length depending on the position on the Lanex screen (blue) and its uncertainty compared to the raw data (black). b) The average energy and maximum diverting energy depending on the screen position for a $17.6\,\mathrm{mrad}$ (blue) and a $1.76\,\mathrm{mrad}$ (red) beam.

The stated energy in Sec. 6.3 and following is the maximum measured energy of electrons W_e, determined by integrating the energy spectrum from the lowest end to

---

[12] This corresponds to a beam which extends over $\pm 0.5\,\mathrm{mm}$ at the entrance, $(0.5 + 0.5\,\mathrm{mm})/568\,\mathrm{mm} = 1.7\,\mathrm{mrad}$

the point in the spectrum, $26\,\mathrm{MeV}$ to W_e at which point the integrated charge equals 95% of the total charge Q_{tot}

$$Q_{tot} = \int\limits_{E_{min}}^{E_{max}} \frac{\mathrm{d}Q}{\mathrm{d}E}\mathrm{d}E \tag{6.1}$$

$$0.95 \overset{!}{=} \frac{1}{Q_{tot}} \int\limits_{E_{min}}^{W_e} \frac{\mathrm{d}Q}{\mathrm{d}E}\mathrm{d}E \tag{6.2}$$

6.2.2 X-ray Spectrum Retrieval

The design of the x-ray filter was of a high priority before this experiment. Such comparatively low laser power laser system are expected to produce low number of photons and as such, it is important to observe as many photons as possible, while simultaneously having enough filter materials on the filter pack as data points to estimate the synchrotron spectrum. A code was composed to optimise the filter pack under these experimental conditions.

X-ray Filter Pack Design Code

The design was intended to maximise the differences between each filtered signal relative to each other, depending on the critical energy of the betatron radiation. The choice of possible materials was taken from a commercial vendor[13] to simplify the production. Materials with significant COSHH issues were exempt from the available elements and alloys, as well as material with thicknesses beyond $30\,\mu\mathrm{m}$ due to their absorption. The remaining substances were considered for their absorption at their specified thickness. Multiple layers of materials were included as long as their combined thicknesses was below $30\,\mu\mathrm{m}$. One can perform the following procedure to optimise the filterpack.

A set number of filters, which depends on the size of the CCD and the binning of the camera is defined. The range of critical energies considered is divided into the number of filters, referred to as $E_{crit,i}$ with i being the filter number. This is done to optimise the retrieval with the filter materials for those critical energies. The quantum efficiency and the filters in the beam path due to the experimental setup are combined to create effective emission spectra. The optimisation algorithm then works as follows:

1. The synchrotron spectra for the first two relevant critical energies $E_{crit,i}$ and $E_{crit,i+1}$ from the range of critical energies are calculated.
2. The algorithm calculated the transmission of both spectra through the filters in the beam path and the reduction of the signal due to the quantum efficiency.

---

[13] https://www.goodfellow.com

3. The transmission through all possible materials m in the list with their respective thicknesses are calculated and integrated over the energy following Eq. (3.5) $C_{m,i} = \alpha \int_{E_{min}}^{E_{max}} ES(E, E_{crit,i}) QE(E) t_m(E) \mathrm{d}E$
4. The difference between both critical energies are calculated as $C_{m,i} - C_{m,i+1}$. This yields in a single value for all materials. The material with its specific thickness, which has the largest difference in signal is chosen as filter material
5. The steps are repeated for the next pair of critical energies

The fourth point is the crucial one. It means that the signal observed by the camera depends on the critical energy. The filter is most sensitive between both critical energies. Here, the code was executed for intended critical energies between $4 - 9\,\mathrm{keV}$ with 6 filters. The low amount of filters ensured a large number of pixels so that the averaged value per filter was determined with less uncertainty.

The number of photons was not known before, but a previous experiment at this laser system made the retrieval with the used filter pack then not possible[14], because of the small number of photons. The previous data indicated around $50\,\mathrm{ph\ px^{-1}}$. The determined combination of filters and their transmission is seen in Fig. 6.6. The tungsten is intended to measure the on-shot noise as it has been discussed in Sec. 3.3.4. The exact thicknesses of the filters are displayed in Table 6.1.

Material	W	Al(98%) Mg(1%) Si(1%)	Al(95%) Mg(5%)	Mg	Mylar $C_{10}H_8O_4$	Kapton $C_{22}H_{10}N_2O_5$
Thickness $[\mu m]$	50	30	22	20	25.4	12.7

Table 6.1: Thicknesses of the materials from the filter pack design code result.

Experimental Filter Pack

The filter pack used in the experiment can be seen detailed in Fig. 6.7 on the left. The actual thicknesses vary slightly from the desired values in Table 6.1. The sum of differences between the filters for some critical energies are taken to quantify the performance compared to the theoretical result as,

$$\Delta(E_{crit}) = \sum_{i=1}^{5} \left| T_{Filter\#i} - T_{Filter\#(i+1)} \right| , \tag{6.3}$$

---

[14] The previous experiment had a filter pack designed with little difference between the critical energies, which was unsuitable for retrieving the critical energy reliably.

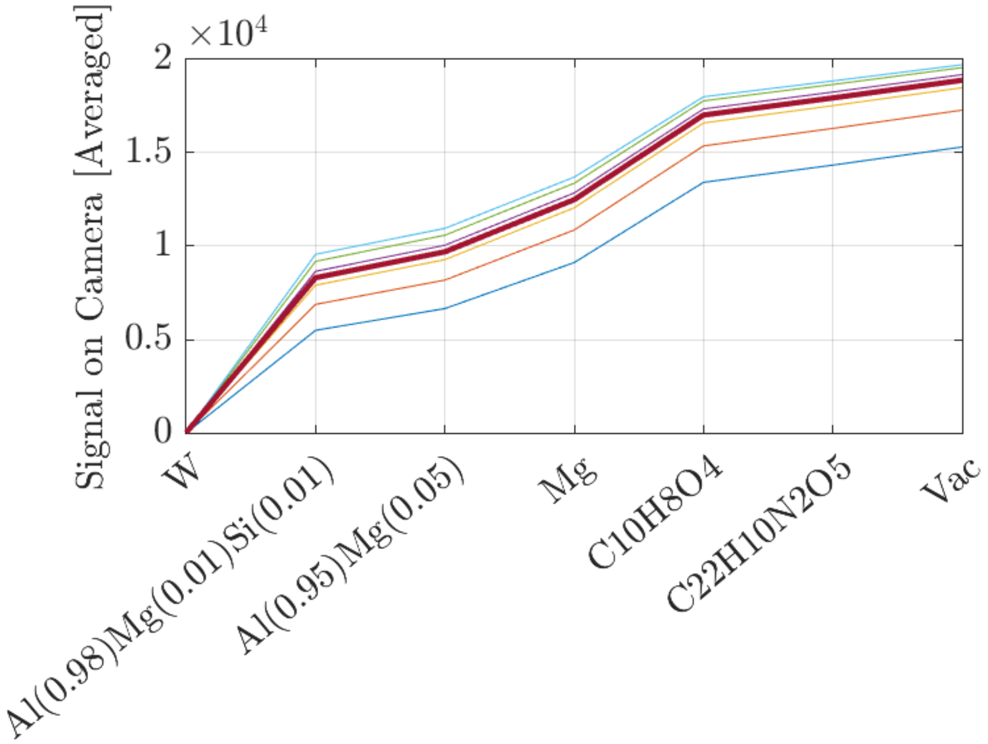

Figure 6.6: Result of the filter pack design code. The different colours correspond to different critical energies between $4 - 9\,\mathrm{keV}$ (dark blue to light blue ascending in camera counts in $1\,\mathrm{keV}$ steps) with the average critical energy $6.5\,\mathrm{keV}$ in red. See Table 6.1 for the thicknesses.

in which the normalised camera signal of Filter 1 (unfiltered background) to the average signal from all filters is $T_{Filter\#1}$. Filter # 2 would be Kapton and so forth. Note, that tungsten is not taken into account as it is only used to estimate the background signal. The result is shown in Table 6.2. The designed filter pack performs better at very low critical energies, but overall the difference is small and works mostly as intended.

Critical Energy [keV]	0.5	2	4	12
Designed Filter Pack [%]	40.3	20.6	14.9	10
Experimental Filter Pack [%]	38.8	20.9	15.2	10.2

Table 6.2: Quantified measure of performance between the designed and experimentally used filter pack.

The right side of Fig. 6.7 shows the 3D designed mount of the filters on the Mylar, which was used to place the filter. The mount was designed for the x-ray camera to ensure alignment. The small holes are connected through the plastic to the other side of the mount with a *zig-zag* pattern to enable the airflow when pumping down or letting up the vacuum chamber, but to still prevent any light from going through. The entire 3D printed mount was covered in $200\,\mathrm{nm}$ Al to preserve the material from oxidation.

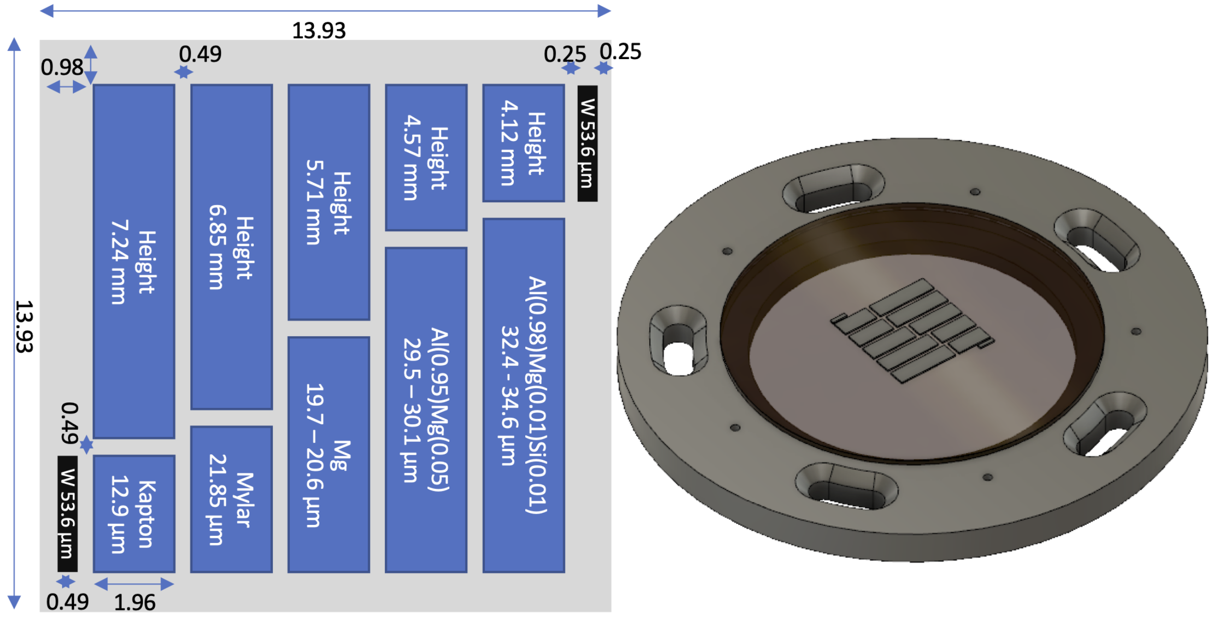

Figure 6.7: Left: Schematic of the final filter pack used in the experiment. The thicknesses are slightly off from the desired values (see text). The numbers are mm if not otherwise stated. Right: The filters are mounted on Mylar in a 3D printed aperture to mount it directly onto the x-ray camera.

Filter Transmission and Counts on the X-ray Camera

Sec. 3.3.3 discussed the procedure of estimating the critical energy and then the number of photons. One requires the average counts on an x-ray camera and knowing the filter transmissions, see Eq. (3.5). The data in the following section was obtained by optimising the average counts on the total chip of the CCD. Here, the relation between the number of photons and the critical energy for constant value on the camera is discussed to explain the reported findings.

A temporary function $\psi(E_{crit})$ is defined, which represents the term of the number of photons solely depending on the critical energy. Let C be the counts on the camera and α the conversion between counts and photon energy. Eq. (3.5) can then be used to define $\psi(E_{crit})$ as,

$$N_{ph} = \frac{C/\alpha}{\int\limits_{1\,\mathrm{eV}}^{300\,\mathrm{keV}} E\,S(E, E_{crit})\,QE(E)\,T(E)\mathrm{d}E}\,, \tag{6.4}$$

$$\rightarrow \psi(E_{crit}) := \frac{1}{\int\limits_{1\,\mathrm{eV}}^{300\,\mathrm{keV}} E\,S(E, E_{crit})\,QE(E)\,T(E)\mathrm{d}E}\,. \tag{6.5}$$

Note that this is defined for the number of photons over an area with transmission $T(E)$ in the defined energy range $1\,\mathrm{eV} - 300\,\mathrm{keV}$. The energy range was chosen to cover enough of the possible energy range of the photons and included additional data points at significant spectral features of the materials, such as transition edges. As the highest signal is found in the non-filtered region of the filter pack (which still has several materials in the path). The non-filtered region is therefore used to calculate the total number of photons at the source, because it provides the highest signal-to-noise ration. The analysis below suggests critical energies around $2\,\mathrm{keV} - 4\,\mathrm{keV}$.

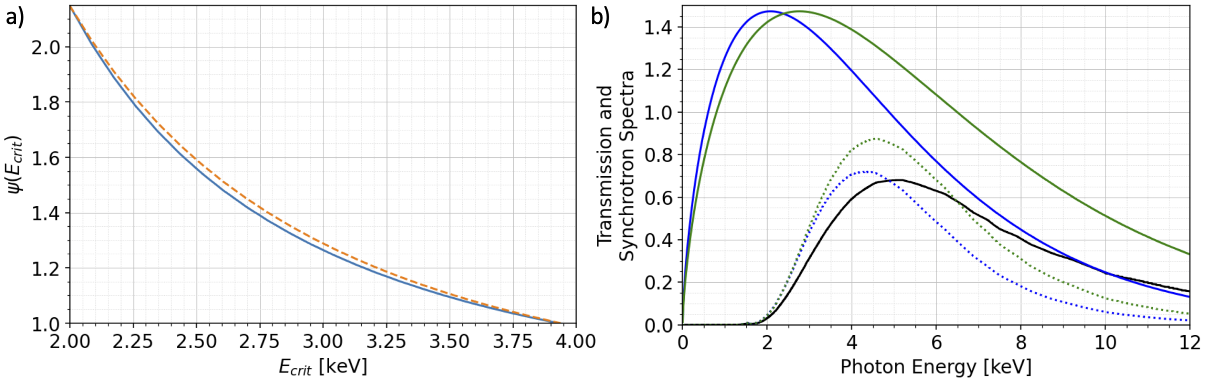

Figure 6.8: a) $\psi(E_{crit})$ depending on the density (blue) and an estimating function for this energy range $\propto 1/E_{crit}^2$ (dashed orange). b) The reduction of signal due to the material in the beam path and the quantum efficiency (black) and synchrotron spectra for $2.5\,\mathrm{keV}$ (blue) and $3.3\,\mathrm{keV}$ (green), as well as the product of the spectra and reduction (dotted lines).

For a measured number of counts, $\psi(E_{crit})$ can be interpreted as the correction on the number of photons due to the filter in the beam path $\psi(E_{crit})$. Fig. 6.8 a) displays $\psi(E_{crit})$ in blue for the calculated range of critical energies. The dashed orange line is an approximation following $\psi(E_{crit}) \propto E_{crit}^{-2}$ and useful to check the results in the following section. Note that this is only valid in the specified energy range and for the set of materials in the beam path.

Fig. 6.8 b) shows two synchrotron spectra with critical energies of $2.5\,\mathrm{keV}$ (blue) and $3.3\,\mathrm{keV}$ (green). Both are normalised to contain the same number of photons. The combination of quantum efficiency and absorption of the materials in the beam path $QE(E)\,T(E)$ are shown in Fig. 6.8 b) in black. This non-filtered transmission curve is mostly smooth peaking around $5\,\mathrm{keV}$ as the materials in the beam path mostly consists of carbon, hydrogen and oxygen, which all have their K-edge below $1\,\mathrm{keV}$ and where absorption suppress the K-edge feature of the Si-CCD, which is around $1.84\,\mathrm{keV}$.

The product of the spectra in Fig. 6.8 b) with the filter transmission is depicted with dotted lines. The lines visualise why the correction factor $\psi(E_{crit})$ decreases with increasing critical energy.

The number of photons is proportional to the measured counts on the x-ray camera and the estimated critical energy as

$$N_{ph} \propto \frac{C}{E_{crit}^2}\,. \tag{6.6}$$

6.3 Bayesian Optimisation of LPWA with Ionisation Injected Electrons

A Bayesian optimisation algorithm was used to increase the average number of counts on the x-ray camera using 1% N_2 doped He gas. Stable, polarised x-rays have been reported previously by Döpp et al.[15], however, the laser power was a magnitude lower in this work, which increases the difficulty of injecting electrons that produce a stable x-ray flux.

The general data acquisition was done by taking 10 shots and averaging the measurements. Such a series is referred to as a *burst*. The algorithm determines a set of machine parameters. The result of the burst updates the Bayesian model, which then determines the next set of parameter that it predicts will produce either a better result or decrease the uncertainty of a region with very large uncertainty. The global maximum and model is more accurately known with increasing number of bursts as the algorithm includes more data.

Focus Shift $[\mathrm{mm}]$	GDD $[\mathrm{fs}^2]$	TOD $[\mathrm{fs}^3]$	FOD $[\mathrm{fs}^4]$	Density $[10^{18}\mathrm{cm}^{-3}]$
-1.2	-987	-20570	1715000	10
2	490	15090	2759900	28

Table 6.3: Parameter space of the Bayesian optimisation for the presented set of data. These parameter have been measured rather then the raw machine inputs. The group delay dispersion (GDD), third- and fourth-order dispersion (TOD and FOD) are all controlled by the Dazzler.

The optimisation was performed in the parameter space specified by Table 6.3. The reason choosing these parameter is that they all change the system: The plasma wave wavelength and length of the plasma ramp at the gas cell entrance is changed with the density. This requires a different focal plane and the self-focusing requirements change and it changes the rate of temporal compression, which affects the choice of the temporal phase of the laser pulse. Note that these are the measured values instead of the set parameters as these were slightly different. The input parameters are the set values on the AO, the backing pressure and the set values in the Dazzler. The displayed values are the measured values from the wavefront sensor, the density extracted from the measured backing pressure and the probe calibration, and the phase terms that have been measured by the SPIDER. The focus shift was calculated by changing the focus term and measuring the focal displacement by moving the focal spot camera prior the experiment.

The goal of the optimisation was to increase the average number of counts on the x-ray camera after subtracting the thermal and read-out noise (darkfield). Fig. 6.9 (a)

---

[15] [62] A. Döpp *et al. Light: Science & Applications* (2017).

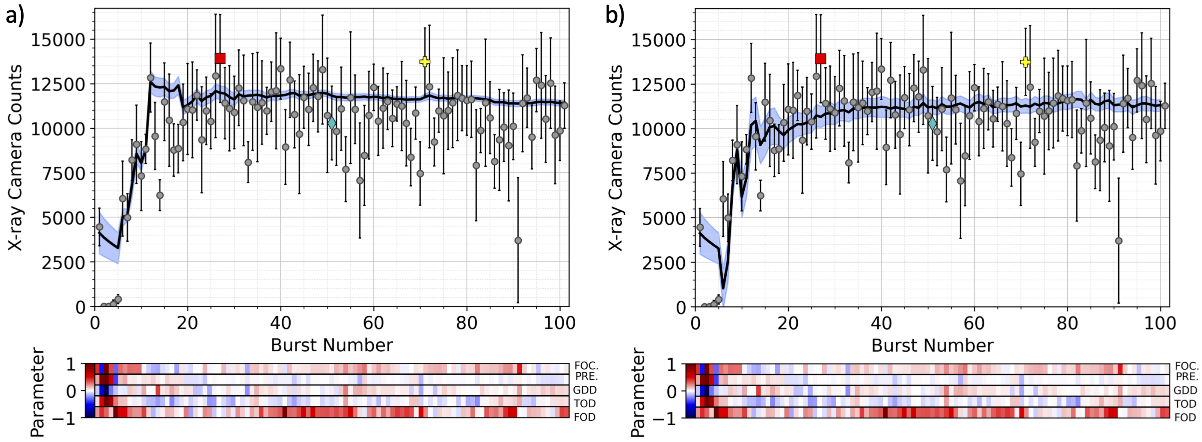

Figure 6.9: Bayesian optimisation of the camera counts. The parameters are shown at the bottom and are normalised to their range. The black line represents the predicted maximum from the GPR and the blue region is the standard error. The red square marks the burst with the highest counts, the cyan diamond the one with the highest brilliance and the yellow cross the one with the highest counts after subtracting shot-noise.

shows the development of the measurements (dots) and the prediction of the global maximum by the Bayesian model (black line with its uncertainty in blue) during the experiment. The red square marks the burst with the highest counts, the yellow cross the one with the highest counts after subtracting shot-noise and the cyan diamond the one with the highest brilliance.

Note that the depicted error bar on the data points are the standard deviations of 10 shots (1 burst). The algorithm requires the average value of a burst and the error of the mean, which is calculated by dividing the shown standard deviation by $\sqrt{N}$, in which N is the number of counts of successful laser shots[16].

As mentioned the input parameter during the experiments were slightly different then the measured values. It is therefore convenient to create a new model with the measured values. This new model with the measured values is shown in Fig. 6.9 b). One can see that the uncertainty of the model increases when using the measured values, which is because the measured values are not as stable. However, the predicted values for the global maximum are within their uncertainties in both cases; $11\,425 \pm 165\,\mathrm{px}$ for the set values and $11\,298 \pm 335\,\mathrm{px}$ for the measured ones.

The algorithm optimised the average counts of the entire CCD chip from the x-ray camera, but the goal should be to increase the shot noise subtracted number of counts of the non-filtered region. This figure would increase the contrast when imaging samples. A new model using the measured input parameters and the noise-free average camera counts of the non-filtered region is shown in Fig. 6.10 a). The shot-noise is

---

[16] Each burst consisted of 10 shots, but the laser didn't fire in 12 out of 1010 shots

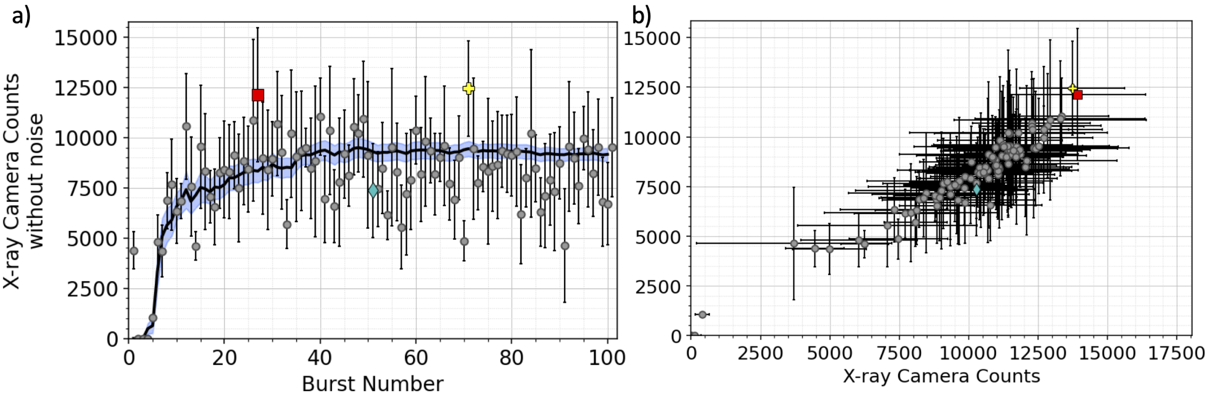

Figure 6.10: a) Bayesian optimisation of the camera counts behind the non-filtered region after subtracting noise. The black line represent again the predicted maximum from the GPR and the blue area the standard error. The markers refer to the same bursts as in Fig. 6.9. b) The average counts for the entire image compared to the noiseless counts behind the non-filtered region.

quite substantial, as can be read in Fig. 6.10 b). This indicates that the experiment would benefit greatly from additional shielding between the electron dump and the x-ray camera. One can interpret that an increase of noise, which is based on charge and electron energy, does also increase the emitted radiated power. But the signal strength is not linear over the entire range, which could be because of the geometry of the diagnostic. The electrons are less deflected from the path towards the x-ray camera as the energy of the electrons increases, potentially increasing the noise measured by the camera.

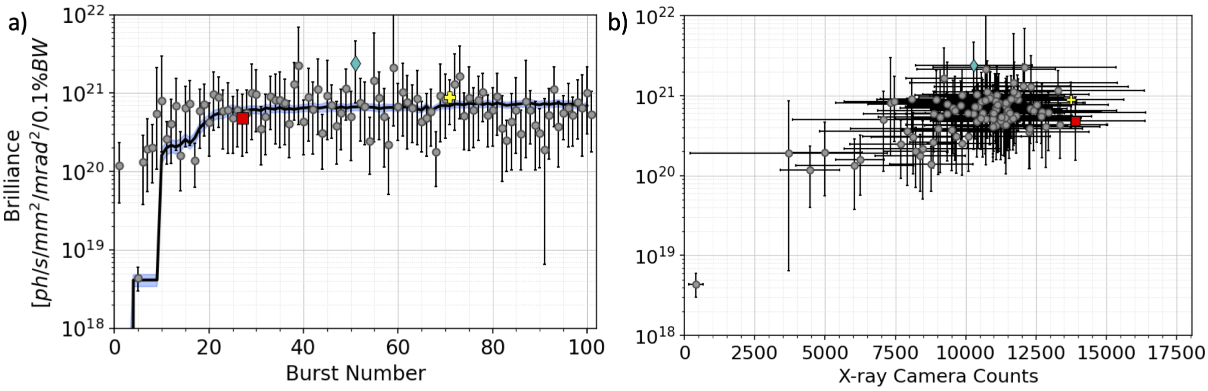

Figure 6.11: a) Bayesian optimisation of the brilliance. The black line again represents the predicted maximum from the GPR and the blue area the standard error. The markers refer to the same bursts as in Fig. 6.9. b) The average counts for the entire image compared to the brilliance. The brilliance is in logarithmic scale for both plots.

Finally, another potential experiment could require the optimisation of the peak brilliance, which is often used as a figure of merit in betatron experiments as discussed before in this work, Ch. 5. The simulated optimisation is seen in Fig. 6.11 a) and the transformation between the average camera counts to the brilliance in b). The shown brilliance is on a logarithmic scale. The correlation between the camera counts and brilliance is not linear. This is, because it can be shown that the number of photons per bandwidth, $\mathrm{ph}\ \ 0.1\%\mathrm{BW}^{-1}$, is proportional to $(N_{ph}ES(E,E_{crit}))_{max}$[17]. However, $(E\ \ S(E,E_{crit}))_{max}$ varies little depending on the critical energy, which can be seen in Fig. 6.12 a). Thus the photons per bandwidth depend mostly $\propto N_{ph} \propto C/E_{crit}^2$, Eq. (6.6). It would be beneficial, to summarise the brilliance in one equation, which shows all dependencies and which values have to be measured to calculate it. Using Eq. (6.6) and the source size (see previous Ch. 5.5.1), the brilliance is proportional to

$$r_\beta = \frac{\alpha_\beta}{\gamma k_\beta} \propto \frac{E_{crit}\lambda_p^2}{\gamma^2} \propto \frac{E_{crit}}{\gamma^2 n_e} \tag{6.7}$$

$$B = \frac{(N_{ph}E\ S(E,E_{crit}))_{max}}{\theta^2\tau(\pi r_\beta^2)} \propto \frac{C}{E_{crit}^2}\frac{\gamma^4 n_e^2}{E_{crit}^2} n_e^{\frac{1}{2}} = \frac{C\gamma^4 n_e^{\frac{5}{2}}}{E_{crit}^4} \tag{6.8}$$

when also assuming that the pulse length is proportional to the plasma wave wavelength. The brilliance depending on the defined variable ψ is shown in Fig. 6.12 b) in a double logarithmic plot[18].

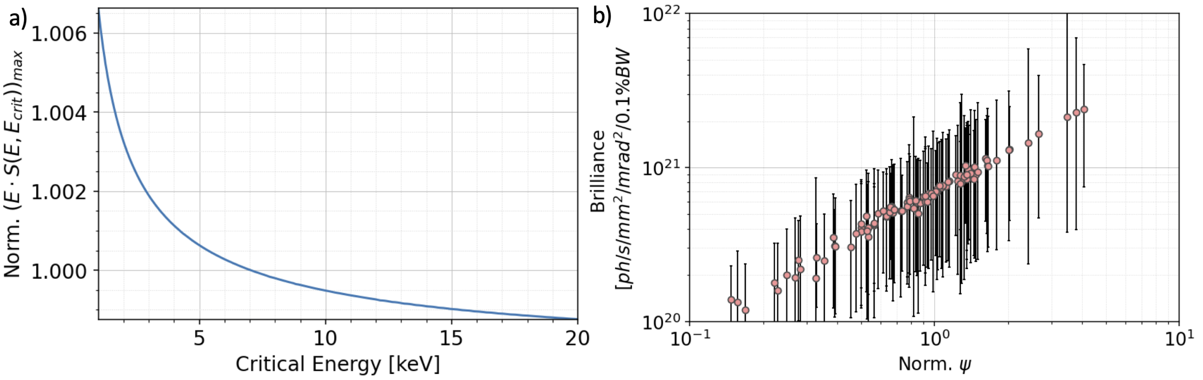

Figure 6.12: a) $(E\ \ S(E,E_{crit}))_{max}$, which is used to calculate the brilliance shows little variation over a large range of critical energies. The brilliance changes less than 1% over the range of $1-20\,\mathrm{keV}$. b) The brilliance vs the normalised generic value ψ as described in the text.

Optimising the average counts is not sufficient to optimise the brilliance, because the brilliance depends on multiple beam parameter. Using multiple diagnostics and combining them to create a figure of merit has not been demonstrated yet and it would be a step forward. The new model of the optimisation in fig. 6.11 does not really represent a true optimisation of the brilliance, but the predicted maximum based on the measurements for optimising the number of counts. This has to be emphasised, because

---

[17] [167] J. C. Wood, PhD Thesis, Imperial College London (2016), Ch. 3.5.7.

[18] The relation should be perfectly linear, but the filter correction is only an approximation, hence the variation.

the true maximum could still be significantly different than the predicted maximum here. This predicted maximum is $6.9 \pm 0.6 \times 10^{20}\,\mathrm{ph\ s^{-1}\,mm^{-2}\,mrad^{-2}\,0.1\%BW^{-1}}$. Note that the uncertainty is the error of the mean and based on the error of the mean from the measurements. However, this is an underestimation, because the shot-to-shot fluctuations per burst were so large that the simulated optimisation did not work with a simple average of the parameters, but had to use the error on the mean as opposed to the previous predictions. The trend is still reasonably well calculated. More accurate analysis on the individual shots will be discussed in as Sec. 6.3.3.

6.3.1 Focus Shift and Density vs. Brilliance

Before going into details on the electron data in combination with the x-ray data, two parameters are discussed in more detail. These seem to dominate the maximisation of the brilliance with respect to their defined degree of freedom[19]. These parameters are the longitudinal shift of the focus and density.

The brilliance compared to both parameter can be seen in Fig. 6.13. Note that the brilliance is depicted in a logarithmic scale and the improvement around the maximum of both is sharp. Three bursts had immeasurable-low brilliance and are added as red dots at the bottom. The values are in fact 0, but this would have been not practical to add in this scale.

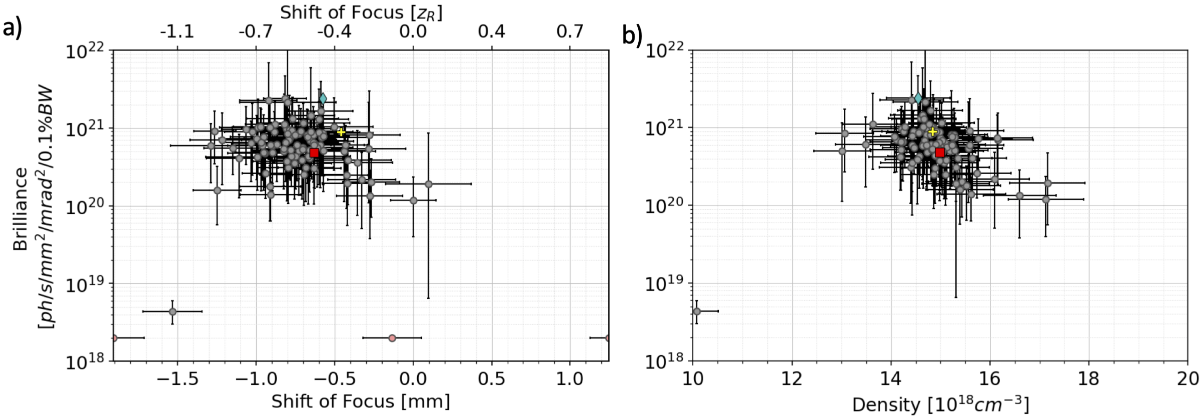

Figure 6.13: a) The shift of the focus versus brilliance. The markers refer to the same bursts as in Fig. 6.9. b) The brilliance versus density. Three shots with immeasurable-low brilliance would be outside of the displayed density range ($> 20 \times 10^{18}\,\mathrm{cm}^{-3}$) and are not displayed here.

The shift of focus is towards the parabola for negative values. The initial position, $0\,\mathrm{mm}$, denotes the optimised spot focussed at the entrance of the gas cell. The precision of which this was determined is not within the displayed range here, because a

---

[19] Even though the average counts were optimised, the brilliance is of physical significance and is used here to compare the different bursts.

direct measurement was not possible. The position was measured with a mirror flipped into the path and therefore the position might have been slightly off.

The top scale on Fig. 6.13 a) shows the shift of focus in units of the Rayleigh lengths. A major improvement is seen within half a Rayleigh length. The spot size would decrease to $w(z = 0.5z_R)/w_0 = \sqrt{1 + (0.5z_R)^2/z_R^2} = 1.1$ of its original value. This a 10% difference. The normalised vector potential, which is linear to the spot size, would also change 10%.

That a change of 10% of the vector potential would increase the brilliance by an order of magnitude seems unlikely, especially concerning other fluctuations of the laser. Hence, it suggests that the improvement is not purely based on adjusting the spot size. Shifting the focal plane is also changing the rate of change of the spot. The rate of change is important when considering the relativistic self-focusing inside the plasma, see Sec. 3.4.2.

Also, the gas leaves the front of the gas cell creating a density up-ramp. The position of the laser spot on the density ramp and the rate of change of the focus spot both change the guiding through the main gas cell and it seems likely that this was what the algorithm enhanced. The density shows similar behaviour in the sense that the window of high brilliance is within a small range of densities.

The correlation on the different parameter to each other is rather challenging as one can see in Fig. 6.14 a) and b) for the shift of focus, density and group delay dispersion. This indicates that the parameters are more than just linearly correlated. Another issue is stability. As the error bars show, the uncertainty is rather large, which is based on the laser system. It can be greatly improved with a more stable system and accurate calibration of the diagnostics.

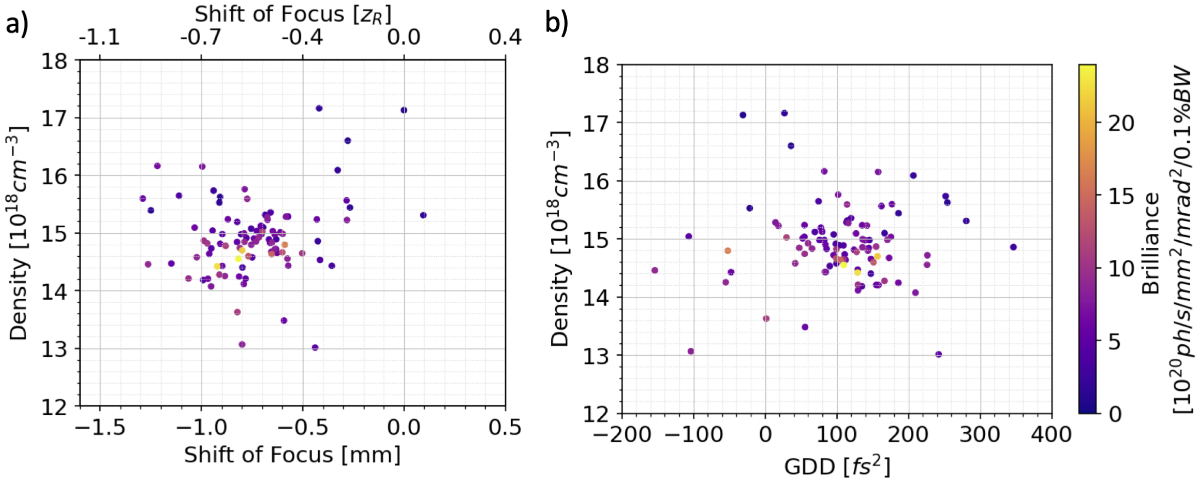

Figure 6.14: a) Shift of focus vs density with colouring of the data points depending on the brilliance. b) The group delay dispersion vs density with the same colouring for the brilliance.

6.3.2 Charge and Electron Bunch Energy vs. Brilliance

Comparing the energy of the electrons, the critical energy and density with the brilliance is trivial as these parameters were used to calculate the brilliance. However, the charge is independent and the charge compared to the brilliance can be seen in Fig. 6.15 a). The plot shows a clear improvement of the brilliance with an increase in injected and accelerated electrons. This suggests that this optimisation is linked with charge increases the injection efficiency rather than optimising the individual parameters of the brilliance (critical energy, electron energy, density). Fig. 6.15 b) shows the total energy in the electrons bunch for electron with an energy $> 26\,\mathrm{MeV}$. This is strongly correlated with the charge as it is calculated by,

$$E_{electron} = \int_{26\,\mathrm{MeV}}^{E_{max}} \frac{\mathrm{d}Q}{\mathrm{d}E} \, E \mathrm{d}E \,, \tag{6.9}$$

in which E_{max} is the maximum energy of the spectrometer[20] and $\frac{\mathrm{d}Q}{\mathrm{d}E}$, the charge distribution per energy interval. The maximum laser energy to electron bunch energy efficiency reached $1.00 \pm 0.22\%$

The coupling efficiency is of high interest for future applications of LPWA such as a particle accelerator[21]. The theoretically calculated coupling efficiency presented by Papp et al.[22] for a $5\,\mathrm{TW}$ laser at $880\,\mathrm{nm}$ is 0.43% and below our experimental observation. However, the investigated system by Papp is for a much shorter and tighter focused pulse and should not be compared without caution.

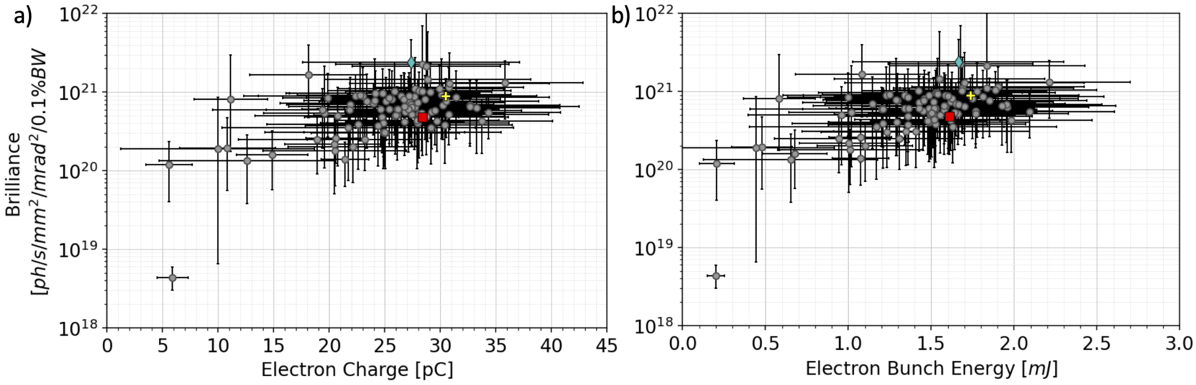

Figure 6.15: a) Charge of the electron bunch for energies $> 26\,\mathrm{MeV}$ and b) total electron bunch energy compared with the brilliance of the x-ray beam. The markers refer to the same bursts as in Fig. 6.9.

---

[20] The value depended on the estimated divergence as discussed in Sec. 6.2 and was at its peak $350\,\mathrm{MeV}$.

[21] [228] C. B. Schroeder *et al.*, Proceedings (2016).

[22] [229] D. Papp *et al.* *NIMA* (2018).

6.3.3 Individual Analysis of Significant Bursts

The large uncertainty seen in the previous plots is based on the shot-to-shot fluctuations of the laser system. Each burst consists of averaged shots and each shot is treated equally with respect to the other shots. Greater accuracy can be achieved by evaluating each shot individually and then calculating a weighted average. The weight is based on the uncertainty of the individual shot. This has not been done previously, because the previous sections analyse the optimisation algorithm. The algorithm required fast computing and the analysis of the brilliance was not available during the experiment.

The following data in Table 6.4 is weighted by the uncertainty of the calculated brilliance. The chosen bursts to display are the one discussed in Sec. 6.3.3. Burst 27 had the highest counts on the x-ray camera, burst 51 the highest average brilliance when the brilliance was averaged without weight and burst 71 had highest counts after subtracting noise.

Burst	Power $[\mathrm{TW}]$	Density $[10^{18}\mathrm{cm}^{-3}]$	W_e $[\mathrm{MeV}]$	E_{crit} $[\mathrm{keV}]$	r_β $[\mathrm{\mu m}]$	Q $[\mathrm{pC}]$	Brilliance $[\Psi]$
27	5.7 ± 0.2	15 ± 2	77 ± 6	3.9 ± 0.2	2.2 ± 0.3	25.8 ± 5.3	0.9 ± 0.6
51	5.5 ± 0.3	14.6 ± 2	101 ± 13	3.1 ± 0.6	1 ± 0.1	27.5 ± 14.1	2.5 ± 0.8
71	5.6 ± 0.2	14.8 ± 2	95 ± 5	2.7 ± 0.3	1 ± 0.1	28.8 ± 4.1	4.1 ± 1

Table 6.4: The results of the weighted average of different parameters for the selected three bursts, which are discussed in Sec. 6.3.3 (Burst 27: highest count; Burst 51: highest average brilliance; Burst 71: highest counts after subtracting noise). W_e is the energy of the electrons. Ψ represents the unit of the brilliance: $10^{20}\mathrm{ph\ s^{-1}\,mm^{-2}\,mrad^{-2}\,0.1\%BW^{-1}}$.

The calculated values of the brilliance here are lower than the predicted maximum of the algorithm, which was $6.9 \pm 0.6 \times 10^{20}\,\mathrm{ph\ s^{-1}\,mm^{-2}\,mrad^{-2}\,0.1\%BW^{-1}}$. This is based on the uncertainty of the high brilliance shots in the bursts. These shots have high brilliance because the critical energy is estimated to be low, increasing the correction from the materials, see Sec 6.2.2. However, the χ^2-fit on the critical energy reveals a larger error and thus are valued lower to calculate this weighted average. The uncertainty of the bursts are significantly lower with this weighted average though, as one can infer from the data in Fig. 6.11 a). Overall, the data shows that the source yielded a brilliance of $4.1 \pm 1.0 \times 10^{20}\,\mathrm{ph\ s^{-1}\,mm^{-2}\,mrad^{-2}\,0.1\%BW^{-1}}$ with a critical energy of $2.7 \pm 0.3\,\mathrm{keV}$ at a power of only $5.6 \pm 0.2\,\mathrm{TW}$.

6.4 Summary and Future Experiments

A sophisticated machine learning algorithm has been utilised to optimise the x-ray source characteristic from a laser-plasma wakefield accelerator at comparatively low laser power. The achieved brilliance is plotted with a red diamond against other experiments in Fig. 6.16, as was done previously in this work. This experiment required the lowest laser power for a betatron beam that could be used for applications, and feature a high brilliance comparable to that from other experiments with a multiple of the laser power here[23]. As a previous experiment shows as well[24], this experiment based on ionisation injection exceeds any similar experiments with self-injection, indicating that the increase in charge based on the localised ionisation of the nitrogen also increase the betatron radiation significantly.

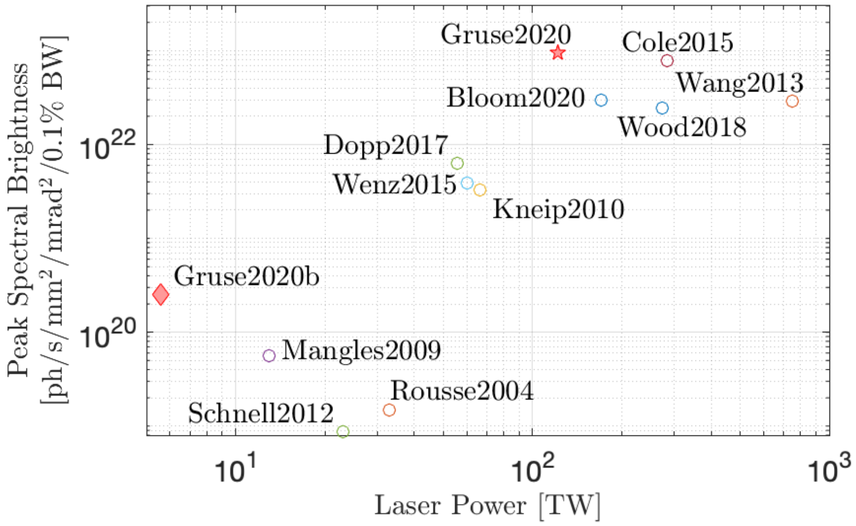

Figure 6.16: Shown are (again) the brightness for different experiments through out literature in respect to laser power, see Fig. 1.5 and Fig. 5.13. This experiment (*Gruse2020b*) is marked with a red diamond additional to the previously added star. This experiment is lowest laser power reported to produce a betatron beam but still exceeds $1 \times 10^{20}\,\mathrm{ph\ s^{-1}\,mm^{-2}\,mrad^{-2}\,0.1\%BW^{-1}}$.

The experimental values found here are still very high compared to the nearest other experiments performed at such low laser power. The ionisation injection and the automated scan based on the Bayesian optimisation gave the experiment this boost. The previous plots show that within an optimised window of the focus and density, the brightness still varies over a magnitude, because of the temporal phase of the laser. All 5 parameters play a role in increasing the number of photons and are correlated with one another. Thus, they need to be adjusted simultaneously. The large difference

---

[23] [59] S. P. D. Mangles *et al. APL* (2009); [60] M. Schnell *et al. PRL* (2012); [61] A. Rousse *et al. PRL* (2004).

[24] [62] A. Döpp *et al. Light: Science & Applications* (2017).

made by small differences in density range and shift in focus indicate the necessity of accurate control. The system has to be finely tuned to emit radiation at such low laser power. An adaptive optic and precise knowledge about the density seems unavoidable.

Chapter 7

Conclusion

Two major research thrusts have been developed as part of this thesis. The first main result of the thesis presented measurements in preparation for multi-staged wakefield acceleration. Adding multiple wakefield accelerators together is essential to achieving higher energies of accelerated electrons and to for example use these electrons in particle colliders. It is a promising approach, because one can overcome the fundamental limitation of energy depletion of the laser pulse inside the plasma. The second topic was the enhancement and the applications of betatron radiation. Two experiments on different laser systems were presented with a large difference in laser power. For the experiment at high power, $> 100\,\mathrm{TW}$, presented in chapter 5, a betatron source was optimised by scanning the plasma density. The betatron source then imaged different industrial samples and proved its potential for imaging low-Z materials. The second experiment presented in chapter 6 investigated betatron emission at a lower laser power. It utilised ionisation injection and Bayesian optimisation to increase x-ray flux and to produce a well-characterised betatron radiation source with the lowest laser power requirement yet demonstrated to the knowledge of the author.

7.1 Reflectivity and Guiding from Plasma-Mirror Reflected Laser Pulses

In the work described in chapter 2.12, a laser pulse was reflected off a plasma-mirror and the quality and reflection coefficient were measured. The laser propagated through a gas cell and the guiding properties were investigated. Simulations were performed and the results from the simulations and measurements were compared. The simulations also gave insights on the wakefield features to investigate possible acceleration of externally injected electrons.

A reflectivity of up to $73.7 \pm 8.9\%$ was achieved for the full laser beam. However, the beam quality of the initial laser beam turned out to be as low as the FWHM of the initial beam enclosed only $19.2 \pm 1.8\%$ of the energy compared to 50% expected for a perfect Gaussian laser profile. A better measurement of the reflectivity of the laser beam is the reflectivity of the central energy and it seemed that this figure is constant and independent from the initial energy. The average reflectivity of the central spot reaches $69 \pm 17\%$ and as one of the highlights of the chapter, the figure is added here Fig. 7.1.

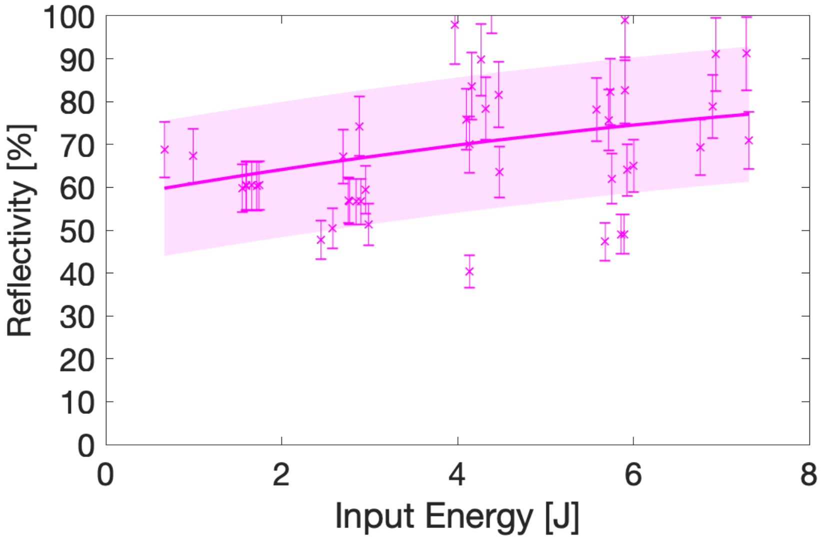

Figure 7.1: Repeated here as a highlight from chapter 2.12: The ratio between the energy reflected from the PM within the FWHM of the focal spot to the initial energy within the FWHM focal spot size.

The reflected beam was then inserted into a gas cell. The reflected laser pulses intensity of up to $1.26 \times 10^{18}\,\mathrm{W\,cm^{-2}}$ or a normalised vector potential of $a_0 = 0.77$. The self-guiding of the reflected laser pulse through the gas cell was investigated for the first time to the knowledge of the author. The energy exiting the gas cell had a strong inverted dependence on the plasma density. It was found that the exiting spot size of the laser beam was on the order of the plasma density wave wavelength. The applied densities ranged between $0.29 \times 10^{18}\,\mathrm{cm^{-3}} - 0.78 \times 10^{18}\,\mathrm{cm^{-3}}$, which corresponds to a plasma wave wavelengths of $62\,\mathrm{\mu m}{-}37.8\,\mathrm{\mu m}$. PIC simulations with EPOCH using different profiles presenting the measured laser pulses were performed. The focus of these simulations was to investigate the effect of the energy in the wings to the wakefield and its effect on the guiding properties. The simulations indicated that the pulse underwent relativistic self-focusing, while still being below the critical power threshold. Some parts of the wings were focused into the plasma channel, increasing the total amount of guided energy and even causing the pulse to focus further. However, this effect depended strongly on the density and the beam profile. While a laser profile that was more Gaussian-shaped showed enhanced focussing, a laser beam with lower quality showed no increase in guiding. This demonstrates the necessity of a good quality laser pulse with high beam quality for reliable wakefield-based acceleration. The analysis of the wakefield inside the simulations showed significant variations between all simulations. The maximum achievable energy gain was $238\,\mathrm{MeV}$ for the highest simulated density. At this density, the initially imperfect beam was focussed into a Gaussian shape. However, the $238\,\mathrm{MeV}$ energy gain decreases on average when considering realistic longitudinal widths for the electron beam.

A simulation of an improved laser beam in which 50% of the initial energy is within the FWHM reflected off the plasma mirror indicates the potential acceleration of an externally injected electron beam to $929\,\mathrm{MeV}$ as highlighted here in Fig. 7.2, which is promising for future experiments. The quality of the laser driver is thus crucial in deciding whether a staged wakefield accelerator can be operated or not.

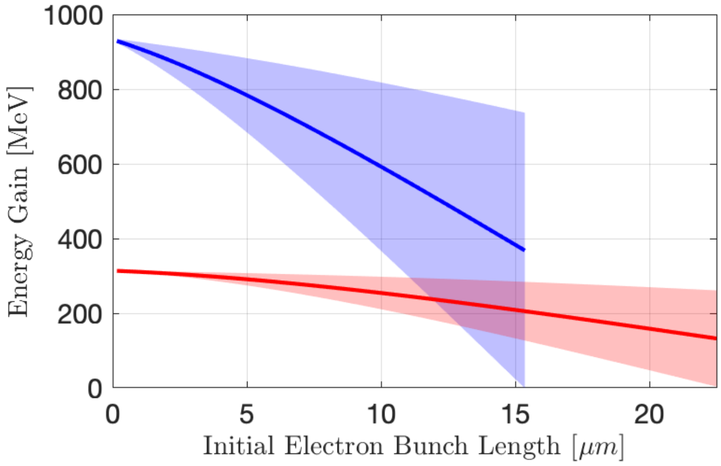

Figure 7.2: To emphasise that future experiments could achieve GeV energy gain, the results found from a simulation presented in chapter 2.12: The estimated energy gain and energy spread for the injected electrons into the wakefield depending on the electron bunch length for a Gaussian beam profile with no energy loss in the wings for $w_{FWHM} = 50\,\mu\mathrm{m}$ at $0.29 \times 10^{18}\,\mathrm{cm}^{-3}$ (red) and $0.78 \times 10^{18}\,\mathrm{cm}^{-3}$ (blue).

Future experiments could benefit from more advanced plasma mirror set-ups as has been demonstrated in Scott et al.[1]. Here, a second laser pulse arrived before the main laser pulse to initiate a uniform plasma. The beam quality was optimised and the reflectivity coefficient reached $96 \pm 2.5\%$ by changing the delay between both pulses. However, the laser pulse intensity was several orders of magnitudes lower, around $\approx 1 \times 10^{15}\,\mathrm{W\,cm}^{-2}$, and an experiment at such intensities as required for wakefield acceleration has not yet been conducted.

---

[1] [230] G. G. Scott *et al. NJP* (2015).

7.2 Enhancement of Betatron Radiation and Imaging Industrial Samples

The betatron radiation from a wakefield accelerator at the Astra-Gemini laser was measured with an indirect x-ray camera while simultaneously measuring electron bunch properties. The electron bunch properties consisted of electron energy and the number of counts on the electron spectrometer camera, which are proportional to the charge in the bunch. The set-up was used to optimise the stability and brilliance of the source by scanning through the plasma density. The maximum in peak energy and electron charge did not correlate with the maximum in photon flux, which might be considered unexpected. When the density was increased, the charge and energy decreased again, while the measured x-ray flux increased on average and became more stable.

These contradictory findings led to the creation of the PIPE/Self-focusing algorithm, inspired by Bloom et al.[2]. This newly developed code introduces a self-focusing term to the pre-injection pulse evolution mechanism formulated by Bloom et al. and solves the equations slightly more generally. It also utilises more accurate equations for the maximum electric fields found in the theory section of this thesis. The fit of the algorithm with the measurements does not explain the secondary point of injection, nor does it explain how the electrons possibly emit more radiation at a higher density.

A second approach to understand the results is presented with 2D simulations using EPOCH at the two densities at which the electron energy is higher, but flux is low (lower density) and at which the electron energy is lower, but the flux is increased (higher density). The 2D simulations allow mostly insights on the laser behaviour in the plasma and the trajectories of the electrons inside the wakefield. The electrons tracked in the simulations do not reach such high energies as measured, which is expected as the group velocity of the laser pulse is not correct in the finite grid size of the simulation code. It turns out that the electrons undergo multiple periods of acceleration and deacceleration and the simple image of electrons being accelerated up to the dephasing length is not necessarily true. A valuable insight is the pulse compression as it seems that a minimum pulse length is reached around $10\,\mathrm{fs}$ and the self-focusing subceeds the matched spot size and follows $\lambda_p/\sqrt{a_0}$ rather than $\sqrt{a_0}\lambda_p$. A strong mismatch between laser spot size and matched density results in an unstable wakefield.

The betatron source was characterised at a density of $4.4 \pm 0.4 \times 10^{18}\,\mathrm{cm}^{-3}$, which showed the highest stability and a brightness of $1.3 \pm 0.6 \times 10^{22}\,\mathrm{ph\ s^{-1}\,mm^{-2}\,mrad^{-2}}\cdot 0.1\%\mathrm{BW}^{-1}$ in the peak and $1.1 \pm 0.7 \times 10^{22}\,\mathrm{ph\ s^{-1}\,mm^{-2}\,mrad^{-2}}\,0.1\%\mathrm{BW}^{-1}$ on average. The brightness exceeds previously reported values, which can be seen in Fig. 7.3 as (*Gruse2020*).

---

[2] [58] M. S. Bloom *et al. PRAB* (2020).

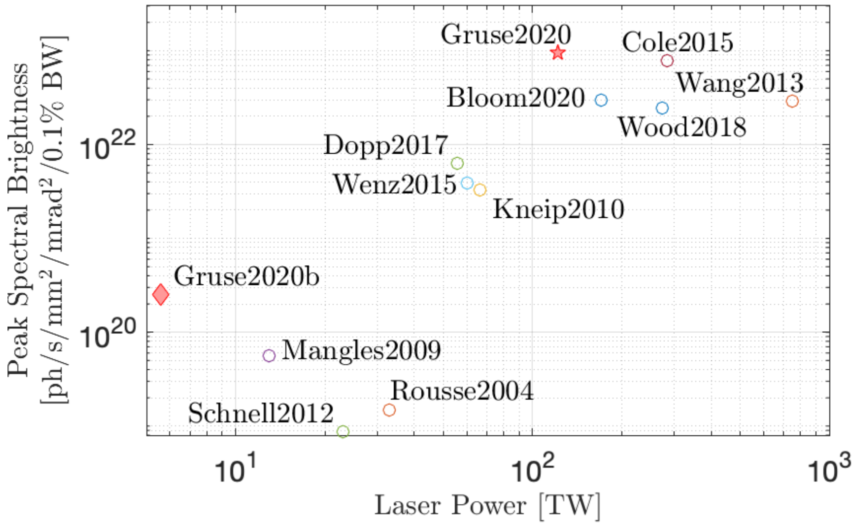

Figure 7.3: To highlight the results, shown again are the brightness for different experiments through out literature in respect to laser power. The values achieved in this work are marked with a star (*Gruse2020*) and (*Gruse2020b*).

The imaging quality of the source showed great capabilities, proven by imaging different resolution targets at different positions. The images had high contrast and lines down to $4\,\mu\mathrm{m}$ separations were visibly distinguishable and their modulation transfer function was presented. A topological sample, which is used in μ-XCT imaging, showed a clear contrast for the different parts when imaged with the source. Furthermore, a pouch battery and kink band failure in a composite cylinder withstand the judgement of industrial partners and the work presented was published[3].

A betatron source has the advantage of being renewable and its repetition rate is limited mostly by the repetition rate of the high power laser system, making it a good candidate for being a future industrial research light-source which is fast and accurate. A full tomography scan of a macroscopic sample has not been demonstrated for industrial imaging. A macroscopic sample is hereby defined as a sample of transverse size, such that the scan requires transverse motion to combine several images to obtain the full view of the sample. This type of scan is the common way of imaging samples with a XCT machine and hence it would be beneficial to see the how the betatron source directly compares. It would require a fast and reliable laser system though, because the scan duration would otherwise be impractical.

Another advantage of the betatron source has been the low divergence and fs-pulse duration, but this uniqueness has not been taken full advantage yet. Imaging a plastic sample, as it is being 3D printed would show the full potential of the betatron source, as the 3D printer requires space so that the source has to be far away and the curing of the plastic in the process would easily be captured within the x-ray pulse duration.

---

[3] [183] J.-N. Gruse *et al. NIMA* (2020).

7.3 Machine Learning on Ionisation Injection LPWA

Betatron radiation was also investigated with a lower power laser system. The calibration of the diagnostics was a significant part of preparing the Bayesian optimisation of electron and x-ray properties. A design code was developed to decide on materials for x-ray absorption to estimate the critical energy of measured betatron signal. Allowing high transmission was necessary to record as much signal as possible due to the low photon flux. The optimisation of the number of counts on the x-ray camera was performed by exploiting increased charge aided by ionisation injection using an N_2-doped He-gas. However, the research also shows that the counts and the brilliance can differ by an order of magnitude and future optimisation would potentially benefit by combining the electron and x-ray diagnostics to improve the brilliance directly.

A closer look at the correlations of the individual parameters with each other indicates that the fine-tuning of the hyperspace parameter of the algorithm and initialisation of the kernel requires just as much attention as setting up a physical experiment. This was shown by the lack of data points in the parameter space of the focus shift. Manual optimisation seems not to be a reasonable alternative though, because comparing multiple input variables with each other offer no obvious linear correlations. The true function of the brilliance depending on the attributing variables is of such high dimensionality that it would take an extraordinary amount of time to fully optimise it when doing sequential 1-dimensional scans of the parameters.

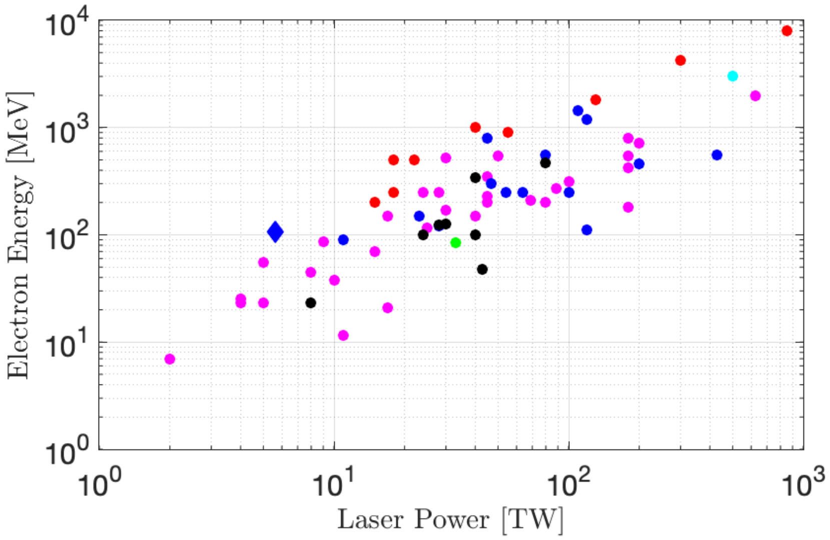

Figure 7.4: The laser power vs electron energy from this experiment is added to Fig. 1.4 b) with a blue diamond. The other reports of ionisation injection based electron energies are also depicted in blue.

The final observation is that the increase in brilliance seems mostly dominated by the amount of injected charge in this parameter range. Extracting finer dependencies requires more accurate diagnostics and more importantly a more stable laser system with less shot-to-shot fluctuations. This is supported by the observation that though individual shots within single bursts used to obtain weighted averaging of the brilliance vary significantly even though they are within the confidence bounds of the averaged values.

The peak brilliance was measured to be $4.1 \pm 1.0 \times 10^{20}\,\mathrm{ph\ s^{-1}\,mm^{-2}\,mrad^{-2}} \cdot 0.1\%\mathrm{BW}^{-1}$ with a critical energy of $2.7 \pm 0.3\,\mathrm{keV}$ at powers as of $5.6 \pm 0.2\,\mathrm{TW}$ at a density of $14.2 \pm 0.2 \times 10^{18}\,\mathrm{cm}^{-3}$. This is to our knowledge the lowest power at which a usable betatron beam has been shown. Furthermore, the energy of the electrons also improved even for such low laser power. The electron energy achieved here was remarkable as well as one can see in Fig. 7.4 and doubles previous report on electron's energy at this laser power level. The electron data showed in one burst a peak energy of $106.8 \pm 2.5\,\mathrm{MeV}$ with a total charge of $17.5\,\mathrm{pC}$.

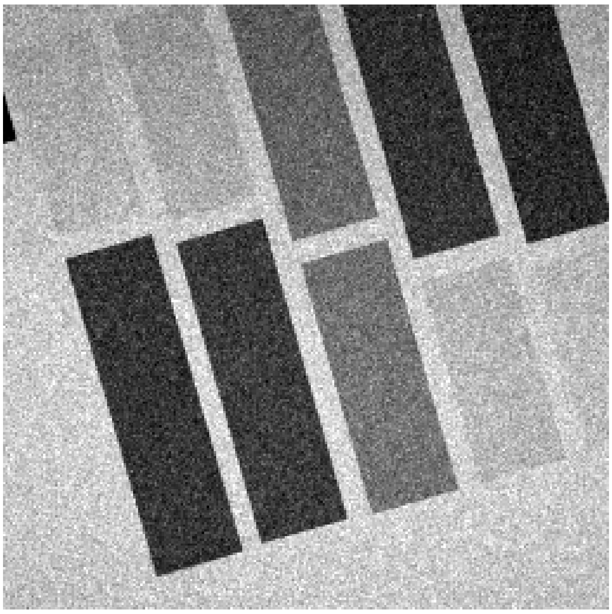

Figure 7.5: Radiograph of the filter obtained from burst 71, which had the highest brilliance. Outlying pixel values beyond 30,000 were removed before adding the images. No other post-processing needed to be applied to the data.

Small facilities and universities which have low-power laser systems can utilise betatron radiation for experiments when employing the shown techniques, such as automation and sophisticated optimisation algorithms. This would create more freedom and the space of creativity for those research groups as they would have easier access to advanced light sources.

Even though not presented in this chapter, the length of the gas cell was also adjustable. A missing parameter, which would be of great interest would be the length of density ramp(s). An effort has been made by using a gas jet in front of the gas cell, but due to spatial constraints and difficulty in obtaining accurate control of the density, the measurements had no conclusion, but one can still expand on this front.

The experiment can be improved in the future further, by optimising the set-up and the applied algorithm. This set-up suffered from high noise because the direct detection camera was next to the electron dump without any shielding. Also, the high energy electrons were flying close to the camera. Both could be improved by using a stronger magnet and a small dedicated lead chamber within the lead chamber to reduce the noise.

As a small highlight, a radiograph of the filter pack from the most brilliant burst can be seen in Fig. 7.5. 10 shots were integrated after extreme outliers (counts over 30,000) were removed. The image shows good contrast between the individual materials, which allowed for the characterisation of the source.

As a final discussion, a possible experiment based on the results of all three chapters could be proposed as the following: The staging of two laser-based accelerator stages could inject an electron beam off-axis in the second gas cell. The plasma wave wavelength could be large so that the electron beam would have a large and well defined distance to the central axis. The large radius of curvature would increase the critical energy. Furthermore, an increase in energy in the second cell would increase the critical energy as well, creating a hard x-ray source. Such a source will penetrate higher Z-materials increasing the applications to possibly metallic industrial samples. One has to find the optimal electron beam supporting such a scenario, which requires optimisation of the input laser beams and gas cell densities. Such a large amount of parameter will need more sophisticated optimisation than sequential 1D scans such as Bayesian optimisation.

Appendix A

Introduction

A.1 Laser Power against Electron Energy

The Fig. 1.4 uses electron energies and laser powers from a large amount of publications, which was used in[1]. The plots are adapted and extended. Added are tables, which references the data to the publication Tabs. A.1 and A.2.

A.2 Laser Power against Peak Brilliance

The laser power compared to the brilliance is shown in the introduction Fig. 1.5, and is updated through out the progression of this work with new experimental values. The peak brilliance of the literature values were recalculated with a standardised formula to compare the values consistently.

The brightness is based on the number of photons per shot N_{ph}, the source size $r_{beta}^2\pi$, the solid angle, which is $\theta_x\theta_y\pi$ for an elliptic beam or $\theta_x\theta_y$ if a square was measured[68] and the pulse length of the laser beam τ. The bandwidth was taken into account using $(0.001ES(E, E_{crit}))_{max} \approx 0.001$[69]. The values stated in this thesis differ slightly, because for one $(0.001ES(E, E_{crit}))_{max}$ was calculated accurately and the x-ray pulse duration was based on the plasma wave wavelength. The pulse duration of the x-ray beam should be as long as the electron beam, emitting the x-rays. And determining the maximum length of the electron beam to the length of the plasma wave gives an upper length of the x-ray pulse.

---

[1] [36] S. P. Mangles. *CAS-CERN Accelerator School: Plasma Wake Acceleration 2014, Proceedings* (2014).

[68] In case of an elliptic beam, $theta$ was calculated using the major and minor radii of the beam and in a rectangle measurements, $theta$ is based on the side length of the rectangle.

[69] [167] J. C. Wood, PhD Thesis, Imperial College London (2016), Ch. 3.5.7.

Table A.1: Publication used in the figures described in this section part 1.

Publication	Citation Link	Laser Power [TW]	Electron Energy [MeV]
Gonsalves:PRL2019	[2]	850	8000
Mirzaie:SciRep2015	[3]	120	1200
Couperus:NatComms2017	[4]	64	250
Swanson:PRSTAB2017	[5]	40	100
Ferri:SciRep2016	[6]	45	348
Ferri:SciRep2016	[7]	45	230
Ferri:SciRep2016	[8]	45	202
Kuschel:PRAB2016	[9]	23	150
Steinke:Nature2016	[10]	28	120
Golovin:PRSTAB2015	[11]	47	300
Thaury:SciRep2015	[12]	28	123
Schnell:JPP2015	[13]	25	115
Khrennikov:PRL2015	[14]	43	48
Leemans:PRL2014	[15]	300	4200
Powers:Natphot2014	[16]	100	250
Sarri:PRL2014	[17]	430	550
Banerjee:PRSTAB2013	[18]	100	315
Wang:NatCom2013	[19]	625	2000
Kim:PRL2013	[20]	500	3000
Chen:PRL2013	[21]	54	250
Corde:NatComms2013	[22]	28	250
Walker:NJP2013	[23]	55	900
Albert:PRL2013	[24]	88	268
Burza:PRSTAB2013	[25]	24	100
Kneip:PRSTAB2012	[26]	69	212
Mo:APL2012	[27]	80	550
Fourmaux:APL2012	[28]	80	470
Brijesh:POP2012	[29]	30	125
Gonsalves:NatPhys2011	[30]	40	341
LundhNatPhys2011	[31]	33	84
Pollock:PRL2011	[32]	200	460
Liu:PRL2011	[33]	45	800
Fourmaux:NJP2011	[34]	80	200
Lu:APL2011	[35]	130	1800
McGuffey:PRL2010	[36]	120	110
Clayton:PRL2010	[37]	110	1450
Ibbotson:NJP2010	[38]	30	520

Table A.2: Publication used in the figures described in this section part 2.

Publication	Citation Link	Laser Power [TW]	Electron Energy [MeV]
Pak:PRL2010	[39]	11	90
Schmid:PRSTAB2010	[40]	8	23
Froula:PRL2009	[41]	200	720
Kneip:PRL2009	[42]	180	800
Kneip:PRL2009	[43]	180	540
Kneip:PRL2009	[44]	180	420
Kneip:PRL2009	[45]	180	180
Schmid:PRL2009	[46]	5	23
Hafz:NatPhot2008	[47]	50	540
RowlandsRees:PRL2008	[48]	15	200
Gamucci:IEEETPS2008	[49]	10	38
Karsch:NJP2007	[50]	18	250
Karsch:NJP2007	[51]	18	500
Ohkubo:PRST AB2007	[52]	17	21
Masuda:POP2007	[53]	4	23
Masuda:POP2007	[54]	2	7
Leemans:NatPhys2006	[55]	40	1000
Reed:APL2006	[56]	40	150
Faure:Nature2006	[57]	24	250
Mangles:PRL2006	[58]	17	150
Leemans:NatPhys2006	[59]	22	500
Hosokai:PRE2006	[60]	11	12
Hidding:PRL2006	[61]	8	45
Hsieh:PRL2006	[62]	5	55
Masuda:JournalPhysiqueIV2006	[63]	4	25
Miura:APL2005	[64]	2	7
Faure:Nature2004	[65]	30	170
Mangles:Nature2004	[66]	15	70
Geddes:Nature2004	[67]	9	86

Appendix B

Theory on LPWA

This appendix chapter investigates some missing derivations in relation with the theory on laser pulses.

B.1 Interpretations of Maxwell's Equations

The Maxwell equation are a set of differential equation, which all describe the nature of the electric and magnetic field and how both change dependent on each other. The equations can be seen in Eq. (2.1). For completion the integral version of these equations are the following

$$\text{Gauss' Law} \qquad \int_S \vec{E}\mathrm{d}\vec{S} = \int_V \frac{\rho}{\epsilon}\mathrm{d}V \tag{B.1}$$

$$\text{Gauss' Law for Magnetism} \qquad \int_S \vec{B}\mathrm{d}\vec{S} = 0 \tag{B.2}$$

$$\text{Faraday's Law of Induction} \qquad \int_L \vec{E}\mathrm{d}\vec{L} = -\frac{\mathrm{d}}{\mathrm{d}t}\int_A \vec{B}\mathrm{d}\vec{A} \tag{B.3}$$

$$\text{Ampère's Circuital Law} \qquad \int_L \vec{B}\mathrm{d}\vec{L} = \mu_0\left(\int_A \vec{J}\mathrm{d}\vec{A} + \epsilon\frac{\mathrm{d}}{\mathrm{d}t}\int_A \vec{E}\mathrm{d}\vec{A}\right) \tag{B.4}$$

in which $\vec{S}$ is the integration over the surface of the volume V. Similar is $\vec{L}$ the path along the side of the area $\vec{A}$.

Gauss' Law describes that the charged enclosed by the volume V is proportional to the electric flux over the surface of that specific volume.

Gauss' Law for Magnetism immediately shows the difference compared to the electric field. Where there are monopoles or electric charges for electric fields there are only dipoles creating magnetic fields. This means that magnetic field lines make loops and do not have ends or sources. In other words, if a closed volume is constructed, all the field lines entering and flowing out are of the same strength.

Faraday's Law combines the electric and magnetic field and is time dependent. The change of the magnetic field in time through an area induces an electric field along its perimeter. Th electric field has closed field lines in comparison to the static electric field described in with Gauss' Law.

Ampère's Circuital Law in this case includes Maxwell's addition in the second summand. The first one describes how magnetic field through a perimeter can be generated by a current enclosed through a surface. Maxwell's addition introduces that time a changing electric field can as well generate a magnetic field. This finally can be combined with the other Maxwell equations so that an electric-magnetic wave can exist in vacuum without any source term.
As a final note the orthogonality of the wavevector and the electro-magnetic fields are described. It follows directly from the differential equation (2.1)

$$\vec{k} \times \vec{E} \propto \vec{B} \tag{B.5}$$

$$\vec{k} \times \vec{B} \propto \vec{E} \tag{B.6}$$

that $\vec{B}$ is orthogonal to $\vec{k}$ and $\vec{E}$, but also that $\vec{E}$ is orthogonal to $\vec{k}$ and $\vec{B}$ and therefore they compose a set of orthogonal vectors.

B.2 Paraxial Ray Wave Equation

With the ansatz in section 2.1 the wave equation can be evaluated using eq. [2.8]

$$\vec{\nabla}^2 \vec{E} - \frac{\eta^2}{c^2}\frac{\partial^2 \vec{E}}{\partial t^2} = 0 \tag{B.7}$$

$$\vec{E} = \vec{E}_A(\vec{x}) \exp^{-i(\omega_0 t - \vec{k}\vec{x})} \tag{B.8}$$

$$\frac{\eta^2}{c^2}\frac{\partial^2 \vec{E}}{\partial t^2} = \frac{\eta^2 \omega_0^2}{c^2}\vec{E} = -k^2 \vec{E} \tag{B.9}$$

$$\frac{\partial \vec{E}}{\partial z} = \exp^{ikz}\left[\frac{\partial \vec{E}_A(\vec{x})}{\partial z} + ik\vec{E}_A(\vec{x})\right] \tag{B.10}$$

$$\frac{\partial^2 \vec{E}}{\partial z^2} = \exp^{ikz}\left[\frac{\partial^2 \vec{E}_A(\vec{x})}{\partial z^2} + 2ik\frac{\partial \vec{E}_A(\vec{x})}{\partial z} - k^2\vec{E}_A(\vec{x})\right] \tag{B.11}$$

$$\Rightarrow \left(\vec{\nabla}^2 + 2ik\frac{\partial}{\partial z}\right)\vec{E}_A(\vec{x}) = 0\ . \tag{B.12}$$

This can be simplified using the *slowly varying envelope approximation* (SVEA), which assumes that the amplitude if the wave travelling in z-direction changes much slower than the oscillation period. In space or in homogeneous environments this is true without doubt. This yield to

$$\left|\frac{\partial^2 \vec{E}_A(\vec{x})}{\partial z^2}\right| \ll \left|k_0 \frac{\partial \vec{E}_A(\vec{x})}{\partial z}\right| \tag{B.13}$$

$$\left(\vec{\nabla}^2 + 2ik\right) \vec{E}_A(\vec{x}) \approx \left(\vec{\nabla}_\perp^2 + 2ik\right) \vec{E}_A(\vec{x}) = 0 \tag{B.14}$$

in which $\vec{\nabla}_\perp = \frac{\partial}{\partial x}\hat{x} + \frac{\partial}{\partial x}\hat{y}$ is the transverse Laplace operator. Using cylindrical coordinate transformation and assuming cylindrical symmetry this results in the *paraxial ray wave equation*

$$\text{with} \qquad \vec{\nabla}_\perp^2 = \frac{\partial^2}{\partial r^2} + \frac{1}{r}\frac{\partial}{\partial r} + \underbrace{\frac{1}{r}\frac{\partial^2}{\partial \phi^2}}_{\text{cylindrical symmetry}\approx 0} \tag{B.15}$$

$$\Rightarrow \qquad \left(\frac{\partial^2}{\partial r^2} + \frac{1}{r}\frac{\partial}{\partial r} + 2ik\right) \vec{E}_A(\vec{x}) = 0 \tag{B.16}$$

B.3 Integration of the Intensity

Starting from equation (2.17) the power from a Gaussian intensity profile is

$$\frac{1}{\mathrm{d}x} \exp(-x^2) = -2x \exp(-x^2) \tag{B.17}$$

$$\int_0^\infty \int_0^{2\pi} r \exp(-2r^2/w^2) \mathrm{d}r \mathrm{d}\phi \underbrace{=}_{x=\sqrt{2}r/w} \frac{w}{\sqrt{2}} \cdot \frac{w}{\sqrt{2}} \cdot 2\pi \cdot \left[-\frac{1}{2} \cdot \exp(-x^2)\right]_0^\infty \tag{B.18}$$

$$P(t) = \frac{1}{2} I(t) \left(\pi w^2\right) \tag{B.19}$$

Now taking care of the time dependent part one get for the energy, one uses the identity for a Gaussian integral as

$$\int\limits_{-\infty}^{\infty} \exp(-x^2)\mathrm{d}x = \sqrt{\pi} \tag{B.20}$$

$$E = \int\limits_{-\infty}^{\infty} P(t)\mathrm{d}t \tag{B.21}$$

$$\int\limits_{-\infty}^{\infty} \exp(-t^2/\tau^2)\mathrm{d}t \underbrace{=}_{x=\sqrt{2}/\tau} \cdot\tau \cdot \sqrt{\pi/2} \tag{B.22}$$

$$E = \frac{1}{2}\left(\pi w_0^2\right)\tau\sqrt{\pi/2}I_0 \tag{B.23}$$

Note that now the peak intensity is used as well as the beam waist at its minimum. As practically one measures the *Full-Width-Half-Maximum* (FWHM) of the **intensity** so that it is convenient to rewrite this into these values by using the identity for the Gaussian distribution with the FWHM as

$$\exp\left(-2r_{1/2}^2/w^2\right) \overset{!}{=} \frac{1}{2} \tag{B.24}$$

$$\Rightarrow r_{1/2}^2/w^2 = \frac{\log(2)}{2} \tag{B.25}$$

$$\Rightarrow w_{\text{FWHM}} = 2r_{1/2} = 2\sqrt{\frac{\log(2)}{2}}w = \sqrt{2\log(2)}w \tag{B.26}$$

with $\log(x)$ being the natural logarithm. By comparing this with the above mentioned equations it follows $x_{\text{FWHM},I} = \sqrt{2\log(2)}\hat{x}$ and with similar derivation $t_{\text{FWHM},I} = 2\sqrt{\log(2)}\tau$, so that one can summarise for the intensity and power

$$E = \underbrace{\left(\sqrt{\frac{\pi}{8\log(2)}}\tau_{\text{FWHM},I}\right)}_{\text{time integration}} \cdot \underbrace{\left(\frac{\pi w_{\text{FWHM},I}^2}{4\log(2)}\right)}_{\text{transverse integration}} \cdot I_0 \tag{B.27}$$

$$E = P_0\left(\sqrt{\frac{\pi}{8\log(2)}}\tau_{\text{FWHM},I}\right) \tag{B.28}$$

A good approximation for the peak intensity of the laser system is then given by the approximation

$$I_0\left[10^{18}\ \mathsf{W/cm}^2\right] = 1.2\cdot 10^5\cdot\frac{E[\mathsf{J}]}{w^2_{\mathsf{FWHM},I}[\mu\mathsf{m}]\cdot\tau_{\mathsf{FWHM},I}[\mathsf{fs}]} \tag{B.29}$$

$$P_0[\mathrm{PW}] = 1.3\frac{E}{\tau_{\mathsf{FWHM},I}[\mathsf{fs}]} \tag{B.30}$$

Giving the Rayleigh-length in terms of the FWHM can be an additional helpful equation, since it estimates the required precision of alignment as within a Rayleigh-length the power varies acceptably low when entering the plasma. The equation changes to

$$z_R = \frac{\pi w_0^2}{\lambda} = \frac{\pi w^2_{\mathsf{FWHM},I}}{2\log(2)\lambda} \approx 2.3\frac{w^2_{\mathsf{FWHM},I}}{\lambda} \tag{B.31}$$

B.3.1 Practical Units for the Normalised Vector Potential

As we have already practical units for the normalised vector potential in respect to the intensity (Eq. (2.23)), it would be experimentally useful to rewrite the power and energy in terms of a_0 (or in their inverse). Using (2.23), the power (B.19) and energy (B.27) yield to

$$P = \frac{1}{2}\pi w_0^2\frac{m_e^2\omega_0^2c^2}{2e^2c\mu_0}a_0 = \frac{pi^3m_e^2c^3}{2\log(2)e^2\mu_0}\frac{a_0^2w^2_{\mathsf{FWHM}}}{\lambda^2} \approx 15.5[\mathrm{GW}]\frac{a_0^2w^2_{\mathsf{FWHM}}}{\lambda^2} \tag{B.32}$$

$$\Rightarrow a_0 = 64.4\frac{\lambda\sqrt{P[\mathrm{TW}]}}{w_{\mathsf{FWHM}}} \tag{B.33}$$

$$E = 1.2\cdot 10^{-5}\frac{\tau_{\mathsf{FWHM}}[\mathrm{fs}]w^2_{\mathsf{FWHM}}a_0^2}{\lambda^2} \tag{B.34}$$

$$a_0 = 294\frac{\lambda}{w_{\mathsf{FWHM}}}\sqrt{\frac{E}{\tau_{\mathsf{FWHM}[\mathrm{fs}]}}} \tag{B.35}$$

B.4 Debye-Length

Starting from the Lorenz gauge for electro-magnetic waves

$$\vec{\nabla}\vec{A} + \frac{1}{c^2}\frac{\partial\phi}{\partial t} = 0\ , \tag{B.36}$$

which introduces the vector potential $\vec{A} = \vec{A}(\vec{x},t)$ and the scalar potential $\phi = \phi(\vec{x},t)$. By defining the magnetic field as shown in eq. (2.5) and using Faraday's Law of Induction shown in eq. (2.1) the electric field can be validated

$$\vec{B} = \vec{\nabla} \times \vec{A} \qquad \text{and} \qquad \vec{\nabla} \times \vec{E} = -\frac{\partial \vec{B}}{\partial t} \tag{B.37}$$

$$\vec{\nabla} \times \vec{E} = -\frac{\partial \vec{B}}{\partial t} = -\vec{\nabla} \times \left(\frac{\partial}{\partial t}\vec{A}\right) \qquad \Rightarrow \qquad \vec{\nabla} \times \left(\vec{E} + \frac{\partial \vec{A}}{\partial t} + {}^{1}\vec{\nabla}\phi\right) = 0 \tag{B.38}$$

A point source is added into the system. This results into electric and magnetic fields and the system will adapt. After a relaxation time the system reaches thermal equilibrium in the plasma so that only static magnetic and electric fields are present it follows that $\frac{\partial \vec{B}}{\partial t} = 0 = \vec{\nabla} \times (\frac{\partial \vec{A}}{\partial t})$ and Eq. (2.5) to $\vec{E} = \vec{\nabla}\phi$. The scalar potential is therefore the electrostatic potential. Before finally deriving the Debye-length the distribution function for this case should be solved. Using the Maxwell-Boltzmann distribution $\exp(E/k_B T)$ and saying that far way from the source, the field can be assumed to be shielded and the electron density can be set equal to the ion density, it follows for the electron density

$$n_e = \int_{-\infty}^{\infty} f(v_e)\mathrm{d}v_e = \int_{-\infty}^{\infty} C \exp\left(-\frac{\frac{1}{2}m_e v_e^2 - e\phi(x)}{k_B T}\right) \mathrm{d}v_e \,. \tag{B.39}$$

The constant C in this term can be solved by using the assumptions above. At $x \to \pm\infty$ the electron density is equal to the undisturbed electron density $n_e(x \to \pm\infty) = n_0 = n_i$ and the ion density. Also the potential is shielded $\phi(x \to \pm\infty) \to 0$ so that it follows with the constant $C = n_0 m_e / 2\pi k_B T$

$$n_e(x) = n_0 \exp\left(\frac{e\phi(x)}{k_B T}\right) \cdot \int_{-\infty}^{\infty} \frac{m_e}{2\pi k_B T} \exp\left(-\frac{\frac{1}{2}m_e v_e^2}{k_B T}\right) \mathrm{d}v_e \tag{B.40}$$

$$n_e(x) = n_0 \qquad \underbrace{\exp\left(\frac{e\phi(x)}{k_B T}\right)}_{\text{for } x \ll 1:\ \exp(x) \approx 1 + x + \frac{x^2}{2} + \cdots} \qquad \approx n_0 \left(1 + \frac{e\phi(x)}{k_B T}\right) \tag{B.41}$$

in which the last approximation is valid assuming that the field potential is much smaller than the thermal energy of the electrons $e\phi \ll k_B T$. With this and the definition of the electric field in terms of the scalar potential differential equation of the scalar potential is derived as

---

[1] Adding the term is legitimated as the curl of a gradient is zero.

$$\Delta\phi = -\vec{\nabla}\vec{E} = -\frac{\rho(x)}{\epsilon_0} \tag{B.42}$$

$$\rho(x) = -e\left(n_e(x) - n_i\right) \approx \frac{n_0 e^2 \phi(x)}{k_B T} \tag{B.43}$$

$$\Delta\phi = \frac{n_0 e^2}{\epsilon_0 k_B T}\phi(x) \tag{B.44}$$

By assuming spherical symmetry of the electric potential the equation has the solution

$$\phi(x) = \phi_0 \exp\left(-\frac{|x|}{\lambda_D}\right) , \tag{B.45}$$

which contains the definition of the Debye-length

$$\lambda_D = \sqrt{\frac{\epsilon_0 k_B T}{n_0 e^2}} . \tag{B.46}$$

B.5 Plasma-Frequency

The plasma frequency is a fundamental parameter in the field of LWPA to describe the behavior of an electron in a plasma. The following equations are used for the derivation as

Equation of motion
$$\frac{\mathrm{d}p}{\mathrm{d}t} = m_e \frac{\mathrm{d}v_e}{\mathrm{d}t} = m_e\left(\frac{\partial v_e}{\partial t} + v_e \frac{\partial v_e}{\partial x}\right) = -eE \tag{B.47}$$

Continuity equation
$$\frac{\partial n_e}{\partial t} + \frac{\partial(n_e v_e)}{\partial x} = 0 \tag{B.48}$$

Gauss Law
$$\epsilon_0 \frac{\partial E}{\partial x} = e(n_i - n_e) . \tag{B.49}$$

Starting with perturbation theory as $n_e = n_{e,0} + n_{e,1}$, in which $n_{e,0}$ is constant and the first term $n_{e,1}$ is the first order of perturbation. Assuming further a constant ion density $n_i = n_{e,0}$, a velocity purely as a distortion $v_e = v_{e,0} + v_{e,1} = v_{e,1}$ and no static background electric field so that $E = E_1$, the equations simplify to

$$m_e \frac{\partial v_e}{\partial t} = -eE_1 \tag{B.50}$$

$$\frac{\partial n_{e,1}}{\partial t} + n_{e,0}\frac{\partial v_e}{\partial x} = 0 \tag{B.51}$$

$$\epsilon_0 \frac{\partial E_1}{\partial x} = -en_{e,1} \tag{B.52}$$

as the multiplication between first order components can be neglected. The ansatz for the parameter of $X_1 = \hat{X}_1 \exp(i(k_p x - \omega_p t))$ results in the equation system

$$-i\omega_p m_e \hat{v_{e,1}} = -e\hat{E}_1 \tag{B.53}$$

$$-i\omega_p \hat{n}_{e,1} = ik_p n_{e,0}\hat{v}_{e,1} \tag{B.54}$$

$$ik_p \epsilon_0 \hat{E}_1 = -e\hat{n}_{e,1} \tag{B.55}$$

which solved for ω_p results in the plasma frequency

$$\omega_p = \sqrt{\frac{n_{e,0}e^2}{m_e \epsilon_0}} \tag{B.56}$$

B.6 Dispersion Relation Details

Section 2.6 is describing the derivation of the refractive index. This section is complementary to go into a few details of the derivations, which are missing. Using Eqs. (2.39)

$$v_\phi = \frac{\omega}{k} = \frac{c^2}{\eta}$$

$$v_G = \frac{\mathrm{d}\omega}{\mathrm{d}k}$$

and the dispersion relation, Eq. 2.44

$$\omega = \sqrt{\omega_p^2 + c^2k^2}$$

yield to

$$v_\phi = \sqrt{\frac{\omega_p^2}{k^2} + c^2} \tag{B.57}$$

$$v_G = \frac{1}{2}\frac{2c^2k}{\sqrt{\omega_p^2 + c^2k^2}} = \frac{c^2}{\sqrt{\frac{\omega_p^2}{k^2} + c^2}} = \frac{c^2}{v_\phi}\ . \tag{B.58}$$

At last, the refractive index can be calculated, by comparing the definition of the phase velocity Eq. (2.39) with the calculated phase velocity in the plasma:

$$v_\phi = \frac{c}{\eta} = c\sqrt{1 + \frac{\omega_p^2}{c^2k^2}} \tag{B.59}$$

$$\Rightarrow \eta^2 = \frac{1}{1 + \frac{\omega_p^2}{c^2k^2}} \frac{1 - \frac{\omega_p^2}{\omega^2}}{1 - \frac{\omega_p^2}{\omega^2}} \tag{B.60}$$

$$\left(1 + \frac{\omega_p^2}{c^2k^2}\right)\left(1 - \frac{\omega_p^2}{\omega^2}\right) = {}^{2} \left(1 + \frac{\omega^2}{c^2k^2} - 1\right) \cdot \left(1 - 1 + \frac{c^2k^2}{\omega^2}\right) = 1 \tag{B.61}$$

$$\Rightarrow \eta = \sqrt{1 - \frac{\omega_p^2}{\omega^2}} \tag{B.62}$$

B.7 Dispersion Relation with Thermal Motion

In this work and the previous treatment the thermal effect on the electrons has been neglected. For completeness a small remark is added in this section. The equation of motion from which the derivation above has been started can be expanded by adding the thermal effect on the momentum due to the thermal pressure[3]

$$mn_0\frac{\partial v_1}{\partial t} == -en_0E_1 - 3k_BT_e\vec{\nabla}n_e \approx 3k_BT_e\frac{\partial n_1}{\partial x}\hat{x} \tag{B.63}$$

in which the term is reduced to its linear order and the higher order terms are neglected. Assuming a planar wave as before and substituting with the equation from sec. B.5 this yields to

$$\omega^2 v_1 = \left(\frac{n_0e^2}{m_e} + \frac{3k_BT_e}{m}k^2\right)v_1 \tag{B.64}$$

$$\omega^2 = \omega_p^2 + \frac{3}{2}k^2v_{th}^2 \tag{B.65}$$

including the thermal velocity $v_{th}^2 := 2k_BT_e/m$.

B.8 Non-linear Refractive Index

The refractive index eq. (2.47) undergoes a correction through three mayor reasons

- relativistic mass of the electrons $m_e = m_{m,0}\gamma$, with that $\hat{\omega}_p^2 = \omega_p^2/\gamma$
- perturbations of the densities $n_e = n_0 + \delta n$

---

[2] Using $\omega_p^2 = \omega^2 - c^2k^2$

[3] [94] F. F. Chen. (1984), Eq. 4-28.

- perturbations of the laser $\omega = \omega_0 + \delta\omega$

in which γ can be replaced using the relations concluded in app. B.9 with $<\gamma>= 1 + a_0^2/4$. Assuming $\omega_p/\omega, a_0, \delta n/n_0, \delta\omega/\omega_0 \ll 1$ the refractive index turn out to

$$\eta = \sqrt{1 - \frac{\hat{\omega_p}^2}{\omega^2}} \tag{B.66}$$

$$\approx 1 - \frac{1}{2}\frac{\omega_p^2}{\omega^2} \cdot \frac{1}{<\gamma>} = 1 - \frac{1}{2}\frac{\omega_p^2}{\omega^2} \cdot \frac{1}{1+\frac{1}{2}a_0^2} \tag{B.67}$$

$$\approx 1 - \frac{1}{2}\frac{\omega_p^2}{\omega^2} \cdot \left(1 - \frac{a_0^2}{4}\right) \tag{B.68}$$

$$\text{with } \omega_p^2 = \frac{e^2}{m_e\epsilon_0}(n_0 + \delta n) \overset{4}{=} \omega_{p,0}^2 \left(1 + \frac{\delta n}{n_0}\right) \tag{B.69}$$

$$\text{and } \frac{1}{\omega^2} = \frac{1}{\omega_0^2} \cdot \frac{1}{\left(1+\frac{\delta\omega}{\omega_0}\right)^2} \approx \frac{1}{\omega_0^2}\left(1 - 2\frac{\delta\omega}{\omega_0}\right) \tag{B.70}$$

$$\eta \approx 1 - \frac{1}{2}\frac{\omega_{p,0}^2}{\omega_0^2} \cdot \left(1 + \frac{\delta n}{n_0}\right)\left(1 - 2\frac{\delta\omega}{\omega_0}\right)\left(1 - \frac{a_0^2}{4}\right) \tag{B.71}$$

$$\approx 1 - \frac{1}{2}\frac{\omega_{p,0}^2}{\omega_0^2} \cdot \left(1 + \frac{\delta n}{n_0} - 2\frac{\delta\omega}{\omega_0} - \frac{a_0^2}{4}\right) . \tag{B.72}$$

The last step ignored all products between perturbations.

B.9 Relativistic Electrons in a Laser Field

The detailed derivation for the relationship between the normalised momentum $\tilde{p}_0$, the Lorentz factor γ and the normalised vector potential a_0. For simplicity the system considers a planar sinusoidal electric field in $\hat{e}_x$ propagating along the $\hat{e}_z$ axis. Starting off with several identity simplifying following equations. The Lorenz equation and the definition of the Lorentz factor yield

---

[4] The variables of kind Y_0 are hereby defined accordingly to $Y(x) = Y(x_0 + \delta x)$ as to $Y(x_0) := Y_0$

$$\vec{p}\frac{\mathrm{d}\vec{p}}{\mathrm{d}t} = \frac{1}{2}\frac{\mathrm{d}\vec{p}^2}{\mathrm{d}t} = -\vec{p}e(\vec{E}+\vec{v}_e\times\vec{B}) = -e\vec{p}\vec{E} - e\,\underbrace{\vec{p}(\vec{v}_e\times\vec{B})}_{=0} \tag{B.73}$$

$$\frac{\mathrm{d}\gamma}{\mathrm{d}t} \overset{5}{=} \frac{\mathrm{d}}{\mathrm{d}t}\sqrt{1+\frac{p^2}{(m_ec)^2}} = \frac{1}{2}\frac{1}{\sqrt{1+\frac{p^2}{(m_ec)^2}}}\frac{1}{(m_ec)^2}\frac{\mathrm{d}\vec{p}^2}{\mathrm{d}t} \tag{B.74}$$

$$\Rightarrow m_ec^2\frac{\mathrm{d}\gamma}{\mathrm{d}t} = \frac{1}{\gamma m_e}\frac{1}{2}\frac{\mathrm{d}\vec{p}^2}{\mathrm{d}t} = -\frac{1}{\gamma m_e}e\vec{p}\vec{E} \tag{B.75}$$

$$\frac{\mathrm{d}}{\mathrm{d}t}W_{kin} = \frac{\mathrm{d}}{\mathrm{d}t}\left(m_ec^2(\gamma-1)\right) = -\frac{1}{\gamma m_e}e\vec{p}\vec{E} = -e\vec{v}_e\vec{E} \tag{B.76}$$

$$\frac{\mathrm{d}\gamma}{\mathrm{d}t} = -\frac{e\vec{v}_e\vec{E}}{m_ec^2}\,. \tag{B.77}$$

Starting from the Lorentz force utilising the vector and scalar potential Eq. (2.5) with the identity $\mathrm{d}\vec{A}/\mathrm{d}t = \partial\vec{A}/\partial t + \left(\vec{v}_e\vec{\nabla}\right))\vec{A}$ the Lorentz force can be arranged as

$$\frac{\mathrm{d}\vec{p}}{\mathrm{d}t} = e\frac{\mathrm{d}\vec{A}}{\mathrm{d}t} - e\vec{\nabla}\left(\vec{v}_e\vec{A}\right) \tag{B.78}$$

thus conclusions about the electron momentum can be examined. As the sinusoidal wave, $\vec{A}$ is restricted to $A\hat{e}_x$, and the propagation to $A = A_0\cos(\omega t - kz)$, Eq. (B.78) leaves

$$\frac{\mathrm{d}p_x}{\mathrm{d}t} = e\frac{\mathrm{d}A}{\mathrm{d}t} \tag{B.79}$$

$$\frac{\mathrm{d}p_y}{\mathrm{d}t} = 0 \tag{B.80}$$

$$\frac{\mathrm{d}p_z}{\mathrm{d}t} = -e\frac{\partial v_xA_0\cos(\omega t - kz)}{\partial z} \tag{B.81}$$

The first row states that the transverse momentum is constant $p_x - eA =$ const. Integrating and choosing an initial stationary particle concludes that

$$p_x = eA = a \Longleftrightarrow \hat{p_x} = a \text{ with } \hat{p_x} := \frac{p_x}{m_ec} = \gamma\frac{v_x}{c} \tag{B.82}$$

and that $p_y = 0$. The momentum in propagation direction is deduced straightforward from the Lorentz equation in common expression, with $\hat{p_z} = p_z/m_ec$, $\vec{B} = B\vec{e}_y$ and $|E_0| = c|B_0|$

---

[5] $\sqrt{1+\frac{p^2}{(m_ec)^2}} = \sqrt{1+\gamma^2\beta^2} = \gamma\sqrt{1/\gamma^2+\beta^2} = \gamma\sqrt{(1-\beta^2)+\beta^2} = \gamma$

$$\frac{\mathrm{d}\hat{p_z}}{\mathrm{d}t} = -\frac{e}{m_e c}\left[\vec{E} + \vec{v} \times \vec{B}\right]_z = -\frac{e}{m_e c}\left[0 + \frac{E_0 v_x \sin(\omega t - kz)}{c}\right] \tag{B.83}$$

$$= -\frac{e v_x E_0 \sin(\omega t - kz)}{m_e c^2} \tag{B.84}$$

recalling Eq. (B.77) gives the equality

$$\frac{\mathrm{d}\gamma}{\mathrm{d}t} = -\frac{e\vec{v}_e \vec{E}}{m_e c^2} = -\frac{e v_x E_0 \sin(\omega t - kz)}{m_e c^2} \tag{B.85}$$

therefore

$$\frac{\mathrm{d}}{\mathrm{d}t}(\gamma - \hat{p_z}) = 0 \tag{B.86}$$

$$\hat{p_z} = \gamma - 1 \tag{B.87}$$

in which a stationary particle is assumed again, $\gamma = 1$ and $\hat{p_z} = 0$. As last connecting both momenta by squaring γ

$$(\hat{p_z} + 1)^2 = \gamma^2 = \sqrt{1 + \left(\frac{\vec{p}}{m_e c}\right)^2}^{\,2} = 1 + \hat{\vec{p}}^{\,2} \tag{B.88}$$

$$1 + 2\hat{p_z} + \hat{p_z}^2 = 1 + \hat{p_x}^2 + \hat{p_z}^2 \tag{B.89}$$

$$\hat{p_z} = \frac{1}{2}\hat{p_x}^2 = \frac{1}{2}a^2 \tag{B.90}$$

$$\Rightarrow \gamma = 1 + \frac{1}{2}a^2 \,. \tag{B.91}$$

The motion can be obtained by integrating Eq. (B.82) and (B.90) with substituting $\tau = t - z(t)/c$, implying $\gamma \mathrm{d}/\mathrm{d}t = \mathrm{d}/\mathrm{d}\tau$ [6]

$$\frac{\mathrm{d}z}{\mathrm{d}\tau} = c\frac{a(\tau)^2}{2} \tag{B.92}$$

$$\frac{\mathrm{d}x}{\mathrm{d}\tau} = c \cdot a(\tau) \tag{B.93}$$

$$\Rightarrow z(\tau) = \frac{c}{2}\int \cos^2(\omega\tau)\mathrm{d}\tau = \frac{c a_0^2}{2}\left[\tau + \frac{1}{2\omega}\sin(2\omega\tau)\right] = \frac{c a_0^2}{8\omega}\left[2\omega\tau + \sin(2\omega\tau)\right] \tag{B.94}$$

$$\Rightarrow x(\tau) = c a_0 \int \cos(\omega\tau)\mathrm{d}\tau = \frac{c a_0}{\omega}\sin(\omega\tau) \,. \tag{B.95}$$

B.10 Co-Moving Frame

The co-moving frame is often used in derivations of laser plasma wakefield acceleration and even in simulations to reduce the simulation box in which the physics are being solved in. The frame propagates with the velocity of the driver. If the driver is a laser pulse, it propagates with the group velocity v_G, thus $\xi = z - v_G t$ and $\tau = t$. The derivative follow as

$$\frac{\mathrm{d}}{\mathrm{d}z} = \frac{\partial \xi}{\partial z}\frac{\mathrm{d}}{\mathrm{d}\xi} + \frac{\partial \tau}{\partial z}\frac{\mathrm{d}}{\mathrm{d}\tau} = \frac{\mathrm{d}}{\mathrm{d}\xi} \tag{B.96}$$

$$\frac{\mathrm{d}}{\mathrm{d}t} = \frac{\partial \tau}{\partial t}\frac{\mathrm{d}}{\mathrm{d}\tau} + \frac{\partial \xi}{\partial t}\frac{\mathrm{d}}{\mathrm{d}\xi} = \frac{\mathrm{d}}{\mathrm{d}\tau} - v_G\frac{\mathrm{d}}{\mathrm{d}\xi} \tag{B.97}$$

and since $v_G \approx c$, the second derivative is often seen as

$$\frac{\mathrm{d}}{\mathrm{d}t} = \frac{\mathrm{d}}{\mathrm{d}\tau} - c\frac{\mathrm{d}}{\mathrm{d}\xi}\ . \tag{B.98}$$

A very common approximation is applied, when the wave is slowly-varying compared to its local variation. Then $\frac{\mathrm{d}}{\mathrm{d}\tau} = 0$, the time component is negligible and the second derivative yields

$$\frac{\mathrm{d}}{\mathrm{d}t} = -c\frac{\mathrm{d}}{\mathrm{d}\xi}\ . \tag{B.99}$$

B.11 Linear Laser-Plasma Wakefield Acceleration

A strong intense and short laser pulse, which is injected into a plasma, create density turbulence through its ponderomotive force and steep gradients. The linear limit of this physics is derived in this section. The physics are based on the continuity equation, the equation of motion and the Gauss law, which all have been used in the section for deriving the plasma frequency B.5. However, here, we will not neglected the force from the laser on the electron motion (the second order). We start from the Lorentz force

$$m_e\frac{\mathrm{d}v}{\mathrm{d}t} = m_e\left(\frac{\partial v}{\partial t} + (v\cdot\nabla)v\right) = -\frac{e}{m_e}(E + v\times B) \tag{B.100}$$

which we rewrite using $v = ca$, valid for small a and by using the relationship between the magnetic field and the vector potential from the Lorenz gauge condition, $B = \nabla\times A = \frac{mc}{e}\nabla\times a$. The higher order terms of the equation end up being

---

[6] Since $\mathrm{d}/\mathrm{d}t = \mathrm{d}\tau/\mathrm{d}t\cdot 1/\mathrm{d}\tau$ with $\mathrm{d}/\mathrm{d}t(t - z(t)/c) = 1 - v_{0z}/c = 1 - (m_e\gamma v_z)/(m_e c\gamma) = 1 - p_z/(m_e c)/\gamma = 1 - p_{0z}/\gamma = 1 - (\gamma - 1)/\gamma) = 1/\gamma$

$$\text{(R.H.S.) } \frac{e}{m_e}v_1 \times B = ca \times (\frac{m_e c}{e}\nabla \times a) = c^2(a \times (\nabla \times a)) \tag{B.101}$$

$$= c^2\left(\frac{1}{2}\nabla a^2 - (a \cdot \nabla)a\right) \tag{B.102}$$

$$\text{(L.H.S.) } (v_1 \cdot \nabla)v_1 = c^2(a \cdot \nabla)a \tag{B.103}$$

If we combine this in Eq. (B.100) and reorder it, we get

$$\frac{\partial v}{\partial t} + c^2(a \cdot \nabla)a = -\frac{e}{m_e}E - \left(c^2\left(\frac{1}{2}\nabla a^2 - (a \cdot \nabla)a\right)\right) \tag{B.104}$$

$$\Rightarrow \frac{\partial v}{\partial t} = -\frac{1}{2}c^2\nabla a^2 - \frac{e}{m_e}E \tag{B.105}$$

Adding Gauss' Law and the continuity equation as a set (restricted to 1 dimension $\nabla \to \partial z$)

$$\frac{\partial E}{\partial z} = -\frac{en_1}{\epsilon_0} \tag{B.106}$$

$$\frac{\partial n_1}{\partial t} + n_{e,0}\frac{\partial v}{\partial z} = 0 \tag{B.107}$$

and taking the time derivative of Eq. (B.107) and inserting Eq. (B.105) and then Eq. (B.106) yield

$$0 = \frac{\partial^2 n_1}{\partial t^2} + n_{e,0}\frac{\partial}{\partial z}\underbrace{\left(-\frac{1}{2}c^2\frac{\partial a^2}{\partial z} - \frac{e}{m_e}E\right)}_{\frac{\partial v}{\partial t}} \tag{B.108}$$

$$0 = \frac{\partial^2 n_1}{\partial t^2} + n_{e,0}\left(-\frac{1}{2}c^2\frac{\partial^2 a^2}{\partial z^2} - \frac{e}{m_e}\underbrace{\left(-\frac{en_1}{\epsilon_0}\right)}_{\frac{\partial E}{\partial z}}\right) \tag{B.109}$$

$$\Rightarrow \frac{\partial^2 n_1}{\partial t^2} + \omega_p^2 n_1 = \frac{1}{2}n_{e,0}c^2\frac{\partial^2 a^2}{\partial z^2} \tag{B.110}$$

Finally, substituting $\xi = z - ct$ and moving into the co-moving frame B.10 in the quasi-static approximation yield in the following set of differential equations

$$\frac{\partial^2 n_1}{\partial \xi^2} + k_p^2 n_1 = \frac{1}{2} n_{e,0} \frac{\partial^2 a^2}{\partial \xi^2} \tag{B.111}$$

$$\xrightarrow{\partial E/\partial\xi = -en_1/\epsilon_0} \frac{\partial}{\partial \xi}\left(\frac{\partial^2 E}{\partial \xi^2} + k_p^2 E\right) = -\frac{1}{2} \underbrace{n_{e,0}\frac{e}{\epsilon_0} \cdot \frac{e}{m_e c^2}}_{\omega_p^2/c^2 = k_p^2} \cdot \frac{m_e c^2}{e} \frac{\partial^2 a^2}{\partial \xi^2} = \frac{\partial}{\partial \xi}\left(-\frac{1}{2} k_p^2 \frac{m_e c^2}{e} \frac{\partial a^2}{\partial \xi}\right) \tag{B.112}$$

$$\Rightarrow \frac{\partial^2 E}{\partial \xi^2} + k_p^2 E = -\frac{1}{2} k_p^2 \frac{m_e c^2}{e} \frac{\partial a^2}{\partial \xi} \tag{B.113}$$

$$\xrightarrow{\partial\Phi/\partial\xi = -E} \frac{\partial^2 \Phi}{\partial \xi^2} + k_p^2 \Phi = \frac{1}{2} k_p^2 \frac{m_e c^2}{e} a^2 \tag{B.114}$$

B.12 Numerical Solution of the Wakefield Generation

For arbitrary pump strength, but quasi-static approximations it is possible to derive a second order derivative for the scalar field so that the electric field and the density can be deduced. In this approximation the assumption $\beta_g \rightarrow 1$ is used, which means that the density perturbation does not alter the light pulse. Starting from the equation in[7] (left the equation number in the book)

$$(\text{Eq. } 4.50) \qquad \gamma = \frac{\sqrt{1+a^2}}{\sqrt{1-u^2}} \tag{B.115}$$

$$(\text{Eq. } 4.54) \qquad \frac{\partial^2 \phi}{\partial \xi^2} = k_p^2 (n-1) \tag{B.116}$$

$$(\text{Eq. } 4.57) \qquad n = \frac{\beta_g}{\beta_g - u} \underbrace{\rightarrow}_{\beta_g \rightarrow 1} \frac{1}{1-u} \tag{B.117}$$

$$(\text{Eq. } 4.58) \qquad \phi = \gamma(1 - u\beta_g) - 1 \underbrace{\rightarrow}_{\beta_g \rightarrow 1} \gamma(1-u) - 1\ . \tag{B.118}$$

It follows with Eq. (B.115) in Eq. (B.118)

$$\phi + 1 = \frac{\sqrt{1+a^2}}{\sqrt{1-u^2}}(1-u) \tag{B.119}$$

$$\underbrace{\frac{(\phi+1)^2}{1+a^2}}_{\equiv C} = \frac{(1-u)^2}{(1-u)(1+u)} \tag{B.120}$$

$$\Rightarrow u = \frac{1-C}{C+1}\ , \tag{B.121}$$

---

[7] [103] P Gibbon. *Short Pulse Laser Interactions with Matter* (2005), Ch. 4.3.

using this identity for Eq. (B.117) and that for Eq. (B.116)

$$n = \frac{1}{1 - \frac{1-C}{C+1}} = \frac{1}{2}\left(1 + \frac{1}{C}\right) \tag{B.122}$$

$$\frac{\partial^2 \phi}{\partial \xi^2} = k_p^2 \left(\frac{1}{2}\left(1 + \frac{1}{C}\right) - 1\right) = \frac{k_p^2}{2}\left(\frac{1}{C} - 1\right) \tag{B.123}$$

$$\Rightarrow \frac{\partial^2 \phi}{\partial \xi^2} = \frac{k_p^2}{2}\left(\frac{1+a^2}{(1+\phi)^2} - 1\right) . \tag{B.124}$$

This differential equation only depends on the laser pulse with the normalised vector potential and k_p, which is for a given density a constant. Substituting $\xi \rightarrow \xi k_p^2$ would it normalise to units of the length of the plasma wavelength.

B.13 Energy Normalisation of the Vector Potential for different Pulse Shape

Different pulse shapes and their linear produced wakefields are discussed in section 2.8.1. In order to compare those pulse shapes, the energy has to remain the same. One can either change the pulse length or the field strength of the laser. Since the pulse shapes vary slightly in definition, it is convenient to define the pulse shape with the pulse length, leaving that parameter fixed. Furthermore, since most literature compares field strengths or energy gain of the electrons in respect to the normalised vector potential, this parameter is fixed as well. However, this yields in different energies for different pulse shapes, which will be calculated.

As a first step, see table B.1 for the different pulse shapes. They are all defined by the parameter of the $FWHM = \xi_{\frac{1}{2}}$ in respect to the intensity, which is $I \propto a^2$ as this is widely used. Note, that the flat top function is constant within $\xi_{\frac{1}{2}}/2$, but 0 outside, and therefore, it is a slightly different definition. In order to calculate the energy of the different pulse shapes, the squared vector potential functions are integrated over their defined space, analogue to $E = \int P(\xi) d\xi$ in Sec. B.3

$$\text{gaussian function:} \int\limits_{-\infty}^{\infty} a_0^2 \exp(-2\xi^2/\sigma^2)\mathrm{d}\xi = a_0^2\sqrt{\frac{\pi}{2}}\sigma = a_0^2\sqrt{\frac{\pi}{4\log(2)}}\xi_{\frac{1}{2}} \tag{B.125}$$

$$\text{super gaussian:} \int\limits_{-\infty}^{\infty} a_0^2 e^{-2\left(\frac{\xi^2}{\sigma^2}\right)^{10}}\mathrm{d}\xi = a_0^2 2^{\frac{19}{20}}\Gamma\left(\frac{19}{20}\right)\sigma = a_0^2\frac{\Gamma(\frac{19}{20})}{\sqrt[20]{4\log(2)}}\xi_{\frac{1}{2}} \tag{B.126}$$

$$\text{cosine function:} \int\limits_{-\xi_{\frac{1}{2}}}^{\xi_{\frac{1}{2}}} a_0^2\cos\left(\frac{\pi\xi}{2\xi_{\frac{1}{2}}}\right)^2\mathrm{d}\xi = a_0^2\xi_{\frac{1}{2}} \tag{B.127}$$

$$\text{flat top:} \int\limits_{-\xi_{\frac{1}{2}}/2}^{\xi_{\frac{1}{2}}/2} a_0^2\mathrm{d}\xi = a_0^2\xi_{\frac{1}{2}} \tag{B.128}$$

and where $\Gamma(x)$ represents the gamma function. If the vector potential ought to remain the same, the energy of the pulse shapes are normalised to the energy of the gaussian pulse shape:

$$\text{super gaussian: } E_s = \sqrt{\frac{4\log(2)}{\pi}}\,\frac{\Gamma(21/20)}{\sqrt[20]{4\log(2)}} \approx 0.92 \tag{B.129}$$

$$\text{cosine function: } E_c = \sqrt{\frac{4\log(2)}{\pi}} \approx 0.94 \tag{B.130}$$

$$\text{flat top: } E_f = \sqrt{\frac{4\log(2)}{\pi}} \approx 0.94 \tag{B.131}$$

Fig. 2.5 depicts all of the different pulse shapes.

Name	Function	$FWHM = \xi_{\frac{1}{2}}$
gaussian function	$a(\xi) = a_0\exp(-\xi^2/\sigma^2)$	$\xi_{\frac{1}{2}} = \sqrt{2\log(2)}\sigma$
super gaussian	$a(\xi) = a_0\exp(-\left(\xi^2/\sigma^2\right)^{10})$	$\xi_{\frac{1}{2}} = 2\sqrt[20]{\frac{\log(2)}{2}}\sigma$
cosine function	$a(\xi) = a_0\cos(\frac{\pi\xi}{2\sigma})$ for $\lvert\xi\rvert \leq \sigma$ else 0	$\xi_{\frac{1}{2}} = \sigma$
flat top	$a(\xi) = a_0$ for $\lvert\xi\rvert \leq \frac{\sigma}{2}$ else 0	$\xi_{\frac{1}{2}} = \sigma$

Table B.1: Pulse shapes used in solving the differential equation for wakefield generation. $\log$ is the natural logarithm.

At last, in order to understand the field strengths, produced by these pulse shapes, the gradient of the of the pulse are of interest as the ponderomotive force, proportional to exactly that, scales the maximum field strength. Sec. 2.8.2 is referring to this topic and is mentioning the gradient of the gaussian and cosine function. These yield

$$\frac{\partial \cos\left(\frac{\pi\xi}{2\xi_{\frac{1}{2}}}\right)^2}{\partial\xi} = \frac{\partial\left(\frac{1}{2}\left(\cos\left(\frac{\pi\xi}{\xi_{\frac{1}{2}}}\right)+1\right)\right)}{\partial\xi} = -\frac{\xi_{\frac{1}{2}}}{2\pi}\sin\left(\frac{\pi\xi}{\xi_{\frac{1}{2}}}\right) \tag{B.132}$$

$$\frac{\partial \exp\left(-\frac{4\log(2)\xi^2}{\xi_{\frac{1}{2}}^2}\right)}{\partial\xi} = -\frac{4\log(4)}{\xi_{\frac{1}{2}}^2}\xi\exp\left(-\frac{4\log(2)\xi^2}{\xi_{\frac{1}{2}}^2}\right) \tag{B.133}$$

and the maximal (minimal) gradient of the cosine function is obviously $\xi_{\frac{1}{2}}/(2\pi) = 0.159\xi_{\frac{1}{2}}$. The minimal gaussian gradient can be found by equalising the second derivative to zero as

$$\frac{\partial\xi\exp\left(-\frac{4\log(2)\xi^2}{\xi_{\frac{1}{2}}^2}\right)}{\partial\xi} = \left(1-\xi^2\frac{4\log(2)}{\xi_{\frac{1}{2}}^2}\right)\cdot\exp\left(-\frac{4\log(2)\xi^2}{\xi_{\frac{1}{2}}^2}\right) \overset{!}{=} 0 \tag{B.134}$$

$$\Rightarrow \xi^2 = \frac{\xi_{\frac{1}{2}}^2}{4\log(2)} \tag{B.135}$$

$$\Rightarrow \left|\frac{\partial\exp\left(-\frac{4\log(2)\xi^2}{\xi_{\frac{1}{2}}^2}\right)}{\partial\xi}\right|_{\text{max}} = \frac{\exp(-1)\xi_{\frac{1}{2}}}{\sqrt{4\log(2)}} = 0.133\xi_{\frac{1}{2}} \tag{B.136}$$

B.14 Transformation of the Energy Gain from the Co-Moving Frame into the Laboratory Frame

The co-moving frame used to display the electric fields in previous part of this work required some transformation in order to calculate the actual energy gain in the laboratory frame. As the velocity of the co-moving frame is the group velocity $v_p = v_G$ Eq. (2.46) of the laser or if etching of the laser pulse is included $v_p = v_G - v_{etch}$ Eq. (2.66)., then when calculating the potential through the electric field, one has to transform into the boosted frame. The Lorentz factor yields

$$\gamma_p = \left(1-\beta_p^2\right)^{-\frac{1}{2}} = \left(1-\eta^2\right)^{-\frac{1}{2}} \tag{B.137}$$

$$\text{or } \beta_p = \beta_G - \beta_{etch} \approx 1 - \frac{3}{2}\frac{\omega_p^2}{\omega^2} : \ \gamma_p = \frac{\omega}{\omega_p\sqrt{\frac{9}{4}\frac{\omega_p^2}{\omega^2}-3}} \tag{B.138}$$

with $\beta_p = v_G/c$ is required to change into the boosted frame. The coordinate system can be transformed into the co-moving frame $\xi = x - v_p t$ to simplify the calculations. Additionally, simulations, be them PIC-codes or numerical solutions of the differential equations are usually in the co-moving frame in the first place. The electric field in the longitudinal direction remains the same $E' = E$. The potential in the boosted frame yields

$$\text{with } x' = \gamma_p(x - v_p t) = \gamma_p \xi \Rightarrow \mathrm{d}x' = \gamma_p \mathrm{d}\xi \tag{B.139}$$

$$\Delta\phi' = \int E' \mathrm{d}x' = \gamma_p \int E \mathrm{d}\xi \tag{B.140}$$

$$\tag{B.141}$$

The energy gain in the boosted frame is then $W' = e\Delta\phi'$ and it has to be transformed back into the laboratory frame with

$$\begin{pmatrix} W \\ cp \end{pmatrix} = \begin{pmatrix} \gamma_p & \gamma_p\beta_p \\ \gamma_p\beta_p & \gamma_p \end{pmatrix} \cdot \begin{pmatrix} W' \\ cp' \end{pmatrix} \tag{B.142}$$

The momentum of the electron in the boosted frame is given by the relativistic momentum $cp' = \sqrt{W'^2 - (m_0c^2)^2}$, which determines the energy in the laboratory frame to be

$$W = e\gamma_p^2 \int E\mathrm{d}\xi + \gamma_p\beta_p \sqrt{\left(e\gamma_p \int E\mathrm{d}\xi\right)^2 - (m_0c^2)^2} \tag{B.143}$$

Note, that the group velocity can be exchanged with the effective reduced group velocity due to etching as Eq. (2.66).

Appendix C

Methods

C.1 Electron Tracking Code

The electron tracking code to calibrate the electron spectrometer was described in Sec. 3.2. This section contains additional information. The set up of the orbit test, referenced in Sec. 3.2 is seen here in Fig. C.1. The resolution of the simulation box was $[N_x, N_y] = [10000, 10000]$ for an area of $150\,\mathrm{mm} \times 150\,\mathrm{mm}$, which yields a resolution step size of $21\,\mu\mathrm{m}$ or $71\,\mathrm{fs}$.

The analytical formula was used to calculate the energy for a $3.75\,\mathrm{mm}$ radius orbit in a $200\,\mathrm{mT}$ dipole magnet field

$$v_e \overset{!}{=} \frac{eB_z\rho}{m_e + \sqrt{1 - \frac{v_e^2}{c^2}}} \tag{C.1}$$

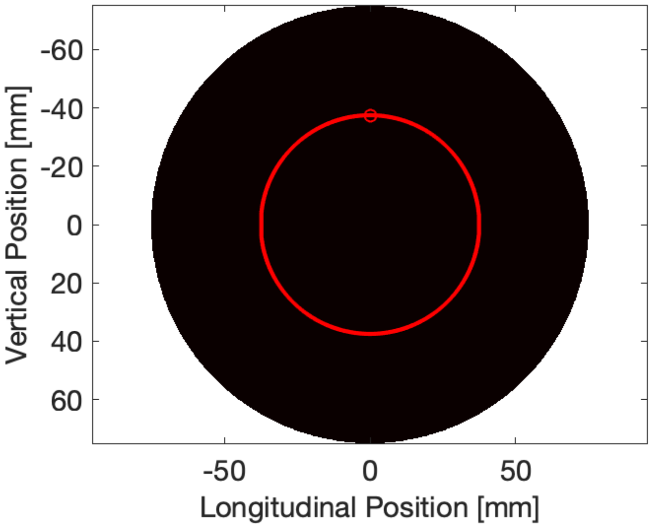

Figure C.1: Simulated electron trajectory in a dipole magnetic field (see text for details) to verify the orbit calculated by the tracking code. The magnet is depicted in black and the electron trajectory in red. Its starting point is the small red circle. The electron has been performed 20 circles when the image was obtained.

C.2 X-ray noise measurement on shot

The noise generated during the process of LPWA can be substantial and obstruct the signal obtained on a sensitive x-ray diagnostic, see 3.3.4. In order to ensure that the signal is noise, a thick high-Z material can be added to the filter pack, which is used to create the relevant data set to estimate the critical energy. To show that the signal behind the filter is truly noise and not based on betatron radiation, a quick estimate can be done. The critical energy and number of photons can be calculate, using the raw data without subtracting the high-Z signal. This should overestimate the critical energy, see Fig. 3.5, but which is endurable for this proof. The theoretical signal passing through the high-Z material can be calculated using the critical energy and number of photons and can be compared to the signal behind the high-Z material. This has been done in Fig. C.2 for the different data sampling methods. The sampling methods are:

- *Average*: Averaging the entire burst
- *Average top 60%*: Sorting the burst by the strongest signal and using the first 60% of the shots
- *Median*: taking the median of the burst as the data
- *Individual*: calculating the signal for each shots and then averaging the resulting values

The reason for the different data sampling methods were to validate the results. The individual method yield in unreliable results for shots with very low signal. This was part of generalising the analysis code for especially self-injection based x-ray analysis. The discussed data in this work is purely ionisation injection and as the signal was high, did not suffer from such high shot-to-shot fluctuations so that all data sampling methods calculated the same critical energy within their confidence bounds. Therefore the individual shots were analysed and evaluated.

The average signal behind the filter is depicted in grey and the theoretical signal for the different methods as crosses. The methods, which do not subtract the Tungsten signal should still have a camera signal close to zero, because the filter should absorb the x-rays. Since that is not the case, the Tungsten signal has to be subtracted prior reconstructing the spectrum. The estimated critical energy is also depicted in the plot and the estimated critical energy is reduce from $\sim 6\,\mathrm{keV}$ down to $\sim 2\,\mathrm{keV}$.

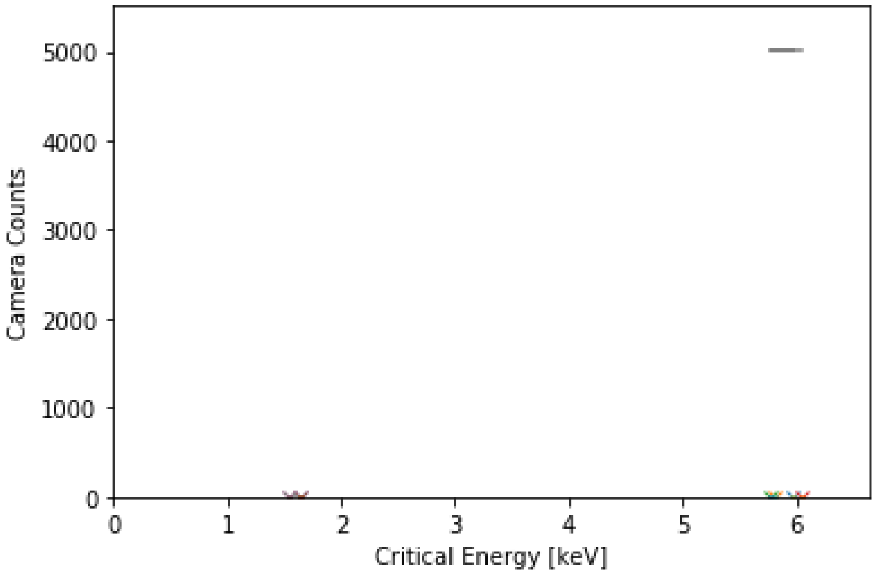

Figure C.2: The camera signal in counts behind the high-Z material (Tungsten) seen in grey. The critical energy estimated by the different data sampling methods, Average:blue; Average top 60%:yellow; Median:green; Integrate:red; Average - T:purple; Average top 60% - T:brown; Median - T:pink; Individual - T:grey). See text for more details.

Appendix D

Staged LPWA

D.1 Mirror Damage in 2017 at the Gemini Experiment for Staging LPWA

A photography of the burned mirror used in the experiment described in Sec. 4 is depicted in Fig. D.1.

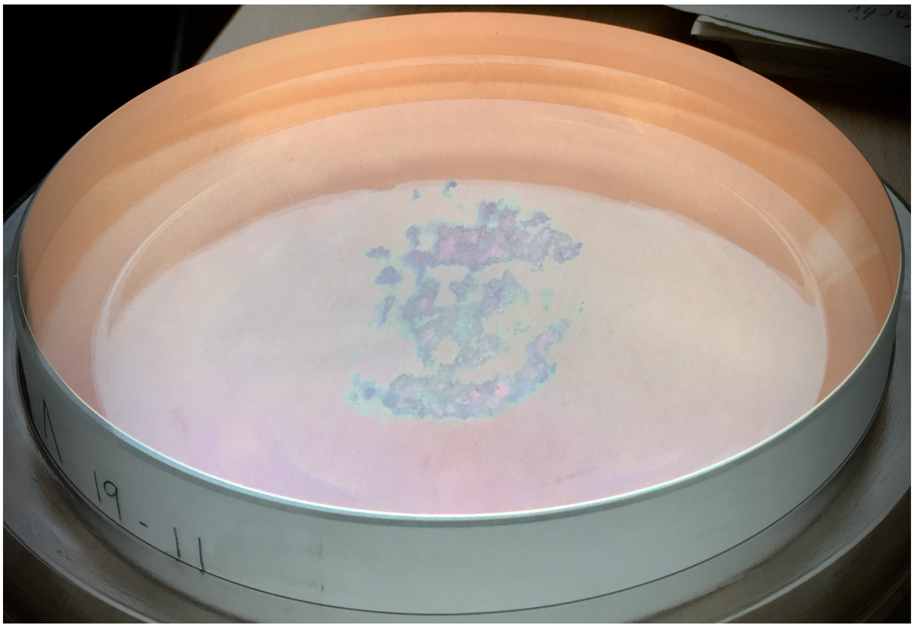

Figure D.1: The dielectric mirror used in the experiment was damaged at energies as low as $3\,\mathrm{J}$.

D.2 Energy Gain of low Density Realistic Laser Beams

This contains additional information to clarify why there was no definite energy spread for the simulations based on the profile from the semi-minor axis at $0.29 \times 10^{18}\,\mathrm{cm}^{-3}$, see Sec. 4.5.1. The focusing wakefield is unstable and continues changing signs for a fixed injection phase. A snapshot shows the irregular focusing field Fig. D.3. The location of the focusing field changing from time step to time step. Hence, why the the white area in Fig.D.2, which indicates the focusing field on the central axis, is so large. The reason is that the intensity profile contains large wing with high intensity relative to the main laser pulse and that the density is low and not focusing the wings into the main plasma channel. Fig. D.2 shows the possible predicted energy gain, but the defocusing field dominate the wakefield and there is no high energy gain with constant focusing force possible. It might be possible that the defocusing and focusing field average themselves out, but the transverse properties of the injected electron bunch would be quite unpredictable.

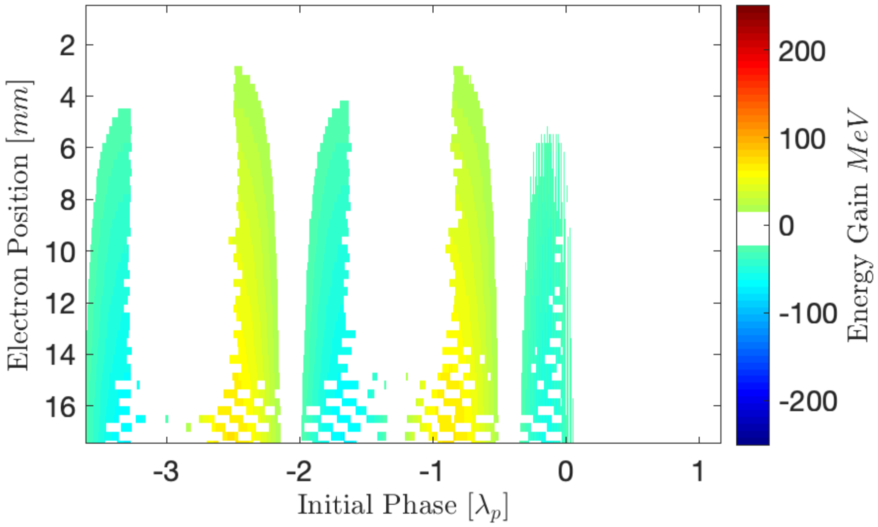

Figure D.2: The possible energy gain of electrons injected in all possible phases of the wakefield. Excluded are phases in which the electron experiences deflection of the transverse electric field. See Fig. D.3.

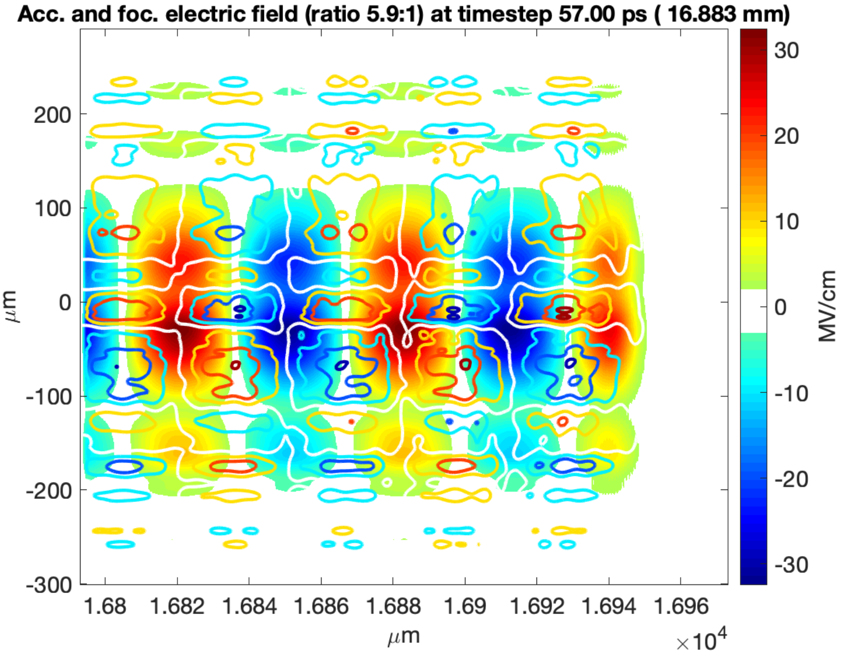

Figure D.3: The electric field for acceleration and transverse focusing of the minor-axis of the realistic laser profile close to the exit of the gas cell shows very low transverse focusing and very little regularity, which does not support electron beam transport. Note that the transverse location of the depicted field very between different time steps as well significantly.

Appendix E

Industrial Imaging

E.1 Calculating the Peak Energy of Electron Spectra

The peak energy of the electron spectra was either automatically calculated scanning the spectrum for a 10^5 counts/MeV dominance and choosing the highest energy or manually, where the signal started dropping. A selection of random electron spectra can be seen in Fig. E.1. As seen, mostly it is quite obvious, which is the most dominant peak energy, but it had to be manually chosen for the red data set for example. Here the spectrum was flat and started dropping where the peak energy was to be set.

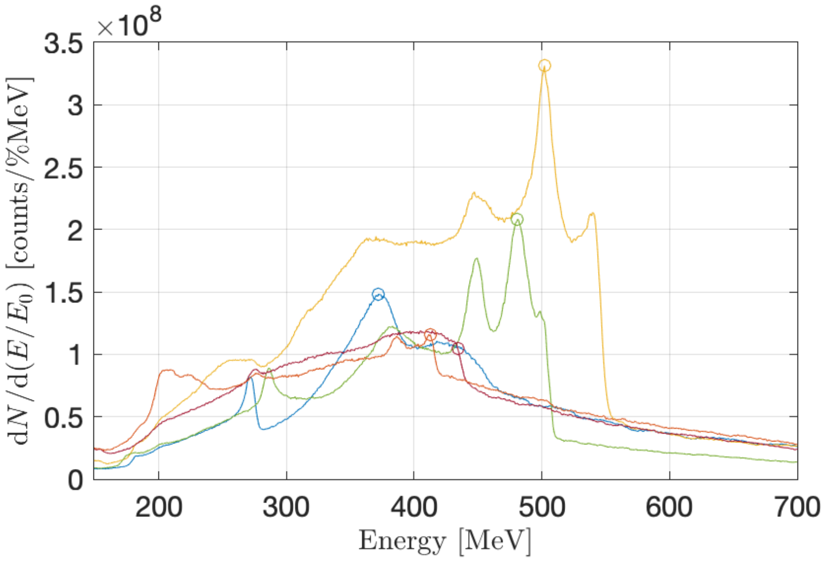

Figure E.1: Random selection of electron spectrum for the density scan in Sec. 5.4 and the determined peak energy.

Fig. E.2 shows some individual shots of the electron energy with the electron spectrometer.

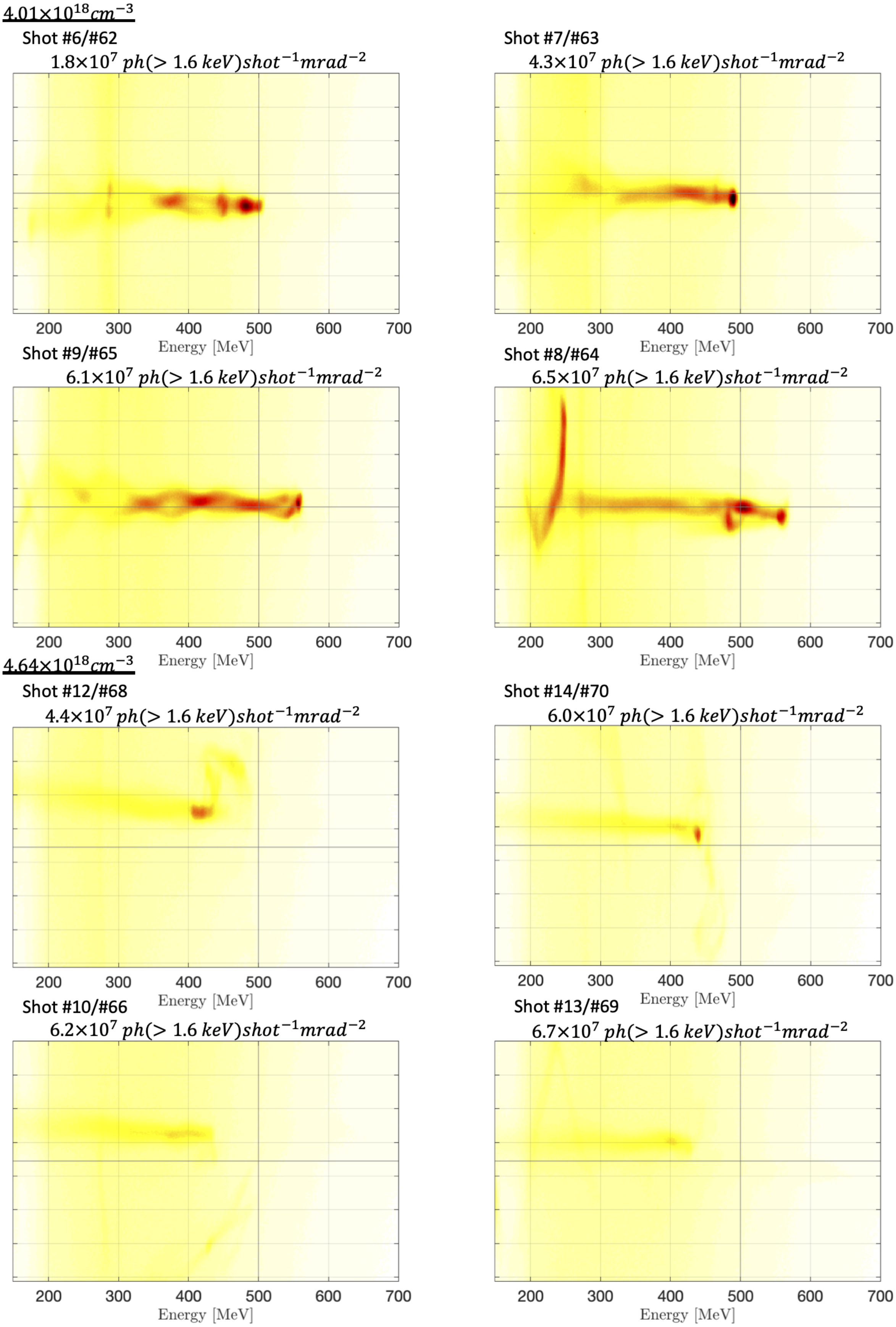

Figure E.2: Signal on the electron spectrometer in the same colour scale for increasing photon flux divided by different densities. $4.01 \times 10^{18}\,\mathrm{cm}^{-3}$ is at the peak of the electron energy and has a large x-ray flux, but very inconsistent. Due to its consistent high x-ray flux, the density of $4.64 \times 10^{18}\,\mathrm{cm}^{-3}$ was later chosen for x-ray imaging.

Bibliography

[1] W. C. Röntgen. *Annalen der Physik*. **300,** 1, pp. 12–17. (1898). (See p. 21)
"Ueber eine neue Art von Strahlen"
DOI: 10.1002/andp.18983000103.

[2] US Department of Public Health. *The Control of Radiation*. URL: https://www.mass.gov/files/documents/2018/09/11/105cmr120.pdf (visited on 10/24/2020) (see . 21, 41).

[3] A Haase and G. L.&. E. Umbach. WORLD SCIENTIFIC (1997). (See p. 21)
Röntgen Centennial.
DOI: 10.1142/3428.

[4] E. Rutherford. *The London, Edinburgh, and Dublin Philosophical Magazine and J. of Sc.* **21,** 125, pp. 669–688. (1911). (See p. 21)
"LXXIX. The scattering of α and β particles by matter and the structure of the atom"
DOI: 10.1080/14786440508637080.

[5] J. D. Cockcroft and E. T. S. Walton. *Nature*. **129,** 3250, pp. 242–242. (1932). (See p. 21)
"Artificial Production of Fast Protons"
DOI: 10.1038/129242a0.

[6] *The PSI proton accelerator*. URL: https://www.psi.ch/en/media/the-psi-proton-accelerator (visited on 08/27/2020) (see p. 21).

[7] E. O. Lawrence and D. Cooksey. *Physical Review*. **50,** 12, pp. 1131–1140. (1936). (See p. 22)
"On the Apparatus for the Multiple Acceleration of Light Ions to High Speeds"
DOI: 10.1103/PhysRev.50.1131.

[8] E. M. McMillan. *Physical Review*. **68,** 5-6, pp. 143–144. (1945). (See p. 22)
"The Synchrotron—A Proposed High Energy Particle Accelerator"
DOI: 10.1103/PhysRev.68.143.

[9] D. W. Kerst. *Physical Review*. **60,** 1, pp. 47–53. (1941). (See p. 22)
"The Acceleration of Electrons by Magnetic Induction"
DOI: 10.1103/PhysRev.60.47.

[10] L. Evans. *NJP*. **9,** 9, pp. 335–335. (2007). (See p. 22)
"The Large Hadron Collider"
DOI: 10.1088/1367-2630/9/9/335.

[11] CERN. *CERN Future Circular Collider*. 2019. URL: https://cds.cern.ch/images/OPEN-PHO-ACCEL-2019-001-2 (visited on 09/01/2020) (see p. 23).

[12] F. R. Elder *et al*. *Physical Review*. **71,** 11, pp. 829–830. (1947). (See p. 23)
"Radiation from Electrons in a Synchrotron"
DOI: 10.1103/PhysRev.71.829.5.

[13] Helmut Wiedemann. Springer (1994). (See p. 24)
Particle accelerator physics.
DOI: 10.1080/08940889408261288.

[14] R. D. Kornberg. *Proceedings of the National Academy of Sciences*. **104,** 32, pp. 12955–12961. (2007). (See p. 25)
"The molecular basis of eukaryotic transcription"
DOI: 10.1073/pnas.0704138104.

[15] J. Dik *et al*. *Analytical Chemistry*. **80,** 16, pp. 6436–6442. (2008). (See p. 25)
"Visualization of a Lost Painting by Vincent van Gogh Using Synchrotron Radiation Based X-ray Fluorescence Elemental Mapping"
DOI: 10.1021/ac800965g.

[16] P. Erdely *et al. Metals.* **6,** 1, p. 10. (2016). (See p. 25)
"In Situ Characterization Techniques Based on Synchrotron Radiation and Neutrons Applied for the Development of an Engineering Intermetallic Titanium Aluminide Alloy"
DOI: `10.3390/met6010010`.

[17] T. Behnke *et al. Technical Design Report | Volume 1 : Executive Summary*. Tech. rep. 2013. URL: `https://ilchome.web.cern.ch/sites/ilchome.web.cern.ch/files/images/pdf/ExecutiveSummary.pdf` (see p. 25).

[18] N. A. Solyak. *AIP Conference Proceedings.* **1086,** 365. (2009). (See p. 25)
"Gradient Limitations in Room Temperature and Superconducting Acceleration Structures"
DOI: `10.1063/1.3080933`.

[19] V. I. Veksler. *CERN Symposium on High Energy Accelerators and Pion Physics*, pp. 80–83. (1956). (See p. 25)
"Coherent principle of acceleration of charged particles"
DOI: `10.5170/CERN-1956-025.80`.

[20] Y. Fainberg. *Uspekhi Fizicheskih Nauk.* **93,** 12, pp. 617–631. (1967). (See p. 25)
"Acceleration of charged particles in a plasma"
DOI: `10.3367/UFNr.0093.196712c.0617`.

[21] T. Tajima and J. M. Dawson. *PRL.* **43,** 4, pp. 267–270. (1979). (See . 26, 51, 80)
"Laser Electron Acceleration".

[22] M. N. Rosenbluth and C. S. Liu. *PRL.* **29,** 11, pp. 701–705. (1972). (See p. 26)
"Excitation of Plasma Waves by Two Laser Beams"
DOI: `10.1103/PhysRevLett.29.701`.

[23] C. E. Clayton *et al. PRL.* **54,** 21, pp. 2343–2346. (1985). (See p. 26)
"Relativistic Plasma-Wave Excitation by Collinear Optical Mixing"
DOI: `10.1103/PhysRevLett.54.2343`.

[24] C. E. Clayton *et al. PRL.* **70,** 1, pp. 37–40. (1993). (See p. 26)
"Ultrahigh-gradient acceleration of injected electrons by laser-excited relativistic electron plasma waves"
DOI: `10.1103/PhysRevLett.70.37`.

[25] N. E. Andreev *et al. Pis'ma Zh. Eksp. Teor. Fiz.* **55,** 10, pp. 551–555. (1992). (See p. 26)
"Resonant excitation of wakefields by a laser pulse in a plasma".

[26] J Krall *et al. PRE.* **48,** 3, pp. 2157–2161. (1993). (See p. 26)
"Enhanced acceleration in a self-modulated-laser wake-field accelerator"
DOI: `10.1103/PhysRevE.48.2157`.

[27] A. Modena *et al. Nature.* **377,** 6550, pp. 606–608. (1995). (See . 26, 60)
"Electron acceleration from the breaking of relativistic plasma waves"
DOI: `10.1038/377606a0`.

[28] E. Esarey *et al. PRL.* **80,** 25, pp. 5552–5555. (1998). (See p. 26)
"Trapping and Acceleration in Self-Modulated Laser Wakefields"
DOI: `10.1103/PhysRevLett.80.5552`.

[29] S. P. D. Mangles *et al. Nature.* **431,** 7008, pp. 535–538. (2004). (See . 26, 59)
"Monoenergetic beams of relativistic electrons from intense laser plasma interactions"
DOI: `10.1038/nature02939`.

[30] C. G. R. Geddes *et al. Nature.* **431,** 7008, pp. 538–541. (2004). (See . 26, 59)
"High-quality electron beams from a laser wakefield accelerator using plasma-channel guiding"
DOI: `10.1038/nature02900`.

[31] J. Faure *et al. Nature.* **431,** 7008, pp. 541–544. (2004). (See . 26, 59)
"A laser plasma accelerator producing monoenergetic electron beams"
DOI: `10.1038/nature02900.1.`.

[32] F. Salehi *et al. Optics Letters.* **42,** 2, pp. 215–218. (2017). (See p. 27)
"MeV electron volt electron acceleration at 1 kHz with < 10 mJ laser pulses".

[33] D. Guénot *et al. Nat. Photonics.* **11,** 5. (2017). (See . 27, 122)
"Relativistic electron beams driven by kHz single-cycle light pulses"
DOI: `10.1038/nphoton.2017.46`.

[34] D. Gustas *et al. PRAB*. **21,** 1, pp. 1–7. (2018). (See . 27, 122)
"High-charge relativistic electron bunches from a kHz laser-plasma accelerator"
DOI: `10.1103/PhysRevAccelBeams.21.013401`.

[35] A. J. Gonsalves *et al. PRL*. **122,** 8, p. 84801. (2019). (See p. 27)
"Petawatt Laser Guiding and Electron Beam Acceleration to 8 GeV in a Laser-Heated Capillary Discharge Waveguide"
DOI: `10.1103/PhysRevLett.122.084801`.

[36] S. P. Mangles. *CAS-CERN Accelerator School: Plasma Wake Acceleration 2014, Proceedings*. **001,** November 2014, pp. 289–300. (2014). (See . 28, 117, 173)
"An overview of recent progress in laser wakefield acceleration experiments"
DOI: `10.5170/CERN-2016-001.289`.

[37] S. Banerjee *et al. PRST - AB*. **16,** 3, pp. 1–12. (2013). (See p. 28)
"Stable, tunable, quasimonoenergetic electron beams produced in a laser wakefield near the threshold for self-injection"
DOI: `10.1103/PhysRevSTAB.16.031302`.

[38] A. Martinez De La Ossa *et al. PRL*. **111,** 24. (2013). (See . 28, 60)
"High-quality electron beams from beam-driven plasma accelerators by wakefield-induced ionization injection"
DOI: `10.1103/PhysRevLett.111.245003`.

[39] M. Tzoufras *et al. PRL*. **113,** 24, pp. 1–5. (2014). (See . 28, 50)
"Improving the self-guiding of an ultraintense laser by tailoring its longitudinal profile"
DOI: `10.1103/PhysRevLett.113.245001`.

[40] S Kuschel *et al. PRL*. **121,** 15, p. 154801. (2018). (See p. 28)
"Controlling the Self-Injection Threshold in Laser Wakefield Accelerators"
DOI: `10.1103/PhysRevLett.121.154801`.

[41] C. McGuffey *et al. PRL*. **104,** 2, pp. 1–4. (2010). (See . 28, 60)
"Ionization induced trapping in a laser wakefield accelerator"
DOI: `10.1103/PhysRevLett.104.025004`.

[42] J. Faure *et al. Nature*. **444,** 7120, pp. 737–739. (2006). (See . 28, 60)
"Controlled injection and acceleration of electrons in plasma wakefields by colliding laser pulses"
DOI: `10.1038/nature05393`.

[43] S. P. D. Mangles *et al. Physics of Plasmas*. **14,** 5, pp. 1–7. (2007). (See p. 28)
"On the stability of laser wakefield electron accelerators in the monoenergetic regime"
DOI: `10.1063/1.2436481`.

[44] A. R. Maier *et al. PRX*. **10,** 3, p. 031039. (2020). (See p. 28)
"Decoding Sources of Energy Variability in a Laser-Plasma Accelerator"
DOI: `10.1103/PhysRevX.10.031039`.

[45] G. Golovin *et al. PRST - AB*. **18,** 1, pp. 1–6. (2015). (See p. 28)
"Tunable monoenergetic electron beams from independently controllable laser-wakefield acceleration and injection"
DOI: `10.1103/PhysRevSTAB.18.011301`.

[46] G. G. Manahan *et al. Nat. Com*. **8,** 1, p. 15705. (2017). (See . 28, 105)
"Single-stage plasma-based correlated energy spread compensation for ultrahigh 6D brightness electron beams"
DOI: `10.1038/ncomms15705`.

[47] M. Migliorati *et al. PRST - AB*. **16,** 1, p. 011302. (2013). (See p. 28)
"Intrinsic normalized emittance growth in laser-driven electron accelerators"
DOI: `10.1103/PhysRevSTAB.16.011302`.

[48] R. Weingartner *et al. PRST - AB*. **15,** 11, pp. 1–5. (2012). (See p. 28)
"Ultralow emittance electron beams from a laser-wakefield accelerator"
DOI: `10.1103/PhysRevSTAB.15.111302`.

[49] Z. Qin *et al. Physics of Plasmas*. **25,** 2, p. 023106. (2018). (See p. 28)
"Ultralow-emittance measurement of high-quality electron beams from a laser wakefield accelerator"
DOI: `10.1063/1.5019987`.

[50] S. Kneip *et al. PRST - AB*. **15,** 2, pp. 2–6. (2012). (See . 28, 66)
"Characterization of transverse beam emittance of electrons from a laser-plasma wakefield accelerator in the bubble regime using betatron x-ray radiation"
DOI: `10.1103/PhysRevSTAB.15.021302`.

[51] C. B. Schroeder *et al.* *Phys. Rev. Spec. Top. - Accel. Beams*. **13,** 10, p. 101301. (2010). (See p. 28)
"Physics considerations for laser-plasma linear colliders"
DOI: `10.1103/PhysRevSTAB.13.101301`.

[52] J. M. Cole *et al.* *PRX*. **8,** 1. (2018). (See . 28, 29, 110, 130, 133)
"Experimental Evidence of Radiation Reaction in the Collision of a High-Intensity Laser Pulse with a Laser-Wakefield Accelerated Electron Beam"
DOI: `10.1103/PhysRevX.8.011020`.

[53] K. Poder *et al.* *PRX*. **8,** 3, p. 031004. (2018). (See . 28, 29, 93)
"Experimental Signatures of the Quantum Nature of Radiation Reaction in the Field of an Ultraintense Laser"
DOI: `10.1103/PhysRevX.8.031004`.

[54] B. Hidding *et al.* *ArXiv*. March. (2019). (See p. 29)
"Plasma Wakefield Accelerator Research 2019 - 2040: A community-driven UK roadmap compiled by the Plasma Wakefield Accelerator Steering Committee (PWASC)"
URL: `http://arxiv.org/abs/1904.09205`.

[55] E. Adli *et al.* *Nature*. **561,** 7723, pp. 363–367. (2018). (See p. 29)
"Acceleration of electrons in the plasma wakefield of a proton bunch"
DOI: `10.1038/s41586-018-0485-4`.

[56] M. Wing. *Philosophical Transactions of the Royal Society A*. **377,** 2151, pp. 1–10. (2019). (See p. 29)
"Particle physics experiments based on the AWAKE acceleration scheme"
DOI: `10.1098/rsta.2018.0185`.

[57] E. Esarey *et al.* *PRE*. **65,** 5, pp. 1–15. (2002). (See . 29, 116, 130)
"Synchrotron radiation from electron beams in plasma-focusing channels"
DOI: `10.1103/PhysRevE.65.056505`.

[58] M. S. Bloom *et al.* *PRAB*. **23,** 6, p. 61301. (2020). (See . 29, 118, 131, 168)
"Bright x-ray radiation from plasma bubbles in an evolving laser wakefield accelerator"
DOI: `10.1103/PhysRevAccelBeams.23.061301`.

[59] S. P. D. Mangles *et al.* *APL*. **95,** 18, pp. 3–5. (2009). (See . 29, 163)
"Controlling the spectrum of x-rays generated in a laser-plasma accelerator by tailoring the laser wavefront"
DOI: `10.1063/1.3258022`.

[60] M. Schnell *et al.* *PRL*. **108,** 7, pp. 1–5. (2012). (See . 29, 66, 163)
"Deducing the electron-beam diameter in a laser-plasma accelerator using x-ray betatron radiation"
DOI: `10.1103/PhysRevLett.108.075001`.

[61] A. Rousse *et al.* *PRL*. **93,** 13, p. 135005. (2004). (See . 29, 163)
"Production of a keV X-Ray Beam from Synchrotron Radiation in Relativistic Laser-Plasma Interaction"
DOI: `10.1103/PhysRevLett.93.135005`.

[62] A. Döpp *et al.* *Light: Science & Applications*. **6,** 11, e17086–e17086. (2017). (See . 29, 110, 141, 155, 163)
"Stable femtosecond X-rays with tunable polarization from a laser-driven accelerator"
DOI: `10.1038/lsa.2017.86`.

[63] J. Wenz *et al.* *Nat. Com.* **6,** May, pp. 1–6. (2015). (See . 29, 110)
"Quantitative X-ray phase-contrast microtomography from a compact laser-driven betatron source"
DOI: `10.1038/ncomms8568`.

[64] S. Kneip *et al.* *Nature Physics*. **6,** 12, pp. 980–983. (2010). (See . 29, 75)
"Bright spatially coherent synchrotron X-rays from a table-top source"
DOI: `10.1038/nphys1789`.

[65] J. C. Wood *et al.* *Scientific Reports*. **8,** 1. (2018). (See . 29, 30, 110, 131)
"Ultrafast Imaging of Laser Driven Shock Waves using Betatron X-rays from a Laser Wakefield Accelerator"
DOI: `10.1038/s41598-018-29347-0`.

[66] J. M. Cole, PhD Thesis: *Diagnosis and Application of Laser Wakefield Accelerators*. Imperial College London. (2015). (See . 29, 81, 82, 131, 148).

[67] X. Wang *et al.* *Nat. Com.* **4,** May. (2013). (See p. 29)
"Quasi-monoenergetic laser-plasma acceleration of electrons to 2 GeV"
DOI: `10.1038/ncomms2988`.

[68] F. Albert and A. G. R. Thomas. *Plasma Phys. Control. Fusion.* **58,** 103001. (2016). (See . 29, 110)
"Plasma Phys. Control. Fusion"
DOI: 10.1088/0741-3335/58/10/103001.

[69] M. Z. Mo *et al. Rev. Sci.* **84,** 12, p. 123106. (2013). (See p. 29)
"Laser wakefield generated X-ray probe for femtosecond time-resolved measurements of ionization states of warm dense aluminum"
DOI: 10.1063/1.4842237.

[70] B. Kettle *et al. PRL.* **123,** 25, p. 254801. (2019). (See . 29, 138)
"Single-Shot Multi-keV X-Ray Absorption Spectroscopy Using an Ultrashort Laser-Wakefield Accelerator Source"
DOI: 10.1103/PhysRevLett.123.254801.

[71] J. M. Cole *et al. Plasma Phys. Control. Fusion.* **58,** 1, p. 014008. (2016). (See . 29, 110)
"Tomography of human trabecular bone with a laser-wakefield driven x-ray source"
DOI: 10.1088/0741-3335/58/1/014008.

[72] A. Döpp *et al. Optica.* **5,** 2, p. 199. (2018). (See . 29, 110)
"Quick x-ray microtomography using a laser-driven betatron source"
DOI: 10.1364/OPTICA.5.000199.

[73] M Vargas *et al. Plasma Phys. Control. Fusion.* **61,** 5, p. 54009. (2019). (See . 30, 110)
"X-ray phase contrast imaging of additive manufactured structures using a laser wakefield accelerator"
DOI: 10.1088/1361-6587/ab0e4f.

[74] A. E. Hussein *et al. Scientific Reports.* **9,** 1. (2019). (See . 30, 110)
"Laser-wakefield accelerators for high-resolution X-ray imaging of complex microstructures"
DOI: 10.1038/s41598-019-39845-4.

[75] B Saleh and M Teich. WILEY (2007). (See . 33, 34, 36, 38, 44)
Fundamentals of Photonics.

[76] M Miyagi and S Nishida. *Applied optics.* **18,** 13, pp. 2237–2240. (1979). (See p. 34)
"Pulse spreading in a single-mode optical fiber due to third-order dispersion: effect of optical source bandwidth."
DOI: 10.1364/AO.18.002237.

[77] K. J. Moh *et al. Applied optics.* **46,** pp. 7544–7551. (2007). (See p. 38)
"Generating radial or azimuthal polarization by axial sampling of circularly polarized vortex beams."
DOI: 10.1364/AO.46.007544.

[78] I. Moreno *et al. Optical Engineering.* **51,** 12, p. 128003. (2012). (See p. 38)
"Polarization manipulation of radially polarized beams"
DOI: 10.1117/1.OE.51.12.128003.

[79] S Carbajo *et al. Optics Letters.* **39,** 8, p. 2487. (2014). (See p. 38)
"Efficient generation of ultra-intense few-cycle radially polarized laser pulses"
DOI: 10.1364/OL.39.002487.

[80] D. Strickland and G. Mourou. *Opt. Commun.* **56,** 3, pp. 219–221. (1985). (See p. 38)
"Compression of amplified chirped optical pulses"
DOI: 10.1016/0030-4018(85)90120-8.

[81] A. Dubietis *et al. Opt. Commun.* **88,** 4-6, pp. 437–440. (1992). (See p. 38)
"Powerful femtosecond pulse generation by chirped and stretched pulse parametric amplification in BBO crystal"
DOI: 10.1016/0030-4018(92)90070-8.

[82] I. Ross *et al. Opt. Commun.* **144,** 1-3, pp. 125–133. (1997). (See p. 38)
"The prospects for ultrashort pulse duration and ultrahigh intensity using optical parametric chirped pulse amplifiers"
DOI: 10.1016/S0030-4018(97)00399-4.

[83] B. E. Schmidt *et al. Nat. Com.* **5,** May, p. 3643. (2014). (See p. 38)
"Frequency domain optical parametric amplification."
DOI: 10.1038/ncomms4643.

[84] S. A. Akhmanov *et al. Physics Faculty, Moscow State University.* **2,** pp. 191–193. (1965). (See p. 39)
"Observation of parametric amplification in the optical range".

[85] G. S. Voronov and N. B. Delone. *Sov. Phys. JETP.* **23,** 1, p. 54. (1966). (See p. 41)
"Many-photon ionization of the xenon atom by ruby laser radiation"
URL: http://www.jetp.ac.ru/cgi-bin/dn/e_023_01_0054.pdf.

[86] A. M. Perelomov *et al. Sov. Phys. JETP*. **23,** 5, p. 924. (1966). (See p. 41)
"Ionization of atoms in an alternating electrical field".

[87] M. V. Ammosov *et al. Sov. Phys. JETP*. **64,** December 1986, pp. 1191–1194. (1986). (See p. 41)
"Tunnel ionization of complex atoms and of atomic ions in an alternating electromagnetic field"
DOI: `10.1117/12.938695`.

[88] L. V. Keldysh. *Sov. Phys. JETP*. **20,** 5, pp. 1307–1314. (1965). (See p. 41)
"Ionization in the field of a strong electromagnetic wave"
DOI: `10.1234/12345678`.

[89] H. R. Reiss. *Physical Review A*. **1,** 3, pp. 803–818. (1970). (See p. 42)
"Semiclassical electrodynamics of bound systems in intense fields"
DOI: `10.1103/PhysRevA.1.803`.

[90] J. Osterholz *et al. PRL*. **96,** 8, pp. 2–5. (2006). (See p. 42)
"Production of dense plasmas with sub-10-fs laser pulses"
DOI: `10.1103/PhysRevLett.96.085002`.

[91] R. P. Drake. Springer (2006). (See p. 42)
High Energy Density Physics : Fundamentals, Inertial Fusion, and Experimental Astrophysics.

[92] H. R. Griem. Cambridge University Press (1997). (See p. 42)
Prinicples of Plasma Spectroscopy.

[93] Y.-K. Kim and M. E. Rudd. *Phys. Rev. A*. **50,** 5, pp. 3954–3967. (1994). (See p. 42)
"Binary-encounter-dipole model for electron-impact ionization"
DOI: `10.1103/PhysRevA.50.3954`.

[94] F. F. Chen. Plenum Press (1984). (See . 43, 185)
Plasma Physics Controlled Fusion.

[95] P. Sprangle *et al. APL*. **53,** 22, pp. 2146–2148. (1988). (See p. 47)
"Laser wakefield acceleration and relativistic optical guiding"
DOI: `10.1063/1.100300`.

[96] P. Sprangle *et al. PRL*. **69,** 15. (1992). (See p. 47)
"Propagation and Guiding of Intense Laser Pulses in Plasmas".

[97] W. B. Mori. *IEEE Journal of Quantum Electronics*. **33,** 11, pp. 1942–1953. (1997). (See p. 50)
"The physics of the nonlinear optics of plasmas at relativistic intensities for short-pulse lasers"
DOI: `10.1109/3.641309`.

[98] C. D. Decker *et al. Physics of Plasmas*. **3,** 5, pp. 2047–2056. (1996). (See p. 50)
"The evolution of ultra-intense, short-pulse lasers in underdense plasmas"
DOI: `10.1063/1.872001`.

[99] J. Faure *et al. PRL*. (2005). (See p. 50)
"Observation of laser-pulse shortening in nonlinear plasma waves"
DOI: `10.1103/PhysRevLett.95.205003`.

[100] J. Schreiber *et al. PRL*. **105,** 23, pp. 1–4. (2010). (See . 50, 124, 126)
"Complete temporal characterization of asymmetric pulse compression in a laser wakefield"
DOI: `10.1103/PhysRevLett.105.235003`.

[101] M. J. Streeter *et al. PRL*. **120,** 25. (2018). (See p. 50)
"Observation of Laser Power Amplification in a Self-Injecting Laser Wakefield Accelerator"
DOI: `10.1103/PhysRevLett.120.254801`.

[102] V Berezhiani *et al. Physics Letters A*. **148,** 67, pp. 6–7. (1990). (See p. 53)
"Relativistic wake-field generation by an intense laser pulse in a plasma"
URL: `https://ac.els-cdn.com/0375960190908134/1-s2.0-0375960190908134-main.pdf?_tid=25e371a4-a2af-11e7-b786-00000aab0f6c{\&}acdnat=1506426059_bfaab6b14dd2fb5e59a0ed886cdb9dea`.

[103] P Gibbon. Imperial College Press (2005). (See . 53, 191)
Short Pulse Laser Interactions with Matter.

[104] S. V. Bulanov *et al. JETP Letters*. **50,** 4, pp. 176–178. (1989). (See p. 53)
"Excitation of ultrarelativistic plasma waves by pulse of electromagnetic radiation".

[105] E. Esarey *et al. Reviews of Modern Physics*. **81,** 3, pp. 1229–1285. (2009). (See . 55, 56)
"Physics of laser-driven plasma-based electron accelerators"
DOI: `10.1103/RevModPhys.81.1229`.

[106] T. D. Arber *et al. Plasma Phys. Control. Fusion*. **57,** 11, p. 113001. (2015). (See . 57, 59, 80, 81)
"Contemporary particle-in-cell approach to laser-plasma modelling"
DOI: `10.1088/0741-3335/57/11/113001`.

[107] R. Fonseca *et al.*, pp. 342–351. (2002). (See p. 59)
"OSIRIS: A Three-Dimensional, Fully Relativistic Particle in Cell Code for Modeling Plasma Based Accelerators"
DOI: `10.1007/3-540-47789-6_36`.

[108] R. Lehe *et al. Comput. Phys. Commun.* **203,** pp. 66 –82. (2016). (See . 59, 140)
"A spectral, quasi-cylindrical and dispersion-free Particle-In-Cell algorithm"
DOI: `https://doi.org/10.1016/j.cpc.2016.02.007`.

[109] W. Lu *et al. PRST - AB*. **10,** 6, pp. 1–12. (2007). (See . 59, 62, 119, 120, 125)
"Generating multi-GeV electron bunches using single stage laser wakefield acceleration in a 3D nonlinear regime"
DOI: `10.1103/PhysRevSTAB.10.061301`.

[110] F. Amiranoff *et al. PRL*. **74,** 26, pp. 5220–5223. (1995). (See p. 59)
"Electron acceleration in Nd-laser plasma beat-wave experiments"
DOI: `10.1103/PhysRevLett.74.5220`.

[111] W. B. Mori *et al. PRL*. **72,** 10, pp. 1482–1485. (1994). (See p. 59)
"Raman forward scattering of short-pulse high-intensity lasers"
DOI: `10.1103/PhysRevLett.72.1482`.

[112] D. W. Forslund *et al. Physics of Fluids*. **18,** 8, pp. 1002–1016. (1975). (See p. 59)
"Theory of stimulated scattering processes in laser-irradiated plasmas"
DOI: `10.1063/1.861248`.

[113] A. Pukhov and J. Meyer-ter Vehn. *APB*. **74,** 4-5, pp. 355–361. (2002). (See p. 60)
"Laser wake field acceleration: The highly non-linear broken-wave regime"
DOI: `10.1007/s003400200795`.

[114] I. Kostyukov *et al. PRL*. **103,** 17, pp. 1–4. (2009). (See p. 60)
"Electron self-Injection in multidimensional relativistic-plasma wake fields"
DOI: `10.1103/PhysRevLett.103.175003`.

[115] A. G. Thomas. *Physics of Plasmas*. **17,** 5. (2010). (See . 60, 66)
"Scalings for radiation from plasma bubbles"
DOI: `10.1063/1.3368678`.

[116] D. Umstadter *et al. PRL*. **76,** 12, pp. 2073–2076. (1996). (See p. 60)
"Laser injection of ultrashort electron pulses into wakefield plasma waves"
DOI: `10.1103/PhysRevLett.76.2073`.

[117] E. Esarey *et al. PRL*. **79,** 14, pp. 2682–2685. (1997). (See p. 60)
"Electron Injection into Plasma Wakefields by Colliding Laser Pulses"
DOI: `10.1103/PhysRevLett.79.2682`.

[118] S. Bulanov *et al. PRE*. **58,** 5, R5257–R5260. (1998). (See p. 60)
"Particle injection into the wave acceleration phase due to nonlinear wake wave breaking"
DOI: `10.1103/PhysRevE.58.R5257`.

[119] C. G. R. Geddes *et al. PRL*. **100,** 21, pp. 1–4. (2008). (See p. 60)
"Plasma-density-gradient injection of low absolute-momentum-spread electron bunches"
DOI: `10.1103/PhysRevLett.100.215004`.

[120] M. Chen *et al. J. Appl. Phys.* **99,** 5, p. 056109. (2006). (See p. 60)
"Electron injection and trapping in a laser wakefield by field ionization to high-charge states of gases"
DOI: `10.1063/1.2179194`.

[121] T. P. Rowlands-Rees *et al. PRL*. **100,** 10, pp. 1–4. (2008). (See p. 60)
"Laser-driven acceleration of electrons in a partially ionized plasma channel"
DOI: `10.1103/PhysRevLett.100.105005`.

[122] A. Pak *et al. PRL*. **104,** 2, pp. 1–4. (2010). (See p. 60)
"Injection and trapping of tunnel-ionized electrons into laser-produced wakes"
DOI: `10.1103/PhysRevLett.104.025003`.

[123] L. L. Yu *et al. Phys. Rev. Lett.* **112,** 12, pp. 1–5. (2013). (See p. 61)
"Two-color laser-ionization injection"
DOI: `10.1103/PhysRevLett.112.125001`.

[124] C. Durfee and H. M. Milchberg. *PRL*. **71,** 15, pp. 2409–2412. (1993). (See p. 61)
"Light Pipe for High Intensity Laser Pulses"
DOI: `10.1103/PhysRevLett.71.2409`.

[125] D. J. Spence *et al. J. Opt. Soc. Am. B*. **20,** 1, p. 138. (2003). (See p. 61)
"Gas-filled capillary discharge waveguides"
DOI: `10.1364/JOSAB.20.000138`.

[126] D. Kaganovich *et al. APL*. **75,** 6, pp. 772–774. (1999). (See . 61, 63)
"Variable profile capillary discharge for improved phase matching in a laser wakefield accelerator"
DOI: `10.1063/1.124508`.

[127] M. S. Kim *et al. APL*. **102,** 20, pp. 100–103. (2013). (See . 61, 63, 69)
"Characteristics of a tapered capillary plasma waveguide for laser wakefield acceleration"
DOI: `http://dx.doi.org/10.1063/1.4807440`.

[128] R. J. Shalloo *et al. Phys. Rev. E*. **97,** 5, p. 053203. (2018). (See p. 61)
"Hydrodynamic optical-field-ionized plasma channels"
DOI: `10.1103/PhysRevE.97.053203`.

[129] P. Sprangle *et al. Phys. Rev. E*. **63,** 5, p. 056405. (2001). (See p. 63)
"Wakefield generation and GeV acceleration in tapered plasma channels"
DOI: `10.1103/PhysRevE.63.056405`.

[130] E. Guillaume *et al. PRL*. **115,** 15, pp. 1–5. (2015). (See p. 63)
"Electron Rephasing in a Laser-Wakefield Accelerator"
DOI: `10.1103/PhysRevLett.115.155002`.

[131] B. B. Pollock *et al. PRL*. **107,** 4, pp. 1–4. (2011). (See p. 63)
"Demonstration of a narrow energy spread, 0.5GeV electron beam from a two-stage laser wakefield accelerator"
DOI: `10.1103/PhysRevLett.107.045001`.

[132] A. Debus *et al. Phys. Rev. X*. **9,** 3, pp. 1–19. (2019). (See p. 63)
"Circumventing the Dephasing and Depletion Limits of Laser-Wakefield Acceleration"
DOI: `10.1103/PhysRevX.9.031044`.

[133] J. P. Palastro *et al. Phys. Rev. Lett.* **124,** 13, p. 134802. (2020). (See p. 63)
"Dephasingless Laser Wakefield Acceleration"
DOI: `10.1103/PhysRevLett.124.134802`.

[134] C. Caizergues *et al. Nat. Photonics*. **14,** 8, pp. 475–479. (2020). (See p. 63)
"Phase-locked laser-wakefield electron acceleration"
DOI: `10.1038/s41566-020-0657-2`.

[135] B. A. Shadwick *et al. Physics of Plasmas*. **16,** 578. (2009). (See . 63, 120)
"Nonlinear laser energy depletion in laser-plasma accelerators"
DOI: `10.1063/1.1842594`.

[136] J. D. Jackson. John Wiley & Sons, Inc. (1999). (See . 65, 67, 68)
Classical Electrodynamics.

[137] Kristjan Poder, PhD Thesis: *Characterisation of self-guided laser wakefield accelerators to multi-GeV energies*. Imperial College London. (2016). (See . 66, 91).

[138] K. T. Phuoc *et al. PRL*. **97,** 22, pp. 1–4. (2006). (See p. 66)
"Imaging electron trajectories in a laser-wakefield cavity using betatron X-ray radiation"
DOI: `10.1103/PhysRevLett.97.225002`.

[139] S. Steinke *et al. Nature*. **530,** 7589, pp. 190–193. (2016). (See . 69, 92)
"Multistage coupling of independent laser-plasma accelerators"
DOI: `10.1038/nature16525`.

[140] J. Luo *et al. PRL.* **120,** 15, pp. 1–6. (2018). (See p. 69)
"Multistage Coupling of Laser-Wakefield Accelerators with Curved Plasma Channels"
DOI: `10.1103/PhysRevLett.120.154801`.

[141] Y. Sentoku *et al. Phys. Rev. Lett.* **90,** 15, p. 155001. (2003). (See p. 70)
"Anomalous Resistivity Resulting from MeV-Electron Transport in Overdense Plasma"
DOI: `10.1103/PhysRevLett.90.155001`.

[142] A. Debayle *et al. Phys. Rev. E.* **82,** 3, p. 036405. (2010). (See p. 70)
"Divergence of laser-driven relativistic electron beams"
DOI: `10.1103/PhysRevE.82.036405`.

[143] G. Raj *et al. Phys. Rev. Res.* **2,** 2, p. 023123. (2020). (See . 70, 93)
"Probing ultrafast magnetic-field generation by current filamentation instability in femtosecond relativistic laser-matter interactions"
DOI: `10.1103/PhysRevResearch.2.023123`.

[144] T. Ichino *et al.*, pp. 201 –207. Springer Series in Optical Sciences (2007). (See p. 70)
Ultrafast Optics V.

[145] C. Rolland and P. B. Corkum. *J. Opt. Soc. Am. B.* **3,** 12, pp. 1625–1629. (1986). (See p. 70)
"Generation of 130-fsec midinfrared pulses"
URL: `https://www.osapublishing.org/DirectPDFAccess/083F3FC8-E3E4-C45D-A6279AF7C388B65D_4542/josab-3-12-1625.pdf?da=1{\&}id=4542{\&}seq=0{\&}mobile=no`.

[146] U Teubner *et al. J. Phys B - At. Mol. Opt.* **34,** 2993, pp. 2993–3002. (2001). (See p. 70)
"Sub-10 fs gating of optical pulses"
URL: `http://iopscience.iop.org/article/10.1088/0953-4075/34/15/306/pdf`.

[147] T. Ceccotti *et al. PRL.* **99,** 18, p. 185002. (2007). (See p. 70)
"Proton Acceleration with High-Intensity Ultrahigh-Contrast Laser Pulses"
DOI: `10.1103/PhysRevLett.99.185002`.

[148] H. C. Kapteyn *et al. Optics Letters.* **16,** 7. (1991). (See p. 70)
"Prepulse energy suppression for high-energy ultrashort pulses using self-induced plasma shuttering"
URL: `https://www.osapublishing.org/DirectPDFAccess/08395F84-A7C7-828E-17D4C13B45AED895_59810/ol-16-7-490.pdf?da=1{\&}id=59810{\&}seq=0{\&}mobile=no`.

[149] B. Dromey *et al. Rev. Sci.* **75,** 3, pp. 645–649. (2004). (See p. 70)
"The plasma mirror - A subpicosecond optical switch for ultrahigh power lasers"
DOI: `10.1063/1.1646737`.

[150] C. Thaury *et al. Nature Physics.* **3,** 6, pp. 424–429. (2007). (See . 70, 93)
"Plasma mirrors for ultrahigh-intensity optics"
DOI: `10.1038/nphys595`.

[151] H Vincenti *et al. Nat. Com.* **5,** p. 3403. (2014). (See p. 70)
"Optical properties of relativistic plasma mirrors."
DOI: `10.1038/ncomms4403`.

[152] B. H. Shaw *et al. Physics of Plasmas.* **23,** 6, pp. 1–9. (2016). (See . 70, 92, 93, 97)
"Reflectance characterization of tape-based plasma mirrors"
DOI: `10.1063/1.4954242`.

[153] A. Debayle *et al. Phys. Rev. E.* **92,** 5, pp. 1–6. (2015). (See p. 70)
"Self-consistent theory of high-order harmonic generation by relativistic plasma mirror"
DOI: `10.1103/PhysRevE.92.053108`.

[154] Z.-Y. Chen and A. Pukhov. *Nat. Com.* **7,** p. 12515. (2016). (See p. 70)
"Bright high-order harmonic generation with controllable polarization from a relativistic plasma mirror"
DOI: `10.1038/ncomms12515`.

[155] C. Hooker *et al. Journal de Physique IV (Proceedings).* **133,** pp. 673–7. (2006). (See p. 71)
"The Astra Gemini project - a dual-beam petawatt Ti:sapphire laser system"
DOI: `10.1051/jp4:2006133135`.

[156] C. J. Hooker *et al. 2008 Conference on Quantum Electronics and Laser Science Conference on Lasers and Electro-Optics, CLEO/QELS*, pp. 2–3. (2008). (See p. 71)
"Commissioning the Astra Gemini petawatt Ti:sapphire laser system"
DOI: `10.1109/CLEO.2008.4552106`.

[157] R. Pattathil. *STFC. Astra Gemini Laser System*. URL: https://www.clf.stfc.ac.uk/Pages/Astra-Target-Area.aspx (visited on 10/11/2017) (see p. 71).

[158] A. G. Glendinning *et al. Phys. Med. Biol.* **46,** 2, pp. 517–530. (2001). (See p. 72)
"Measurement of the response of Gd 2 O 2 S:Tb phosphor to 6 MV x-rays"
DOI: 10.1088/0031-9155/46/2/317.

[159] E. Süli and D. F. Mayers. "Initial value problems for ODEs". *An Introduction to Numerical Analysis*. May 2020. Cambridge University Press, 2012. Chap. 12, pp. 310–360. DOI: 10.1017/cbo9780511801181.013 (see . 72, 73).

[160] S. R. Nagel, PhD Thesis: *Studies of Electron Acceleration Mechanisms in Relativistic Laser-Plasma Interactions*. Imperial College London. (2009). (See . 73, 74).

[161] S. Kneip, PhD Thesis: *Laser Plasma Accelerator and Wiggler*. Imperial College London. (2010). (See p. 74).

[162] J. R. Janesick *et al. OpticalEngineering*. **26,** May, pp. 692–714. (1987). (See p. 74)
"Scientific charge-coupled devices".

[163] Andor. *Direct Detection Processing*. Tech. rep. 1995, pp. 114–176. DOI: 10.1007/978-3-540-49206-1_4 (see . 74, 76, 79).

[164] B. L. Henke *et al.* **54,** 2, pp. 181–342. (1993). (See . 74, 76, 114)
"X-ray interactions: Photoabsorption, scattering, transmission, and reflection at E = 50-30, 000 eV, Z = 1-92"
DOI: 10.1006/adnd.1993.1013.

[165] I. Fujieda *et al. IEEE Transactions on Nuclear Science*. **38,** 2, pp. 255–262. (1991). (See p. 75)
"X-ray and Charged Particle Detection with CsI(Tl) Layer Coupled to a-Si:H Photodiode Layers"
DOI: 10.1109/23.289306.

[166] J. G. Rocha *et al. Proceedings of IEEE Sensors*. **3,** pp. 1257–1260. (2004). (See p. 75)
"Modeling of the performance of scintillator based X-ray detectors"
DOI: 10.1109/icsens.2004.1426409.

[167] J. C. Wood, PhD Thesis: *Betatron Radiation from Laser Wakefield Accelerators and its Applications*. Imperial College London. (2016). (See . 75, 131, 158, 173).

[168] Hamamatsu. *X-Ray Scintillator*. 2020. URL: https://www.hamamatsu.com/resources/pdf/etd/FOS_ACS_GPXS_ALS_TXPR1024E.pdf (see p. 75).

[169] T. S. Huang *et al. IEEE Transactions on Acoustics, Speech, and Signal Processing*. **27,** 1, pp. 13–18. (1979). (See p. 78)
"A Fast Two-Dimensional Median Filtering Algorithm"
DOI: 10.1109/TASSP.1979.1163188.

[170] C. D. Baird *et al. CLF Annual Report 2017-18*, pp. 1–6. (2020). (See p. 79)
"Plasma density optimisation of laser-wakefield acceleration for high-brightness bremsstrahlung emission applied to advanced manufacturing imaging".

[171] N. Lopes. Personal communication: NHairCut2D.m - Median Like Noise Removal. Mar. 30, 2018 (see p. 79).

[172] J. P. Boris. *Proceedings of the Conference on the Numerical Simulation of Plasmas 4th*. July, pp. 3–67. (1971). (See p. 81)
"Relativistic Plasma Simulation - Optimization of a Hybrid Code".

[173] A. Taflove and S. C. Hagness. Artech House (1995). (See p. 81)
Computational Electrodynamics: The Finite-Difference Time-Domain Method.

[174] R. Courant *et al. Mathematische Annalen*. **100,** (1928). (See p. 81)
"Über die partiellen Differenzengleichungen der mathematischen Physik".

[175] B. M. Cowan *et al. Journal of Computational Physics*. **230,** 1, pp. 61–86. (2011). (See p. 82)
"Characteristics of an envelope model for laser-plasma accelerator simulation"
DOI: 10.1016/j.jcp.2010.09.009.

[176] H.-E. Tsai *et al. Phys. Plasmas*. **24,** 013106. (2017). (See p. 92)
"Self-aligning concave relativistic plasma mirror with adjustable focus"
DOI: 10.1063/1.4973432.

[177] B. H. Shaw, PhD Thesis: *Laser-plasma interactions from thin tapes for high-energy electron accelerators and seeding compact FELs*. University of California, Berkeley. (2015). (See p. 92).

[178] C. Kittel. W. H. Freeman (1980). (See p. 95)
Thermal physics.

[179] I. H. Malitson. *J. Opt. Soc. Am.* **55,** 10, p. 1205. (1965). (See p. 95)
"Interspecimen Comparison of the Refractive Index of Fused Silica"
DOI: `10.1364/josa.55.001205`.

[180] THORLABS. *Reflectance of Optics with Unprotected Gold Coating*. 2020. URL: `https://www.thorlabs.com/images/TabImages/Thorlabs_Unprotected_Gold_CoatingM03.xlsx` (visited on 09/06/2020) (see p. 95).

[181] THORLABS. *Reflectance of Optics with Protected Silver Coating*. 2020. URL: `https://www.thorlabs.com/images/TabImages/Thorlabs_Protected_Silver_Coating.xlsx` (visited on 09/06/2020) (see p. 95).

[182] R. D'Arcy *et al. PRL*. **122,** 3, p. 034801. (2019). (See p. 106)
"Tunable Plasma-Based Energy Dechirper"
DOI: `10.1103/PhysRevLett.122.034801`.

[183] J.-N. Gruse *et al. NIMA*, p. 164369. (2020). (See . 109, 136, 169)
"Application of compact laser-driven accelerator X-ray sources for industrial imaging"
DOI: `10.1016/j.nima.2020.164369`.

[184] K Ta Phuoc *et al. Physics of Plasmas*. **14,** 8. (2007). (See p. 110)
"Demonstration of the ultrafast nature of laser produced betatron radiation"
DOI: `10.1063/1.2754624`.

[185] B. Mahieu *et al. Nat. Com.* **9,** 1, p. 3276. (2018). (See . 110, 138)
"Probing warm dense matter using femtosecond X-ray absorption spectroscopy with a laser-produced betatron source"
DOI: `10.1038/s41467-018-05791-4`.

[186] S. Kneip *et al. APL*. **99,** 9, pp. 1–4. (2011). (See . 110, 111)
"X-ray phase contrast imaging of biological specimens with femtosecond pulses of betatron radiation from a compact laser plasma wakefield accelerator"
DOI: `10.1063/1.3627216`.

[187] M. Stampanoni *et al. Developments in X-Ray Tomography V*. Vol. 6318, pp. 63180M–63180M–14. (2006). (See p. 111)
"Trends in synchrotron-based tomographic imaging: the SLS experience"
DOI: `10.1117/12.679497`.

[188] S. Fourmaux *et al. NJP*. **13,** (2011). (See p. 111)
"Demonstration of the synchrotron-type spectrum of laser-produced Betatron radiation"
DOI: `10.1088/1367-2630/13/3/033017`.

[189] F. Träger, pp. 1153–1164. Springer Berlin Heidelberg (2012). (See p. 111)
Springer Handbook of Lasers and Optics.

[190] A. Buck *et al. Nature Physics*. **7,** 7, pp. 543–548. (2011). (See p. 116)
"Real-time observation of laser-driven electron acceleration"
DOI: `10.1038/nphys1942`.

[191] Z. H. He *et al. NJP*. **15,** (2013). (See p. 122)
"High repetition-rate wakefield electron source generated by few-millijoule, 30 fs laser pulses on a density downramp"
DOI: `10.1088/1367-2630/15/5/053016`.

[192] Japan Inspection Instruments Manufacturers' Association (JIMA). *JIMA-C006-R:2011 Micro resolution chart for X-ray*. 2012. URL: `http://www.jima.jp/content/pdf/rt_ct-02cata02.pdf` (visited on 08/25/2020) (see . 130, 134).

[193] K. Acatay. "Carbon fibers". *Fiber Technology for Fiber-Reinforced Composites*. Ed. by M. Ö. Seydibeyoğlu *et al.* Woodhead Publishing Series in Composites Science and Engineering. Elsevier, 2017, pp. 123–151. DOI: `10.1016/B978-0-08-101871-2.00006-0` (see p. 133).

[194] J. P. Kruth *et al. CIRP Ann.-Manuf. Techn.* **60,** 2, pp. 821–842. (2011). (See p. 136)
"Computed tomography for dimensional metrology"
DOI: `10.1016/j.cirp.2011.05.006`.

[195] L. A. Feldkamp *et al. J. Opt. Soc. Am. A*. **1,** 6, pp. 612–619. (1984). (See p. 136)
"Practical cone-beam algorithm".

[196] R. Schmitt and C. Niggemann. *Meas. Sci. Technol.* **21,** 5. (2010). (See p. 136)
"Uncertainty in measurement for x-ray-computed tomography using calibrated work pieces"
DOI: `10.1088/0957-0233/21/5/054008`.

[197] J. Kumar *et al.* *Meas. Sci. Technol.* **22,** 3. (2011). (See p. 136)
"Analysis of the effect of cone-beam geometry and test object configuration on the measurement accuracy of a computed tomography scanner used for dimensional measurement"
DOI: `10.1088/0957-0233/22/3/035105`.

[198] P. Müller *et al.* *IJMQE.* **3,** 2, pp. 107–115. (2012). (See p. 136)
"A study on evaluation strategies in dimensional X-ray computed tomography by estimation of measurement uncertainties"
DOI: `10.1051/ijmqe/2012011`.

[199] J. Hiller *et al.* *Meas. Sci. Technol.* **23,** 8. (2012). (See p. 136)
"Physical characterization and performance evaluation of an x-ray micro-computed tomography system for dimensional metrology applications"
DOI: `10.1088/0957-0233/23/8/085404`.

[200] S. Carmignato. *CIRP Ann.-Manuf. Techn.* **61,** 1, pp. 491–494. (2012). (See p. 136)
"Accuracy of industrial computed tomography measurements: Experimental results from an international comparison"
DOI: `10.1016/j.cirp.2012.03.021`.

[201] J. A. B. Angel *et al.* *General rights Inter laboratory comparison on Industrial Computed Tomography CIA-CT comparison.* Tech. rep. 01. DTU Mechanical Engineering, 2013 (see p. 136).

[202] A. Townsend *et al.* *Addit. Manuf.* **23,** pp. 422–432. (2018). (See p. 136)
"An interlaboratory comparison of X-ray computed tomography measurement for texture and dimensional characterisation of additively manufactured parts"
DOI: `10.1016/j.addma.2018.08.013`.

[203] M. Loveridge *et al.* *Batteries.* **4,** 1, p. 3. (2018). (See p. 137)
"Looking Deeper into the Galaxy (Note 7)"
DOI: `10.3390/batteries4010003`.

[204] M. Ebner *et al.* *Science.* **342,** 6159, pp. 716–720. (2013). (See p. 138)
"Visualization and Quantification of Electrochemical and Mechanical Degradation in Li Ion Batteries"
DOI: `10.1126/science.1241882`.

[205] P. Pietsch *et al.* *Nat. Com.* **7,** 1, p. 12909. (2016). (See p. 138)
"Quantifying microstructural dynamics and electrochemical activity of graphite and silicon-graphite lithium ion battery anodes"
DOI: `10.1038/ncomms12909`.

[206] L. Nowack *et al.* *Scientific Reports.* **6,** 1, p. 21479. (2016). (See p. 138)
"Rapid Mapping of Lithiation Dynamics in Transition Metal Oxide Particles with Operando X-ray Absorption Spectroscopy"
DOI: `10.1038/srep21479`.

[207] J. Wang *et al.* *Nat. Com.* **7,** 1, p. 12372. (2016). (See p. 138)
"Visualization of anisotropic-isotropic phase transformation dynamics in battery electrode particles"
DOI: `10.1038/ncomms12372`.

[208] S. C. Garcea *et al.* *Composites Science and Technology.* **156,** pp. 305–319. (2018). (See p. 138)
"X-ray computed tomography of polymer composites"
DOI: `https://doi.org/10.1016/j.compscitech.2017.10.023`.

[209] L. R. Pickard *et al.* *21st International Conference on Composite Materials.* (2017). (See p. 139)
"Tracking the Evolution of a Defect, Characteristic of Afp Layup, During Cure With in-Process Micro-Ct Scanning"
URL: `http://www.bristol.ac.uk/composites/`.

[210] L. R. Pickard. *Dissertation. University of Bristol.* (2019). (See p. 139)
"Towards Efficient Composites Manufacture Through In-Process Monitoring and Knowledge Management"
URL: `https://bris.on.worldcat.org/oclc/1126650182`.

[211] D. F. Sentis *et al.* *Composites Part A: Applied Science and Manufacturing.* **92,** pp. 51–61. (2017). (See p. 139)
"3D in situ observations of the compressibility and pore transport in Sheet Moulding Compounds during the early stages of compression moulding"
DOI: `https://doi.org/10.1016/j.compositesa.2016.10.031`.

[212] P. Mason *et al.* *Optica.* **4,** 4, pp. 438–439. (2017). (See p. 140)
"Kilowatt average power 100 J-level diode pumped solid state laser"
DOI: `10.1364/OPTICA.4.000438`.

[213] L. Gizzi *et al. NIMA*. **909,** pp. 58–66. (2018). (See p. 140)
"A viable laser driver for a user plasma accelerator"
DOI: `10.1016/j.nima.2018.02.089`.

[214] C. L. Haefner *et al. Proceedings Volume 10241, Research Using Extreme Light: Entering New Frontiers with Petawatt-Class Lasers III*. Vol. 10241, p. 1024102. (2017). (See p. 140)
"High average power, diode pumped petawatt laser systems: a new generation of lasers enabling precision science and commercial applications"
DOI: `10.1117/12.2281050`.

[215] W. P. Leemans. *Workshop held at Lawrence Berkeley National Laboratory*. (2017). (See p. 140)
"Report of Workshop on Laser Technology for k-BELLA and Beyond".

[216] N. Delbos *et al. NIMA*. **909,** pp. 318–322. (2018). (See p. 140)
"LUX – A laser–plasma driven undulator beamline"
DOI: `10.1016/j.nima.2018.01.082`.

[217] Z.-H. He *et al. Nat. Commun.* **6,** 1, p. 7156. (2015). (See p. 143)
"Coherent control of plasma dynamics"
DOI: `10.1038/ncomms8156`.

[218] M. J. V. Streeter *et al. Appl. Phys. Lett.* **112,** 24, p. 244101. (2018). (See p. 144)
"Temporal feedback control of high-intensity laser pulses to optimize ultrafast heating of atomic clusters"
DOI: `10.1063/1.5027297`.

[219] S. J. D. Dann *et al. Phys. Rev. Accel. Beams*. **22,** 4, p. 041303. (2019). (See p. 144)
"Laser wakefield acceleration with active feedback at 5 Hz"
DOI: `10.1103/PhysRevAccelBeams.22.041303`.

[220] R. J. Shalloo *et al.*, pp. 1–10. (2020). (See p. 144)
"Automation and control of laser wakefield accelerators using Bayesian optimisation"
URL: `http://arxiv.org/abs/2007.14340`.

[221] J. Mockus. "The Bayesian approach to global optimization". *Syst. Model. Optim.* Berlin/Heidelberg: Springer-Verlag, 1982, pp. 473–481. DOI: `10.1007/BFb0006170` (see p. 144).

[222] B. Shahriari *et al. Proc. IEEE*. **104,** 1, pp. 148–175. (2016). (See p. 144)
"Taking the Human Out of the Loop: A Review of Bayesian Optimization"
DOI: `10.1109/JPROC.2015.2494218`.

[223] N. Srinivas *et al. ICML 2010*. Vol. 58. 5, pp. 3250–3265. (2010). (See p. 144)
"Information-Theoretic Regret Bounds for Gaussian Process Optimization in the Bandit Setting"
DOI: `10.1109/TIT.2011.2182033`.

[224] V. Leroux *et al. Opt. Express*. **28,** 6, p. 8257. (2020). (See p. 144)
"Description of spatio-temporal couplings from heat-induced compressor grating deformation"
DOI: `10.1364/OE.386112`.

[225] FASTLITE. *Dazzler*. 2020. URL: `https://fastlite.com/produits/dazzler-ultrafast-pulse-shaper/` (visited on 09/04/2020) (see p. 144).

[226] I. Optics. *Haso4*. 2020. URL: `https://www.imagine-optic.com/product/haso4-broadband-2/` (visited on 09/04/2020) (see p. 145).

[227] L. R. Dalesio *et al. NIMA*. **352,** 1-2, pp. 179–184. (1994). (See p. 146)
"The experimental physics and industrial control system architecture: past, present, and future"
DOI: `10.1016/0168-9002(94)91493-1`.

[228] C. B. Schroeder *et al. AIP Conf. Proc.* Vol. 1777. October, p. 020001. (2016). (See p. 161)
"Efficiency considerations for high-energy physics applications of laser-plasma accelerators"
DOI: `10.1063/1.4965590`.

[229] D. Papp *et al. NIMA*. **909,** November 2017, pp. 145–148. (2018). (See p. 161)
"Laser wakefield acceleration with high-power, few-cycle mid-IR lasers"
DOI: `10.1016/j.nima.2018.01.050`.

[230] G. G. Scott *et al. NJP*. **17,** 3, p. 33027. (2015). (See p. 167)
"Optimization of plasma mirror reflectivity and optical quality using double laser pulses"
DOI: `10.1088/1367-2630/17/3/033027`.

[231] M. Mirzaie *et al.* *Scientific Reports*. **5,** pp. 1–9. (2015)
. “Demonstration of self-truncated ionization injection for GeV electron beams”
DOI: 10.1038/srep14659.

[232] J. P. Couperus *et al.* *Nat. Com.* **8,** 1, pp. 1–7. (2017)
. “Demonstration of a beam loaded nanocoulomb-class laser wakefield accelerator”
DOI: 10.1038/s41467-017-00592-7.

[233] K. K. Swanson *et al.* *PRAB*. **20,** 5, pp. 1–6. (2017)
. “Control of tunable, monoenergetic laser-plasma-accelerated electron beams using a shock-induced density downramp injector”
DOI: 10.1103/PhysRevAccelBeams.20.051301.

[234] J. Ferri *et al.* *Scientific Reports*. **6,** June, pp. 1–10. (2016)
. “Effect of experimental laser imperfections on laser wakefield acceleration and betatron source”
DOI: 10.1038/srep27846.

[235] S. Kuschel *et al.* *PRAB*. **19,** 7, pp. 1–9. (2016)
. “Demonstration of passive plasma lensing of a laser wakefield accelerated electron bunch”
DOI: 10.1103/PhysRevAccelBeams.19.071301.

[236] C. Thaury *et al.* *Scientific Reports*. **5,** pp. 2–8. (2015)
. “Shock assisted ionization injection in laser-plasma accelerators”
DOI: 10.1038/srep16310.

[237] M. Schnell *et al.* *Journal of Plasma Physics*. **81,** 4. (2015)
. “Characterization and application of hard X-ray betatron radiation generated by relativistic electrons from a laser-wakefield accelerator”
DOI: 10.1017/S0022377815000379.

[238] K. Khrennikov *et al.* *PRL*. **114,** 19, pp. 1–5. (2015)
. “Tunable all-optical quasimonochromatic Thomson X-ray source in the nonlinear regime”
DOI: 10.1103/PhysRevLett.114.195003.

[239] W. P. Leemans *et al.* *PRL*. **113,** 24, pp. 1–5. (2014)
. “Multi-Gev electron beams from capillary-discharge-guided subpetawatt laser pulses in the self-trapping regime”
DOI: 10.1103/PhysRevLett.113.245002.

[240] N. D. Powers *et al.* *Nat. Photonics*. **8,** 1, pp. 28–31. (2014)
. “Quasi-monoenergetic and tunable X-rays from a laser-driven Compton light source”
DOI: 10.1038/nphoton.2013.314.

[241] G. Sarri *et al.* *PRL*. **113,** 22, pp. 1–5. (2014)
. “Ultrahigh brilliance multi-MeV γ-ray beams from nonlinear relativistic thomson scattering”
DOI: 10.1103/PhysRevLett.113.224801.

[242] H. T. Kim *et al.* *PRL*. **111,** 165002. (2013)
. “Enhancement of Electron Energy to the Multi-GeV Regime by a Dual-Stage Laser-Wakefield Accelerator Pumped by Petawatt Laser Pulses”
DOI: 10.1103/PhysRevLett.111.165002.

[243] S. Chen *et al.* *PRL*. **110,** 15, pp. 1–5. (2013)
. “MeV-energy X rays from inverse compton scattering with laser-wakefield accelerated electrons”
DOI: 10.1103/PhysRevLett.110.155003.

[244] S. Corde *et al.* *Nat. Com.* **4,** pp. 1–7. (2013)
. “Observation of longitudinal and transverse self-injections in laser-plasma accelerators”
DOI: 10.1038/ncomms2528.

[245] P. A. Walker *et al.* *NJP*. **15,** (2013)
. “Investigation of GeV-scale electron acceleration in a gas-filled capillary discharge waveguide”
DOI: 10.1088/1367-2630/15/4/045024.

[246] F. Albert *et al.* *PRL*. **111,** 23, pp. 1–5. (2013)
. “Angular dependence of betatron X-ray spectra from a laser-wakefield accelerator”
DOI: 10.1103/PhysRevLett.111.235004.

[247] M. Burza *et al.* *PRST - AB*. **16,** 1, pp. 3–7. (2013)
. “Laser wakefield acceleration using wire produced double density ramps”
DOI: 10.1103/PhysRevSTAB.16.011301.

[248] M. Z. Mo *et al.* *APL*. **100,** 7, pp. 1–4. (2012)
. “Quasimonoenergetic electron beams from laser wakefield acceleration in pure nitrogen”
DOI: 10.1063/1.3685464.

[249] S. Fourmaux *et al.* *APL*. **101,** 11. (2012)
. “Quasi-monoenergetic electron beams production in a sharp density transition”
DOI: 10.1063/1.4752114.

[250] P. Brijesh *et al.* *Physics of Plasmas*. **19,** 6. (2012)
. “Tuning the electron energy by controlling the density perturbation position in laser plasma accelerators”
DOI: 10.1063/1.4725421.

[251] A. J. Gonsalves *et al.* *Nature Physics*. **7,** 11, pp. 862–866. (2011)
. “Tunable laser plasma accelerator based on longitudinal density tailoring”
DOI: 10.1038/nphys2071.

[252] O. Lundh *et al.* *Nature Physics*. **7,** 3, pp. 219–222. (2011)
. “Few femtosecond, few kiloampere electron bunch produced by a laser-plasma accelerator”
DOI: 10.1038/nphys1872.

[253] J. S. Liu *et al.* *PRL*. **107,** 3, pp. 2–5. (2011)
. “All-optical cascaded laser wakefield accelerator using ionization-induced injection”
DOI: 10.1103/PhysRevLett.107.035001.

[254] H. Lu *et al.* *APL*. **99,** 9, pp. 1–4. (2011)
. “Laser wakefield acceleration of electron beams beyond 1 GeV from an ablative capillary discharge waveguide”
DOI: 10.1063/1.3626042.

[255] C. E. Clayton *et al.* *PRL*. **105,** 10, pp. 3–6. (2010)
. “Self-guided laser wakefield acceleration beyond 1 GeV using ionization-induced injection”
DOI: 10.1103/PhysRevLett.105.105003.

[256] T. P. Ibbotson *et al.* *NJP*. **12,** (2010)
. “Investigation of the role of plasma channels as waveguides for laser-wakefield accelerators”
DOI: 10.1088/1367-2630/12/4/045008.

[257] K. Schmid *et al.* *PRST - AB*. **13,** 9, pp. 1–5. (2010)
. “Density-transition based electron injector for laser driven wakefield accelerators”
DOI: 10.1103/PhysRevSTAB.13.091301.

[258] D. H. Froula *et al.* *PRL*. **103,** 21, pp. 1–4. (2009)
. “Measurements of the critical power for self-injection of electrons in a laser wakefield accelerator”
DOI: 10.1103/PhysRevLett.103.215006.

[259] S. Kneip *et al.* *PRL*. **103,** 3, pp. 8–11. (2009)
. “Near-GeV acceleration of electrons by a nonlinear plasma wave driven by a self-guided laser pulse”
DOI: 10.1103/PhysRevLett.103.035002.

[260] K. Schmid *et al.* *PRL*. **102,** 12, pp. 1–4. (2009)
. “Few-cycle laser-driven electron acceleration”
DOI: 10.1103/PhysRevLett.102.124801.

[261] N. A. Hafz *et al.* *Nat. Photonics*. **2,** 9, pp. 571–577. (2008)
. “Stable generation of GeV-class electron beams from self-guided laser-plasma channels”
DOI: 10.1038/nphoton.2008.155.

[262] A. Gamucci *et al.* *IEEE Transactions on Plasma Science*. **36,** 4 PART 4, pp. 1699–1706. (2008)
. “Advanced diagnostics applied to a laser-driven electron-acceleration experiment”
DOI: 10.1109/TPS.2008.2000898.

[263] S. Karsch *et al.* *NJP*. **9,** (2007)
. “GeV-scale electron acceleration in a gas-filled capillary discharge waveguide”
DOI: 10.1088/1367-2630/9/11/415.

[264] T. Ohkubo *et al. PRST - AB*. **10,** 3, pp. 1–6. (2007)
. “Temporal characteristics of monoenergetic electron beams generated by the laser wakefield acceleration”
DOI: `10.1103/PhysRevSTAB.10.031301`.

[265] S. Masuda *et al. Physics of Plasmas*. **14,** 2, pp. 1–8. (2007)
. “Energy scaling of monoenergetic electron beams generated by the laser-driven plasma based accelerator”
DOI: `10.1063/1.2434248`.

[266] W. P. Leemans *et al. Nature Physics*. **2,** 10, pp. 696–699. (2006)
. “GeV electron beams from a centimetre-scale accelerator”
DOI: `10.1038/nphys418`.

[267] S. A. Reed *et al. APL*. **89,** 23, pp. 1–4. (2006)
. “Photonuclear fission with quasimonoenergetic electron beams from laser wakefields”
DOI: `10.1063/1.2400400`.

[268] S. P. Mangles *et al. PRL*. **96,** 21, pp. 1–4. (2006)
. “Laser-wakefield acceleration of monoenergetic electron beams in the first plasma-wave period”
DOI: `10.1103/PhysRevLett.96.215001`.

[269] T. Hosokai *et al. PRE*. **73,** 3, pp. 1–8. (2006)
. “Observation of strong correlation between quasimonoenergetic electron beam generation by laser wakefield and laser guiding inside a preplasma cavity”
DOI: `10.1103/PhysRevE.73.036407`.

[270] B. Hidding *et al. PRL*. **96,** 10, pp. 3–6. (2006)
. “Generation of quasimonoenergetic electron bunches with 80-fs laser pulses”
DOI: `10.1103/PhysRevLett.96.105004`.

[271] C. T. Hsieh *et al. PRL*. **96,** 9, pp. 7–10. (2006)
. “Tomography of injection and acceleration of monoenergetic electrons in a laser-wakefield accelerator”
DOI: `10.1103/PhysRevLett.96.095001`.

[272] S. Masuda *et al. Journal De Physique. IV : JP*. **133,** pp. 1127–1129. (2006)
. “Experimental observation of monoenergetic electron beam generated by laser-driven plasma acceleration”
DOI: `10.1051/jp4:2006133229`.

[273] E. Miura *et al. APL*. **86,** 25, pp. 1–3. (2005)
. “Demonstration of quasi-monoenergetic electron-beam generation in laser-driven plasma acceleration”
DOI: `10.1063/1.1949289`.